PhD thesis

Université de Limoges

University of Limoges

ED 609 - Sciences et Ingénierie des Matériaux, Mécanique, Énergétique (SIMME)

Institut de recherche sur les céramiques (IRCER)

Thesis submitted for the degree of

Doctor of Philosophy of Limoges University

Specialization: Ceramic Materials and Surface treatments

Presented by

Imad Khlifi

On November 27, 2019

Optimisation of optical methods for strain field measurements dedicated to the characterisation of the fracture behaviour of refractories: Application to magnesia-based materials

Supervised by M. Marc Huger, M. Jean-Christophe Dupré and M. Octavian Ion Pop

JURY :

President of the jury

M. Thierry Cutard, Professor, ICA Albi (ICAA), Ecole des Mines d'Albi (France)

Reviewers

M. Dietmar Gruber, Associate Professor, Chair of Ceramics, Montanuniversität Leoben (Austria)

M. Giovanni Bruno, Professor, BAM Berlin, Potsdam University (Germany)

Examiners

M. Marc Huger, Professor, IRCER, University of Limoges

M. Jean-Christophe Dupré, Researcher, PPRIME, University of Poitiers

M. Octavien Pop, Associate Professor, GC2D, University of Limoges

Invited

M. Martin Geith, Project manager, RHI-Magnesita (Austria)

M. Pascal Pilate, Refractories development, Belgian Ceramic Research Centre (Belgium)

BY NC ND

Acknowledgements

Firstly, I would like to express my utmost gratitude to Professor Marc Huger for the interesting scientific discussions, precious technical help and unconditional encouragement during the most difficult steps of this PhD. His own passion and commitment to science will certainly remain a source of inspiration in my future endeavours.

I am very grateful for the precious help and advice provided by Jean-Christophe Dupré throughout this PhD. My thanks also go to Pascal Doumalin for his availability and his ability to bring insightful criticism. Special thanks to Octavian Pop for his sympathy and for sharing his hands-on experience in research with me.

My sincere thanks also go to all members of the jury and especially Professor Thierry Cutard for doing me the honour of being the president of the jury, Dietmar Gruber and Giovanni Bruno for reviewing my work and providing insightful comments.

I am very proud and grateful to be part of the FIRE (Federation for International Refractory research and Education) network. This research has been carried out thanks to FIRE project Delta, which brought in expertise from both academic and industrial partners. From the academic side, I would like to thank PhD candidate Simon Etzold and Professor Thorsten Tonnesen from RWTH (Aachen, Germany) for their collaboration and support during the beginning of my thesis. From the industrial side, many thanks to Sido Sinnema from Tata Steel (Netherlands) for his strong commitment to the FIRE network and his positive attitude. Special mention to Martin Geith and Ulrich Marshall from RHI-Magnesita (Austria) for their close collaboration during my PhD.

I would like to thank Stéphane Morel for his advice and expertise on the fracture behaviour of quasi-brittle materials, which helped set up interesting comparisons with the approach developed in the research work. In the same way, thanks to Pascal Pilate for bringing interesting suggestions to my PhD work and sharing his knowledge on post-mortem SEM observations of Wedge Splitting samples.

Many thanks to Damien André for helping me set up the Linux environment and for introducing me to python programming. His support during this research was very helpful in many ways.

Special mention to colleagues from the mechanical workshop, Gilles Desvergne, Sébastien Faure, Jean-michel Reigue, Alexandre Bonnet and Nicolas Lory (peace be upon him). I am extremely grateful for the time and dedication they have put to help me during my PhD, their technical support was incredibly valuable.

BY NC ND

To all colleagues from IRCER laboratory and ENSIL-ENSCI school, including administrative and accounting departments, thank you for making this journey so enjoyable. In particular, thank you Nadine Tchefranoff for your reactivity and efficiency in dealing with the numerous paperwork associated with conferences and related trips.

This human experience would not have been complete without my colleagues from the IRCER laboratory that have proved to be good friends during my time in Limoges. My thanks go to Fanny and Eugène for welcoming me in the TMC team and their valuable support. To Andrezj, Aliz, Christina, Diana, Fateh, Guy, Halima, Hatim, Imane, Ilona, Karolina, Moustapha, Rafael, Siham, Soufiane, Thi and Yassine, thanks for making this journey an enjoyable one, with many good memories. Special thanks to Robert and Farid for their commitment and dedication to always losing with dignity (most of the time) at billiard pool and baby-foot.

I could not forget to thank my parents and my brother for their unconditional moral support in all my endeavours; they have always been beside me. Many thanks to my family and friends for their encouragement. Last but not least, this PhD and my time in Limoges would not have been the same without my life companion, Justine. I am deeply touched by her daily support and for bringing me happiness every day.

BY NC ND

Droits d’auteurs

Cette création est mise à disposition selon le Contrat :
« **Attribution-Pas d'Utilisation Commerciale-Pas de modification 3.0 France** »
disponible en ligne : *http://creativecommons.org/licenses/by-nc-nd/3.0/fr/*

Table of content

BY NC ND

BY NC ND

BY NC ND

General introduction

Refractories are granular inorganic materials that are used mostly in industrial applications involving high temperatures and corrosive environments, such as steel, cement, lime, ceramic, non-ferrous metals, and energy sector among others. These materials are often a result of complex formulations involving multiple raw materials in order to tailor refractory properties to fit the specifications required by each industrial application. In this regard, each application requires specific thermochemical and thermomechanical properties to ensure good operating conditions for the industrial process but also for the safety of the plant and the workers therein. Therefore, the cost of a refractory is not only defined by the cost of raw materials but also by the potential economic and safety loss for the end-consumer in case of critical failures in their production process. This is one of the main drivers for refractory development where an increased service life is sought by increasing refractory performance for applications with severe solicitations such as high corrosion or thermal shocks.

The case of thermal shock is usually a complex one as it involves high stresses locally that can lead to significant crack growth, which in turn might accelerate refractory wear due to infiltration by corrosive products. In this sense, the thermal shock resistance of refractories is considered to be a key material property, which is known to be closely linked to crack propagation resistance. The latter is often associated with a non-linear mechanical behaviour that promotes strain-to-rupture instead of strength, leading to a more “flexible” material. In fact, most refractories exhibit deviations from pure linear elasticity due to strong heterogeneities in their microstructure, such as large aggregates, pores and microcracks. These features are sometimes introduced voluntarily to promote energy-consuming mechanisms that limit crack propagation. Ultimately, material design for thermal shock applications relies on a deep understanding of microstructure-property relationships.

Previous works on this topic have been carried out in the IRCER laboratory (Limoges, France) with many collaborations nationally (France) and internationally through FIRE (Federation for International Refractory research and Education) projects. The FIRE network regroups academic and industrial partners that promote refractory research programs and share a remarkable skillset in this domain.

Thanks to these collaborations, a significant experience has been acquired over the past 15 years in the characterisation of the thermomechanical and fracture behaviour of refractory materials with a non-linear mechanical behaviour. In particular, during the PhD of Renaud Grasset-Bourdel (2011), the impact of thermal damage on the thermomechanical behaviour of

BY NC ND

magnesia-spinel refractories with simplified compositions was investigated extensively. Given the thermal expansion mismatch between magnesia and spinel leading to microcrack networks, it was necessary to consider magnesia as a matrix and spinel as inclusions in a two-phase model material approach for a better understanding of microstructure influence. These materials were investigated by using advanced experiments. Indeed, tensile tests and the Wedge Splitting Test (WST) have underlined the non-linear character of the mechanical behaviour and the high level of fracture energy of these materials, respectively. Moreover, the application of optical methods in the PhD of Younés Belrhiti (2015), in particular Digital Image Correlation (DIC), provided a rich set of information about material strain fields and fracture in relation to initially microcracked materials. The observation of the crack branching phenomenon in magnesia-spinel materials was a key result.

Ultimately, these studies have brought the required knowledge and expertise to tackle the different topics in relation with the thermal shock resistance of refractories.

In the present PhD thesis, a thorough investigation of the thermomechanical properties of magnesia-spinel and magnesia-hercynite refractories will be proposed, with an emphasis on fracture behaviour monitoring using a refined DIC method, called 2P-DIC, developed by the Pprime Institute (Poitiers, France). The main challenges of this PhD reside in the understanding of the influence of thermally induced microcracks, related to inclusion nature and fraction, on the complex fracture behaviour of magnesia-based materials. In relation to this, a novel fracture analysis based on the application of a refined DIC method is developed and optimised.

In the first chapter of this thesis, the state-of-the-art regarding refractory thermomechanical and fracture behaviour along with optical kinematic field measurement techniques is established. After introducing the origins of thermal stress in refractories, the thermo-elastic and energetic approaches of thermal shock resistance are presented. The mechanical and fracture behaviours of refractories are then discussed to propose key microstructure design criteria for enhancing crack propagation resistance. The development of Digital Image Correlation is then presented extensively with a focus on existing methods and their effectiveness in fracture mechanics problems.

In chapter II, the magnesia-based materials investigated in this research work are introduced along with conventional material characterisation methods. The industrial context of these materials is given with an emphasis on the main solicitations leading up to the development of new magnesia-based refractories using simplified compositions. The latter approach is presented along with the associated compositions of model materials. Moreover,

CC BY NC ND

characterisation methods that will be used to observe material microstructures and measure elastic properties at high temperature are presented.

Subsequently, in chapter III, the coupling of the WST and a refined-DIC method is investigated in order to develop an effective fracture characterisation approach. After presenting the Wedge Splitting Test and the associated sample preparation steps, a discussion follows on the impact of experimental conditions on the measurement of displacement fields by DIC. A refined-DIC method, developed specifically for fracture monitoring, is then presented while its accuracy is evaluated through a series of analyses and comparisons.

Following these method-oriented chapters, the fourth chapter focuses on investigating the key microstructural features that influence the thermomechanical properties of the magnesia-spinel and magnesia-hercynite model materials. Extensive microstructure observations and elastic property measurements at high temperatures are correlated in an attempt to understand the main impact of thermally induced microcracks on material properties.

Finally, in chapter V, the fracture behaviour of the model materials is analysed by using the WST coupled with 2P-DIC. The impact of microcrack networks on fracture energy and material brittleness is evaluated and correlated with inclusion nature and content. In conjunction with this, crack propagation resistance is measured during the WST based on crack lengths obtained from 2P-DIC. Lastly, a novel thermal shock test bed is applied for the first time on a selection of model materials.

BY NC ND

Chapter I

BY NC ND

Chapter I. State of the art regarding refractory thermomechanical and fracture behaviour along with optical kinematic field measurement techniques

I.1. Origins of thermal stresses in refractories

I.1.1. During processing of the refractory

The origins and implications of thermal stress can be traced back to the thermal history and the nature of the material. In the case where a homogeneous and isotropic material with a uniform temperature T_0 is gradually subjected to a temperature T_f, the sample would remain stress-free as long as it is not restrained from moving. Conversely, if the boundaries of the sample are restrained from moving (as shown in Figure I-1), then stresses will arise because of temperature variation. These stresses can be expressed according to Kingery [King55] as:

$$\boldsymbol{\sigma} = \frac{\mathbf{E.\alpha.(T_0 - T_f)}}{\mathbf{(1-\nu)}} \qquad \text{Eq. I.1}$$

Where E is Young's modulus, α the coefficient of thermal expansion and *v* the Poisson's ratio of the material. From this expression, it is clear that Young's modulus and the thermal expansion coefficient play an important role in the amplitude of stress induced by a temperature variation ΔT.

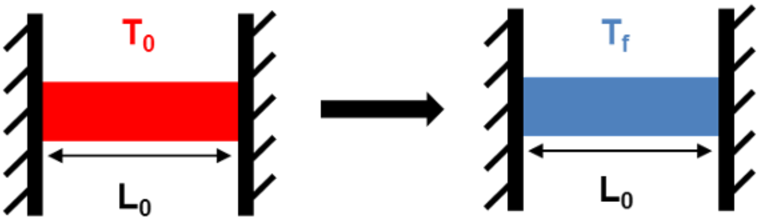

Figure I-1 : Slab subjected to a uniform temperature variation (adapted from [Gras11])

Such a simple case can be transposed to more complex problems to include refractory materials. In fact, refractories can be described as heterogeneous polycrystalline materials with possible anisotropic properties. Therefore, stresses of thermal origin can originate from a thermal expansion mismatch between refractory phases or due to anisotropy of single crystals. The nature of the induced stresses and their amplitude are of crucial concern, during cooling after sintering of the refractory, as it can alter final material properties significantly.

BY NC ND

The complexity of describing the high temperature behaviour of heterogeneous materials, such as refractories, often calls for more simplified approaches. At a local scale, considering a simplified two-phase isotropic material composed of a continuous matrix surrounding a spherical inclusion, it is possible to describe three different configurations [Sels61, TeGH06] when the material is uniformly cooled down from its sintering temperature T_0. These configurations highlight the influence of the thermal expansion mismatch between the matrix and the inclusion ($\Delta\alpha = \alpha_{matrix} - \alpha_{inclusion}$) on the nature of the thermally induced stresses (Figure I-2).

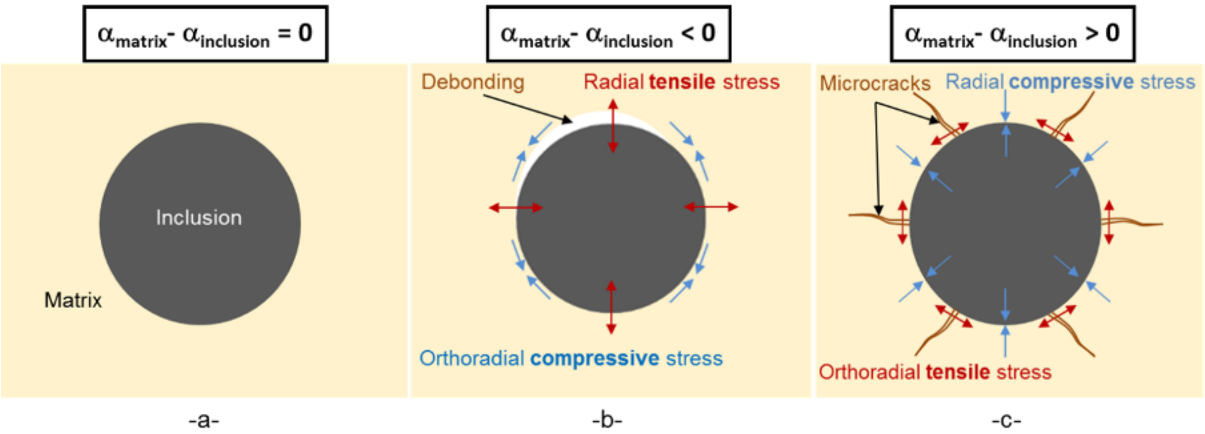

Figure I-2 : Configurations of stress distributions in the matrix during cooling for a) Δα=0, b) Δα<0 and c) Δα>0 (adapted from [Tess03])

- When Δα = 0, the matrix and the inclusion contract at the same rate. Therefore, no internal stresses arise during cooling which leads to a free-stress state.
- When Δα < 0, slower contraction of the matrix compared to the inclusion leads to compressive orthoradial stress and tensile radial stress. This stress state is likely to induce debonding between the matrix and the inclusion, as cracking in ceramics occurs in tension most of the time.
- When Δα > 0, faster contraction of the matrix in relation to the inclusion induces tensile orthoradial stress and compressive radial stress. The tensile orthoradial stresses are likely to lead to the initiation and propagation of cracks radially from the inclusion.

Therefore, in most cases, thermally induced stresses lead to defects in the microstructure that inevitably decrease material's elastic properties and subsequently reduce its strength. The amplitude of strength reduction is a factor of critical importance, it depends strongly on the amplitude of stress that is generated within the matrix by the inclusions. Indeed, in addition to

BY NC ND

the magnitude of thermal expansion mismatch, factors such as inclusion shape, volume fraction and Young's modulus mismatch also have an important impact on the stresses induced within the matrix [LiBr89]. The influence of these thermally induced microstructural features is an important topic with strong implications on material's thermomechanical properties.

I.1.2. During refractory service life

In an industrial context, refractory materials are very likely to be subjected to thermal shocks or repeated thermal cycling during their service life. These sudden variations in temperature can cause severe thermal gradients and therefore, proportionally to the CTE, induce important thermal strains. These thermal strains will lead, in turn, to stresses in the refractory lining that are proportional to Young's modulus. In Figure I-3, the cases of cooling (descending thermal shock) and heating (ascending thermal shock) at a constant rate are described using temperatures ($T_{surface}$, $T_{average}$ and T_{center}) and stress distributions within a homogeneous slab.

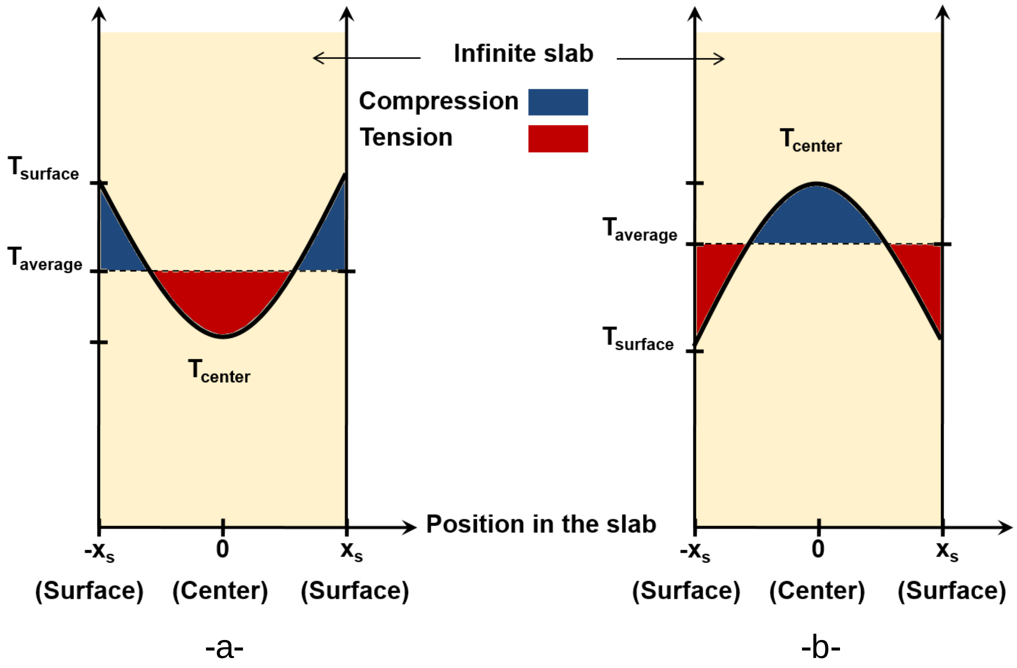

Figure I-3 : Temperature and stress distributions in cases of a) ascending thermal shock and b) descending thermal shock (adapted from [King55])

BY NC ND

For an ascending thermal shock, the surface of the slab is retained from expanding normally by the tensile stresses applied by the centre, which is cooler than the surface. In this case, the surface is in compression. Inversely, a descending thermal shock would lead to compressive stresses in the centre and tensile stresses in the surface. This configuration can be critical as it can lead to the occurrence of critical cracks on the surface of the slab.

These temperature gradients can have a dramatic influence on refractory service life when operating conditions lead to high thermal stresses. In fact, significant refractory cracking can take place due to unusual operating conditions or inappropriate refractory shape and properties. Therefore, improving refractory service life in the industry requires numerous observations and thorough case studies since thermal shock is a complex phenomenon that does not depend solely on a refractory's thermomechanical properties. In addition to this, thermal shock is always coupled with other solicitations, such as chemical attacks and infiltration corrosion. Figure I-4 shows an example of a refractory product that is subjected to several thermal shocks during its service life in the continuous casting process in the steel industry [Peru00].

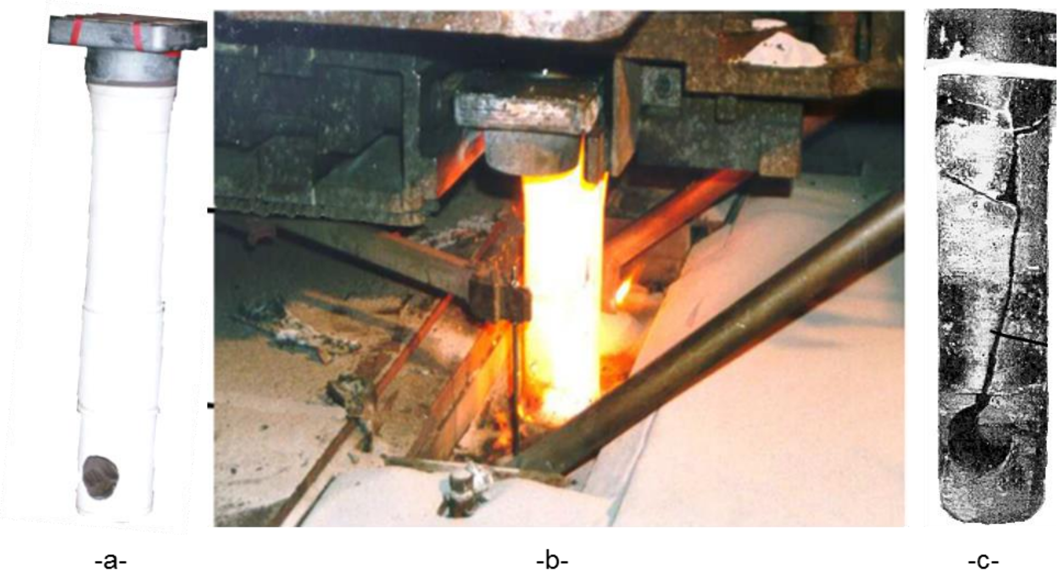
-a- -b- -c-

Figure I-4 : Illustration of a) Submerged entry nozzle (SEN) before use, b) SEN in service [Peru00] and c) Cracked SEN [YOIN98]

In summary, refractories are subjected to a number of coupled solicitations ranging from thermochemical attacks to thermomechanical stress coming from thermal gradients induced by thermal shocks. Therefore, the initiation and propagation of cracks due to thermal stress can be critical in many ways, thus reducing the overall performance of refractories. In this

BY NC ND

sense, the development of reliable refractory materials for thermal shock applications must rely on appropriate design criteria that take into account the complexity of fracture mechanisms.

I.2. Fracture behaviour of refractories

I.2.1. Thermal shock resistance

Part of the thermomechanical load applied to a refractory is associated with thermal cycling or thermal shocks. As discussed previously, thermal shocks can lead to either compressive or tensile stresses, the latter being most critical for crack initiation and propagation in refractories. For this reason, the thermal shock resistance of a refractory is one of the key material properties that need to be enhanced.

As such, two theories based on linear fracture mechanics have been developed during the 1950s and 1960s to define a framework for improving thermal shock resistance.

On one hand, the thermo-elastic approach proposed by Kingery [King55], describes thermal shock for a homogeneous and continuous material with a linear elastic mechanical behaviour. In this approach, a critical temperature variation ΔT_c is considered for when the induced thermal stress becomes equal to the strength of the material, thus leading to fracture. Depending on the heat transfer rate of the slab, two thermal shock resistance parameters (R and R') were defined accordingly.

$$\mathbf{R} = \frac{\boldsymbol{\sigma_t}.(\mathbf{1}-\boldsymbol{\nu})}{\mathbf{E}\boldsymbol{\alpha}} \qquad \text{Eq. I.2}$$

And

$$\mathbf{R'} = \boldsymbol{\lambda}.\mathbf{R} \qquad \text{Eq. I.3}$$

Where σ_t (in MPa) is the strength and λ (in $W.m^{-1}.K^{-1}$) the thermal conductivity of the material. The first thermal shock resistance parameter, R (in K), corresponds to ΔT_c. Therefore, increasing the value of R and R' would increase the material's ability to resist a critical temperature variation ΔT_c. Using this approach to define design criteria for improving the thermal shock resistance of refractories, by increasing R and R', would mean increasing the strength of the material while having low Young's modulus and thermal expansion. In other words, this approach relies on improving the crack initiation resistance of the material to avoid the occurrence of cracks. From a material science point of view, refractory constituents must be tuned and processing conditions optimised to have the lowest possible number of defects,

BY NC ND

thus increasing strength. However, for practical reasons, this can prove to be very challenging given that refractories always contain coarse aggregates leading to heterogeneous microstructures that inevitably contain numerous defects.

On the other hand, the energetic approach by Hasselman [Hass63, Hass69] takes into account penny shaped cracks distributed homogeneously in the material. Stress field interactions from neighbouring cracks and stress relaxation are not considered in the initial assumption. Similarly to the previous approach, thermal shock resistance parameters were defined:

$$\mathbf{R''''} = \frac{\boldsymbol{\gamma_S}.\mathbf{E}}{\boldsymbol{\sigma_t^2}} \qquad \text{Eq. I.4}$$

And

$$\mathbf{R_{st}} = \sqrt{\frac{\boldsymbol{\gamma_S}}{\boldsymbol{\alpha^2}.\mathbf{E}}} \qquad \text{Eq. I.5}$$

Where γ_S (in J/m^2) is the fracture surface energy, a material property. The first parameter R”” (in m) is the thermal shock damage resistance parameter, it measures the degree of damage tolerance during loading. Therefore, it allows for a comparison between brittle and ductile materials that exhibit low and high fracture surface energies respectively. In a way, maximizing this parameter is supposed to prevent unstable crack propagation which is usually associated with brittle materials.

The second parameter, R_{st} (in K.m$^{1/2}$) is the quasi-stable crack growth resistance defined to address the growth of large initial cracks in a material.

Ultimately, Hasselman’s thermal shock resistance parameters relate to the resistance to crack propagation. Thus, in order to increase the thermal shock resistance, parameters R’’’ and R_{st} must be maximised. However, both R”” and R_{st} depend on E and σ_t and seem to be inversely related to $\frac{\sigma^2}{E}$, which corresponds to the stored elastic strain energy [Popo99]. By using a simple approximation, $E.\alpha^2 \cong \sigma^2/E$, R’’’ and R_{st} now have the same dependency on the stored elastic strain energy. This energy is the driving force for crack initiation and propagation. Therefore, according to Hasselman, this energy should be minimized in order to improve the thermal shock resistance. From a material science perspective, it means decreasing the strength of the material in a controlled manner by introducing defects in the form of cracks for instance.

While high strength can be an appreciable material parameter, it could be detrimental to a refractory’s thermal shock resistance if it is used as a design criterion for tailoring material properties [Brad04]. Indeed, having a high nominal strength usually results in considerable strength loss when a crack is initiated [LCHB74]. This is commonly associated with a brittle

BY NC ND

fracture that can prove catastrophic in industrial use. Nevertheless, most industrial refractories have defects that result from processing and sintering. The inevitable flaws that result from processing are usually viewed as a compromising feature to the reliability of a material or a structure. Nonetheless, Hasselman’s attempt to provide thermal shock design criteria for refractories conveys defects as a way to increase the thermal shock resistance, which is a convenient approach for the development of refractory materials with a good thermal shock resistance.

In the end, the energetic approach by Hasselman is the most appropriate for designing refractories for thermal shock applications. The direct relation between thermal shock resistance and crack propagation resistance opens the way for a thorough consideration of a refractory’s fracture behaviour [Hass85]. Essentially, appropriate theoretical and experimental frameworks are sought for the design of refractories with enhanced fracture properties.

I.2.2. Refractory microstructure design

I.2.2.1. Non-linear mechanical behaviour and fracture behaviour of refractories

The mechanical behaviour of refractories has gathered interest from mechanical and material scientists alike. Whether it is for identifying constitutive laws using complex simulation models or designing enhanced material properties, the mechanical behaviour of refractories usually leads to questions about fracture.

Indeed, given the heterogeneous microstructure of refractories, deviations from linear elasticity are commonly observed as they lead to a non-linear mechanical behaviour [GoGS78]. This behaviour is associated to a brittleness concept that measures the gap to linearity [HaTs97]. As such, purely elastic materials are likely to exhibit a brittle behaviour through unstable failure, while non-linear and ductile materials are more effective in dissipating stored elastic energy through microstructural features that prevent the abrupt ruin of the material.

Refractories are typically considered quasi-brittle due to their non-linear mechanical behaviour, unlike most fine ceramic materials that exhibit a brittle and purely linear elastic behaviour with limited strain to rupture (Figure I-5).

BY NC ND

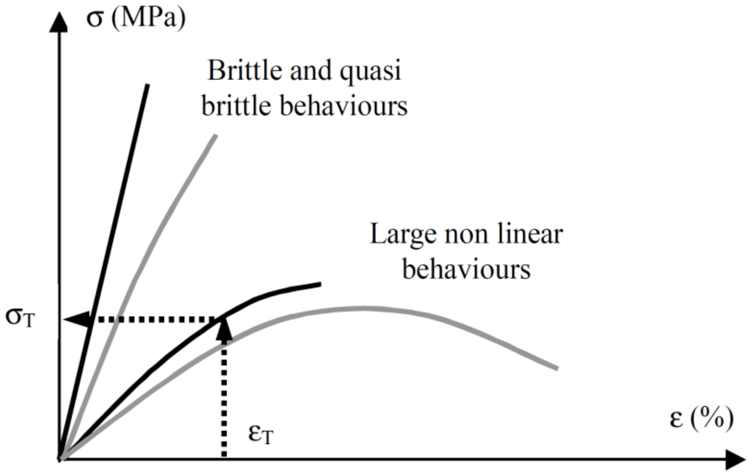

Figure I-5 : Typical tensile stress-strain behaviour observed in refractories [HTCG07]

In this sense, a high strain to rupture is sought for refractory materials, usually at the cost of strength since both parameters are mutually exclusive, to avoid abrupt failures associated with brittle materials. This trade-off between maximum strain at rupture and strength is essentially one that favours a specific fracture behaviour. Hence, despite decreasing strength, a non-linear mechanical behaviour is considered to be beneficial for improving the crack propagation resistance of refractories and thus, the thermal shock resistance. Therefore, some form of strain accommodation must be promoted within the microstructure to reduce the brittleness of refractories.

In spite of the non-linearity of a refractory's mechanical behaviour, the maximum achievable strain to rupture remains limited due to the absence of notable plasticity and the intrinsically linear elastic behaviour of most refractory constituents used in the industry. As a result, the fracture behaviour of refractories is quasi-brittle at best instead of being ductile. Nevertheless, some promising microstructure design routes have been put forward using either inspiration from naturally flexible materials such as itacolumite [HTCG07] and nacre like structures [BMMV14, PBPC18], or from the design of engineered ceramic composites that exhibit a high toughness. From the latter, the crack propagation resistance can be improved by the introduction of fibres or whiskers in the microstructure that can effectively slow down crack propagation [Rice81]. In a similar way, some ceramics exhibit stress-induced martensitic transformations which can act as a shield to further crack propagation [EvHe80, Evan90]. Therefore, to achieve a quasi-brittle fracture behaviour with increased crack propagation resistance in a refractory, it is necessary to have a deep insight on the microstructural features that are likely to be activated during crack growth.

BY NC ND

In fact, the microstructure of refractories is often composed of large size aggregates and microcracks that contribute to its heterogeneity. These features also have an important impact during the propagation of a crack as they contribute to the development of the so-called fracture process zone (FPZ). The FPZ concept describes energy dissipating mechanisms in materials such as plastic deformation, diffuse damage, cracking and other inelastic phenomena. Figure I-6 depicts some of the main FPZ mechanisms that operate during crack propagation in a typical refractory material. The effects are dominated by microcrack toughening [HoEG75, Evan76, EvFa84] and bridging mechanisms [Lang79], the interaction of these features has an important impact on FPZ development and elastic energy dissipation [AmBu88].

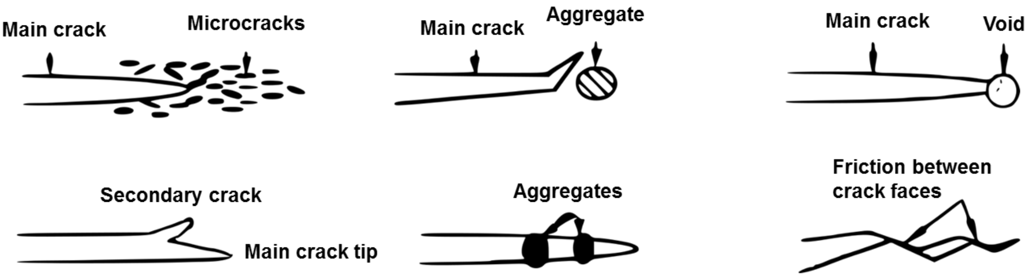

Figure I-6 : Detailed overview of the main FPZ mechanisms [ShSO95]

A fully developed FPZ is composed of two main regions (Figure I-7), namely, the frontal process zone and the following wake region. On one hand, the frontal zone usually contains micro-cracks and voids that consume the elastic energy stored at the crack tip front, thus leading to more strain accommodation prior to the maximum load and a more stable fracture thereafter. On the other hand, the wake region is located behind the crack and serves mainly as a debonding and bridging area for large grains that can prevent the crack from propagating much further.

BY NC ND

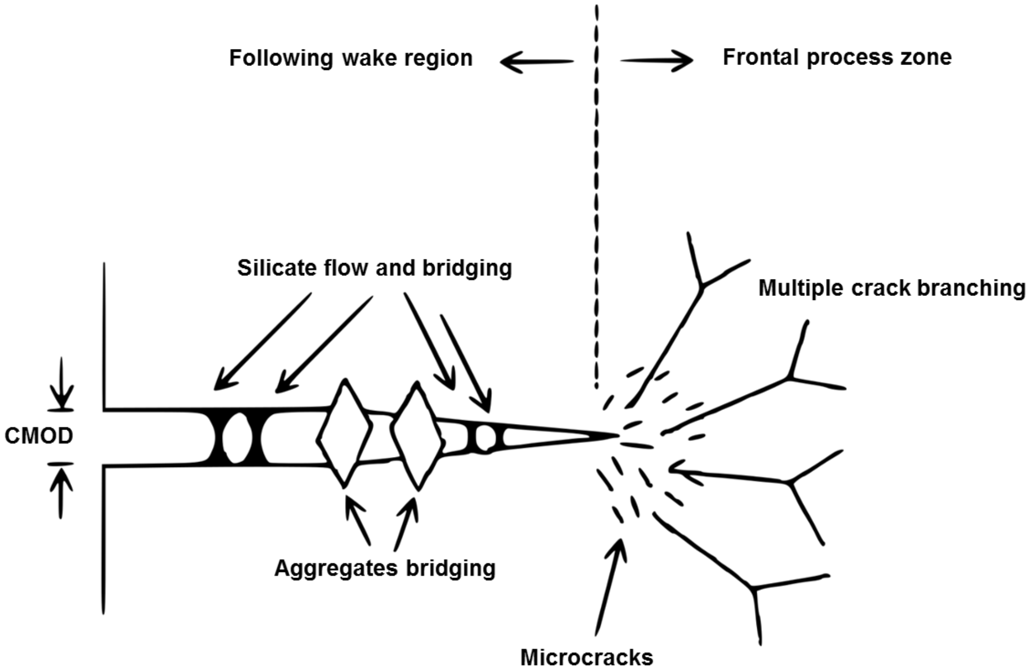

Figure I-7 : Schematic of FPZ development in a refractory material [Brad04]

The implications of FPZ development and the associated energy dissipation on the increase of crack propagation resistance lead to questions regarding optimal microstructure designs that promote toughening mechanisms. In fact, as discussed in section I.1.1, microcracks can be generated in the microstructure from a thermal expansion mismatch between the matrix and aggregates during sintering of the refractory. Indeed, when α_{matrix}-$\alpha_{inclusion}$> 0, microcracks propagate radially from aggregates leading to the creation of a network of microcracks. In this way, microcracks can be voluntarily introduced, in a controlled manner, to increase the material's ability to accommodate strain and thus increase the fracture energy.

Moreover, a network of microcracks is likely to contribute significantly to the overall development of a FPZ's size, the extension of which is beneficial for improving the crack propagation resistance. Indeed, an interconnected network of microcracks could provide those characteristics due to diffuse damage and the crack branching phenomenon that further extend the FPZ size. Furthermore, optimal aggregate properties as well as shape and size can be investigated to enhance crack deviation in the crack front and the interlocking of crack faces in the wake region. Indeed, aggregates with a high strength and roughness along with weak grain boundary junctions with the matrix are likely to cause crack deviations. In this sense, aggregates with an angular shape and a sufficiently large aspect ratio (i.e more elongated) [HoBr85] would increase the debonding length to further improve their crack bridging capacity in the wake region. The interaction of these individual mechanisms operating in two different

BY NC ND

regions in the FPZ can be highly beneficial for improving the crack propagation resistance. Synergy between the different FPZ phenomena is mainly one that contributes to the extension of the overall FPZ size, this crucial aspect is relatively unexplored due to the complexity of the mechanisms involved during crack propagation.

Ultimately, the chemical and granulometric composition of a refractory must be tailored to optimise the microstructure in a way that improves the crack propagation resistance. The FPZ being the main source of energy dissipating phenomena, it is important to ensure that this region is developed to a large extent. As such, pre-existing damage in the frontal zone that promotes the occurrence of crack branching and crack bridging phenomena in the wake region are likely to be the main contributors. Numerous authors using different fracture mechanics methods and fracture tests, detailed in the following sections, have studied this aspect.

I.2.2.2. Brief overview on fracture mechanics

Fracture mechanics have led to the development of extensive methods to deal with fracture mechanisms of materials and mechanical structures. It started with linear elastic fracture mechanics (LEFM) that considers an elliptical crack propagating in an elastic, homogeneous and isotropic medium [GrTa21]. The work of Griffith on the dependency relationship between defect size and strength has led to the development of the global or, energetic approach to fracture. This approach describes fracture based on an energetic balance between stored elastic energy and energy dissipated by the creation of a new crack surface. Thus, an energy release rate concept, G, was defined by Griffith as the energy consumed per unit area of newly created crack surface. It was mainly applied in the case of an ideally brittle solid to assess crack propagation stability using a criterion, G_C based on material surface energy γ_S.

$$\mathbf{G = \frac{dU_p}{dA}} \qquad \text{Eq. I.6}$$

$$\mathbf{G_c = 2.\gamma_f} \qquad \text{Eq. I.7}$$

Where U_P is the potential energy change to create an increment A of fracture surface. Using G_C from Eq. I.7 as a criterion, stable crack propagation is achieved when $G=G_C$ while unstable crack propagation is when $G>G_C$. This criterion is only valid for purely brittle materials such as glass and some fine grain ceramics due to the absence of energy dissipating mechanisms.

BY NC ND

Indeed, the surface energy of most ceramic materials is around 1 J/m^2, while in practice, much higher effective energies are observed especially for quasi-brittle and ductile materials.

Alternatively in fracture mechanics, the local asymptotic approach relies on studying the singular stresses associated to a crack by using stress intensity factors (SIF) introduced by Irwin [Irwi57] for different modes of fracture (Figure I-8). These SIFs depend on stress and geometry of the sample as well as crack tip coordinates.

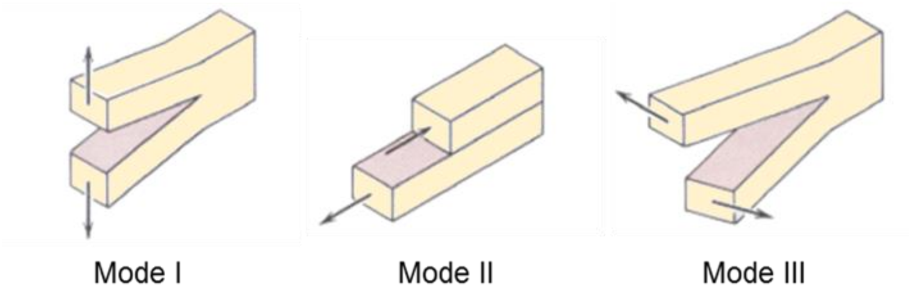

Figure I-8 : Different fracture modes: Opening (Mode I), In-plane shearing (Mode II) and Tearing (Mode III)

The definition of fracture modes allows for a better description of fracture, whereby stress and displacement can be formulated using Taylor expansions according to the crack tip position and vicinity. As pointed in Figure I-9, three zones are distinguished in the asymptotic approach. The first one is the immediate vicinity of the crack tip where stresses are infinite, the second one is a stress singularity zone with a 1/r^2 dependency and finally, the third one is the far-field stress zone.

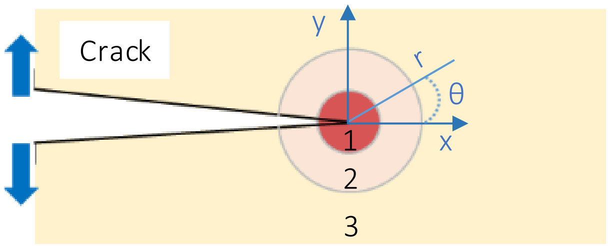

Figure I-9 : Distinction of a propagating crack's coordinates and zones in an elastic medium

The singular stresses in the second zone have gathered much of the interest in the development of the LEFM framework and beyond in fracture mechanics. Indeed, the

cc BY NC ND

description of stress singularities using the asymptotic local approach relies on analytical or numerical solutions of stress and displacement [West39, Irwi57].

In the same way as for the global approach, a crack propagation criterion called toughness (K_{IC}) has been defined. This parameter is the critical value of SIF in opening mode, which is the most commonly observed failure mechanism as it results from tensile loading. Toughness is considered as the material's crack propagation resistance, which is an intrinsic material property. As such, the asymptotic approach provides a fracture criterion that may be used for the design of materials with an enhanced fracture resistance.

The fundamental works of Irwin and Griffith in the LEFM framework were mainly destined to describe brittle solid fracture problems. In fact, LEFM is limited when materials deviate from linear elasticity as they exhibit some form of non-linearity due to plasticity or damage. In such cases, LEFM considers non-linear effects to be confined at the crack tip, whereby phenomena at the vicinity of the crack are neglected to a certain extent. While this might be the case for most fine ceramic materials at low temperatures, it is only partially true for materials with a non-linear behaviour such as refractories.

Therefore, many theories were developed on the basis of LEFM to address the fracture of quasi-brittle and ductile materials, such as non-linear fracture mechanics (NLFM). In the NLFM approach, the path independent J-integral method by Rice [Rice68] is worth mentioning as it was extensively used to study the fracture of materials with large scale yielding such as metals. It relies on calculating contour integrals remotely from the crack tip field. Additionally, a relationship was established [Rice68] between mode 1 SIF, energy release rate and J-integral as shown in Eq. I.8.

$$\mathbf{G} = \frac{\mathbf{K_I^2}}{\mathbf{E}} = \mathbf{J} \qquad \text{Eq. I.8}$$

For the specific case of quasi-brittle refractory materials, the vicinity of the crack tip concentrates most of the non-linear phenomena that consume the stored elastic energy during crack propagation through the FPZ. The description of fracture in this case is more practical from an energetic standpoint given the complexity of mechanisms involved (see section I.2.2.1). The propagation of a stable crack, over an area ΔA, in a steady state during a fracture test leads to the following description [SaBr86], Eq. I.9.

$$-\frac{\Delta \mathbf{U}_P}{\Delta \mathbf{A}} = \frac{\Delta \mathbf{U}_C}{\Delta \mathbf{A}} + \frac{\Delta \mathbf{U}_{IR}}{\Delta \mathbf{A}} \qquad \text{Eq. I.9}$$

BY NC ND

Where U_P is the potential energy change of the loading-sample system, U_C is the energy associated to crack extension under linear elastic conditions and U_{IR} the potential energy associated with irreversible processes leading to a non-linear mechanical behaviour.

Examples of the latter include elastic energy stored in the wake region due to crack bridging, dissipation of frictional energy through interlocking aggregates and plasticity at the crack tip front. From Figure I-10, a graphical method is shown whereby, the decomposition of ΔU_P into ΔU_C and ΔU_{IR} can be determined from an experimental load displacement curve. The graph highlights the load-displacement curve of a sample under a steady-state crack tip loading configuration at different loading states. The area under the loading and unloading path ABCD corresponds to ΔU_P (total energy consumed during a crack extension Δa), where AEB corresponds to ΔU_C and AEBDC relates to ΔU_{IR}.

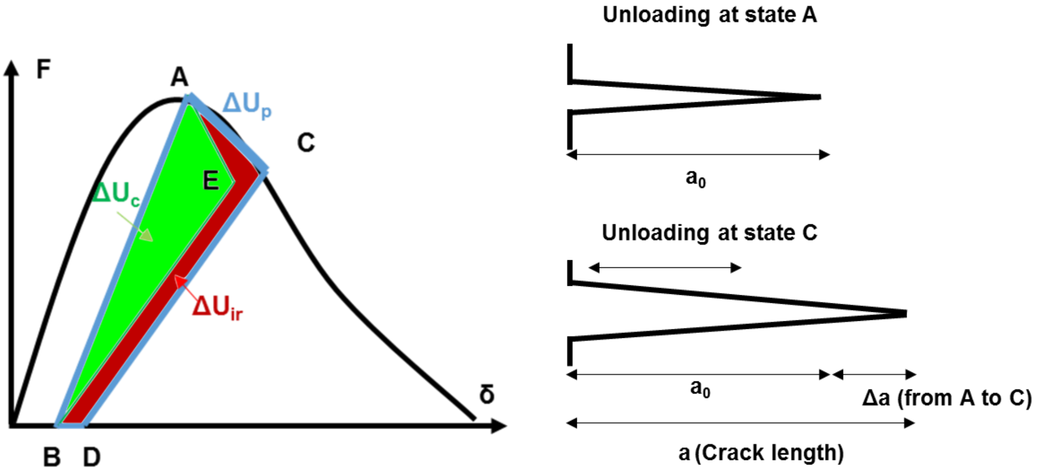

Figure I-10: Graphical separation of the non-linear fracture toughness and the irreversible energy [SaBr86]

However, given the complexity of a refractory's microstructure and the occurrence of a FPZ during crack propagation, measurement of the fracture area necessary to determine fracture energies becomes a challenging topic. This is mainly so because in quasi-brittle materials, the crack does not propagate in a straight fashion crossing the sample from one end to the other. Attempts have been made to estimate the crack length indirectly using the concept of equivalent crack length from the compliance method [TaPl85]. In this approach, non-linear effects are assumed to be directly linked to the extension of the main crack and therefore, to an increase in compliance. While this method might prove to be appropriate for certain materials with an elastic behaviour, it is not adapted for materials that exhibit damage and multiple crack branches [KnPa86]. Such is the case for refractories destined for thermal shock

BY NC ND

applications, which contain complex microstructural features that lead to extensive FPZ development. Conversely, direct visualisation methods for the evaluation of the crack length might be a promising alternative, albeit with their own limitations [BoKP85].

Ultimately, the global and the asymptotic local approaches are complementary in fracture mechanics. The recent development of the local approach to fracture in the 80s [Pine92], might prove essential in refining the description of fracture mechanisms. This approach models fracture based on local criteria that rely on micromechanical modelling and a perfect knowledge of the stress-strain field at the crack tip. Alternatively, despite its shortcomings, the global approach has many benefits regarding fracture characterisation given the availability of standard fracture tests and a practical energy-based description of fracture mechanisms that includes materials with a non-linear mechanical behaviour. In fact, given the inelastic phenomena that occur in these quasi-brittle materials, it is necessary to consider appropriate experimental testing and methods that take into account their non-linear character.

I.2.2.3. Experimental fracture mechanics and the R-curve behaviour

The effective fracture energy of refractories is an important fracture parameter that may be used to characterise crack propagation resistance and thus, the thermal shock resistance. Particularly so, since the surface energy used in Griffith's approach for brittle materials is not valid for refractory materials. In fact, the surface energy is based on thermodynamic calculations relating to Gibbs free energy, which is associated to the creation of a smooth crack surface. Using this energy as a fracture criterion would mean disregarding crucial energy dissipating mechanisms occurring in refractories, such as microcracking and crack tortuosity at microscopic scale among other phenomena detailed previously in section I.2.2.1. Therefore, there is a clear need for the measurement of an effective fracture energy based on appropriate fracture tests and methods.

For this reason, it is important that a stable fracture be ensured when performing a fracture test. This is particularly difficult to achieve in brittle and quasi-brittle materials since the elastic energy stored by the loading machine-sample system is released abruptly, breaking the sample in two halves. The most effective ways to circumvent this problem include reducing the elastic energy stored in the loading device and performing tests on pre-cracked or pre-notched samples.

Most experiments in fracture mechanics rely on indirect tensile tests, such as three-point bending, brazillian test and the compact tension test. The single edge notched beam (SENB) test (Figure I-11) has been extensively used in the past for its simplicity and easy

BY NC ND

implementation to measure effective fracture energies. The samples usually contain a notch to force crack propagation in the region of maximum tensile stress in each of the mentioned experiments. The notch type can have an important influence on strength and on the stability of crack propagation. Indeed, from Figure I-11.c, the stress distribution at the front of a sharp notch points at an important stress concentration directly in front of the notch, which is likely to be released abruptly and lead to unstable fracture.

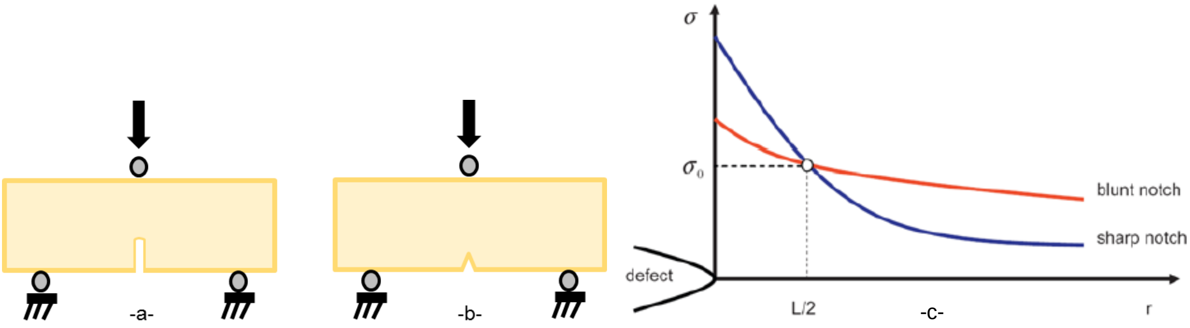

Figure I-11 : Specimen configuration of SENB test with a) Blunt U-notch, b) sharp V-notch and c) Stress distribution at a blunt and sharp notch tip [JCCS17]

For instance, SENB tests (Figure I-11.a and b) permit the measurement of effective fracture energies that may be conveniently used in Hasselman's approach to evaluate the thermal shock resistance parameters [Naka65, LCHB74] using the work of fracture method [Naka64].

The work of fracture method relies on measuring the area under the experimental load-displacement curve to measure the so-called work of fracture, γ_{WOF}.

$$\gamma_{\mathbf{WOF}} = \frac{\mathbf{W}}{\mathbf{2.A}} \qquad \text{Eq. I.10}$$

Where W (can be associated with U_P presented previously) is the energy required to create a fracture surface A. The work of fracture corresponds to the energy required to propagate a crack, as opposed to crack initiation energy. The latter can also be measured from a SENB test using a sharp notch and a low notch to depth ratio (Figure I-11-b) to favour unstable crack propagation. Therefore, the energy required to initiate a crack γ_{NBT} [BrSr66] can be deduced from the measured toughness and material's Young's modulus using the following relation (Eq. I.11).

$$\gamma_{\mathbf{NBT}} = \frac{\mathbf{K_{Ic}}}{\mathbf{2.E}} \qquad \text{Eq. I.11}$$

cc BY NC ND

The ratio between crack propagation resistance and crack initiation resistance can be used as a good estimate for thermal shock damage resistance [NaAB81], where a high ratio relates to a higher energy consumption from crack propagation rather than initiation. This has a direct impact on crack propagation stability, as shown in Figure I-12.

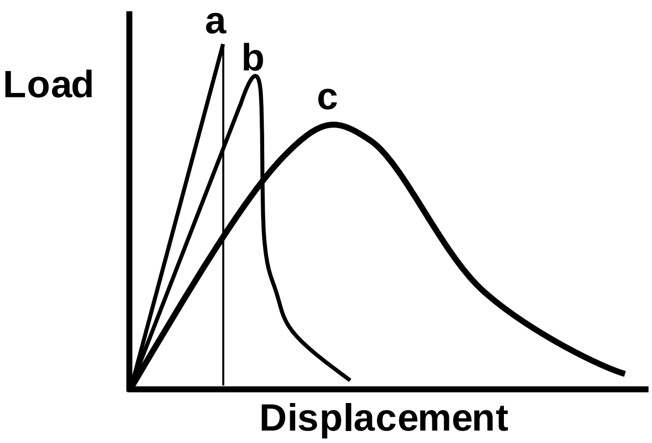

Figure I-12 : Load displacement curves for a) Unstable, b) Semi-stable and c) Stable crack growth (adapted from [AkWa03])

These experimental methods have contributed significantly to the evaluation of fracture energies and toughness values for ceramics and other brittle materials. However, given the quasi-brittle nature of refractories and the associated development of a FPZ, experimental considerations must be taken with regard to the fracture surface to specimen volume ratio. This ratio should be high enough in order to ensure that the FPZ is fully developed and not confined during the fracture test. In fact, the size effect has many implications including the validity of fracture energy values measured using common fracture tests [BaKa91, BaPl97]. Nevertheless, thanks to large volume test specimens, fracture tests such as the compact tension and the wedge-splitting test offer a more representative area for crack propagation. The latter has been applied by numerous researchers to characterize the fracture behaviour of concrete and refractories [BrWi90a, HRKT96].

Using one of the aforementioned fracture tests, the so-called resistance curves (R-curves) can be calculated. These R-curves give an insight on the influence of FPZ development on the fracture behaviour, which is a key information in the design of refractories with an enhanced crack propagation resistance. Indeed, from Figure I-13, the theoretical evolution of an R-curve as a function of crack length shows the impact of FPZ extension through the successive development of the frontal zone and the wake region. The interaction of the main crack with

BY NC ND

the microcracked frontal zone leads to a first increase of the R-curve, which is followed by a more important increase once the wake region is fully developed before a plateau-like regime is reached.

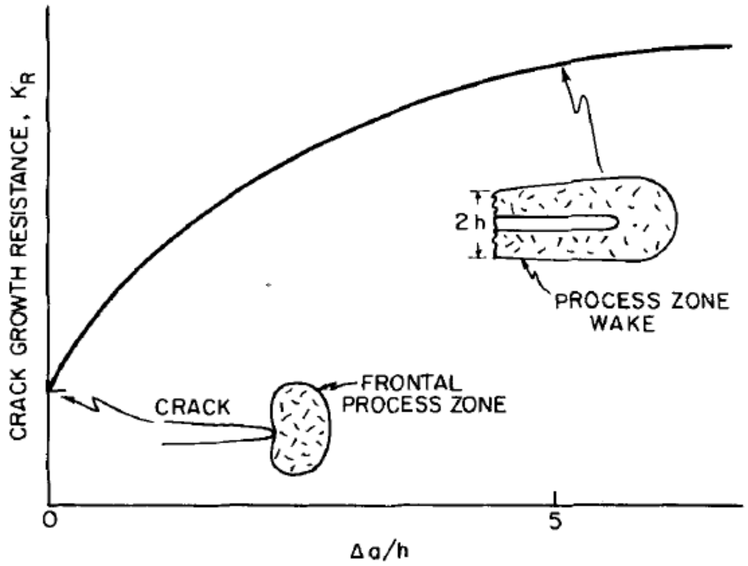

Figure I-13 : Theoretical evolution of R-curve in a microcracking brittle solid [EvFa84]

Experimental R-curves (Figure I-14) are determined from load-displacement curves of fracture test results, numerous methods have been developed [SaBr86, SYGI88, SaBr93] to evaluate the essential fracture parameters that describe the fracture process namely, crack length and fracture energy.

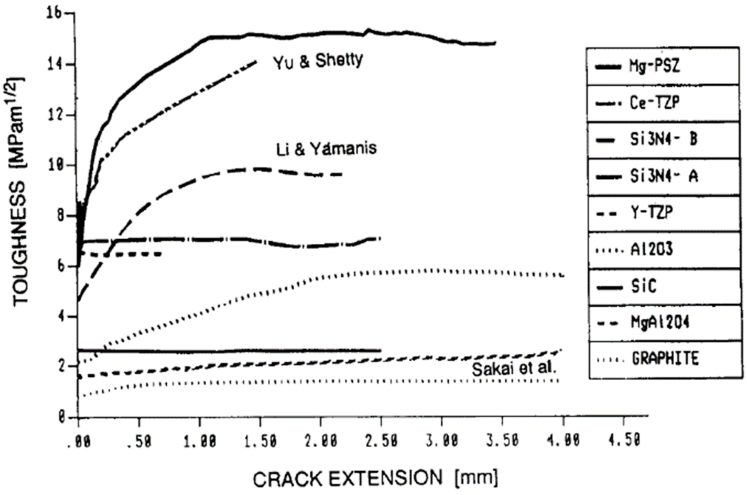

Figure I-14 : Experimental R-curves of various ceramics from the compact tension test specimen [StRS90]

The development of the FPZ during fracture of refractories and some ceramics has been associated with a rising R-curve concept, where the crack propagation resistance of the material increases with crack length (Figure I-14). The analysis of experimental R-curves led to the identification of important microstructural features that have the most effective impact on improving crack propagation resistance of ceramics [Evan90]. Among these features, transformation toughening, dispersion of fibres and strong particles (metallic for instance) have been deemed as very effective. Nevertheless, the full extent of energy dissipating mechanisms' effectiveness within a specific FPZ remains largely unexplored due to the complexity of mechanism interactions and other phenomena [Gang16].

Appropriate experimental characterization of fracture is essential for the understanding of important fracture mechanisms and their impact on the fracture behaviour of refractories. Even more so, establishing a relationship between fracture properties and refractory microstructure is key in designing materials with enhanced crack propagation resistance. Therefore, advanced experimental tools such as optical methods could provide a fine understanding of FPZ influence and the underlying mechanisms driving its extension during crack propagation.

I.2.3. Project FIRE Delta

The Federation for International Refractory Research and Education (FIRE) is a network of academic and industrial partners that promotes refractory research programs. Project FIRE Delta is the latest program within this global network, operating between 2016 and 2020. The main partners within project FIRE Delta are:

- Academic partners: University of Aachen (Germany), University Leoben (Austria), University of Limoges (France) and University of Orléans (France).
- Industrial partners: Raw material suppliers (Alteo and Imerys), refractory producers (Pyrotek and RHI-Magnesita) and end-users (Posco and Tata Steel).

The main topic of the project is the thermomechanical modelling of refractories. It involves a multiscale approach, which goes from the microstructure to the validation of lining structure. Indeed, the main objectives of the project are to provide a better understanding of microstructure-property relationships, measure thermal and mechanical properties required for numerical simulation and model industrial refractory linings using non-linear homogenisation methods. Master and PhD students in partner laboratories, which have the necessary expertise, address these topics.

BY NC ND

The present PhD thesis is focused on the measurement of mechanical and thermomechanical properties of refractories as well as providing an understanding of microstructure property relationships. In this sense, RHI-Magnesita company has provided the materials for this research work, which will be detailed in Chapter II.

I.3. Digital Image Correlation (DIC)

I.3.1. Overview on the development of optical methods and application of DIC

Non-contact optical methods for the measurement of kinematic fields have seen a surge in their development in the last 40 years. Given the recent development of CCD cameras and numerical processing techniques, optical methods are deemed as affordable and easy to implement in an experimental setup involving mechanical characterization. In addition to the obvious practical advantage of non-contact methods over conventional contact techniques, such as strain gages and extensometers, optical methods are considerably more effective in measuring and analysing kinematic fields. Indeed, the measurement area is only limited by the field of view, therefore giving access to a large amount of measurement points that can be used conveniently to obtain local or full kinematic fields. Consequently, the application of optical methods has become commonly accepted by many scientific communities as an effective way to enrich classical analyses. Experimental mechanics have thus seen a notable evolution in the way experiments are designed, monitored and analysed.

Digital image correlation (DIC) is one of the most commonly used optical methods for measuring full-field displacements. This technique was developed by a research group from South Carolina in the USA in the 80’s [PeRa82, PRSC83] and has seen many important developments that contributed to improving its measurement accuracy and computation time [SWPR83, ChRS85, BMSP89]. Many studies have sought to assess the uncertainties and errors coming from different sources in order to make DIC more robust and reliable for more applications. This has clearly led to the success of this method as an advanced mechanical characterization tool. It has been used at different scales, depending on the acquisition device, going from the macroscopic scale using CCD cameras to microscopic scale with optical microscopy and SEM acquisition [SuLM97, JiLK08]. 3D measurements are also made possible for various mechanical and fracture characterisation experiments thanks to calibrated stereovision systems using two cameras or more [LCSP93, LuCS94, Orte09].

Consequently, the ever-increasing performances of DIC and associated methods have sparked interest among researchers developing refractories to further understand material

BY NC ND

behaviours. The field of application of DIC has expanded from standard mechanical characterisation of materials to fracture mechanics and even to high temperature applications involving refractories. However, given the mechanical behaviour of refractories [Davi79], low strains (<10^{-2}) are usually exhibited prior to fracture. Reliable and accurate measurements of strains between 10^{-4} and 10^{-2} are thus expected from DIC. The measurement of low strains remains a challenge for DIC techniques for various reasons related to image noise and errors specific to DIC used to process images [ABDD13]. Nevertheless, the application of DIC has been performed successfully at room temperature [BeHR05, RNCO07, BGGD12, BHCP14] to characterise the mechanical behaviour of refractories as well as their fracture behaviour [LRMB11, BPGD15, VNCR16, DaGH17]. On the other hand, the application of DIC at high temperatures is another challenging topic where the experimental conditions can alter strain measurements significantly [LRMB12, GLTC14, MCSZ16], despite the increased strains exhibited by refractories at high temperatures [Davi79]. During creep tests for instance, attempts have been made to characterise the asymmetric behaviour of a refractory up to 1350°C [LeLH15], while an attempt has been made at measuring strain fields with a 3D-DIC setup that proved to be much more challenging [DNRC13].

The advent of DIC as a reliable characterisation method also helped shape its development towards more specific needs and applications, notably coupling DIC with numerical simulation, some of which are detailed in the following sections.

I.3.2. Measurement of in-plane displacement fields

In DIC, the displacement field is measured by comparing two digital images corresponding to two different states of mechanical solicitation called the reference state and the deformed state. Reference and deformed images are represented by the functions f and g respectively, which represent image grey levels. By assuming the conservation of the optical flux, a plane material transformation ϕ links coordinates of the reference state (*X*) to ones of the deformed state (*x*) (Figure I-15) by the following equation (Eq. I.12).

$$\boldsymbol{\phi}(\mathbf{X}) = \mathbf{x} \qquad \text{Eq. I.12}$$

The material transformation is a first-order Taylor expansion approximation of the kinematic field associated with the centre of subsets (D) within a regular grid called Zone Of Interest (ZOI). The approximation is defined by the vector $\underline{\mathrm{q}} = (\mathrm{u}, \mathrm{v}, \frac{\partial \mathrm{u}}{\partial \mathrm{x}}, \frac{\partial \mathrm{u}}{\partial \mathrm{y}}, \frac{\partial \mathrm{v}}{\partial \mathrm{x}}, \frac{\partial \mathrm{v}}{\partial \mathrm{y}})$, which has two components of displacement (u,v) and four components of local gradients.

BY NC ND

The best values of the q vector are found by minimising a correlation coefficient C, which measures the degree of similarity between f and g (Eq. I.13)

$$\mathbf{C} = \mathbf{1} - \frac{\sum_{\mathbf{X}\in\mathbf{D}}\left(\mathbf{f}(\mathbf{X})-\bar{\mathbf{f}}_{\mathbf{D}}\right).\left(\mathbf{g}\left(\boldsymbol{\phi}(\mathbf{x})\right)-\bar{\mathbf{g}}_{\mathbf{D}}\right)}{\sqrt{\sum_{\mathbf{X}\in\mathbf{D}}\left(\mathbf{f}(\mathbf{X})-\bar{\mathbf{f}}_{\mathbf{D}}\right)^{2}}.\sqrt{\sum_{\mathbf{X}\in\mathbf{D}}\left(\mathbf{g}\left(\boldsymbol{\phi}(\mathbf{x})\right)-\bar{\mathbf{g}}_{\mathbf{D}}\right)^{2}}} \qquad \text{Eq. I.13}$$

Where f_D and g_D are the average grey level values on subset (correlation window) D in the reference state and subset ϕ(D) in the deformed state respectively. This optimisation process is performed in each of the subsets defined in the ZOI using a least-squares minimisation procedure. Using this algorithm, iterations are performed until a satisfactory uncertainty is reached. Once the global displacement has been calculated, an interpolation of grey levels is performed to achieve subpixel precision. The strain field can then be calculated by finite differences from four adjacent subsets using the measured displacement field.

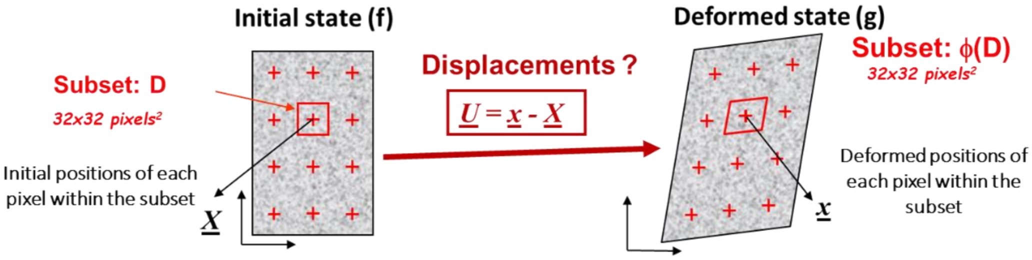

Figure I-15 : Schematic of DIC principle [BCDD11]

The accuracy of DIC is strongly linked to calculation parameters. Indeed, parameters such as subset shape function and interpolation method have a direct impact on the systematic errors of DIC [ScBS00, ScSu02], which might lead to bias in the measurement of displacement fields. Therefore, subset size and spacing must be defined appropriately as they have a strong impact on measurement accuracy (Figure I-16).

BY NC ND

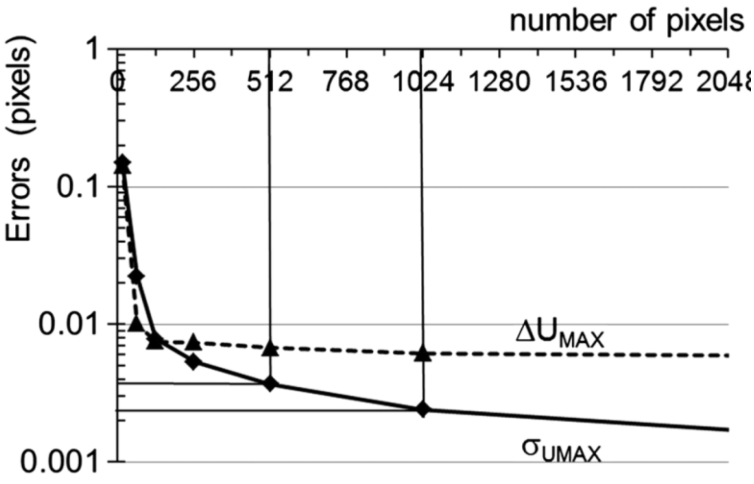

Figure I-16 : Systematic and random errors (ΔU_{max} and σ_{umax} respectively) as a function of number of pixels in a subset [DDHG15]

In fact, many studies have shown that subset size is directly related to measurement accuracy [WSBS09] where a large subset enhances the accuracy by minimizing random errors [DDHG15]. Moreover, the spacing between subsets has a direct influence on the accuracy of strain measurements, as shown in the following equation (Eq. I.14) for a 1D strain calculation.

$$\boldsymbol{\Delta\varepsilon = \frac{2.\Delta U}{l_0}} \qquad \text{Eq. I.14}$$

Where $\Delta\varepsilon$ and ΔU are the uncertainty over strain and displacement values respectively and, l_0 is the distance between two subsets.

The subset-based DIC method described above is commonly known as the local approach given that DIC matching algorithm is performed in each subset within the ZOI by using kinematic assumptions only. Another family of correlation methods, called global approach have been developed mainly to provide regularised fields [HiRo06] to overcome the ill-posed problem of determining displacements solely based on matching image grey levels. In this approach, the matching process is done over the whole ZOI contrarily to the local approach. Some mathematical regularisations of the displacement field are usually applied as a mechanical filter to the purely optical experimental data [RoHL12]. In this sense, the global approach may be adapted to finite elements to be coupled with numerical simulation analyses of the same nature [SPWS05]. Moreover, global DIC methods include the so-called integrated approaches [LPRH09] that make use of advanced regularisation and ensure consistent kinematics between measurement and simulation. The regularisation is based on either analytical solutions or finite element calculations of displacement fields for the direct

BY NC ND

identification of key material properties during mechanical characterisation [BeHR05, BeHR06, RoHi06].

The two methods, namely local and global approaches to DIC, are quite different depending on the purpose and the expected outcome of the experimental investigation. In the one hand, the global approach has many advantages when DIC results are to be coupled with numerical simulation models for validation or identification of material parameters, which is typically the case for mechanical scientists. On the other hand, the local approach fits perfectly with the needs of material scientists that seek to characterise, as accurately as possible, the behaviour of the material with minimal assumptions on its mechanical behaviour.

Therefore, using the local approach and basic kinematic assumptions on the material transformation, the experimental conditions ought to be enhanced in order to limit potential error sources and bias on the measurement of displacement fields.

I.3.3. Source of errors and key experimental considerations

As mentioned previously, the correlation technique is based on the conservation of the optical flow. In other words, any significant artificial change of lighting or contrast during image acquisition can alter the reliability of the measurement. Therefore, a great attention has to be paid to this primordial aspect during image acquisition. The measurement chain of DIC consists in a camera, controlled lighting and a high contrast sample that is being loaded (Figure I-17). Any factor that might come in-between elements of the measurement chain during an experiment is likely to introduce bias in the measured displacement and strain fields. For instance, the variation of camera-sample distance and parallelism between the sample surface and the camera during an experiment may lead to measurement bias. This experimental aspect is key when characterising the mechanical behaviour of a refractory, where a reliable measurement accuracy and robustness is required from the measurement method given the low strains exhibited by these materials.

BY NC ND

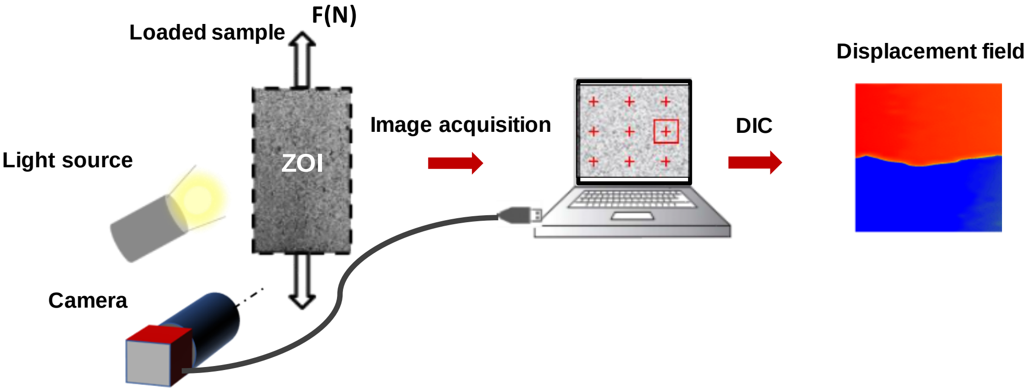

Figure I-17 : Schematic of DIC acquisition setup and computation

Essentially, performing reliable DIC measurements on a sample requires that a high contrast random pattern be applied to the sample's surface that is to be measured. In fact, the accuracy of DIC measurements depends highly on the quality of the speckle pattern since it serves as the basis for the matching process [LSBS06]. The speckle pattern has to offer enough contrast through grey level gradients and a grey level distribution that spans over a large area of the histogram (Figure I-18). Furthermore, the size of speckles is another concern as it affects measurement accuracy and spatial resolution; an optimum number of pixels per speckle comprised between 3 and 15 is required to achieve optimal pattern matching. Some criteria have been defined in the literature to assess the viability of an experimentally obtained speckle pattern [CrBD13, PYKP17]. Not only that, some studies have reported on optimal speckle patterns [Boss13, BHRC17] that may be generated virtually then printed physically on the surface of the sample [MZMS15]. These techniques might prove to be ineffective on some material surfaces but they offer a promising route for enhancing the quality of speckle patterns and their repeatability. Nevertheless, in practice, speckle patterns can be produced easily using spray paint and speckle quality determined through histogram distribution and mean speckle size.

BY NC ND

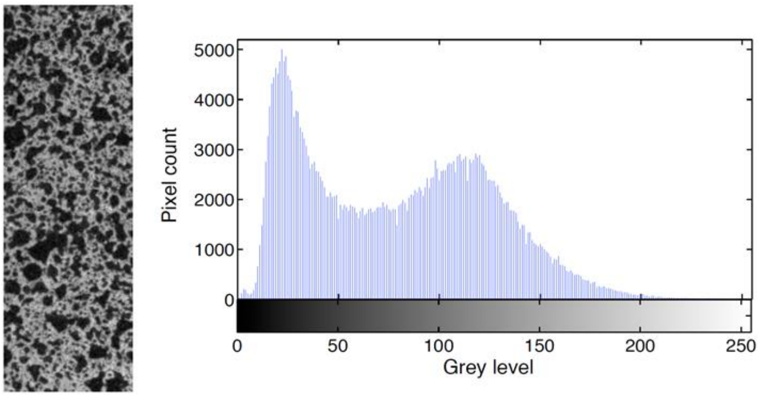

Figure I-18 : Example of an experimental spray-painted speckle pattern and its grey level distribution [RNCO07]

Moreover, DIC measurement accuracy also depends on external sources of error that might be associated to disturbances during image acquisition. In fact, during the preparation of the acquisition setup, proper alignment of the sample in relation to the acquisition system must be done to ensure the parallelism between the sample surface and the camera. During an experiment, out-of-plane displacement might hinder the accuracy of in-plane displacements, as shown in Figure I-19.

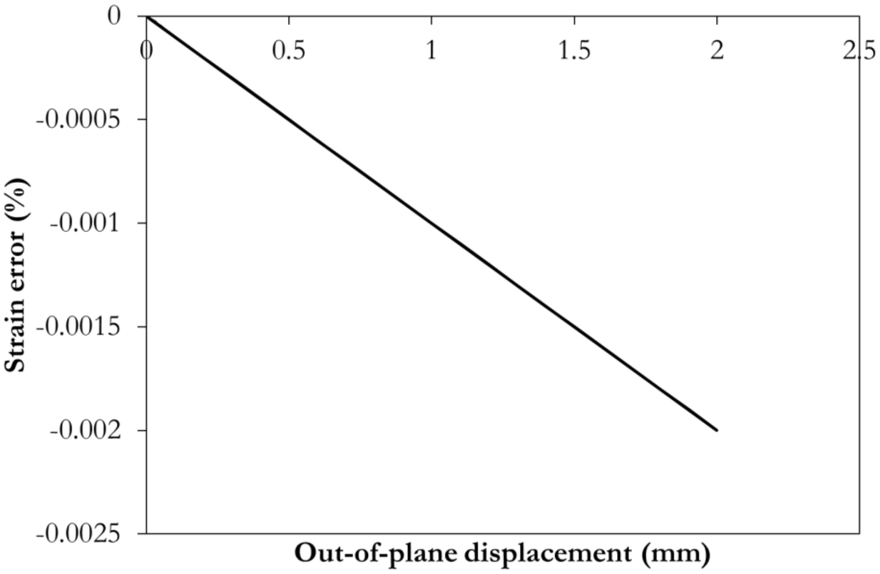

Figure I-19: Strain errors induced by out-of-plane displacements

In fact, external disturbance sources can lead to the displacement of the camera in relation to the sample (without loading). Indeed, even subtle ground vibrations during acquisition might lead to a change in the camera-object distance, thus inducing bias in strain measurements (Figure I-20).

BY NC ND

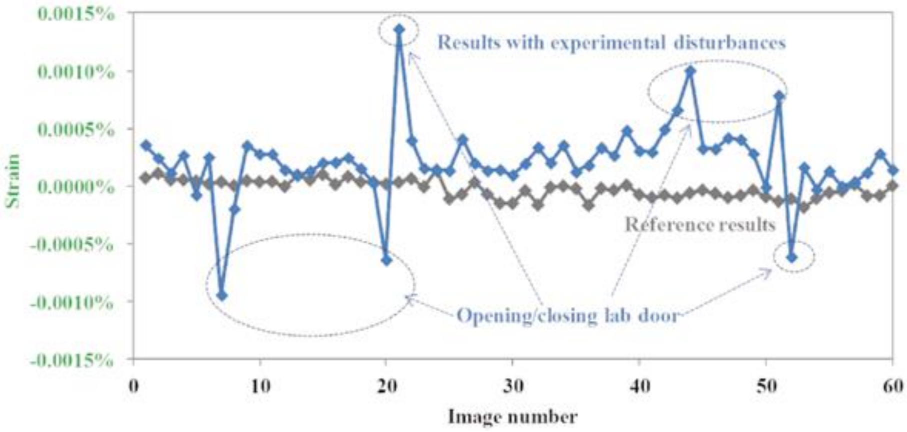

Figure I-20 : Influence of external vibrations on the accuracy of DIC measurements by using large subsets with large spacing [Belr15]

Furthermore, undesired temperature variations during image acquisition, coming from inappropriate lighting, may lead to bias in the results due to dilation of the sample for example (Figure I-21).

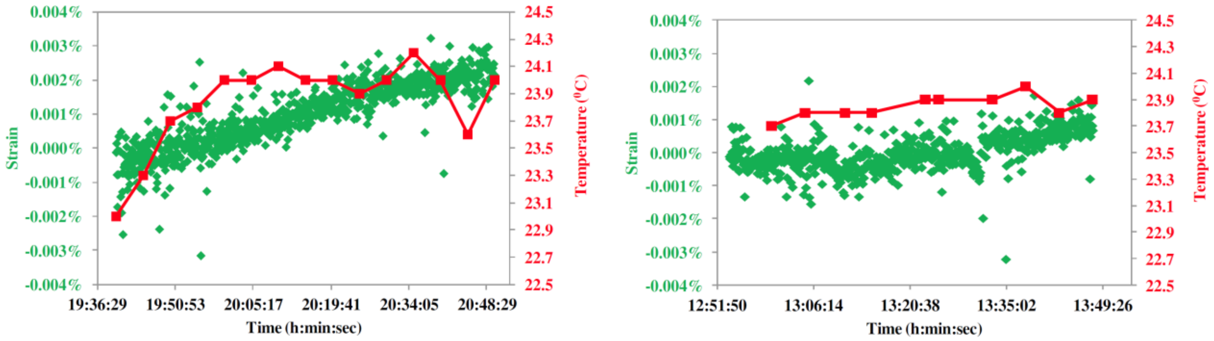

-a- -b-

Figure I-21 : Influence of temperature variation on strain measurements using a) Halogenic lights and b) LED lights [Belr15]

All of these experimental considerations must be accounted for during image acquisition in order to achieve optimal conditions. In fact, this aspect is crucial when dealing with the measurement of materials that exhibit a relatively low strain to fracture. This is the case for refractories as they show limited strain to rupture (10^{-3} at best), which is comparatively much lower than for metallic or organic materials (over 10^{-2}), but higher than that of fine-grained ceramics. In light of this, DIC has been used successfully to characterise the mechanical behaviour of refractories as shown by the example in Figure I-22. Indeed, comparing DIC strain measurement accuracy using large subsets with that of well-established strain gages, it can

BY NC ND

be seen that DIC is well suited for strain measurements in refractories. Indeed, an accuracy around 10^{-5} could be obtained with sufficiently large subsets (256x32 px^2) with an important spacing (600x32 px^2) in the strain direction.

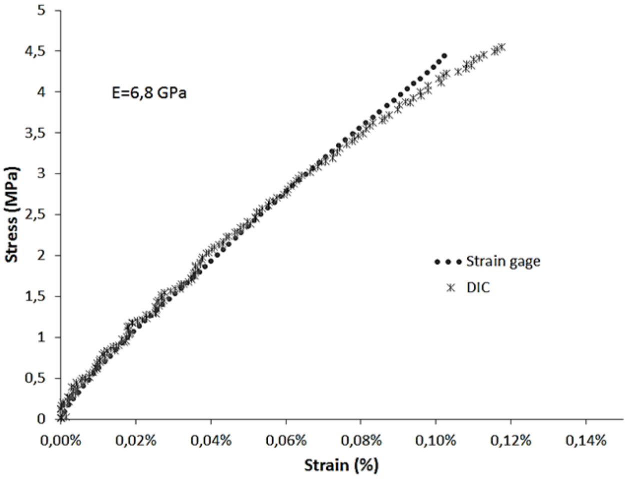

Figure I-22 : Comparison of refractory stress-strain curves obtained by strain gages and DIC during a four-point bending test

I.3.4. Application to fracture mechanics problems

DIC has been applied in many fracture characterisation studies involving different materials [SuHB01, ZhZh13]. The evaluation of strain fields during cracking is marked by uncertainties and leads to an approximate assessment of crack features. Indeed, perturbations of the measured displacement field and the subsequently calculated strain field can be caused by discontinuities crossing subsets within the ZOI (i.e no continuity of the optical flow is ensured) [DDHG15]. These perturbations hinder not only the determination of the displacement field, but also crack position and length, which are essential features of fracture mechanics. These limitations, specific to fracture, come from the kinematic assumptions of DIC, which are comprised in the framework of continuum mechanics. Therefore, an adaptation of classical DIC methods is necessary to address fracture mechanics problems. Many DIC methods have thus been adapted to account for such discontinuities during the calculations.

In the global or integrated approach, finite-element DIC (FE-DIC) has been extended to X-DIC [RéRH07, CZZH10, NHVV11], referring to the enriched kinematics of X-FEM that take into account discontinuities, automatically, without re-meshing. As mentioned previously, these methods have a good synergy with numerical simulation studies, but the determination of fracture parameters, such as SIF, remains sensitive to crack tip position especially in cases

BY NC ND

where damage and multiple cracks prevail. Other methods rely on calculating J-integrals using DIC coupled with FEM [BMTM12, BMCH17], while these methods might be less sensitive to crack position, they are, nevertheless, sensitive to crack geometry which has a direct impact on the calculation of J-integrals from contour integrals.

In the local DIC approach, an enriched method called H^k-DIC uses Heaviside functions that take into account displacement jumps associated with discontinuities, including multiple cracks crossing a single subset [VHCF15]. Moreover, a point-wise DIC method using a genetic optimisation algorithm [JiBr05] considers each pixel separately to circumvent the problem of discontinuities. Another point-wise DIC method makes use of a two-step algorithm that measures displacements at pixel level using a quad-tree process, then sub-pixel displacements are obtained by a differential technique [SXMF11]. A different approach uses a subset splitting procedure [PoBa10], whereby split subsets have different kinematics. In this method, cracks are detected based on the definition of a mask as in other approaches [Helm08, PaWL10, FaBH13], which leads to a more accurate measurement of strain fields around cracks. In fact, the use of masks with appropriate segmentation techniques [CBHF17] can provide some advantages in accurately defining the crack and subsequently measuring its length and opening displacement.

For instance, using the adapted procedure of subset-splitting, the authors managed to bypass the limitations of standard DIC when a crack occurs, namely an unreliable kinematic field coming from a bad correlation quality as shown in Figure I-23.

BY NC ND

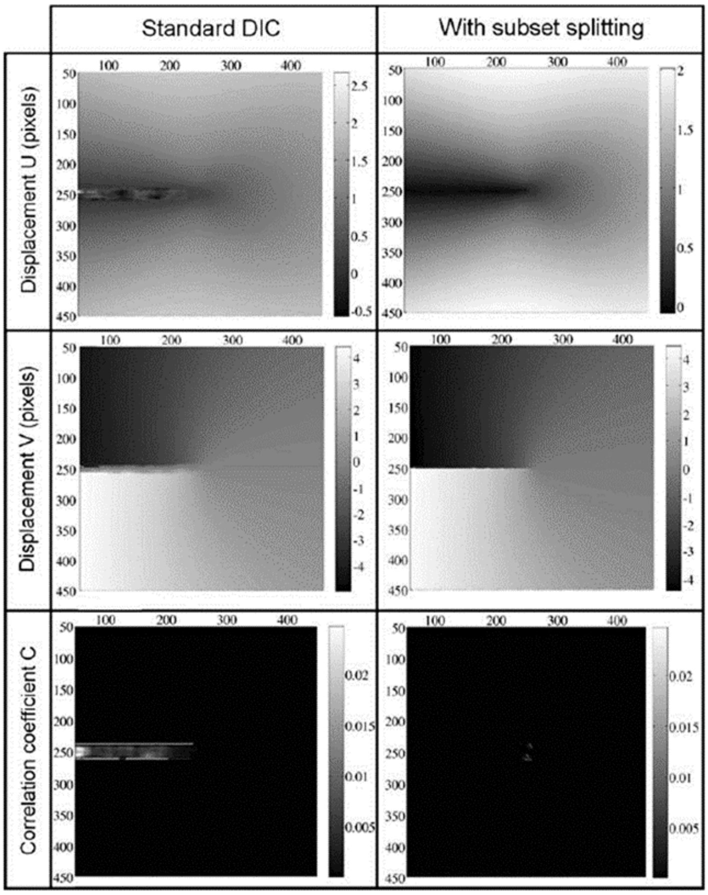

Figure I-23 DIC results for a mode I horizontal crack using "Standard" DIC and subset splitting method [PoBa10]

In the end, these original methods generally seek to exclude the crack from strain field measurements while providing a more refined description of cracks after a thresholding step. Thus, most of these methods have proved to be effective in characterising the fracture behaviour through calculation of SIFs or J-integrals, but improvements on crack description remain at the centre of developments for further adjustments to the DIC technique.

BY NC ND

I.4. Conclusion

The sections detailed in this first chapter provided an overview on state-of-the-art concepts and approaches dealing with the thermal shock resistance of refractories. From the origins of thermal stress to actual thermal shock solicitations, refractory material’s mechanical behaviour plays a major role in improving the thermal shock resistance.

Indeed, deviations from a purely linear elastic mechanical behaviour through appropriate microstructure design have been presented as an effective way to enhance refractory thermomechanical properties. In particular, the understanding of the fracture behaviour of refractories is an essential aspect of developing materials with improved crack propagation resistance, which is strongly linked to thermal shock resistance according to Hasselman. In this sense, key microstructure-property design criteria can be defined in order to promote the development of a fracture process zone, entailing increased elastic energy consumption and thus, a reduced brittleness.

From an experimental point of view, the advent of methods such as Digital Image Correlation (DIC) provides many advantages over classic strain measurement techniques. Indeed, DIC is a non-contact method that exhibits many advantages including the ability of measuring full strain fields during a variety of mechanical and fracture tests. Therefore, coupling this method with fracture experiments can lead to a thorough characterisation of refractory material’s fracture behaviour.

In the following chapters, materials with pre-fabricated microcracks presenting a non-linear mechanical behaviour, designed specifically for this study, will be presented. One of the main goals is to provide a thorough characterisation of microstructure-thermomechanical property relationships, with an emphasis on the fracture behaviour. The latter will be studied using a refined DIC method.

BY NC ND

Chapter II

BY NC ND

Chapter II. Materials and conventional methods

II.1. Introduction

In this chapter, a close insight on the nature of refractories used specifically in the cement industry is presented, while the main solicitations during rotary kiln operations are detailed. Then, required material properties are discussed with an emphasis on the thermomechanical properties, which are deemed essential in the development of refractories. Evolving industrial constraints around rotary kilns and legislation around the use of some refractory materials is reviewed in relation to state-of-the-art materials being used currently as a lining. These materials will constitute the basis for the investigation in order to promote key microstructure-thermomechanical property relationships and the understanding of their fracture behaviour, which will be studied in the following chapters.

Due to the complexity of industrial refractory compositions, it has been decided in the early stage of this FIRE project to consider a simplified composite approach involving materials with an industrial scope. Therefore, in the second section of this chapter, specially designed model materials are defined and presented.

The experimental methods used in the investigation range from classical physical property measurements, conventional methods for thermomechanical characterisation to advanced fracture behaviour analysis using refined DIC. The latter will be detailed in the next chapter and used to characterise the fracture behaviour of materials subsequently. In this chapter, only conventional techniques will be presented with an emphasis on critical experimental factors related to the application to refractory materials.

II.2. Model materials: A simplified approach

II.2.1. Industrial context

The production of Portland cement requires a series of thermal treatments endured by raw materials passing through different feeds, most important of which is the rotary kiln. The latter is one of the main industrial installations in a cement plant; it serves to produce clinker mainly from limestone and clay with some other additions. The feed is primarily alkaline (basic) in nature, it travels the rotating kiln on a refractory lining at temperatures ranging from 1000°C to 1450°C in the different parts of the kiln shown in Figure II-1.

BY NC ND

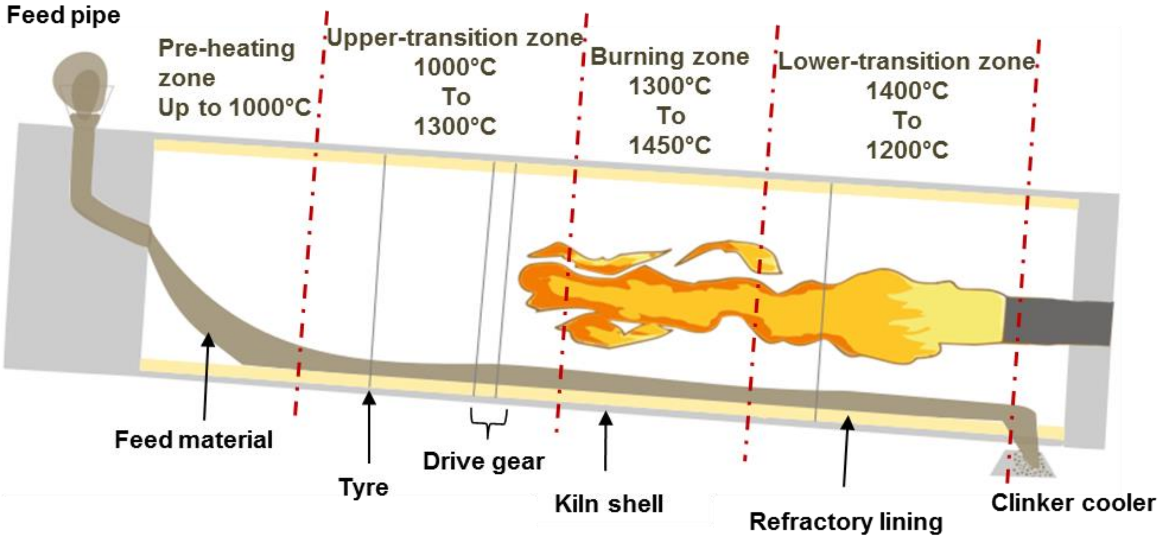

Figure II-1 : Simplified schematic of a cement rotary kiln

After grinding and pre-heating, the raw material mix enters the rotary kiln from the feed pipe for a series of thermal treatment steps involving many chemical reactions. During this travel time, refractories are subjected to extreme environments with changing thermal and chemical conditions depending on the zone within the kiln. Infiltration of alkali salts and sulphurs in the refractory bricks is one of the main wear mechanisms up to the upper transition zone. The infiltration can lead to formation of a dense and brittle brick layer that might induce cracks and therefore, lead to the spalling of a part of the brick.

Moreover, in the upper transition zone, thermal shocks might occur due to temperature variations, thus increasing the thermomechanical load on the refractory lining. At the end of the upper transition zone and in the burning zone, clinker liquid phase is formed which can further infiltrate the brick if no stable protective clinker layer is formed at this stage of the process on the refractory lining.

Finally, in the lower transition zone, the chemical wear is reduced since clinker starts to crystallise and liquid phase content is greatly reduced. However, mechanical abrasion by clinker is increased and temperature variations due to cooling can lead to a greater occurrence of thermal shocks.

These solicitations add up with the thermal gradient within the refractory bricks, which can be quite high in some parts of the kiln. For instance, in the tyre section of the kiln, higher mechanical stresses are present and thermal gradients between the hot face of the brick, which is at 1200°C, and the cold face, at 400°C, can lead to formation of cracks and even spalling. Moreover, the ever-increasing diameters and rotation speeds of rotary kilns in recent years

BY NC ND

induce higher stresses on the refractory lining. Therefore, close monitoring of the operating conditions of the kiln are of crucial importance to the safety of the brick lining. As an example, the distortion of a kiln shell into an oval shape is a common problem that is encountered during operation [Shub01]. Kiln ovality can have catastrophic consequences on the lining if not monitored correctly. Moreover, overheating in the burning zone can lead to an excess of liquid clinker that could increase infiltration of the bricks. This effect is boosted by the use of alternative fuels [MoUl03] that lead to more instability of the operating conditions by introducing volatile components that further increase the chemical wear of the lining.

Refractories have to withstand these harsh working conditions by avoiding any pre-mature degradation of their properties. Figure II-2 summarises the main refractory wear mechanisms during rotary kiln operation. These results convey the importance of thermomechanical solicitations and infiltration by salts as crucial factors for refractories.

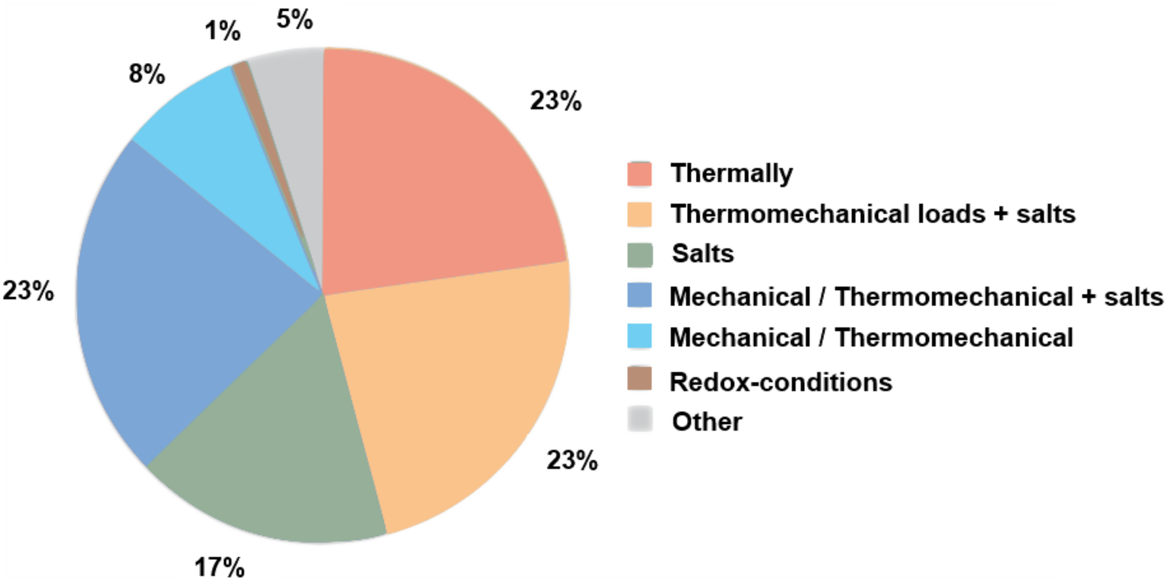

Figure II-2 : Main wear mechanisms acting on refractories in cement rotary kilns based on post-mortem analyses [BaSo01]

In these extreme working conditions, the service life of a refractory lining depends mainly on its resistance to the main solicitations in the rotary kiln. Namely, chemical wear and infiltration that embrittle the refractory material, along with the thermomechanical load and successive thermal shocks that can lead to crack initiation and propagation. The mixed nature of these solicitations often means that a refractory has to exhibit a good infiltration resistance, especially in the burning zone through the formation of a stable clinker coating, and a very

BY NC ND

good thermal shock resistance among other properties such as, corrosion resistance and abrasion resistance.

In order to ensure the reliability of the rotary kiln and the protection of the steel shell, two refractory linings are usually installed, as shown in the schematic in Figure II-3. Namely, the working refractory lining, which is in direct contact with the feed material consisting of clinker, and the safety lining that serves mainly as an additional insulating layer to protect the kiln shell.

A stable clinker coating on top of the working lining is generally sought to protect the refractories from excessive infiltration in the burning zone, as it can lead to a significant reduction of refractory service-life.

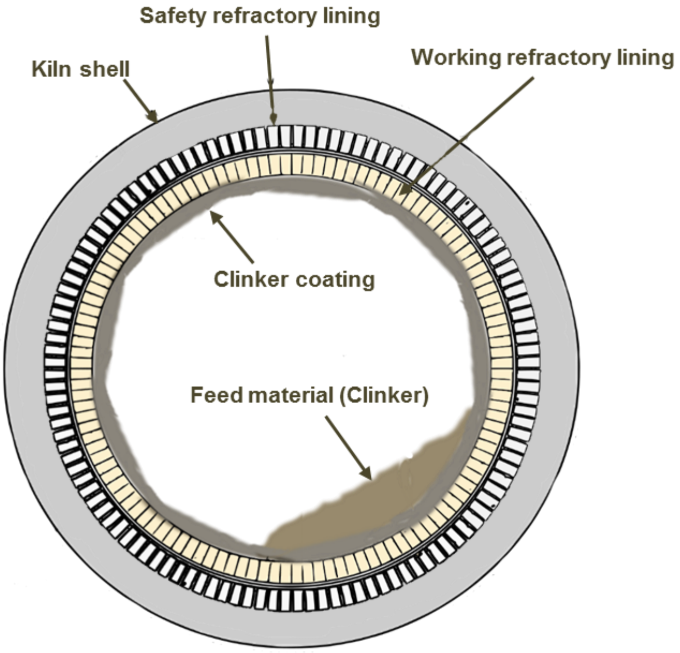

Figure II-3 : Cross section of the burning zone in a cement rotary kiln

In the end, the working conditions of a refractory lining in the cement rotary kiln define the choice of a refractory type for it is an important part of the industrial installation. Indeed, the cost of a stopped industrial installation due to a problem in the kiln can amount to important economic losses for the exploiting company. Therefore, a good knowledge of the kiln operating conditions, specific to each plant, must be used to adequately line the kiln with refractory materials that exhibit optimal properties.

BY NC ND

II.2.2. Industrial refractory materials

The main type of refractories used in cement rotary kilns is fired magnesium-oxide (MgO) bricks with some additions that help tailor material properties. Magnesia is used mainly due to its basic nature, giving it a good resistance to corrosion. However, magnesia alone is not well adapted for the whole lining mainly due to its poor thermal shock resistance coming from its high CTE and Young's modulus. Therefore, a secondary mineral is often added to magnesia to confer the necessary thermomechanical properties to the brick. For a long time, chromium oxide (chromite) ore was added to magnesia then pressed and sintered to form a brick with excellent thermal shock resistance properties, good coatability and a low cost of manufacturing. However, the use of chromite proved to be toxic due to the cancerogenic nature of CrO_4^{2-} [Bray85], producing Cr (VI) as a result, leading to disposal problems. Therefore, in most countries, including the European Union, the use of chromite was limited, which prompted research for alternative materials to substitute chromite and provide similar or better thermal shock resistance.

Consequently, many alternative compositions were investigated, important of which is the addition of magnesium spinel ($MgAl_2O_4$) aggregates to magnesia-based bricks. The production of magnesia spinel products dates back to an Austrian patent in 1932, where alumina was added to Periclase in order to form spinel by reaction sintering. While some interest was sparked by research early on [EuHu60], magnesia spinel materials did not find industrial success, despite its outstanding properties, until the end of the 70s. Material properties were thus thoroughly investigated during the 80s [CoHo82, DaFF88], which confirmed the superior properties of magnesia-spinel materials over magnesia-chromite. By that time, the production of synthetic spinel made this raw material readily available, at a lower cost, for the production of magnesia-spinel bricks at an industrial scale. In fact, this prompted industrial interest for the use of magnesia-spinel bricks, especially as they proved to be well suited for replacing chromite as they provide a 1.5 to 2 time increase in refractory lining service-life [TKHT91].

This improvement was mainly due to increased thermomechanical performances and optimised coating formation. For the former, extensive studies showed that the origins of the improved thermal shock resistance were strongly related to an increase of material toughness coming from the thermal expansion mismatch between magnesia and spinel [ARRW04, AkWR04, GAHG12, GAHC13]. Indeed, the mismatch leads to the formation of a microcrack network as discussed in I.1.1 and has a positive effect on improving crack propagation resistance (from section I.2.2). Moreover, coating formation and adherence in the burning zone

BY NC ND

is also regarded as a key parameter where increased reactivity is often sought by using fine sintered spinel [GuPR05] and the addition of iron oxide [Kane00].

Further research led to new chrome-free alternative materials, the development of which relied on the microstructure design of magnesia-based materials through the addition of components from the spinel group such as, spinel ($MgAl_2O_4$), hercynite ($FeAl_2O_4$), galaxite ($MnAl_2O_4$) and pleonaste ($(Mg,Fe)Al_2O_4$). The main purpose for the addition of such components is to enable an improved thermomechanical behaviour by promoting the development of a network of microcracks as a result of CTE mismatch leading to fracture process zone (FPZ) development.

In hindsight, magnesia-hercynite bricks have proven to be excellent candidates for the lining of cement rotary kilns due to their excellent resistance against corrosion by alkali salts and their enhanced thermomechanical properties, especially in comparison to regular magnesia-spinel composites [NiGS06]. In fact, hercynite has been gathering more interest in recent years as an alternative flexibilising additive as many studies have highlighted the positive influence of hercynite on the sintering of refractory bricks [JCYL15, RLCR15], the corrosion resistance [SJPB14] and thermal properties [DZXZ16]. It has been observed that the presence of hercynite generally leads to an ever-evolving microstructure in the refractory system due to interdiffusion mechanisms between hercynite and magnesia at high temperatures. The influence of such mechanisms on the thermomechanical behaviour and the fracture behaviour of magnesia-hercynite bricks is still not fully understood as the microstructure is marked with complex features.

The search for alternative bricks encouraged non-empirical methods in the industry and thus, promoted interactions with the academic world to provide a better understanding of microstructure-property relationships that would lead to the material by design approach in the development of refractories with enhanced properties. Indeed, the chemical composition of a refractory and the resulting microstructure play a major role in defining material properties. By using an approach based on the definition of model materials, it is possible to investigate the impact of key microstructural features on the thermomechanical properties of simplified refractory compositions.

II.2.3. Model refractory materials

Magnesia-Spinel refractories used in the industry are usually composed of numerous constituents with different granulometries that are destined, most of the time, to confer required properties for the refractory to fulfil end-user specifications. Indeed, industrial refractory compositions are often developed using key microstructure design criteria to optimise a certain

BY NC ND

number of important properties. Among these properties, the thermomechanical behaviour of magnesia-spinel refractories is an important aspect, which is closely linked to their fracture behaviour.

Therefore, for microstructure design purposes, simplified refractory compositions can provide a close insight on the impact of multiple varying microstructural parameters on the thermomechanical properties. Thus, the main parameters that will be investigated are the nature of the spinel group inclusion and its content within the magnesia-based bricks, which have a direct impact on the microstructure heterogeneities that induce a peculiar fracture behaviour.

The materials used in the study were delivered as part of project FIRE Delta by RHI-Magnesita company based in Leoben, Austria. As such, magnesia-spinel materials were defined according to relevant previous research and performance during operation in cement rotary kilns, where magnesia-hercynite materials have shown improved thermomechanical properties. Therefore, four sets of materials have been produced mainly to provide a comprehensive comparison of their thermomechanical properties and fracture behaviour. A “pure” magnesia material is used as a reference for the production of Magnesia-Spinel composites with different contents of $MgAl_2O_4$ and $FeAl_2O_4$ spinels. In this model composite approach, monophasic magnesia (both aggregates and fine particles) is referred to as the matrix while the spinel, introduced in the form of aggregates, account for inclusions.

The main objective of the study is to provide a better understanding of the influence of different spinel group additions on the fracture behaviour of magnesia-based materials. This will be done mainly through a deep microstructure characterisation.

II.2.3.1. Pure magnesia brick

Magnesium oxide, Periclase in its natural form, is an ionic solid with a cubic crystal structure. As mentioned previously in section II.2.2, this material has been extensively used as a refractory material given its high melting temperature (≅2850 °C). The production process of pure MgO bricks is briefly described below.

Sintered magnesia raw material with a purity over 98% is used in the production of bricks. Fine particles (<1 mm) and aggregates (<5 mm) are used for the elaboration of magnesia bricks. The granulometric distribution is optimised to improve pressing conditions. The powder and aggregates are mixed then pressed using a nominal pressure of 120 MPa. Then, the brick is sintered at a temperature around 1600°C. Physical properties of the bricks have been measured and reported in Table II-1.

BY NC ND

Table II-1 : Physical properties of pure MgO brick

Sample	True density (g/cm^3)	Bulk density (g/cm^3)	Porosity (%)	Thermal expansion (200-400°C)
Pure MgO	3.58	2.98	14.3%	$13.3.10^{-6}$

The produced bricks are of prismatic shape with dimensions of 220x110x100 mm^3. As shown in Figure II-4, aggregates (brown and white) are visible on the brick surface. On the micrograph in Figure II-4.c, a clear distinction can be made between the magnesia aggregates and the magnesia fine particles.

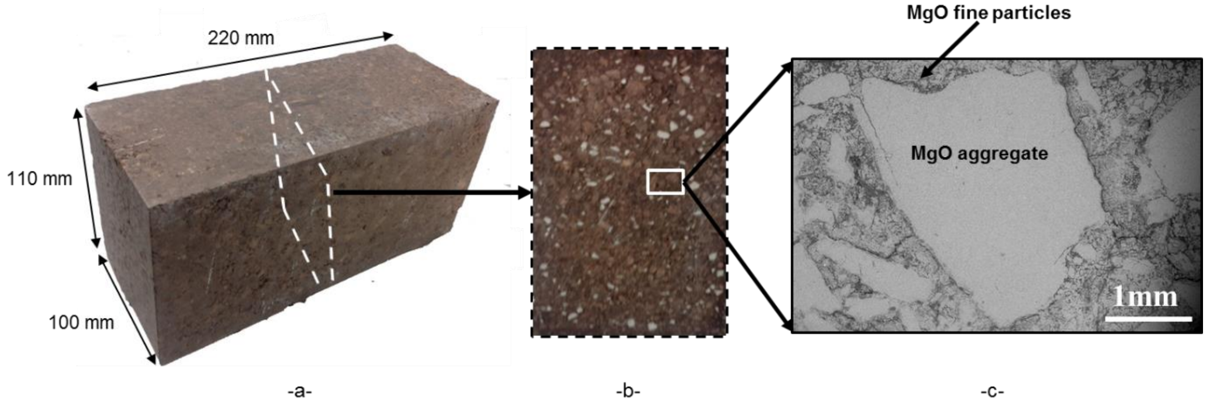

Figure II-4 : Multiscale overview of a) "Pure" MgO brick, b) Aggregates within the brick and c) SEM micrograph of a typical microstructure

Pure MgO bricks will mainly serve as a basis for composite bricks containing other types of aggregates, such as Magnesia-Spinel.

II.2.3.2. Magnesia-based composite bricks

As mentioned previously, compounds from the spinel group are commonly used in the composition of magnesia-based bricks. The spinel group includes oxides with the formula AB_2O_4, which crystallise in the cubic crystal system. In normal spinel, cations A (divalent) and B (trivalent) occupy tetrahedral and octahedral sites, respectively. Therefore, many compounds exist in this group, but only a few have been used extensively in refractory compositions. Among them, $MgAl_2O_4$ and $FeAl_2O_4$, called spinel and hercynite respectively, have proved to be quite interesting alternative solutions to the use of chromite in the past as

BY NC ND

they provide enhanced thermomechanical properties. An overview of spinel and hercynite raw materials is presented in Figure II-5.

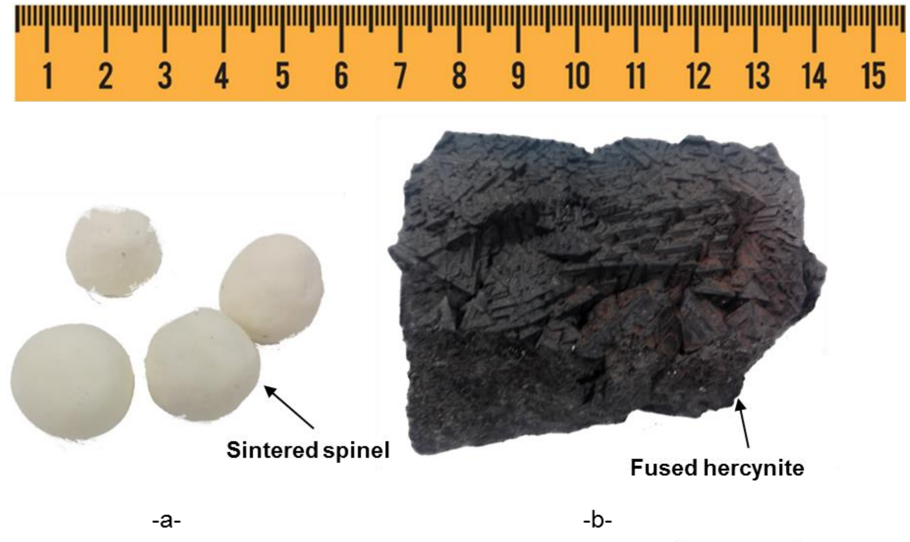

-a- -b-

Figure II-5 : Overview of a) sintered spinel and b) fused hercynite

Synthesised aggregates from these compounds have been used to produce magnesia-based composite bricks, using a similar pressing and sintering process. The characteristics of the spinel and hercynite compounds used in the elaboration process are reported in Table II-2.

Table II-2 : Physical properties of spinel group aggregates

Aggregate (1-3 mm)	Theoretical density (g/cm^3)	Bulk density (g/cm^3)	Closed porosity (%)	Melting point (°C)
Spinel	3.58	3.35	6.4%	2135
Hercynite	4.39	4.21	4%	1780

Moreover, the thermal expansion of MgO, spinel and hercynite has been measured up to 1350 °C using a heating rate of 5°C/min. The results were compared with handbook values [Fei95] for the heating step in Figure II-6.

BY NC ND

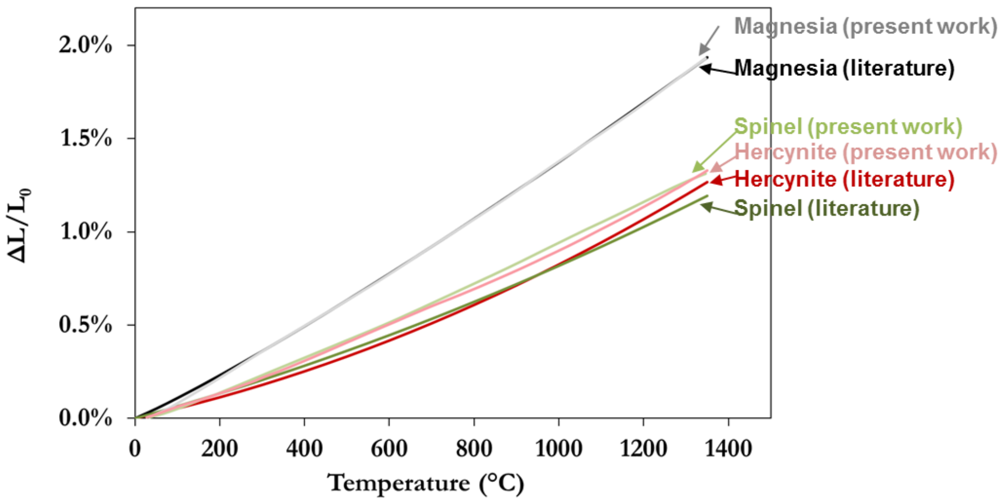

Figure II-6 : Evolution of the thermal expansion of MgO, Spinel and Hercynite combining experimental results and data from literature [Fei95]

For the magnesia sample, our thermal expansion measurements are very similar to those found in the literature. For spinel and hercynite materials, a shift towards higher thermal expansion values can be noticed for the measured curves. Nevertheless, the curve shapes for the latter are not so different from the ones found in the literature, especially at high temperatures. The CTE of each phase has been calculated and reported in Table II-3 for two temperature ranges, namely 200-400 °C and 1000-1200 °C.

Table II-3: Summary of measured and literature CTE values for magnesia, spinel and hercynite during heating

Material	Coefficient of thermal expansion (10^{-6} °C^{-1})			
	200-400 °C		1000-1200 °C	
	Present work	Literature	Present work	Literature
Magnesia	13.2	13.3	16.3	15.8
Spinel	8.9	7.44	11.0	10.4
Hercynite	8.7	6.96	11.7	12.1

The CTE of magnesia is much higher than that of spinel and hercynite, whose CTE is very much at the same level. Indeed, spinel and hercynite have a very comparable thermal expansion behaviour, which leads to a similar CTE mismatch level when used in a magnesia

BY NC ND

material. In addition to this, spinel and hercynite also have rather similar elastic properties [AnIs95]

Three types of magnesia-based composites containing different proportions of inclusions are presented, the MS type contains spinel inclusions, MH contains hercynite and MSH contains both spinel and hercynite. Therefore, inclusions from the spinel group, in the form of aggregates sized 1 to 3 mm, replace a proportion of magnesia aggregates in the same size range according to the compositions detailed in Table II-4.

Table II-4 : Composition (in wt. %) of refractory composite bricks

Bricks	Composition			Bulk density (g/cm^3)	Porosity (%)
	MgO (Matrix)	$MgAl_2O_4$ (Aggregate)	$FeAl_2O_4$ (Aggregate)		
MS5	95%	5%	_	2.94	15.24%
MS15	85%	15%	_	2.91	15.93%
MS25	75%	25%	_	2.9	16.25
MH5	95%	_	5%	2.95	15.43
MH15	85%	_	15%	2.98	15.91
MH25	75%	_	25%	3.04	15.64
MSH5	95%	5%		2.94	15.25
MSH15	85%	15%		2.92	16.21
MSH25	75%	25%		2.92	16.42

On one hand, all of the presented materials have a similar level of porosity of about 16%. On the other hand, the bulk density of MS and MSH composites decreases with increasing spinel content, while for MH composites the tendency is reversed. The latter is justified by the high bulk density of hercynite, which brings the composite density up, while the former decreases because of lower spinel density compared to magnesia. This straightforward description might not be complete given the non-linear evolution of the composite bulk density with increasing inclusion content. Therefore, this tendency will be investigated more thoroughly and discussed in the next chapters.

The visual overview in Figure II-7 exhibits some bricks (MS5, MSH5 and MH5) with their respective cross sections showing the coarse microstructure of the materials. Indeed,

BY NC ND

aggregates of different types can be distinguished within the MgO matrix, which is mostly of brown colour (with some white MgO aggregates). Moreover, spinel and hercynite have an off-white and black colour respectively.

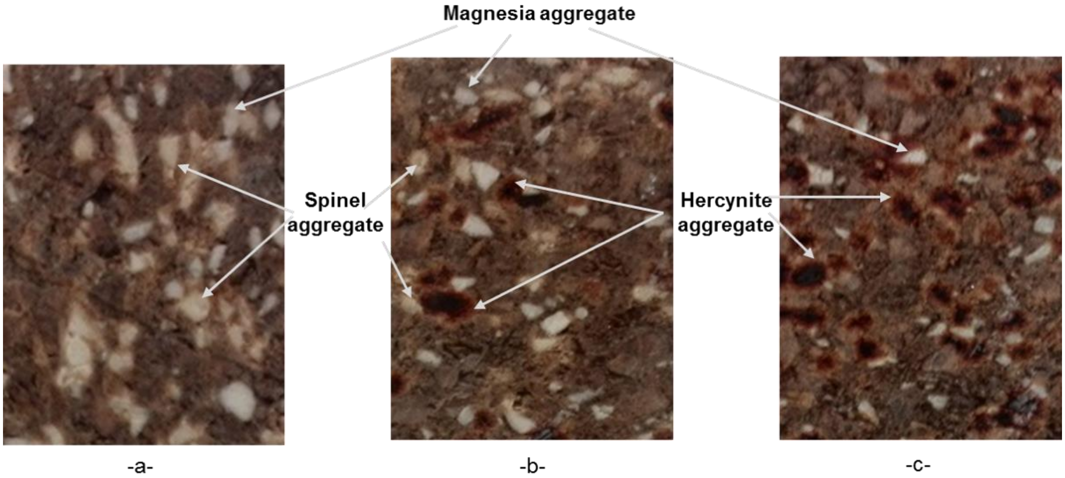

Figure II-7 : Overview of brick and cross section of a) MS5, b) MSH5 and c) MH5

The model materials detailed herein, will be characterised thoroughly in the next chapters. This simplified composite approach is destined to shed light on important microstructural features induced by the addition of spinel aggregates on essential thermomechanical and fracture properties.

II.3. Conventional methods

The characterisation of material phase compositions and elastic properties at high temperatures has been carried out to grasp the leading implications of the main physico-chemical interactions on the macroscopic thermomechanical behaviour. Conventional X-ray diffraction (XRD) analyses have been used to provide information about the crystallographic phase composition while an ultrasonic technique and acoustic emission have been employed at high temperatures to correlate the evolution of the microstructure with Young’s modulus.

II.3.1. X-ray diffraction: Rietveld refinement

X-ray diffraction (XRD) provides an essential source of information for material characterisation, such as crystal phase identification leading to the understanding of microstructural phenomena that have an impact on properties. Therefore, the main purpose

CC BY NC ND

for using XRD in this study were to identify crystalline phases, using the JCPDS ICDD database, and their quantity using Rietveld refinements. The latter consists in the analysis of experimental diffraction patterns, obtained by XRD on powders, by comparison with refined crystal structure models.

Experimental data was obtained on a fine ground powder, whose particle size was below 8 µm to ensure good quality of measurements that can be used for Rietveld refinements. A Bruker D8 Advanced diffractometer with a Bragg-Brentano geometry was used for the measurement of powder diffraction patterns while TOPAS 4-2 software was later used in the refinement process.

The experiments were performed between a 2θ of 5° and 75° with a step of 0.01° and a time step of 0.475 s. Moreover, rotation of the sample holder was activated to increase counting statistics of the measured powder. These parameters have been chosen in order to improve the quality of the measurement. Thus, the resolution of the diffraction pattern and background was improved by reducing air-scattering effects through an anti-scatter knife edge. A narrow divergence slit of 0.2° was always set to keep a constant volume of the sample under the incident beam during the experiment, further improving the instrument's resolution.

The experimentally obtained diffraction pattern is used for the pattern-fitting procedure involving crystal structure models from the literature. This method, known as the Rietveld refinement method [Riet69], uses a least-squares fitting algorithm to provide a quantitative analysis of crystal parameters (atomic coordinates and lattice parameters) and phase composition. The model crystal structures used in the analysis are compared to experimental data through a series of refinements involving different parameters, related to the experiment and the sample itself, using an appropriate fitting strategy. Fitting parameters are refined mainly to adjust model crystal structure's peak position, shape and intensity.

The quality of a Rietveld refinement is determined by the quality of the fitting between experimental and simulated patterns. In this sense, two quality factors have been used to assess the quality of fitness between experimental and simulated patterns. On the one hand, R_{wp} evaluates the quality of fitness for the whole pattern according to Eq. II.1.

$$\mathbf{R_{wp}} = \left(\frac{\sum_i \mathbf{w_i}[\mathbf{y_i}(\mathbf{exp})-\mathbf{y_i}(\mathbf{calc})]^2}{\sum_i \mathbf{w_i}[\mathbf{y_i}(\mathbf{exp})]^2}\right)^{1/2} \qquad \text{Eq. II.1}$$

Where w_i is the weight function of $y_i(exp)$ and $y_i(calc)$, the experimental and calculated intensities at step i, respectively.

BY NC ND

On the other hand, R-bragg, or R_B, determines the quality of the refined crystal structure as follows (Eq. II.2).

$$\mathbf{R_B} = \left(\frac{\sum_{hkl}|\mathbf{I_{hkl}}(\mathbf{exp})-\mathbf{I_{hkl}}\,(\mathbf{calc})|}{\sum_{hkl}|\mathbf{I_{hkl}}(\mathbf{exp})|}\right) \qquad \text{Eq. II.2}$$

Where I_{hkl} is the intensity expressed as a function of the structure factor F_{hkl} and the multiplicity m as I_{hkl}=m. F_{hkl}.

A minimum value for these quality factors is sought before validating the refined crystal structure and the resulting pattern fit. Values of R_{wp} and R_b below 12 and 4, respectively, are targeted for each refinement. While these numerical factors constitute a good indication of the quality of fitting, false minima can be obtained even with refined parameters that are physically meaningless. Therefore, an appropriate step by step fitting strategy usually involves a progressive increase in the refinable parameters to achieve the best fit.

The parameters refined during the analysis can be experimental and material related. Figure II-8 shows the main guidelines of the refinement strategy used in the analysis. Throughout the analysis, the background is modelled with a polynomial function with several refinable parameters.

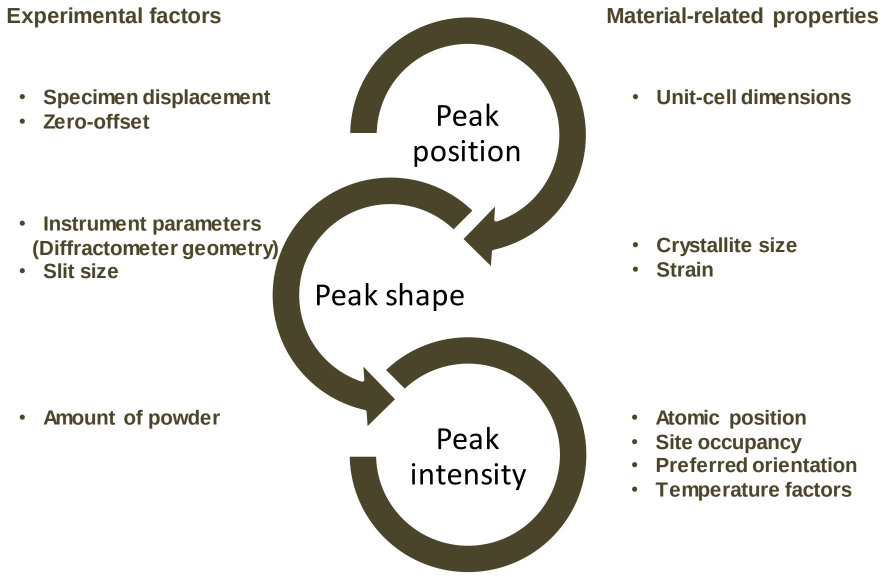

Figure II-8 : Step by step refinement strategy and important parameters [MVCL99]

Prior to any structural refinements, background and experimental factors must be refined using appropriate analytical functions. The knowledge of instrument parameters, mainly relating to

BY NC ND

diffractometer geometry, is an important input relating to experimental conditions. Moreover, the emission profile of the X-ray source was determined on NIST LaB_6 SRM 660b standard since no monochromator was used during the measurements.

II.3.2. Scanning electron microscopy

Observations of sample microstructures was done using a FEI Quanta 450 FEG scanning electron microscope (SEM). The microscope is equipped with an X-ray dispersive energy (EDS) probe to perform chemical analyses on the materials. Given the nature of the investigated materials, back-scattered electron micrographs were taken to highlight the chemical contrast between the different constituents.

One of the challenges of SEM observations is image quality resulting from sample preparation. Indeed, the composite nature of the materials and the presence of pre-fabricated microcracks in the microstructure make the grinding and polishing steps critical during sample preparation for SEM. Therefore, machined samples were impregnated in an epoxy resin (IP, Presi) and a hardener. The composition of the resin can be changed by addition of ethanol in order to alter its viscosity and improve its impregnation ability. This way, for the specific case of crack propagation observation using SEM, the resin has been adapted to enable easier infiltration of fine cracks.

Therefore, a procedure was specifically developed for soft and brittle composite refractories in order to achieve the best surface finish. The grinding and polishing protocol was performed using water-based lubricants and a force of about 25N as detailed in Table II-5.

Table II-5: Polishing protocol for SEM sample preparation

Polishing disc (From Struers)	Abrasive	Polishing time (in minutes)
MD-Piano 500	Diamond 31 µm	2
MD-Piano 1200	Diamond 12 µm	3
MD-Largo	Polycrystalline diamond suspension 9 µm	12
MD-Largo	Polycrystalline diamond suspension 3 µm	12
MD-Nap	Polycrystalline diamond suspension 1 µm	12

BY NC ND

II.3.3. Ultrasonic long bar mode at high temperature

The main purpose of the high temperature ultrasonic measurement method is to investigate the evolution of material elastic properties during a thermal cycle. This low-frequency method uses the so-called long bar configuration to perform measurements at high temperature, where a longitudinal ultrasonic wave is sent using a magnetostrictive transducer to the sample [GaPL85]. This configuration imposes some geometrical constraints on the sample. Thus, a parallelepipedic sample whose lateral dimensions are lower than the signal wavelength must be used [PFLR74]. In fact, measurement parameters, such as wavelength and sample geometry, are strictly dependent on the nature of the investigated material and the heterogeneity of the microstructure.

An alumina waveguide, glued to the sample using a refractory cement, is used to ensure thermal isolation between the furnace and the transducer, as depicted in the schematic of Figure II-9, showing the principle of the technique.

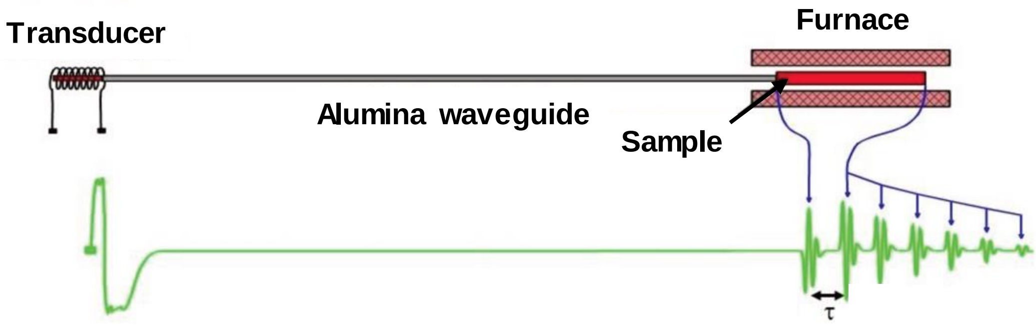

Figure II-9 : Schematic of ultrasonic measurements in long bar mode [HuFG02]

Ultrasonic measurements in long bar mode have been commonly used in the past to evaluate the elastic properties of refractories at high temperatures [TeGH06]. Young’s modulus is evaluated during a thermal cycle by measuring the round-trip time for a longitudinal wave through the sample with the knowledge of its bulk density according to Eq. II.3.

$$E = \rho . \left(\frac{2.L}{\tau}\right)^2 \qquad \text{Eq. II.3}$$

Where ρ is the bulk density of the material, L the length of the sample and τ the round-trip time for the longitudinal wave.

BY NC ND

The definition of sample dimensions and experimental conditions was performed based on the optimisation of the signal to noise ratio. Therefore, parallelepipedic samples with dimensions of 12x12x120 mm^3 have been used to ensure that a representative sample is taken with regard to the size of large aggregates (up to 3 mm). The frequency of the transducer and the waveguide diameter were chosen to account for material peculiarities, such as defects and grain size. Indeed, heterogeneities such as pores and microcracks tend to have a damping effect on the signal, therefore reducing its quality after reflection by the sample's back end. Experimental conditions have been summed up in Table II-6.

Table II-6: US measurements' experimental parameters

Sample dimensions	12x12x120 mm^3
Transducer frequency	60 kHz
Waveguide diameter	10 mm

Experiments have been performed up to 1400°C with a heating rate of 5°C/min. Temperature has been measured using a thermocouple placed conveniently close to the sample, while ultrasonic reflections have been recorded using a receiver.

As mentioned previously, the measurement of Young's modulus according to this method is sensitive to interatomic bonds at the structural level but also heterogeneities at the microstructural scale of the material. For instance, large aggregates, pores and microcracks are a common feature in refractories, which will have an impact on the propagation of the longitudinal wave. Therefore, materials that are prone to exhibit thermally induced damage, such as magnesia-spinel or magnesia-hercynite materials, are likely to present a hysteretic Young's modulus evolution as a function of temperature. Indeed, Figure II-10, shows a typical evolution of elastic properties at high temperatures for two types of materials.

BY NC ND

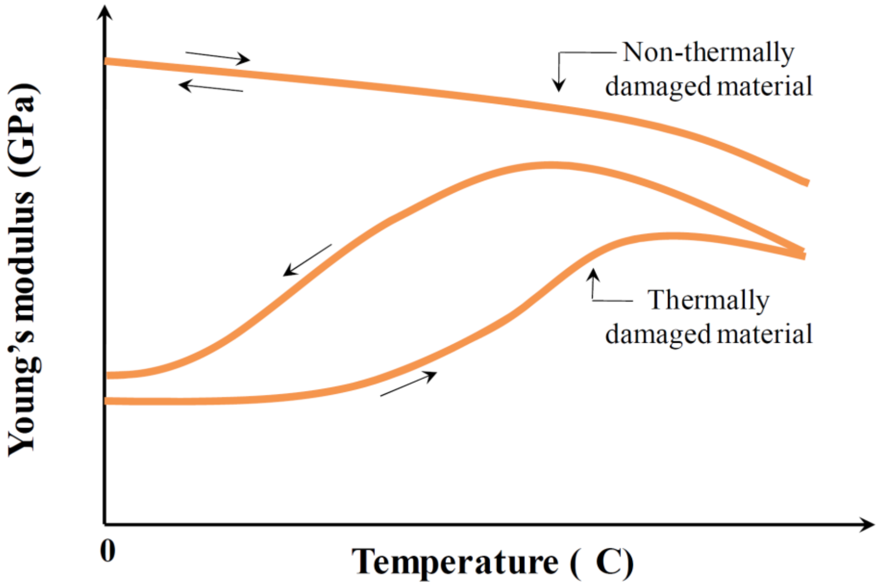

Figure II-10 : Typical Young's modulus evolution as a function of temperature for a non-damaged material and a thermally damaged material

II.3.4. Acoustic emission at high temperature

The acoustic emission (AE) technique is a non-destructive characterisation method that records and then analyses acoustic waves coming from a sample. AE is the result of the propagation of a transient elastic wave relating to a localised source within the sample. Therefore, AE events might occur when a sample is subjected to an external solicitation, such as mechanical and thermal loads. Indeed, AE events are usually associated to microstructural phenomena involving a rapid energy burst, such as crack initiation and propagation. The AE method is sensitive and non-directional, which means that measurements are done independently from where the energy release originates within the sample. The application of this method has been done mostly to monitor crack propagation during mechanical tests [BKIP08], often at room temperature. Its application at high temperatures has been achieved for many materials to follow phase transformations [PPMH10], cement hydration [Ceau04] and the occurrence of damage [CSLH08] among other physical phenomena. Therefore, in refractory materials that exhibit microcrack network formation during cooling after sintering, AE signals can be recorded and then analysed [BTHC08]. Such is the case for magnesia-spinel materials in [GAHG12], where recorded AE events relate to the occurrence of damage resulting from a thermal expansion mismatch between magnesia matrix and spinel inclusions.

BY NC ND

Figure II-11 depicts the experimental setup for the application of AE at high temperatures. A parallelepipedic sample, with dimensions of 5x5x25 mm^3, is placed on top of a sharp alumina wave-guide.

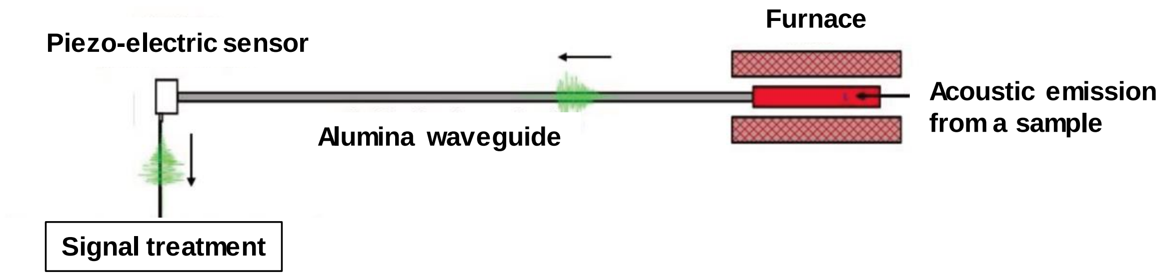

Figure II-11 : Schematic description of high temperature acoustic emission setup [CSLH08, Gour16]

In order to avoid parasitic signals, no coupling agent is used between the sample and the waveguide. The furnace is similar to the one used in ultrasonic measurements and can go up to 1550°C.

The recorded AE signals are mainly burst-like emissions relating to an event occurring in the microstructure. These emissions are usually referred to as hits and correspond to a short high-energy signal (Figure II-12.a). A hit is characterised by the number of counts, rise time, amplitude (in Db) and duration of the hit. Moreover, given the nature of the investigated materials and their behaviour at high temperatures, burst-type AE signals are expected due to the occurrence of microcracks during cooling of the materials (Figure II-12.b). Therefore, acquisition parameters have been set to account only for AE signals above an amplitude threshold of 35 dB in order to avoid noise interference. Other parameters such as:

- Peak Definition Time (PDT), helps define the maximum amplitude of the signal. The value was fixed at 200 µs.
- Hit Definition Time (HDT), gives the total duration of a hit. Value was fixed at 1000 µs.
- Hit Lockout Time (HLT), limits echo effects on the recorded AE signal. Value was fixed at 1000 µs.

BY NC ND

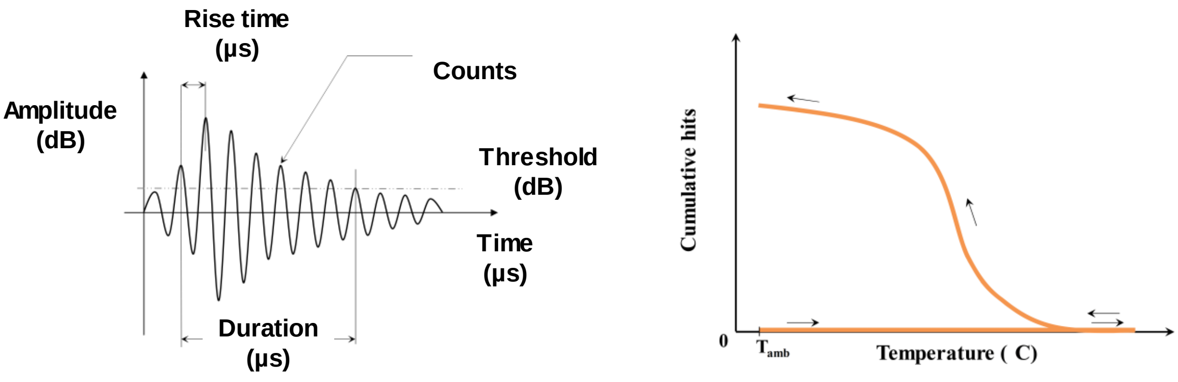

-a-

-b-

Figure II-12: Schematic of a) burst-type AE signal [Mige11] and b) typical AE evolution for a thermally damaged material [Gras11]

AE measurements have been performed using the same experimental conditions as for ultrasonic measurements to supplement Young's modulus evolution with information regarding microstructure evolution during the thermal cycle. Indeed, the association of ultrasonic measurements and AE provides a good basis for establishing a link between thermomechanical properties and microstructure related events.

II.4. Conclusion

In this chapter, thermomechanical loads in cement rotary kilns were highlighted as an important cause for reduced refractory service life. Therefore, in many parts of the furnace, magnesia-spinel group materials are used by taking advantage of the CTE mismatch between magnesia and spinel inclusions to promote microcrack occurrence within the microstructure. As discussed in Chapter I, microcrack networks can greatly benefit the thermal shock resistance of refractories.

In this sense, magnesia-spinel group composites with a simplified composition were designed and produced to evaluate the impact of thermally induced damage on the thermomechanical and fracture behaviours. In particular, the influence of regular spinel and hercynite aggregates on the microstructure of magnesia refractories is sought, whereby they are expected to have a strong impact on thermomechanical properties and the fracture behaviour of the model composites.

An appropriate set of experimental techniques has been presented, which will be used to carry out microstructure and thermomechanical property investigations. One of the main

BY NC ND

goals of this study is to provide an understanding of microstructure-thermomechanical property relationships that can help design materials with enhanced properties.

BY NC ND

Chapter III

BY NC ND

Chapter III. Refined Digital Image Correlation (DIC) coupled with the Wedge Splitting Test: Optimisation of experimental conditions and subsequent analysis

III.1. Introduction

The application of optical methods during a fracture experiment, such as the Wedge Splitting Test (WST), offers an interesting panel of analysis tools that can be used to evaluate displacement fields all over the test specimen. Indeed, the accurate measurement of displacements is necessary to ensure that a reliable fracture characterisation can be achieved after the WST.

Therefore, the optimisation of experimental conditions, including sample preparation, is investigated thanks to optical methods. In particular, the importance of crack opening displacement measurement is emphasised through a detailed analysis involving comparison of individual WST parts' displacements.

In addition to this, fracture characterisation is enriched by the use of DIC to monitor crack propagation through strain field calculation. A refined DIC method destined to provide accurate crack representation and length quantification is applied.

III.2. Experimental setup and sample preparation

III.2.1. The Wedge Splitting Test (WST)

The WST has been first introduced by Tschegg [Tsch86] as a method for fracture characterisation used mainly on concrete [BrWi90b, Tsch91] at the beginning. This experiment was favoured over other fracture tests, especially for materials with a coarse microstructure such as concrete and refractories [HaTs97], because it ensures stable crack propagation in relatively large specimens.

Indeed, the WST offers an ideal configuration to achieve stable crack propagation and measure fracture parameters such as the nominal notch tensile strength (σ_{NT}) and the specific fracture energy (G_f). The testing setup is composed of four load transmission parts, namely two supports and two rolls, a linear support placed at the bottom of the sample and a wedge as shown in Figure III-1.

BY NC ND

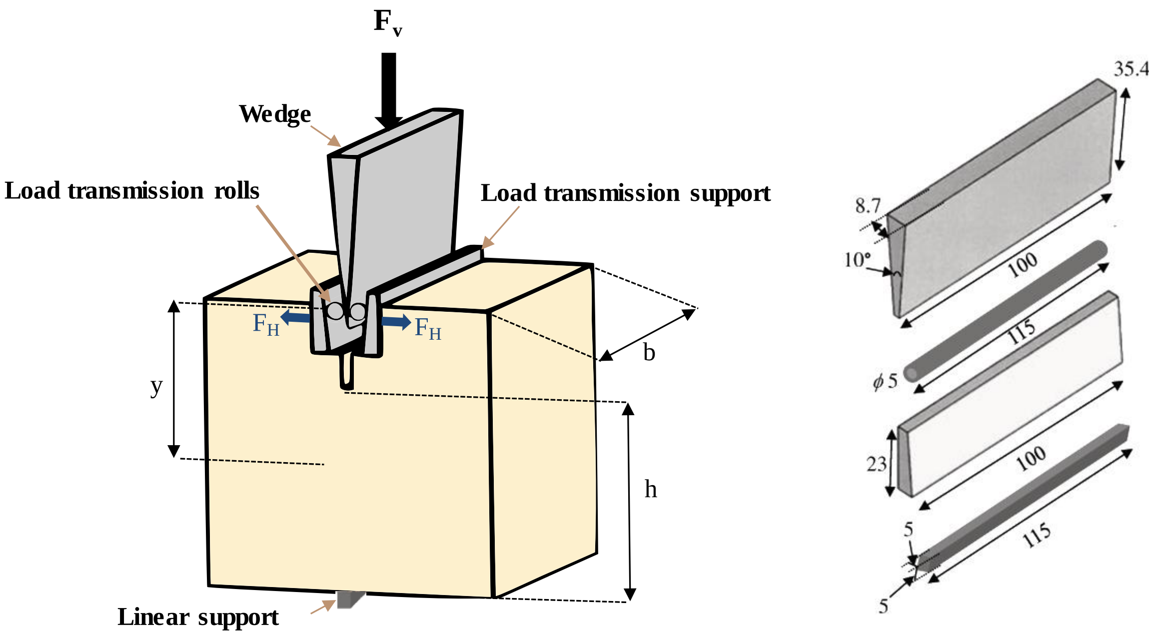

Figure III-1: Schematic of WST setup and dimensions of load transmission parts [Belr15]

The load is transmitted from the wedge to the sample thanks to the metallic supports, where the vertical load F_V applied by the wedge is converted into a horizontal load F_H. This setup, made of very rigid parts, contributes to limiting the elastic energy stored in the testing machine and thus promotes stable crack propagation. Cubic samples of 100x100x100 mm^3 have been machined from model refractory bricks in order to produce the groove and the starter notch for crack propagation. The dimensions of the groove and the notch are 24x22.5x100 mm^3 and 3.5x12x100 mm^3 respectively.

During the preparation of the WST, the initial positioning of the metallic parts on the sample groove is an important step. Indeed, without applying any pre-load, the wedge must be maintained in a vertical position while the metallic rolls must be placed at the same horizontal level to ensure an optimal load transfer throughout the experiment. Therefore, a WST setup procedure was defined in order to provide optimal positions for the WST parts, as shown in Figure III-2.

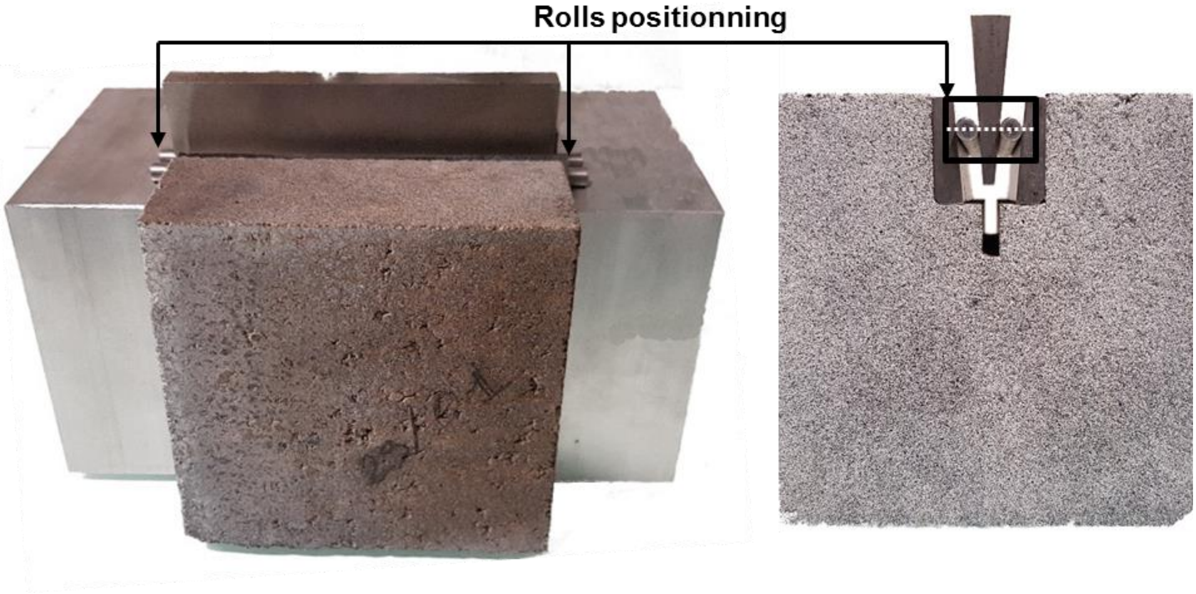

Figure III-2: WST preparation step, positioning of rolls on the same horizontal plane

The preparation of the WST is done on a planar surface using the support in Figure III-2 to place the metallic rolls on the same plane. Since no load is applied at this stage, the stability of the setup is strongly dependant on small surface imperfections of the groove area, where the metallic supports are placed. This point will be investigated in detail later in this chapter.

Loading is performed using a crosshead speed of 0.5 mm/min. The applied vertical load F_V is recorded along with the crosshead vertical displacement δ_V. Then, horizontal load and displacement can be deduced from the associated vertical components using Eq. III.1 and Eq. III.2:

$$\mathbf{F_H} = \frac{\mathbf{F_V}}{\mathbf{2.tan(\alpha/2)}} \qquad \text{Eq. III.1}$$

$$\boldsymbol{\delta_H = 2.\delta_V.\tan(\alpha/2)} \qquad \text{Eq. III.2}$$

Where α, equal to 10°, is the angle of the wedge. The accurate measurement of the horizontal load and displacement is a key point during WST experiments. Particularly so for the horizontal displacement as it should represent crack opening displacement (COD), an essential fracture parameter used to plot the horizontal load-COD curve. For this reason, this parameter is measured directly as load-point displacement using DIC instead of deducing it from crosshead vertical displacement, as will be explained in the next section.

BY NC ND

From the maximum load and specimen dimensions, the nominal notch tensile strength can be calculated using Eq. III.3

$$\sigma_{NT} = \frac{F_{H\,max}}{b.h} + \frac{6F_{H\,max}.y}{b.h^2} \qquad \text{Eq. III.3}$$

Where F_{Hmax} is the maximum horizontal load, b and h are the width and the height of the fracture surface and y the vertical distance between the load-point and the centre of gravity of the fracture area.

The total fracture energy can then be calculated from the total area under the horizontal load-COD curve (Figure III-3) according to the integral in Eq. III.4.

$$G_T = \frac{1}{A}\int_0^{\delta_{H\,max}} F_H \,.\, d\delta_H \qquad \text{Eq. III.4}$$

Where A is the projected fracture surface area, δ_H the COD and δ_{Hmax} represents its maximum value during the fracture test. However, for practical reasons, the fracture energy is calculated up to 15% of the maximum horizontal load as shown in Figure III-3.a.

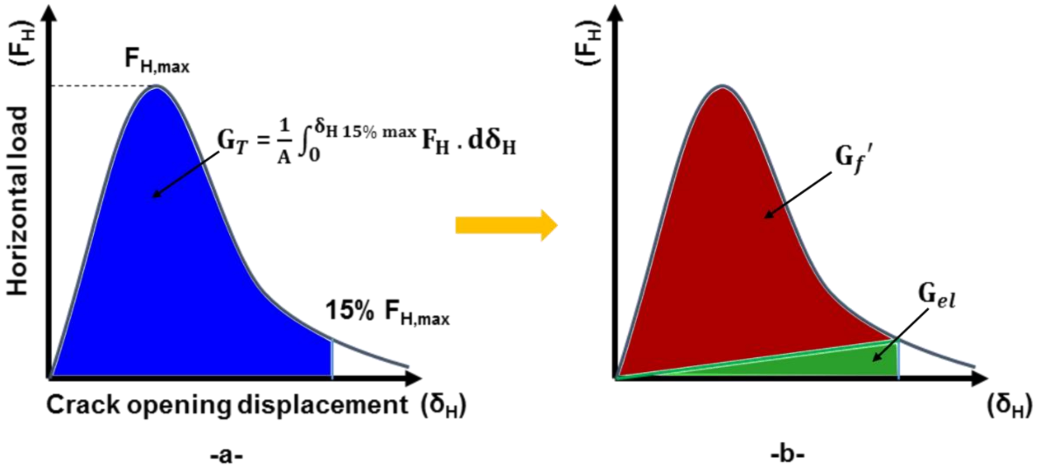

Figure III-3 : Typical Horizontal load-COD curve and area under the curve corresponding to a) total energy and b) decomposition of total energy into fracture (red) and elastic (green) energies

In this case, the total energy can be decomposed into an elastic contribution and the actual fracture energy, which relates to the energy consumed by the FPZ during crack propagation. Indeed, since fracture is not completely reached at 15% of the maximum load, some residual elastic energy is expected to be stored in the sample and included in the total energy. Therefore, the fracture energy is deduced from the difference between the total energy and the elastic energy (Figure III-3.b), which is expressed following Eq. III.5 and Eq. III.6.

$$\mathbf{G_{el}} = \frac{1}{2} . \mathbf{F_H \delta_H} \qquad \text{Eq. III.5}$$

$$G_f' = G_T - G_{el} \qquad \text{Eq. III.6}$$

The elastic energy is calculated at each loading state by assuming an elastic material behaviour.

The measurement of fracture energies depends on accurate measurements of the COD, which can be deduced directly from crosshead vertical displacement, this is a common approach used in previous studies. Therefore, it might be more suitable to completely monitor the WST experiment to measure the COD with a higher accuracy as will be detailed in the next sections.

III.2.2. Specific sample preparation for the application of optical methods

The characterisation of the fracture behaviour of magnesia-spinel refractories using the WST and optical methods requires appropriate sample preparation for accurate measurements of the crack opening displacement. Moreover, the COD can be assessed accurately using DIC or marker tracking if favourable experimental conditions are reached, where no disturbance is allowed to alter the kinematic chain of measurement going from the sample to the camera. This is particularly important for most refractories, including magnesia-spinel model materials, which are expected to exhibit low strains when tested at room temperature.

In order to apply optical methods during the WST experiment, sample surface must be prepared to provide enough contrast. In the case of DIC, a speckle pattern is applied on the sample surface by using spray paint, as shown in Figure III-4. As such, an opaque white layer was applied before droplets of black paint were sprayed.

CC BY NC ND

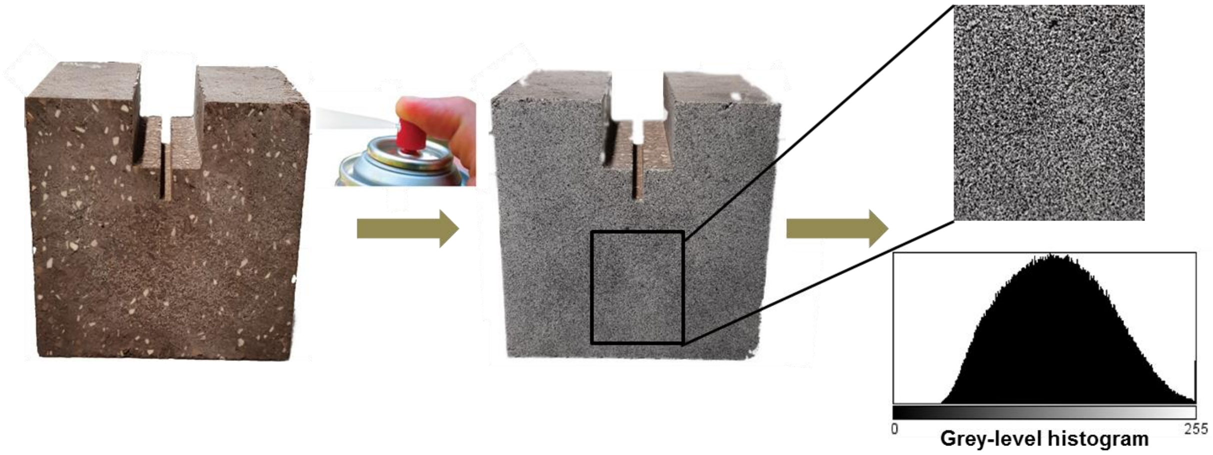

Figure III-4: Speckle pattern application on a sample surface

The resulting pattern is usually assessed by checking the histogram representing the grey level distribution, which should be as large as possible. The application of a speckle pattern is a critical step prior to DIC measurements as it affects measurement accuracy.

Therefore, in order to achieve a satisfactory pattern, it is important to have a certain control on the black droplets sprayed on top of the white layer. When using spray paint for instance, the pressure applied on the nozzle has an influence on the size and the flow rate of the droplets. Moreover, the angle of spraying also has an influence on the final outcome. Figure III-5 shows the protocol for applying optimal speckle patterns using spray paint.

BY NC ND

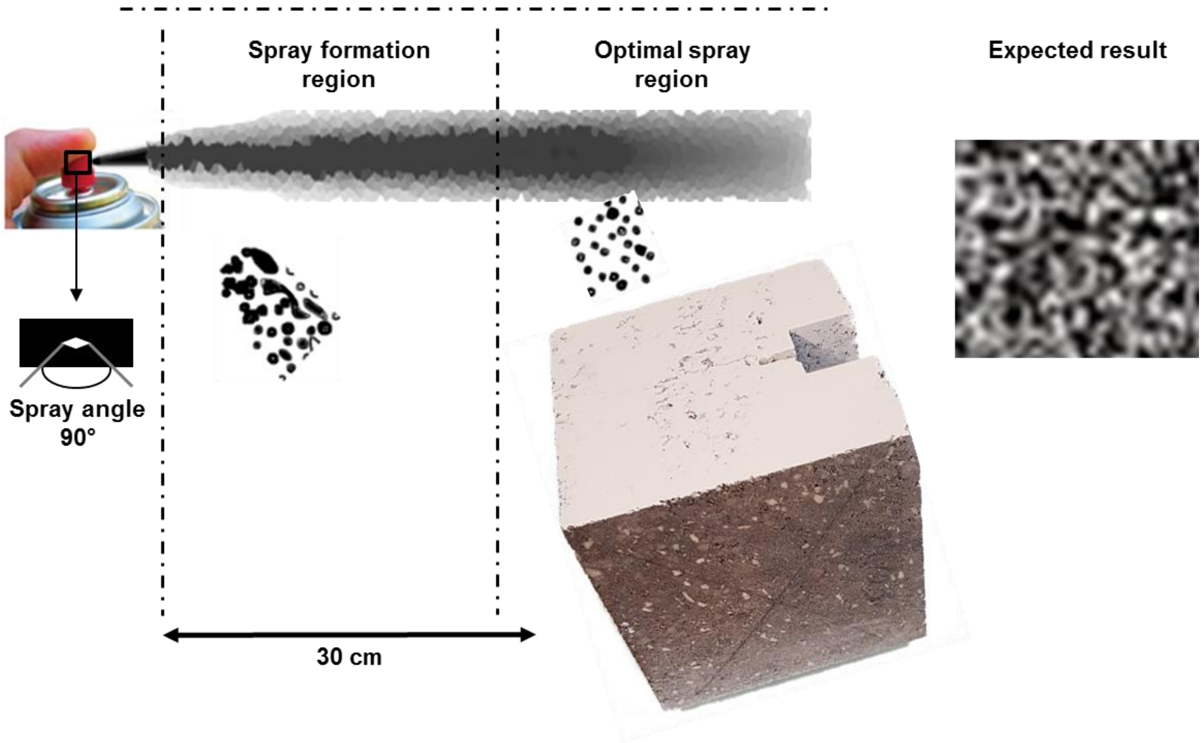

Figure III-5: Description of speckle pattern application on a WST sample using spray paint

Spraying is done in a parallel direction to the inclined sample surface of interest, where droplets are expected to fall down by gravity within the optimal spray region. A distance of approximately 30 cm between the spray and the sample is recommended to avoid large droplet deposition on the sample. Indeed, in the spray formation region located directly after the orifice, large droplets break-up from the core liquid paint due to liquid-ambient gas disturbances. Therefore, at 30 cm from the sample, mild pressure should be applied on the nozzle to achieve a medium rate flow with relatively small droplets in the optimal spray region while sweeping over the sample. Obviously, the applied pressure depends on the type of nozzle and the nozzle-sample distance.

In the end, the main goal behind this preparation is to achieve an optimal speckle pattern that can ultimately be verified by criteria such as mean speckle size, the sum of square subset intensity gradients and mean intensity gradient among others developed more recently [LSBS06, SZXG16, PYKP17].

The final experimental setup is presented in Figure III-6. The WST sample is placed in front of a CMOS camera and LED lights are used as a cold light source to provide sufficient illumination without heating the sample, an effect that can have a strong impact on measurements as discussed in I.3.3. Moreover, markers were put on the metallic parts of the WST to follow their displacement during the test using the marker tracking method.

BY NC ND

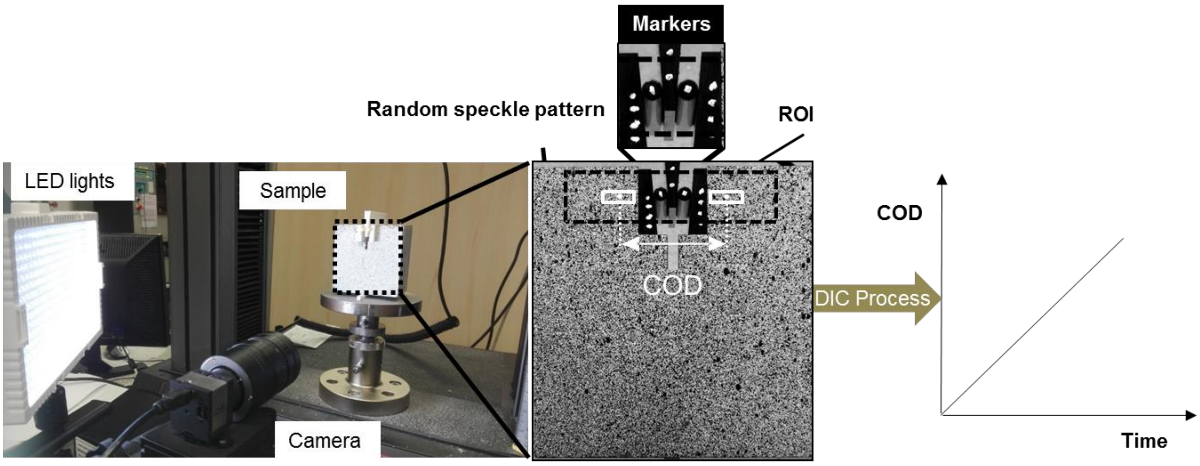

Figure III-6 : Experimental setup for the application of DIC and marker tracking during WST

Images are acquired throughout the experiment at a rate of one image per second. The images are then processed using the DIC Correla software to measure the displacement fields. The application of DIC during a WST experiment is twofold: Firstly to measure the COD by DIC and then to monitor crack propagation by a refined method called 2P-DIC.

Given the sensitivity of optical methods to noise coming from ground vibrations and thermal variations, a preliminary study was conducted to validate the accuracy of DIC measurements prior to any WST experiment. Then, the displacement of WST parts was analysed during an experiment to assess the accuracy of COD determination.

III.3. Optimisation of experimental conditions

III.3.1. Thermal stability during the experiment

The application of optical methods, be it DIC or marker tracking, requires stable experimental conditions for accurate measurements. Therefore, any external influence may have an impact on the kinematic chain of measurement. This is even more important for refractory materials as they usually exhibit low strains, making it challenging to obtain accurate measurements using DIC for such low values of strain ($\cong 0.1\%$).

For this reason, it is important to ensure that stable experimental conditions are reached before images are acquired. As presented previously, the experimental setup for the coupling of WST with optical methods is prepared by taking great care in avoiding external nuisance parameters such as ground vibrations and temperature variations in the room. Therefore, the sample is placed in the laboratory 4 hours prior to the test.

BY NC ND

Another parameter that can be of significant importance is camera heating, which occurs in two steps. When the camera is plugged, the electronic components heat up leading to an increase of temperature, as reported previously [Belr15]. For this reason, the camera is plugged one hour before performing measurements. The second step of camera heating occurs during image acquisition, when a link is established between the camera and the monitor displaying the acquired images in a live configuration.

To evaluate the impact of the latter case, the external temperature of the camera was measured using a K-type thermocouple during image acquisition of a vitreous silica sample (not very sensitive to thermal variations due to a very low thermal expansion coefficient). Then, images were processed using widely spaced large subsets (256x64 px² subsets spaced by 800x64px²) to optimise measurement accuracy coming from Correla (DIC software). The images were acquired without any mechanical loading, only to assess the accuracy of DIC measurements.

As shown in Figure III-7, the external temperature of the camera during image acquisition increases by 0.7 °C during a period of approximately 5 minutes. This seemingly small external temperature variation corresponds to a variation of the camera sensor’s temperature by approximately 7°C to 9°C, according to information displayed by the camera’s software. This change is enough to provoke a non-negligible bias in strain measurements, therefore altering the characterisation of strain by DIC.

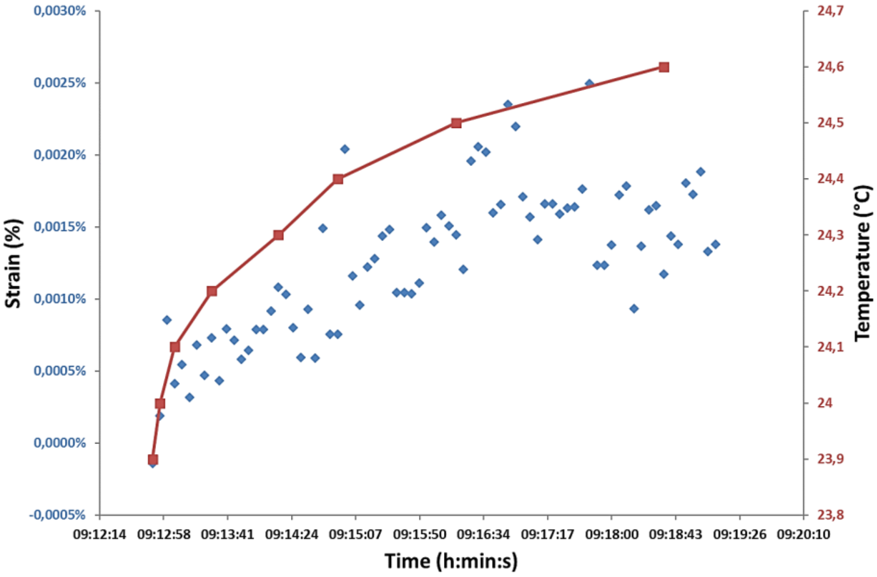

Figure III-7: Influence of temperature on the strain measured by DIC on a sample

In order to circumvent this problem during fracture experiments, the camera is put in continuous acquisition mode for 30 minutes approximately prior to experiments (enough time to reach a steady-state regime for the camera sensor's temperature).

When all of these experimental parameters are controlled, DIC measurements can present a high accuracy. Indeed, as shown in Figure III-8, a reference measurement was performed where no disturbance parameters were allowed. Thus, strain measurements with a standard deviation of 10^{-6} were achieved. However, this value was obtained by taking widely spaced large subsets, which are not always an option during mechanical characterisation experiments.

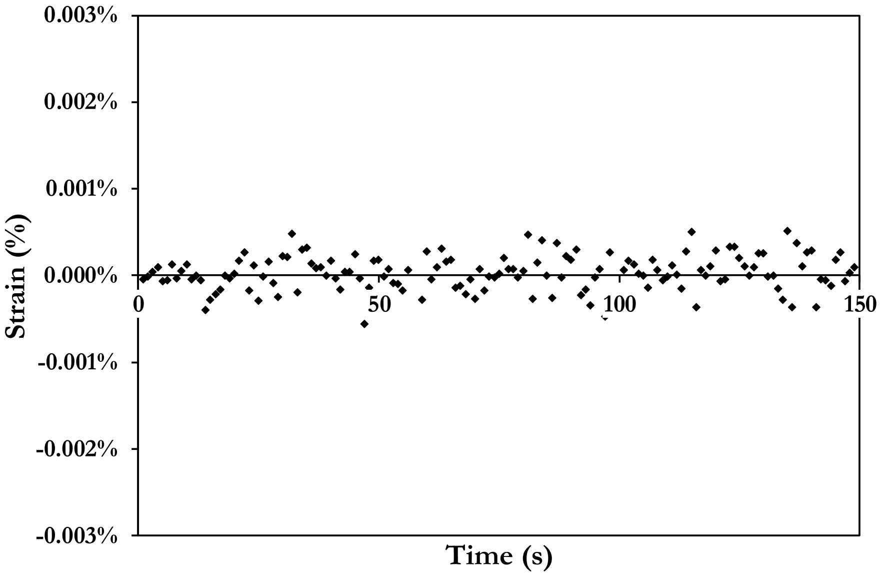

Figure III-8: The evolution of strain as a function of time with limited measurement disturbance

Therefore, when all experimental key-points are addressed during an experiment, DIC strain measurements can provide reliable and accurate characterisation of material behaviour. Indeed, the DIC method can realistically measure strains as low as 10^{-5} in testing conditions, which is appropriate for materials that exhibit low fracture strains such as refractories. In this sense, the DIC technique can be considered on par with other well proven methods, such as strain gages, especially with its ability to access strain fields anywhere on the sample as long as it is included in the image.

III.3.2. Application of optical methods to monitor displacements related to WST

Aside from the stability of the optical measurement system, the WST setup itself involves an intricate interaction of metallic pieces that is prone to parasitic displacements.

BY NC ND

Indeed, small surface irregularities and roughness in the groove area of the sample along with contact pressure are sufficient to provoke unwanted displacements between the metallic pieces, especially at the beginning of loading. Therefore, the accurate measurement of the COD as the load-point displacement is not a straightforward issue in the WST setup used in the present research study.

The measurement of the COD during the WST can be performed using different methods, including DIC and marker tracking. The easiest way to access the COD is by simply deducing it from the crosshead vertical displacement using Eq. III.2. However, given the noise and parasitic displacements associated with the loading machine, these displacements are known for not being very accurate. Therefore, using this method, a curvature is obtained at the beginning of loading. Figure III-9 illustrates this experimental aspect, which is believed to be directly related to the measurement of displacements.

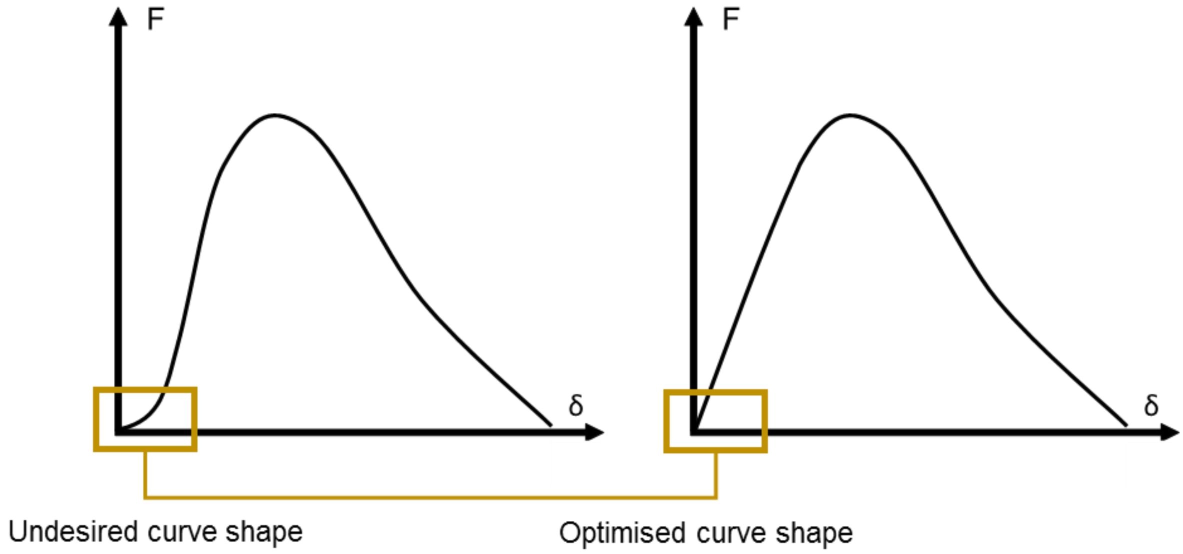

Figure III-9: Schematic description of WST curve shape at the beginning of loading

In order to measure COD values accurately, LVDT sensors can be used for example [Gang16]. But naturally, the application of optical methods is more suitable since no contact is necessary between the measurement system and the sample.

The COD can be considered as the horizontal displacement of the rolls, the metallic supports or the adjacent sample area. Therefore, the analysis of the respective displacements can be done using the marker tracking method (explained in Annex A) for the metallic parts and DIC for the sample, as highlighted in Figure III-10.

BY NC ND

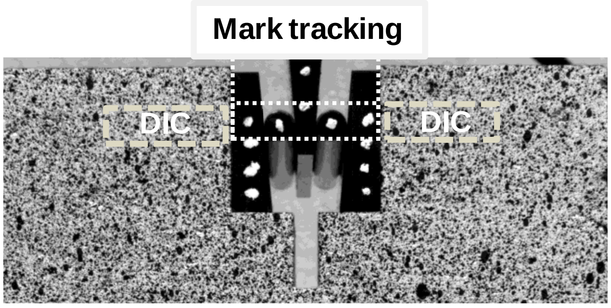

Figure III-10: Markers and subsets used for displacement measurements

Nevertheless, in order to measure fracture energies accurately, which is the main goal behind WST experiments, it is more appropriate to measure the COD at the load application point by avoiding any parasitic displacements coming from the loading device itself.

Before the WST experiment is started, a low pre-load of 5N was applied to ensure contact between the loading plate and the wedge. The graph in Figure III-11 shows the evolution of the vertical displacement of the crosshead, the wedge and the rolls. The vertical displacements of the crosshead and the wedge are on a comparable level, while roll displacement is about half that of the wedge.

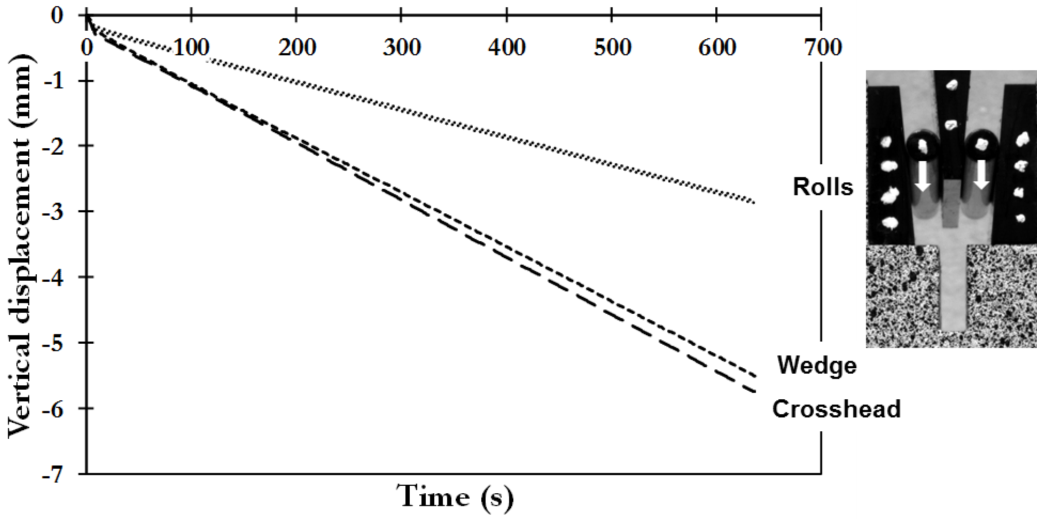

Figure III-11: Evolution of the vertical displacement of the crosshead, wedge and rolls as a function of time during a WST

The vertical displacement of the rolls is allowed by this WST setup mainly to limit friction effects during loading, which could have a detrimental effect on the fracture characterisation. However, due to this vertical component, roll horizontal displacement would present

BY NC ND

disturbances given roll rotation and the shape of the metallic supports, on which they move down.

Nevertheless, horizontal displacements can be measured elsewhere on the adjacent metallic supports or the sample. A first evaluation was done using markers on the former, where the marker tracking method provided the displacement of each metallic support, as shown in Figure III-12.

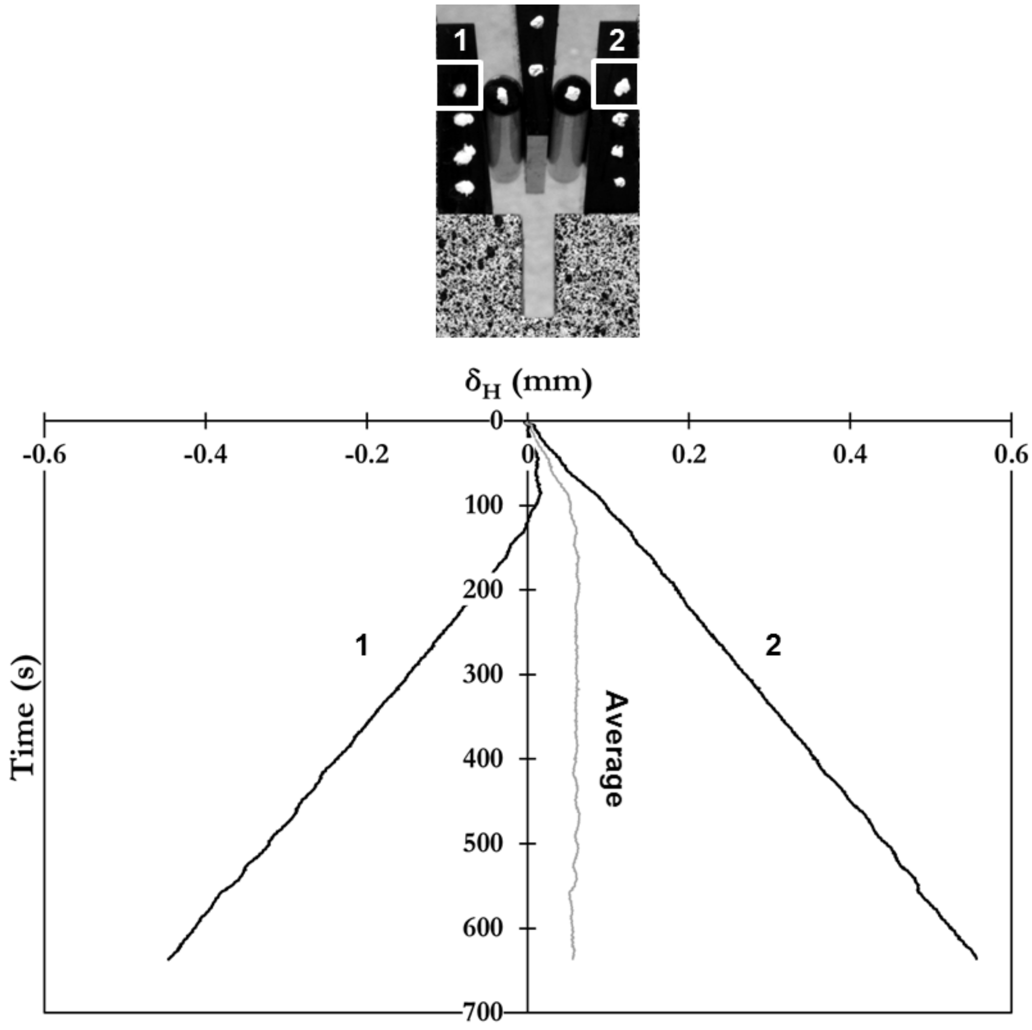

Figure III-12: Evolution of horizontal displacements as a function of time for one marker position of metallic supports and average of the support displacements

These results reveal a slight sample shift at the beginning of loading, which leads to the displacement of both supports to the right side coming from the rotation of the sample with regard to the bottom support. Nevertheless, metallic support displacements are quite accurate

BY NC ND

in following the opening of the crack throughout the WST, as suggested by the relatively constant curves' average.

Nevertheless, in order to evaluate the extent of roll displacement influence on COD determination, the latter was calculated using four marker positions and reported in Figure III-13. As shown on the image inset, COD 1 corresponds to markers located at the initial position of the rolls while COD 2 refers to markers taken at the very bottom of supports.

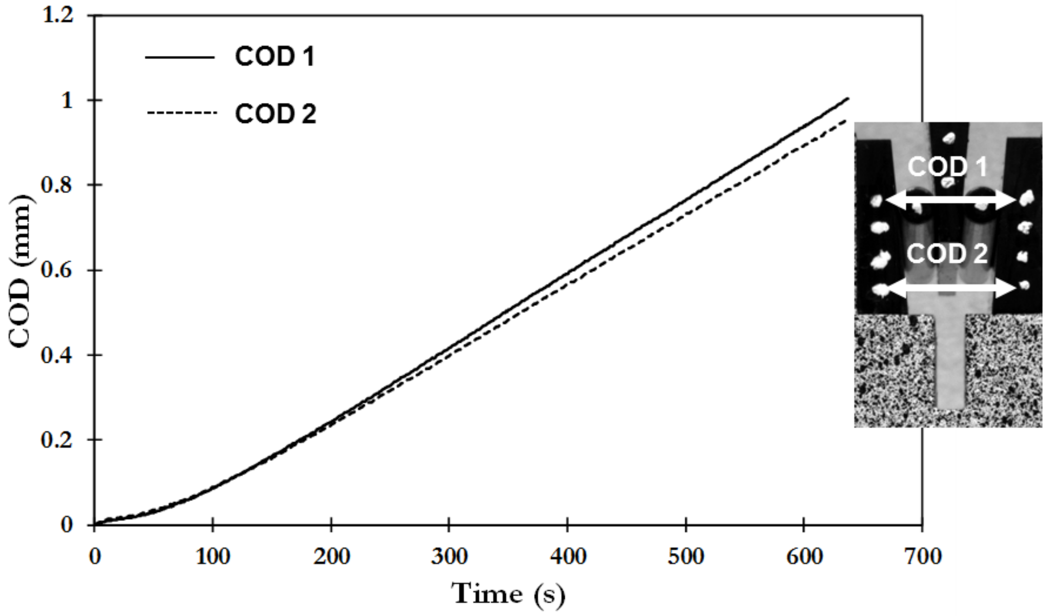

Figure III-13: Evolution of COD as a function of time for two marker positions on the metallic supports of the WST equipment

The results indicate that only a slight difference exists between COD 1 and COD 2, the extent of which is 0.05 mm at the end of the experiment, coming from the flexural component of the WST (Figure III-14).

BY NC ND

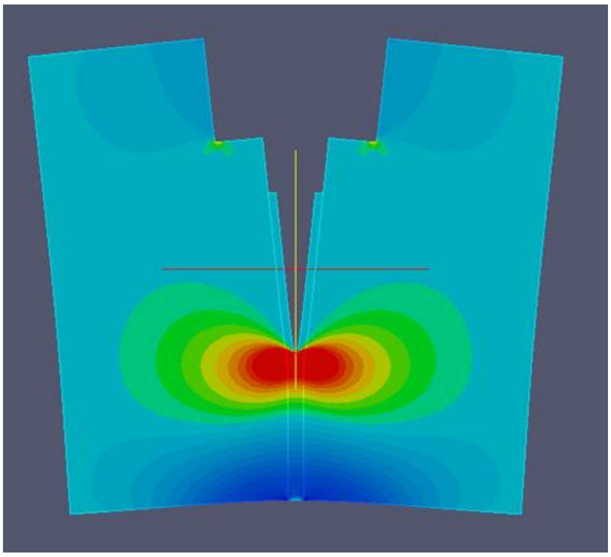

Figure III-14: Amplified deformation of a WST sample from a linear elastic simulation

Finally, horizontal displacements were measured on the sample using DIC to provide a comprehensive comparison of δ_H measurements leading to optimal COD determination for WST characterisation. The graph in Figure III-15 shows lower values of COD calculated on the sample compared to the supports and the wedge. Indeed, when the measurement is performed directly on the sample through DIC subsets, parasitic displacements coming from the setup of WST parts are overcome. Subsequently, $\delta_{H,Sample}$ (DIC)< $\delta_{H,Supports}$ (Marker tracking)< $\delta_{H,Wedge}$ (Marker tracking deduced from vertical displacement).

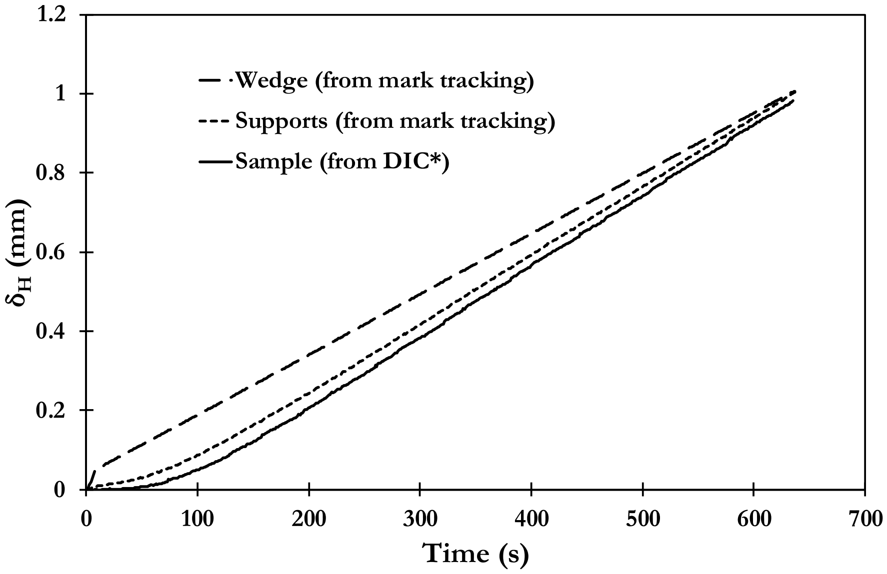

Figure III-15: Evolution of wedge, supports and sample δ_H as a function of time during a WST

BY NC ND

In addition to this, up to 50 seconds in the experiment, the part of the curve corresponding to the beginning of loading raises some questions as different curve shapes can be noticed. While support and sample δ_H curves follow the same trend with slightly different slopes, the wedge exhibits a different behaviour. This difference is likely to have an impact on the whole WST curve.

Indeed, the graph in Figure III-16 plots the difference between δ_H curves deduced from the wedge's vertical displacement and the one measured on the sample as well as the difference between support and sample horizontal displacements.

The evolution of these curves demonstrates that an increasing difference between metallic parts, namely the wedge and the supports, and the sample occurs up to 110 seconds during this experiment. The peak of these curves coincides with the maximum load of the WST experiment, after which, the δ_H differences start to decrease. These results suggest that prior to the peak load of the WST, metallic part displacement rates are higher than that of the sample. This is most likely due to contact pressure between the metallic parts along with imperfect contact between the parts and the sample. The trend is reversed after the peak load as crack propagation occurs and sample displacement rate becomes higher than that of the metallic parts.

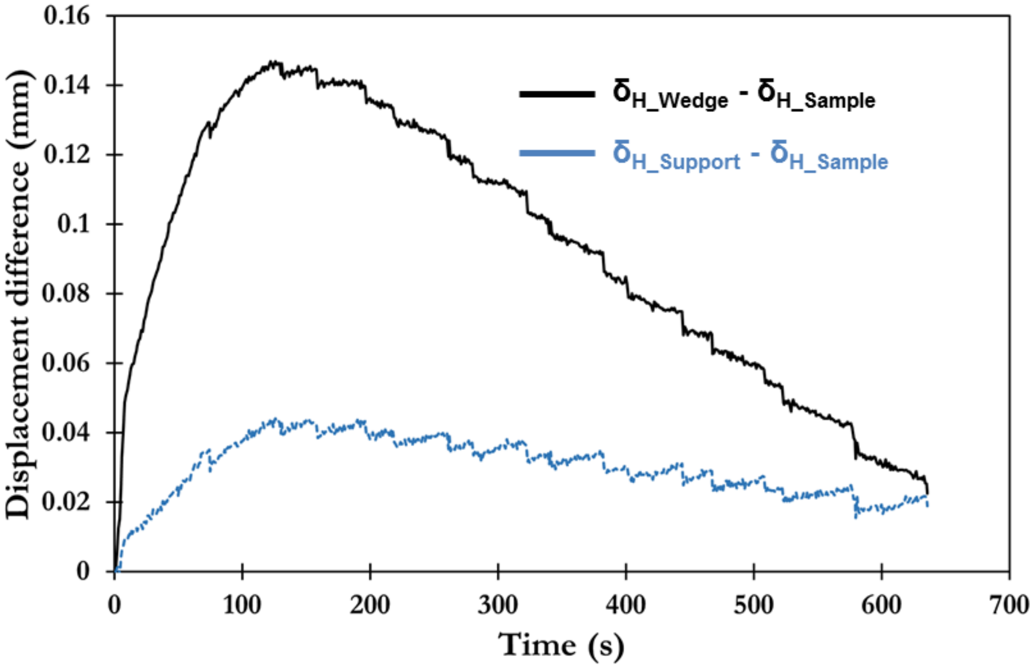

Figure III-16: Horizontal displacement differences between the wedge, support and sample

BY NC ND

Figure III-17 shows complete WST curves using CODs deduced from the sample and the wedge.

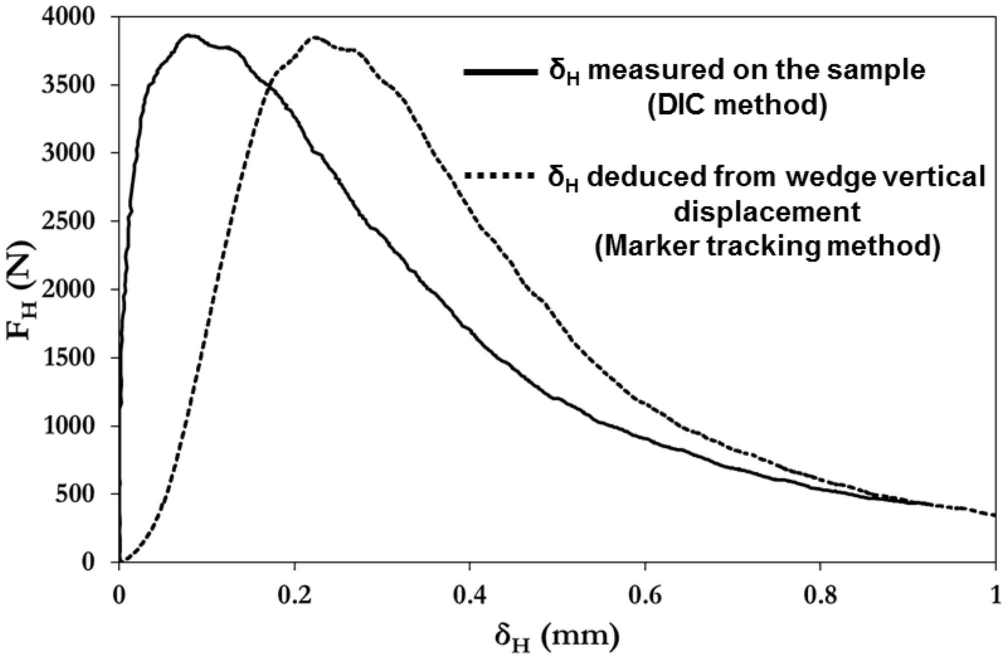

Figure III-17: WST curves plotted using COD measured directly on the sample and COD deduced from Wedge displacement

The WST curve obtained from wedge displacements shows a clearly unusual curve shape at the beginning of loading, as schematised previously in Figure III-9. This curvature at the beginning hinders the slope during loading, therefore altering the actual material behaviour. On the other hand, when COD is measured directly on the sample using DIC, the curvature problem is overcome. Moreover, while the curve shape at the beginning is different, the impact on the area under the curve is not so important after all. Indeed, only a slight difference is measured between both WST curves.

In the end, COD measured on the sample provides the best results as no altering of the material behaviour is induced by measurements coming from parasitic WST part displacements. Thus, a robust measurement of fracture energies can be achieved this way.

BY NC ND

III.4. Refinement of fracture behaviour analysis in the WST: Application of 2P-DIC

III.4.1. Application of DIC during a WST

The application of DIC during a fracture experiment, such as the WST, can reveal crack presence and its propagation through strain field measurement and analysis. Indeed, the monitoring of crack propagation during a WST experiment can highlight essential features relating to a refractory's fracture behaviour.

By choosing small overlapping DIC subsets with dimensions of 32x32 px^2 spaced by 16x8 px^2 (Figure III-18), spatial resolution of the measurement can be improved.

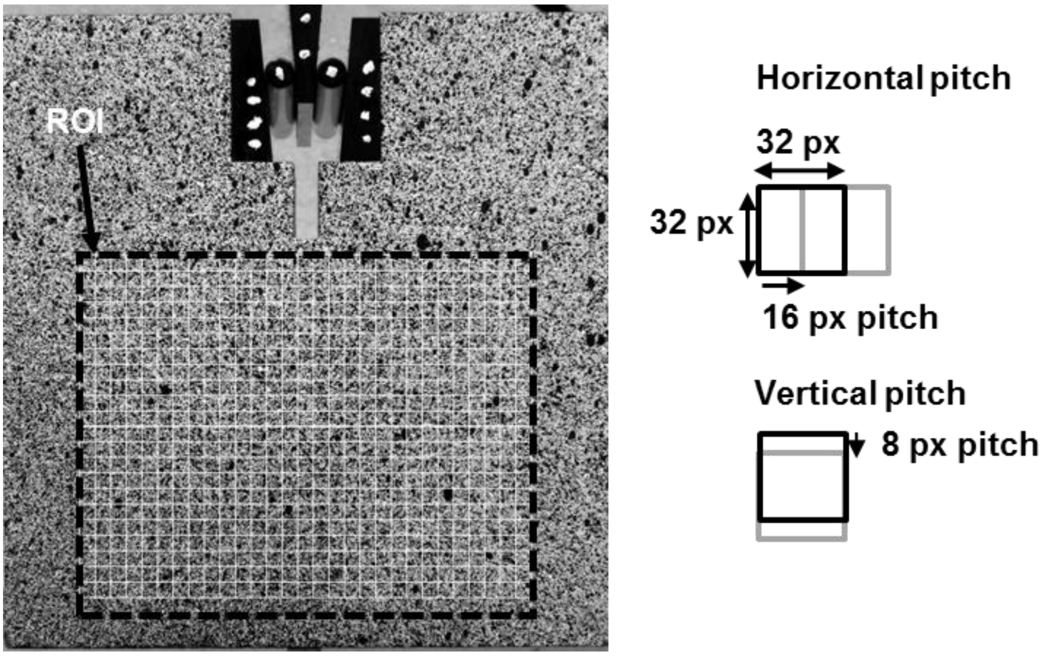

Figure III-18: DIC Region Of Interest (ROI) and subset parameters for crack propagation analysis

However, this increased spatial resolution comes at the expense of measurement accuracy. Therefore, a strain threshold must be used to isolate the crack from the measurement noise. A discussion about this critical point will be presented later in this chapter.

Figure III-19 shows crack propagation during a WST, where some crack deviation occurs. This feature is an important phenomenon in microcracked materials such as refractories.

BY NC ND

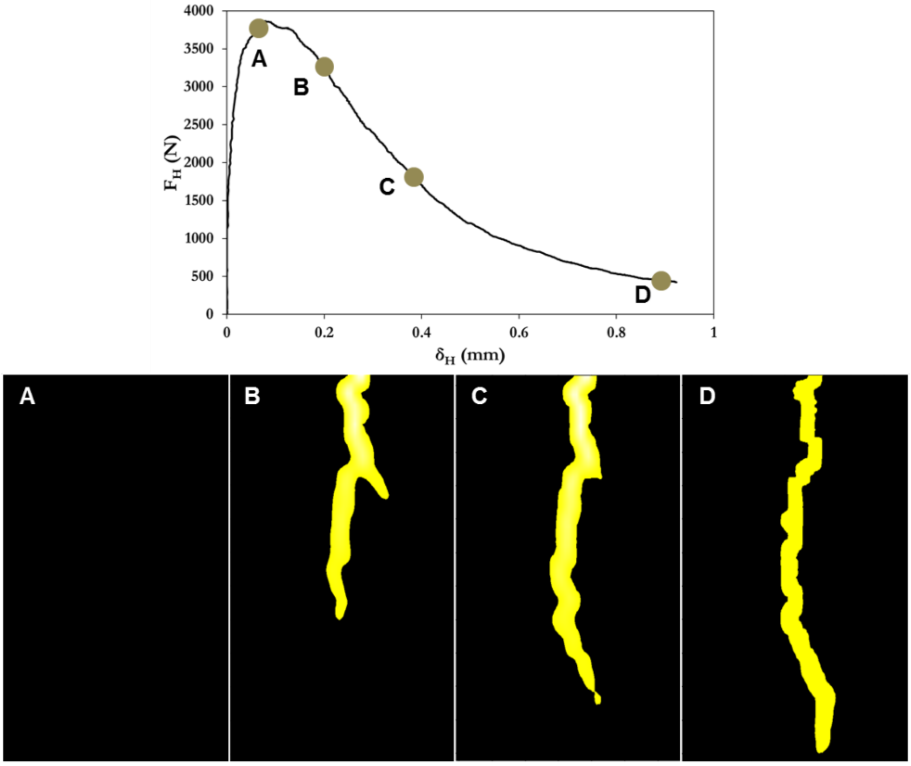

Figure III-19: Crack propagation images during a WST using strain fields obtained from DIC

While the tortuous crack path can be clearly visualised and followed throughout the WST experiment, the crack spatial resolution is clearly not ideal and thus, not optimised for further measurements of crack features. Indeed, this limitation of DIC is due to the hypothesis of continuous material transformations within subsets during image processing. Therefore, the occurrence of a crack leads to a perturbation of the correlation coefficient, and thus to the strain field. In fact, when the crack is comprised within a subset, a pseudo-strain is observed even if no strain should be associated with the crack itself.

For this reason, the standard subset-based DIC method used for displacement field measurements is not optimised for the fracture analysis of the WST.

III.4.2. Refined DIC method: 2P-DIC principle

Given the aforementioned limitations of DIC application in fracture characterisation, an adaptation of the standard matching process is required for optimisation of crack spatial resolution and subsequent analysis [Huss14]. Therefore, a novel method developed by the PEM team in the Pprime institute, called Two-Parts DIC (2P-DIC), has been used for its proven reliability in fracture problems [DDBK17]

BY NC ND

The 2P-DIC process uses the same principle as subset-based DIC detailed in section I.3.2. In this refined method, an additional hypothesis is introduced whereby each subset is likely to contain a discontinuity. In this regard, each subset *D* is divided at the position x=X_C in two separate parts D_1 (x < X_C) and D_2 (x > X_C) as shown Figure III-20 with an orientation θ of the boundary. The pixels at the boundary, corresponding to X_C position; are not taken into account in the matching process.

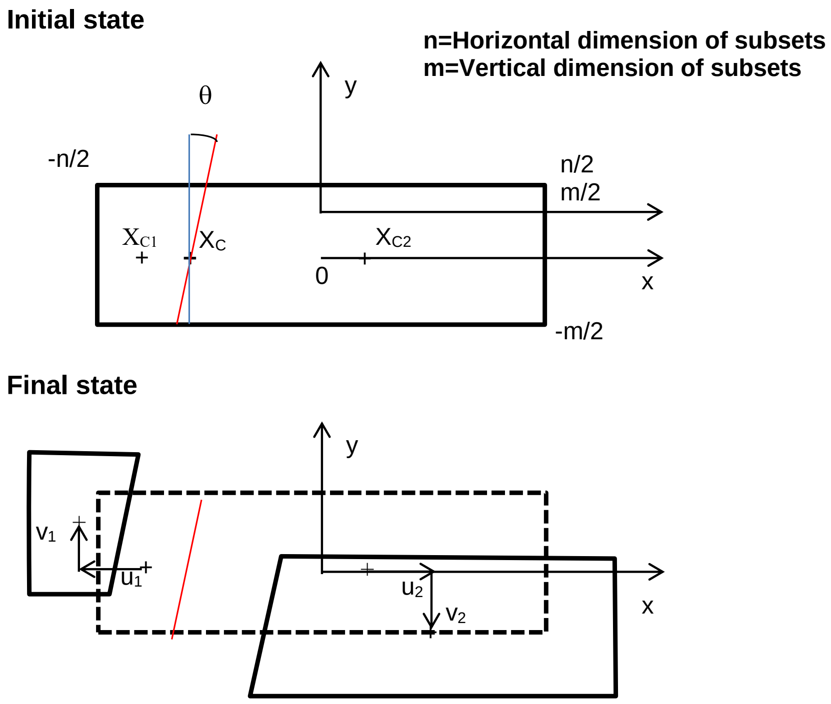

Figure III-20: Schematic of 2P-DIC subset splitting procedure [DDBK17]

Therefore, for a given value of X_C and θ, the correlation coefficient is formulated according to Eq. III.7.

$$\mathbf{C_{XC}(X_c, \theta, \underline{Q}) = \textstyle\sum_{D_1} c^2(\underline{q_1}) + \sum_{D_2} c^2(\underline{q_2})} \qquad \text{Eq. III.7}$$

Where $\underline{q_i} = \left(u_i, v_i, \frac{\partial u_i}{\partial x}, \frac{\partial u_i}{\partial y}, \frac{\partial v_i}{\partial x}, \frac{\partial v_i}{\partial y}\right)$ the vector of material transformation parameters in the part D_i.(i=1,2). The vector $\underline{Q}$ represents all kinematic unknowns of D and is the gathering of two vectors $\underline{q}_1$ and $\underline{q}_2$.

The correlation coefficient, $C_{XC}(\underline{X_c, \theta, Q})$, is minimised during the optimisation process where optimal values of X_C, θ and $\underline{Q}$ are sought. This process is performed for each value of X_C with increments of one pixel going from -n/4 to n/4 while θ varies between -50° and 50° with a pitch

BY NC ND

of 10°. In this sense, values of X_C outside the [-n/4, n/4] bracket are not taken into account given the limited accuracy of DIC when very small subsets are used. Given that local stresses associated to the crack are null, local strain gradients can be neglected in $\underline{Q}$ and only rigid body displacements may be considered.

This whole process is performed in the ZOI of an image according to the initially defined subset dimensions and spacing. Given that cracks are not looked for in zones that are outside of the $X_C \in$[-n/4, n/4] bracket, a horizontal spacing of n/2 is taken to avoid any dead zones during the calculations.

At the end of the analysis, crack position, opening and rotation are determined. However, since this method relies on the initial assumption of introducing displacement discontinuities in each subset, discontinuities are always found as long as there is strain. Therefore, unless the software is dealing with perfect images (without noise), a pseudo-strain threshold must be defined in order to separate the artificial cracks from the physical ones. In a similar way to standard DIC, a pseudo-strain threshold is defined to determine crack presence. It is calculated according to Eq. III.8 as the ratio between the initial distance between the centres of the two subset parts and the same distance evaluated in the deformed state.

$$\boldsymbol{\varepsilon = \frac{\sqrt{(XC_2 - XC_1 + u_2 - u_1)^2 + (v_2 - v_1)^2}}{XC_2 - XC_1} - 1} \qquad \text{Eq. III.8}$$

Subsequently, crack presence can be determined per a user defined pseudo-strain threshold ε_S. In fact, this threshold relates directly to crack opening, which is an important material fracture parameter.

With the refined 2P-DIC approach, the hypothesis of material discontinuity is applied to each subset and can lead to subset splitting. Therefore, an increased crack spatial resolution can be expected compared to standard DIC. In the end, a similar approach to that used in DIC analysis can be performed using 2P-DIC.

III.4.3. Theoretical accuracy of discontinuity characterisation using 2P-DIC

In order to validate the accuracy of 2P-DIC measurements, synthetic speckle images were generated and subjected to a series of tests using different correlation parameters [DDBK17]. In this section, the case of discontinuity propagation will be considered to validate crack position and length measurement accuracy by 2P-DIC.

BY NC ND

Therefore, a discontinuity of length L_{imp} is created in the middle of the synthetic images and a horizontal displacement U_{imp} is imposed on the right part (as shown in Figure III-21 for a brittle fracture), then DIC and 2P-DIC calculations are performed using various subset sizes. Moreover, noise can be added to the simulated images in order to be closer to experimental conditions.

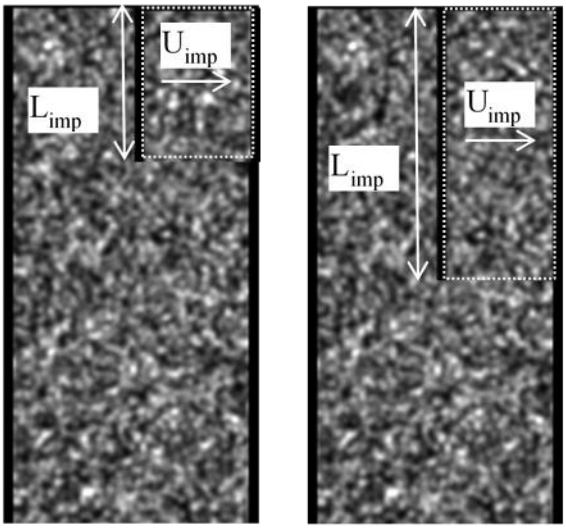

Figure III-21: Synthetic speckle images used for accuracy evaluation of DIC and 2P-DIC [DDBK17]

Such is the case in the results reported in Figure III-22, where a known discontinuity length has been applied to noisy images (i.e similar to a real image) while measuring the length with DIC and 2P-DIC methods using various pseudo-strain thresholds for crack detection.

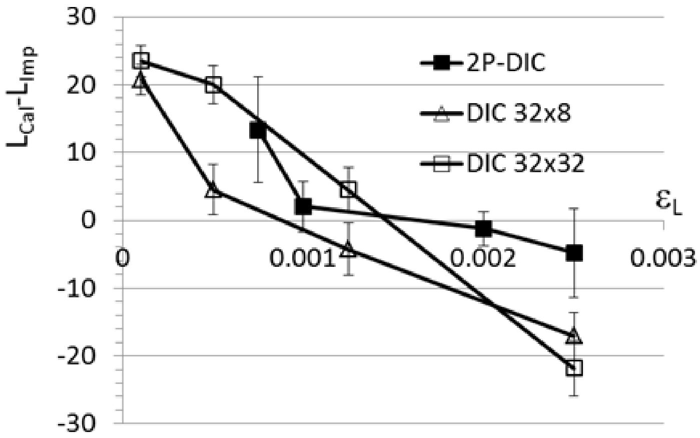

Figure III-22: Bias and random errors between discontinuity lengths calculated, by DIC and 2P-DIC, and known imposed ones (L_{cal}-L_{imp}) for a noisy simulated image [DDBK17]

The curves show the impact of pseudo-strain threshold choice on the measured crack length by DIC and 2P-DIC. Low values of L_{cal}-L_{imp} suggest that both DIC and 2P-DIC can provide accurate crack lengths, but for DIC, this is strongly dependant on threshold values. Conversely, 2P-DIC appears to be much more reliable, especially for threshold values above 0.001, as random errors and bias are minimised significantly compared to DIC.

Moreover, the spatial resolution of discontinuities depends strongly on DIC and 2P-DIC method principles. Indeed, in the case of DIC, crack definition depends on the spatial resolution of strain measurements, while for 2P-DIC, the subset-splitting procedure leads to an uncertainty of only one pixel in the definition of a discontinuity. From Figure III-23, bias and random errors related to the transversal position of a discontinuity is reported for DIC and 2P-DIC using two different subset sizes.

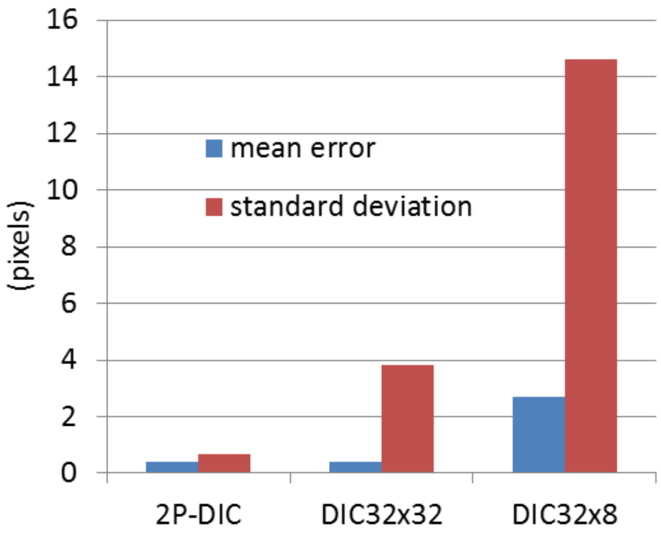

Figure III-23: Discontinuity transversal position errors [DDBK17]

The results clearly indicate that 2P-DIC provides a much more accurate determination of crack position with very minimal random errors. While DIC can provide a similar mean error of one pixel with subsets of 32x32px^2, the high standard deviation would lead to uncertain results.

Therefore, in discontinuity related aspects, such as crack length and position, 2P-DIC has proven to be much more reliable than DIC. In this sense, the 2P-DIC method can be used for the evaluation of crack length, which is an important addition to standard WST experiments as it can enrich fracture characterisation significantly.

BY NC ND

III.4.4. Quantitative analysis of damage evaluation by 2P-DIC

III.4.4.1. Crack length measurement evaluation and choice of pseudo-strain threshold

The coupling of standard DIC and WST has been carried out in the past to visualise crack propagation and measure crack length during mechanical tests, including the WST[BHCP14, Belr15]. Given recent contributions to the development of 2P-DIC [Huss14, DDHG15], it is now possible to develop a more systematic approach where crack length measurements are performed during WST experiments as a way to evaluate Fracture Process Zone (FPZ) influence in refractories. From sections I.2 and II.2.3, FPZ development in refractories, such as magnesia-spinel materials, depends on the presence of pre-fabricated microcrack networks. These microcracks can grow and promote the occurrence of the crack branching phenomenon, which is an important energy dissipating mechanism in the FPZ.

As discussed previously, the application of 2P-DIC in a fracture analysis follows the same procedure as for standard DIC albeit with different subset dimensions for 2P-DIC due to its specific treatment requiring rectangular shapes. For comparison purposes, 2P-DIC was applied for the same set of images as those presented in Figure III-18, using subset dimensions of 64x16 px^2 spaced by 32x8 px^2.

Figure III-24 shows images of the evolution of the FPZ using standard DIC and compared to 2P-DIC during a WST of the same industrial magnesia-based refractory.

BY NC ND

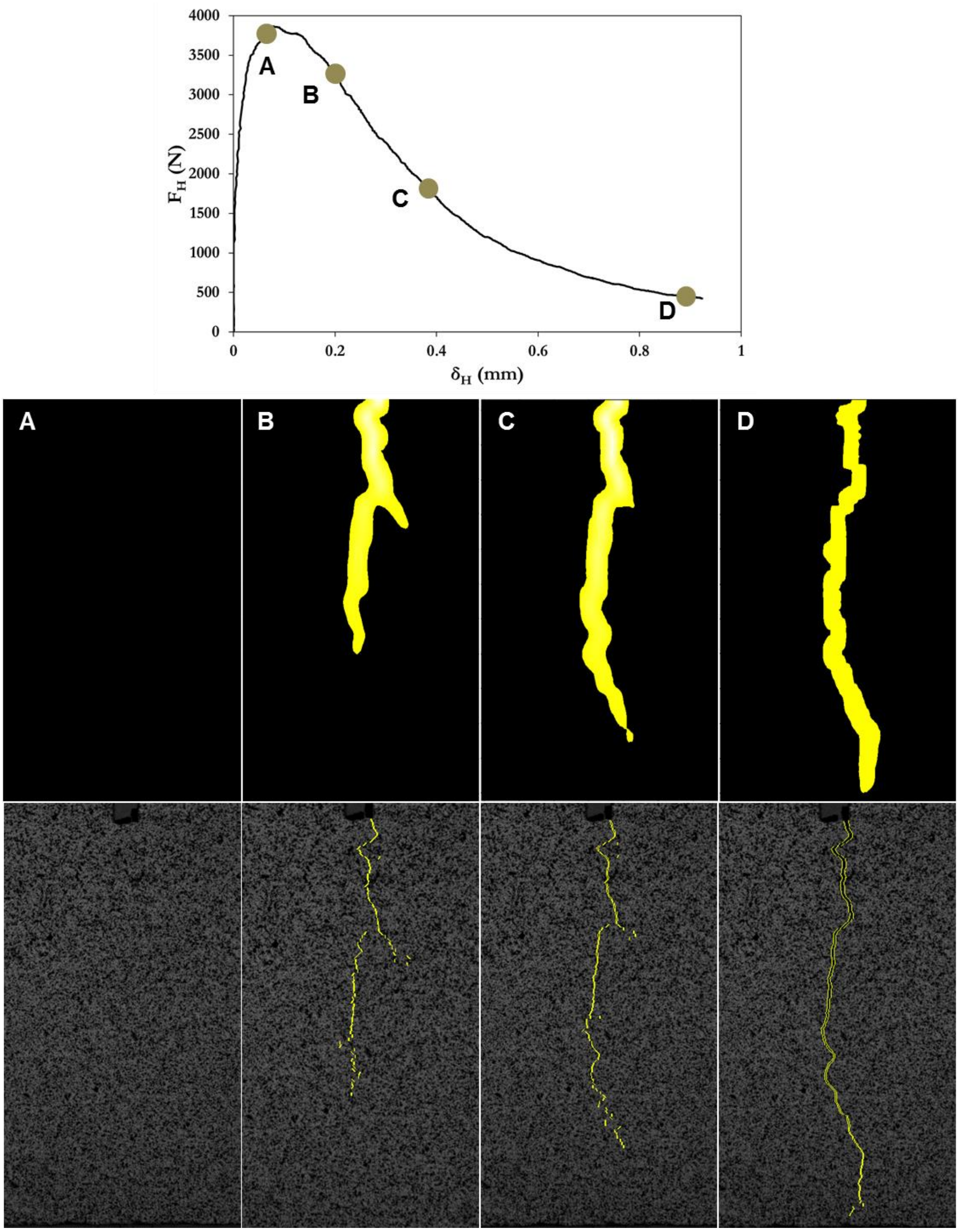

Figure III-24: Comparison of DIC and 2P-DIC images relating to crack propagation during a WST experiment

Similar crack propagation patterns can be noticed between DIC and 2P-DIC, but the latter exhibits a much more enhanced crack spatial resolution as expected (III.4.3). Indeed, from the basic principle of 2P-DIC, crack position (given by XC value) is defined with an uncertainty equal to one pixel, which is not the case for standard DIC. This increased spatial resolution leads to a finer description of crack edges and deviations, which are more pronounced in the case of 2P-DIC.

Given the enhanced crack spatial resolution of 2P-DIC images, the crack length can be measured using an appropriate pseudo-strain threshold based on the conclusions of section III.4.3. In practice, pseudo strain threshold values are chosen by taking into account technique limitations (anything below 0.001 is likely to be noise), image quality and material behaviour. In fact, image quality can have a strong impact if a poor speckle pattern quality is used for calculations but this can be controlled as explained in III.2.2. Moreover, according to 2P-DIC measurement principle, the pseudo-strain threshold relates directly to material critical crack opening displacement rather than strain to rupture.

Therefore, during WST characterisation, a straightforward analysis, involving comparison of different threshold values, is performed to determine the optimal pseudo-strain threshold for crack length evaluation. As shown in Figure III-25, a threshold of 0.001 leads to a high discontinuity length value due to noise, but a value of 0.002 already seems to remove much of it. Nevertheless, a value of 0.003 is deemed optimal for crack length evaluation as most of the noise is removed at this point.

BY NC ND

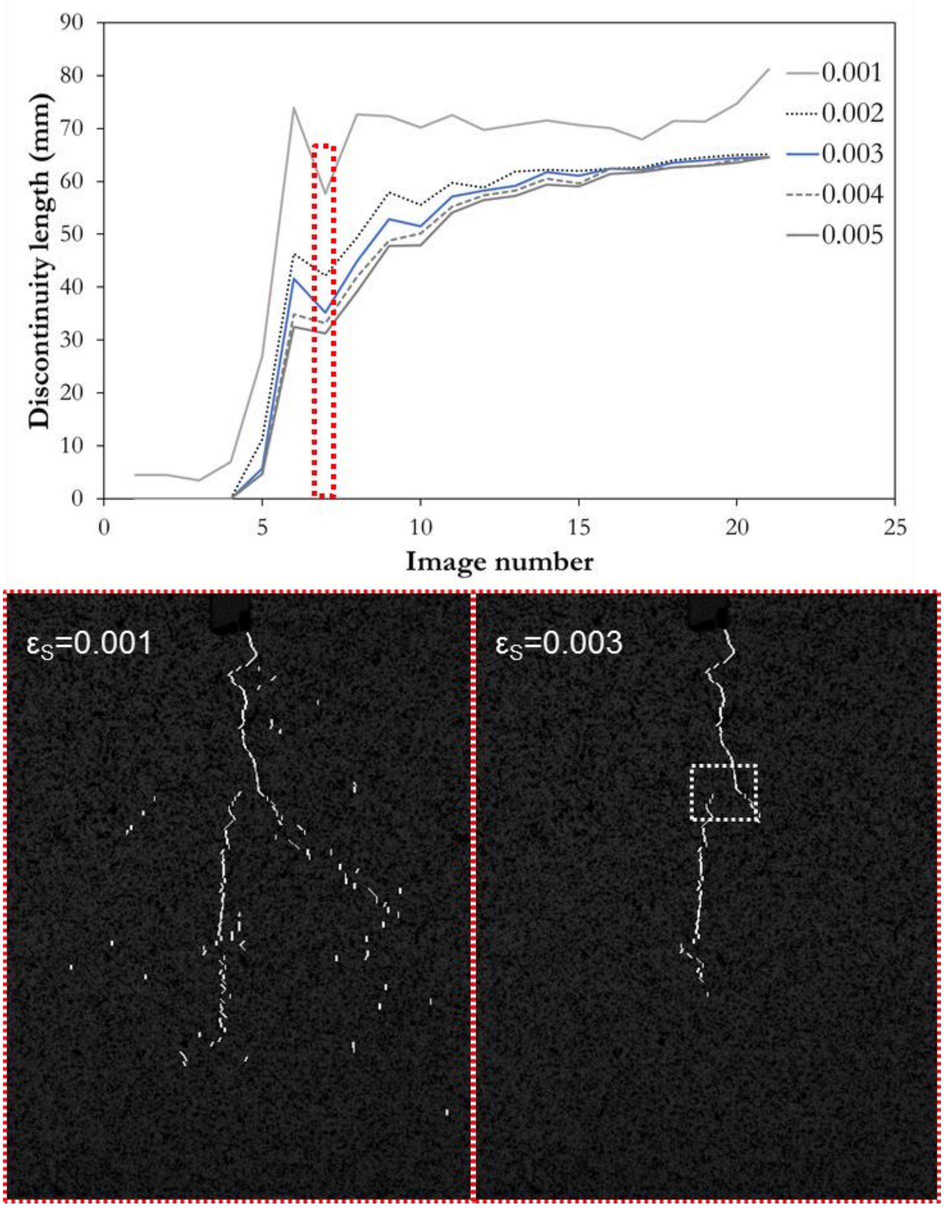

Figure III-25: Evolution of discontinuity length measured during a WST by 2P-DIC using different threshold values

By choosing an optimal threshold value (0.003), discontinuity length effectively corresponds to a crack length by leaving out influence coming from image noise. Moreover, as highlighted in the image corresponding to $\varepsilon_S=0.003$ in Figure III-25 using a dashed rectangle, the main crack is missing a link. This limitation can be attributed to insufficient crack rotation during the 2P-DIC process. This could be a future development to further improve crack characterisation using 2P-DIC.

BY NC ND

Nonetheless, 2P-DIC provides some interesting ways to analyse FPZ development. In this sense, two types of crack lengths can be measured using 2P-DIC, namely equivalent crack length and damage length as shown in Figure III-26.

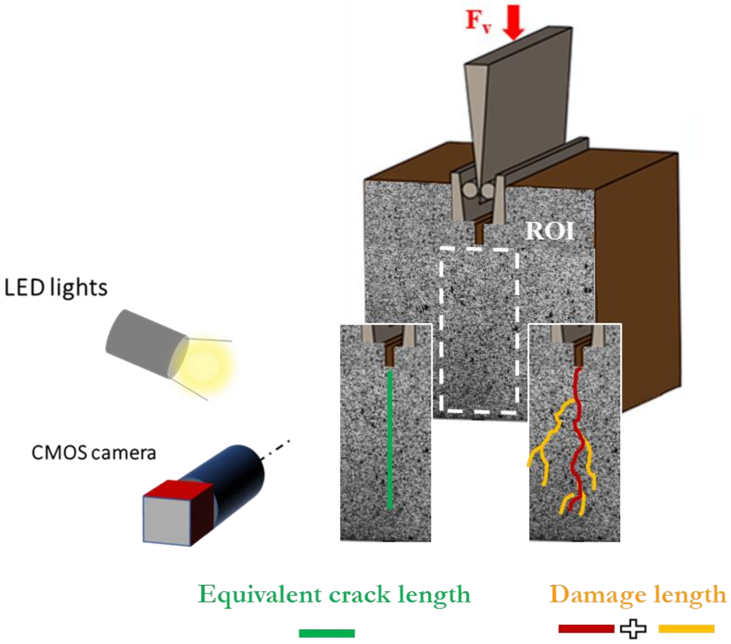

Figure III-26: Types of crack lengths quantified by 2P-DIC

The equivalent crack length corresponds to a straight line going from the root of the notch to the vertical position of the bottom-most subset that contains a crack. On the other hand, damage length calculates the sum of all vertical or inclined subset segments affected by a discontinuity, meaning all crack features including deviations and secondary branches.

However, as noted on Figure III-25 for all curves including for a threshold of 0.003, crack length evolution exhibits some drops from one image to the other. This suggests that crack length from state t_i can be higher than crack length at state t_{i+1}, which is not in accordance with the definition of a crack. This measurement artefact is due to the principle of discontinuity detection in 2P-DIC (and DIC methods in general) which is based on strain value thresholding, thus if a local strain value corresponding to a crack in t_i decreases in t_{i+1}, the discontinuity disappears from a numerical point of view. Local strain decrease is justified, and especially observed using 2P-DIC, when secondary cracks are away from the main crack tip during unloading because of stress decrease in the crack wake region [Gras11].

Therefore, a cumulated damage length concept has been introduced which curbs this measurement artefact as shown in Figure III-27.

BY NC ND

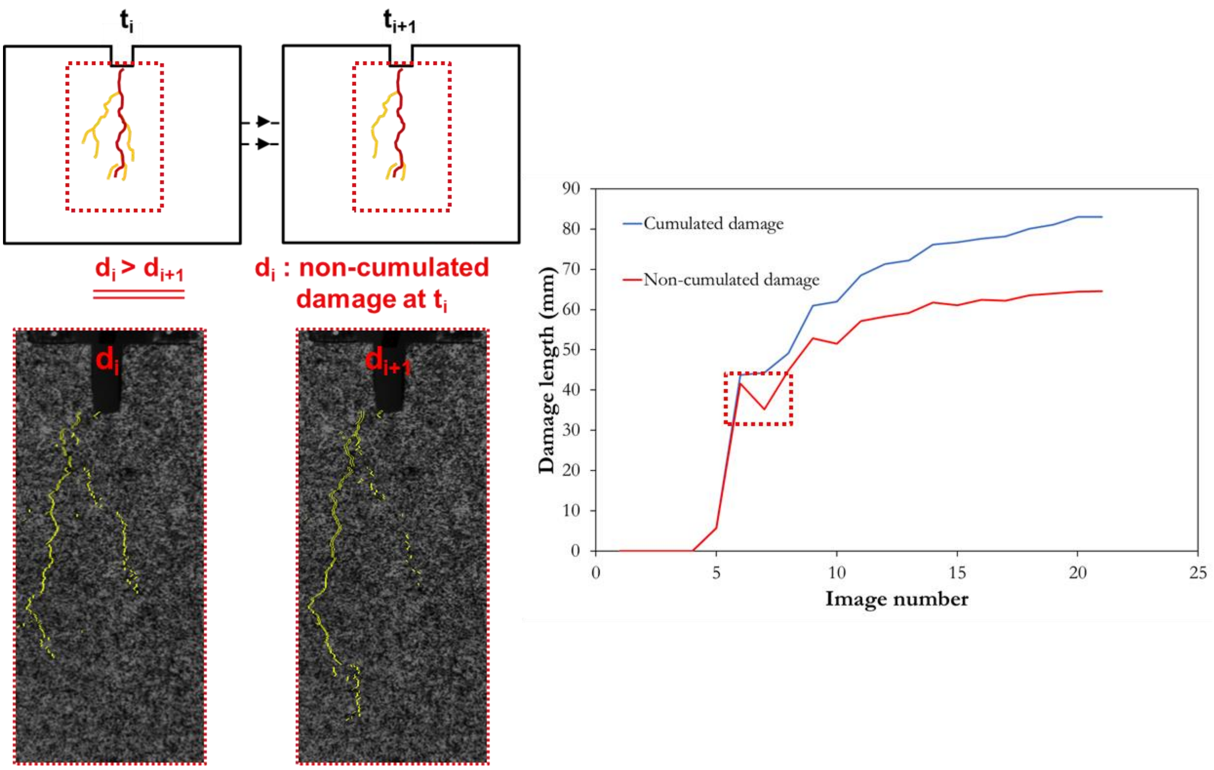

Figure III-27: Example of local strain decrease leading to artificial crack closure during a WST and cumulated damage measured by 2P-DIC

The cumulated damage length takes into account all of the cracks that may have appeared during the WST experiment. This parameter will be used for the rest of the 2P-DIC analyses to highlight the degree of cracking during a WST and for comparison with the equivalent crack length to extract a damage zone length corresponding to FPZ influence on the fracture behaviour. This advanced fracture characterisation relies on accurate crack representation and quantification. Therefore, another step is taken to validate crack length quantification using 2P-DIC.

III.4.4.2. Validation of 2P-DIC crack length measurement using SEM observations

In order to validate crack length measurement by 2P-DIC, a post-mortem observation was performed on the WST sample presented previously using SEM. The main goal of this analysis is to compare crack features and length between 2P-DIC and SEM observations.

Therefore, a cylinder with a diameter of 30 mm was machined from the upper part of the cracked area, just below the notch in the post-mortem WST sample, 25 mm of which contains the crack. The same sample surface used for 2P-DIC measurements was prepared for SEM observations to ensure a proper comparison. Therefore, the paint layer used as a speckle was

BY NC ND

first removed and then successive steps of polishing were undertaken using relatively fine grained polishing paper to prepare a planar surface for SEM. Observations were then carried out and images were acquired then assembled to form one global image containing the whole 25 mm of the cracked sample.

The global image is then treated using a series of image analysis tools to extract the main crack path and ignoring the secondary crack branches. The image treatment protocol is summarised in Figure III-28.

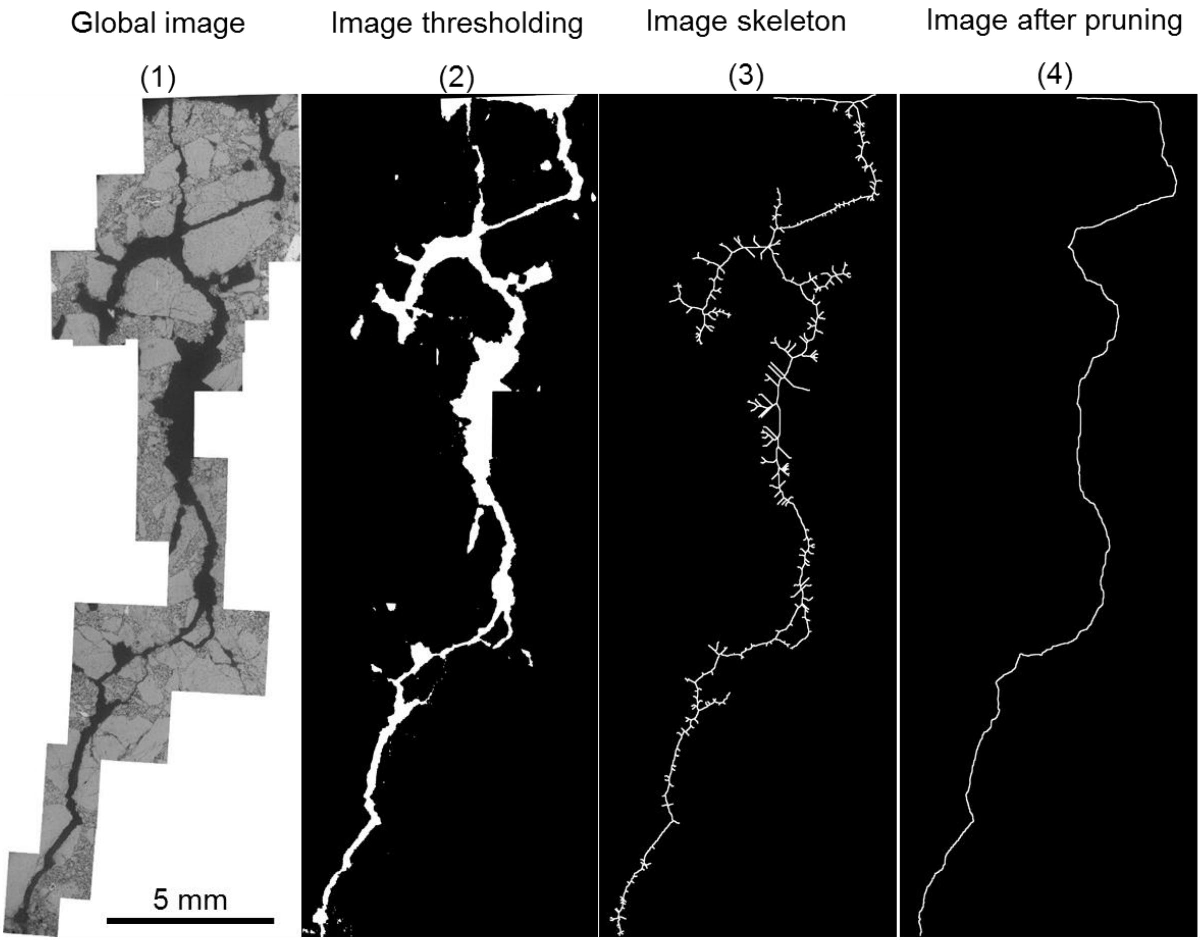

Figure III-28: Global SEM image analysis steps to extract the main crack path

Once the crack path is obtained, the length is measured and then compared with the 2P-DIC image. As shown in Figure III-29, the main crack deviations are highlighted by blue dashed horizontal lines between the SEM and 2P-DIC image. As a first observation, the 2P-DIC image follows the same trend as the SEM one but some subsets come short of being linked to others due to insufficient inclination limited by the 2P-DIC algorithm. Nevertheless, the overall

BY NC ND

outcome of 2P-DIC is very close to the post-mortem sample observed under SEM. In fact, the crack length measured on the global SEM image was estimated at 31.5 mm while the 2P-DIC crack measures 28.7 mm, which is a rather small difference.

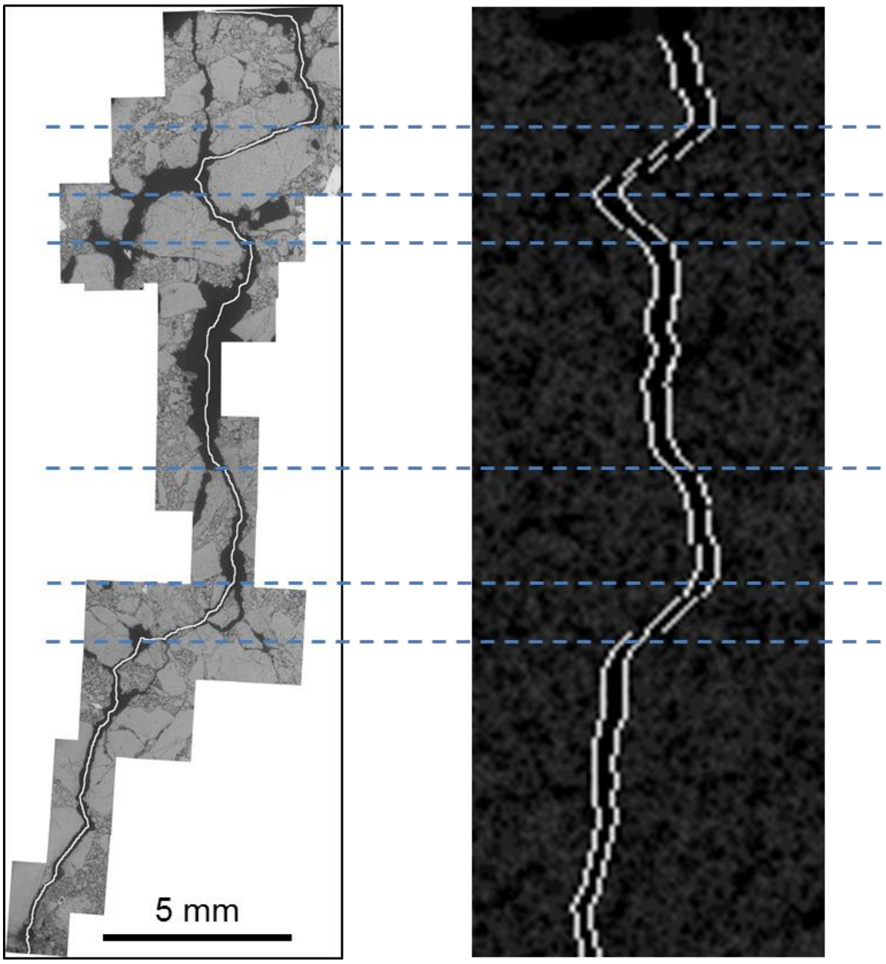

Figure III-29: Comparison of SEM observation of post-mortem WST sample and 2P-DIC image of the same sample during the WST

Therefore, 2P-DIC detects the main crack path with a very good accuracy as suggested by the comparison with post-mortem SEM observations. This validates the reliability of 2P-DIC as a method to measure crack lengths during fracture experiments such as the WST, which will be used to enrich fracture characterisation. Ultimately, 2P-DIC provides ways to refine the understanding of the fracture behaviour of quasi-brittle refractory materials.

BY NC ND

III.5. Conclusion

In this chapter, the WST was presented as a reliable fracture experiment to characterise the fracture behaviour of refractory model materials. This way, fracture energies can be measured and interpreted based on microstructure observations of model materials in the coming chapters.

Given the effectiveness of coupling DIC methods and the WST, a first investigation was carried out to determine the crack opening displacement accurately using DIC. After validating COD measurements on the sample as the least prone to parasitic displacements, the focus of DIC application shifted to crack propagation characterisation using a refined method developed by the Pprime Institue in Poitiers.

Indeed, the challenging topic of crack length measurement requires appropriate methods that can tackle limitations from continuum mechanics used in regular DIC. By using a novel subset-splitting procedure in the image treatment algorithm, 2P-DIC introduces a discontinuity hypothesis within each subset that allows detection of crack position with a one pixel accuracy.

The principle of the 2P-DIC method and its performances regarding crack length and position evaluation make it a powerful tool for crack propagation monitoring. Indeed, using 2P-DIC during a WST enabled the visualisation of the FPZ with an enhanced crack spatial resolution. Subsequently, different crack lengths were measured and used for the estimation of FPZ influence on the fracture behaviour. Especially since crack lengths measured by 2P-DIC have shown a very satisfactory accuracy when compared to measurements performed on the post-mortem sample using SEM observations and image analysis tools.

These conclusions highlight the main ideas and principles that will be used in the experimental approach dealing with the fracture behaviour of model refractory composites in the last chapter. Indeed, the combination of methods such as DIC, 2P-DIC and the WST opens up new perspectives for fracture characterisation.

BY NC ND

Chapter IV

BY NC ND

Chapter IV. Key microstructural features driving the thermomechanical behaviour of magnesia-based model materials

IV.1. Introduction

The microstructure design of magnesia-spinel refractories for thermomechanical applications relies on the promotion of thermally induced crack networks coming from the CTE mismatch between magnesia and members of the spinel group. In this sense, model materials (presented in Chapter II) containing spinel inclusions of different chemistry, namely regular spinel and hercynite, and in different amounts are investigated.

Firstly, microstructural observations and measurements relating to the microstructure are performed with an emphasis on peculiarities distinguishing each class of materials. The impact of these peculiarities is here assessed from a physico-chemical point of view. In particular, the main objective of this first part is to shed light on the occurrence of thermally induced damage and other phenomena given the extensive research existing in the literature.

Elastic property measurements were carried out at high temperatures in order to evaluate the thermomechanical behaviour of the model materials. In fact, a similar approach was applied during the PhD of Renaud Grasset-Bourdel (2011), dealing mainly with the thermomechanical properties of regular magnesia-spinel, which has proven to be effective in comparing different model materials. Given the range and industrial scope of materials investigated in this research, thermomechanical characterisations are expected to consolidate the results obtained by Renaud Grasset-Bourdel while providing new insight, especially for Hercynite-containing materials.

Finally, by using the main conclusions from microstructure characterisation, an attempt is made to provide an understanding of the thermomechanical behaviour for each class of the model materials.

IV.2. Microstructure characterisation of magnesia-based model materials

IV.2.1. Microstructure observations and chemical analyses

The micrographs in Figure IV-1, Figure IV-2 and Figure IV-3 provide an overview of the typical microstructure of pure magnesia, magnesia-spinel and magnesia-hercynite composites, respectively. From these micrographs, key microstructural features can be observed, such as grain boundaries in magnesia aggregates or microcracks within MS and MH composites.

BY NC ND

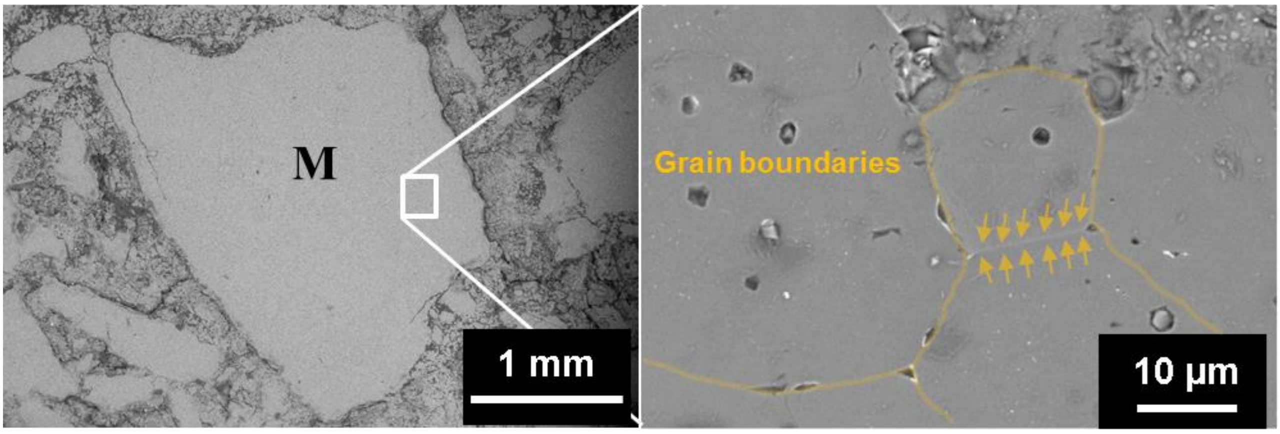

-a- -b-

Figure IV-1: SEM micrographs of a) Magnesia aggregate in magnesia matrix and b) high magnification zoom on the aggregate

Given their granulometric and chemical compositions, a clear pattern can be observed in these materials, where large magnesia and spinel group aggregates are embedded in a magnesia matrix. Moreover, microcracks originating from spinel group aggregates and propagating within the magnesia matrix can be clearly noticed for both regular spinel and hercynite containing materials. This characteristic feature occurs during cooling after sintering as a result of CTE mismatch between magnesia and spinel group aggregates. It is one of the main thermomechanical property design parameters in these materials.

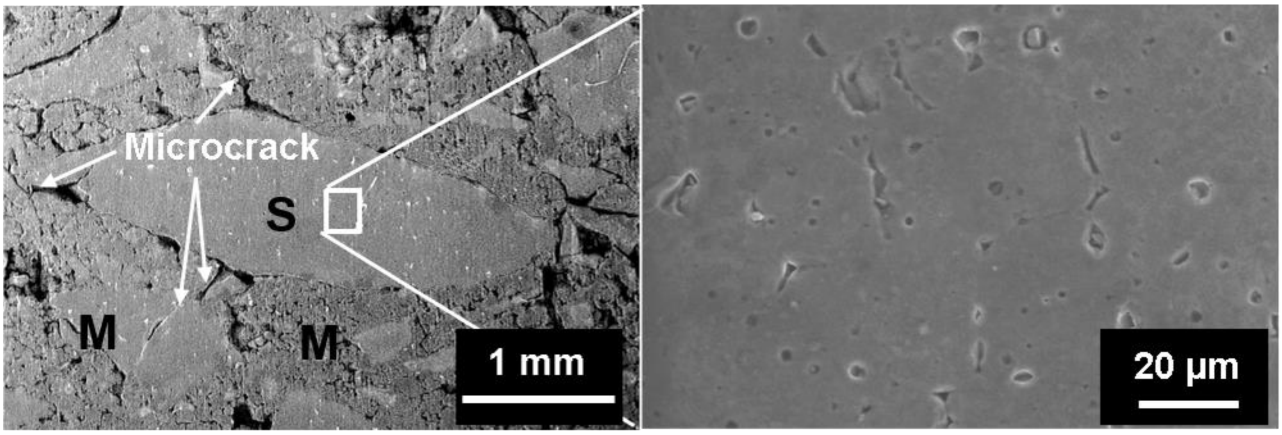

-a- -b-

Figure IV-2: SEM micrographs of a) Spinel aggregate in magnesia matrix and b) high magnification zoom on the aggregate

BY NC ND

While the material microstructure of MS is relatively easy to apprehend, especially given previous works, hercynite-containing materials exhibit added complexity from first microstructural observations. In addition to microcracks propagating from the hercynite aggregates, some bright spots can be identified in the magnesia matrix and also on the hercynite aggregate.

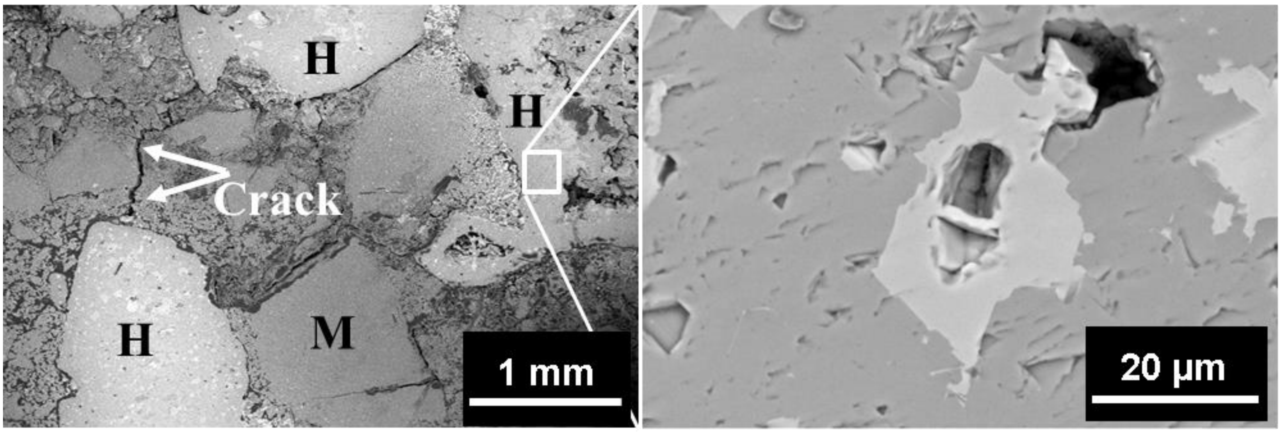

-a- -b-

Figure IV-3: SEM micrographs of a) Hercynite aggregate in magnesia matrix and b) high magnification zoom on the aggregate

Further observations of MH materials reveal that some hercynite aggregates contain a large pore in the middle with a characteristic bright area visible around aggregates. The latter feature hints at the presence of a relatively large diffusion zone, as shown in Figure IV-4. In fact, these two features might be the result of extensive interdiffusion mechanisms during high temperature sintering.

BY NC ND

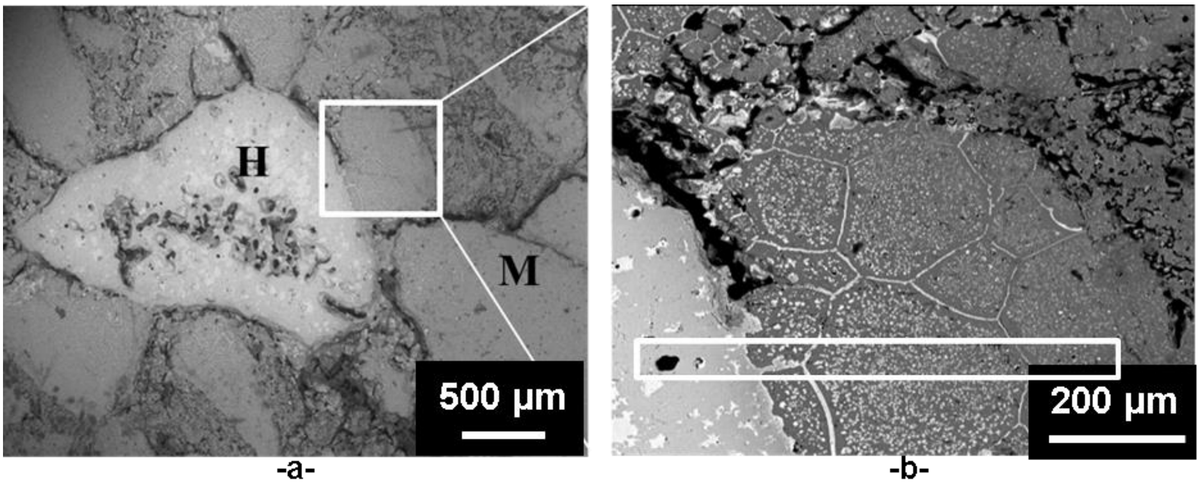

Figure IV-4: **SEM micrographs highlighting a) a hercynite aggregate with large pores in the centre and b) a diffusion zone around hercynite**

Therefore, EDS chemical analyses were performed to investigate the diffusion mechanisms at the origin of the interaction between hercynite and magnesia. Measurements were carried out by taking multiple profile lines crossing the hercynite grain and the diffusion zone within the matrix, and then these lines were averaged to obtain the chemical composition over the highlighted area (Figure IV-5). Moreover, impurities such as calcium (blue curve in Figure IV-5) were not taken into account as they are present in very low amounts. The graph in the figure plots the evolution of the chemical species over a distance of 770 microns.

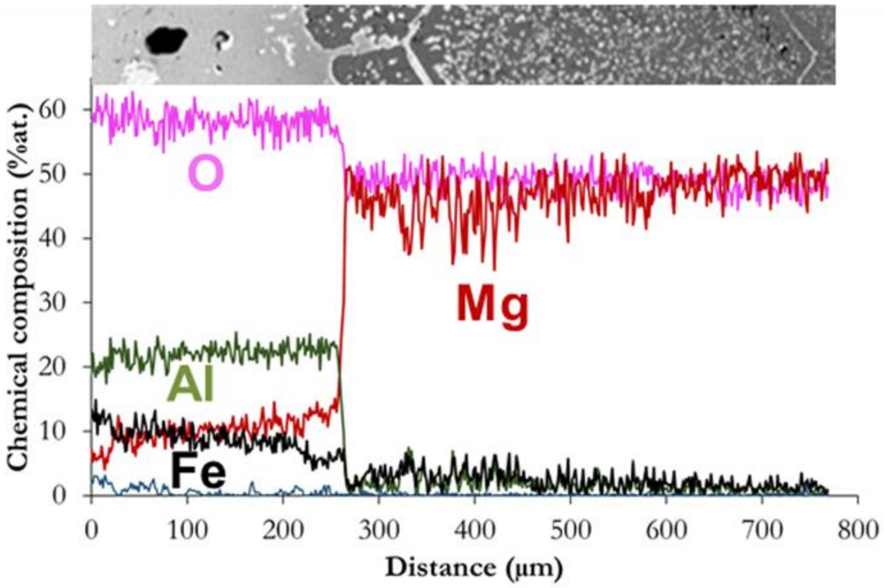

Figure IV-5: EDS analysis of the diffusion zone

BY NC ND

These results indicate the presence of Mg in the hercynite aggregate, which contains Fe, Al and O originally, while relatively small amounts of Al and Fe can be found in the Mg rich matrix. Indeed, precipitates forming the so-called diffusion zone are composed of Mg, Fe, Al and O atoms.

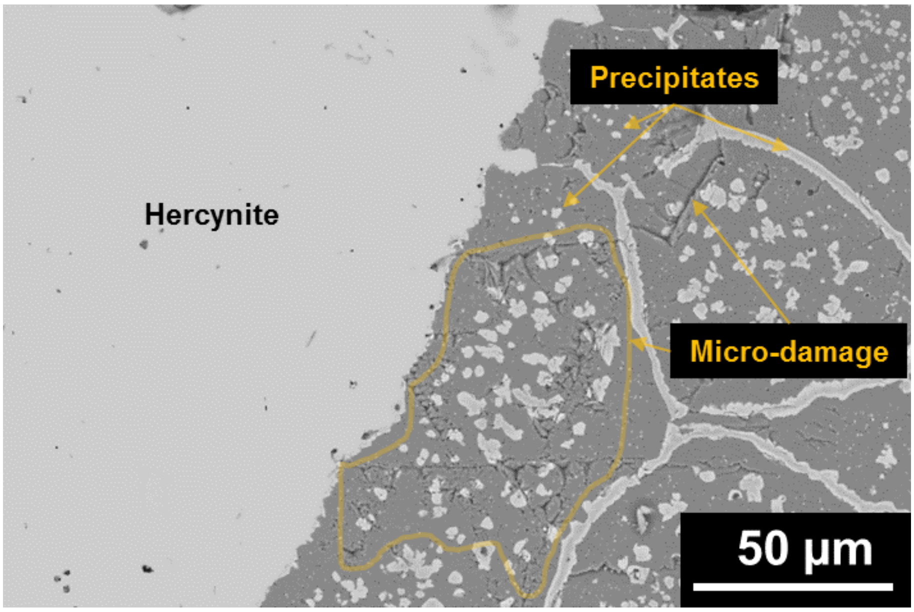

Figure IV-6: Micrograph highlighting diffusion zone precipitates and micro-damage occurrence

The distribution of chemical species along these profile lines suggests that interdiffusion mechanisms occur in MH and MSH at high temperatures, leading to Fe and Al diffusing from hercynite to magnesia and Mg from the matrix to the inclusion [LLYT12, JSBS17]. The microstructure, as shown in Figure IV-6, is deeply influenced by the formation of these precipitates as many sub-areas can be identified in the matrix, with patterns resembling magnesia grain morphology observed in Figure IV-1.b. Therefore, precipitate formation takes place mainly in magnesia grain boundaries, but also within the grains.

Moreover, the presence of large pores within hercynite hints at a potentially faster diffusion rate of iron towards magnesia. This difference in diffusion rates leads to vacancy nucleation and coalescence in the hercynite grain leaving large holes within the grain [FaGZ07, LWZX08], this phenomenon is also known as the Kirkendall effect. This effect, reported extensively in metallic alloys and in the fabrication of hollow nanoparticles [FaGZ07], points to a vacancy driven diffusion mechanism where a differential in diffusion coefficients between two atoms might exist. The whole mechanism is summarised in Figure IV-7.

BY NC ND

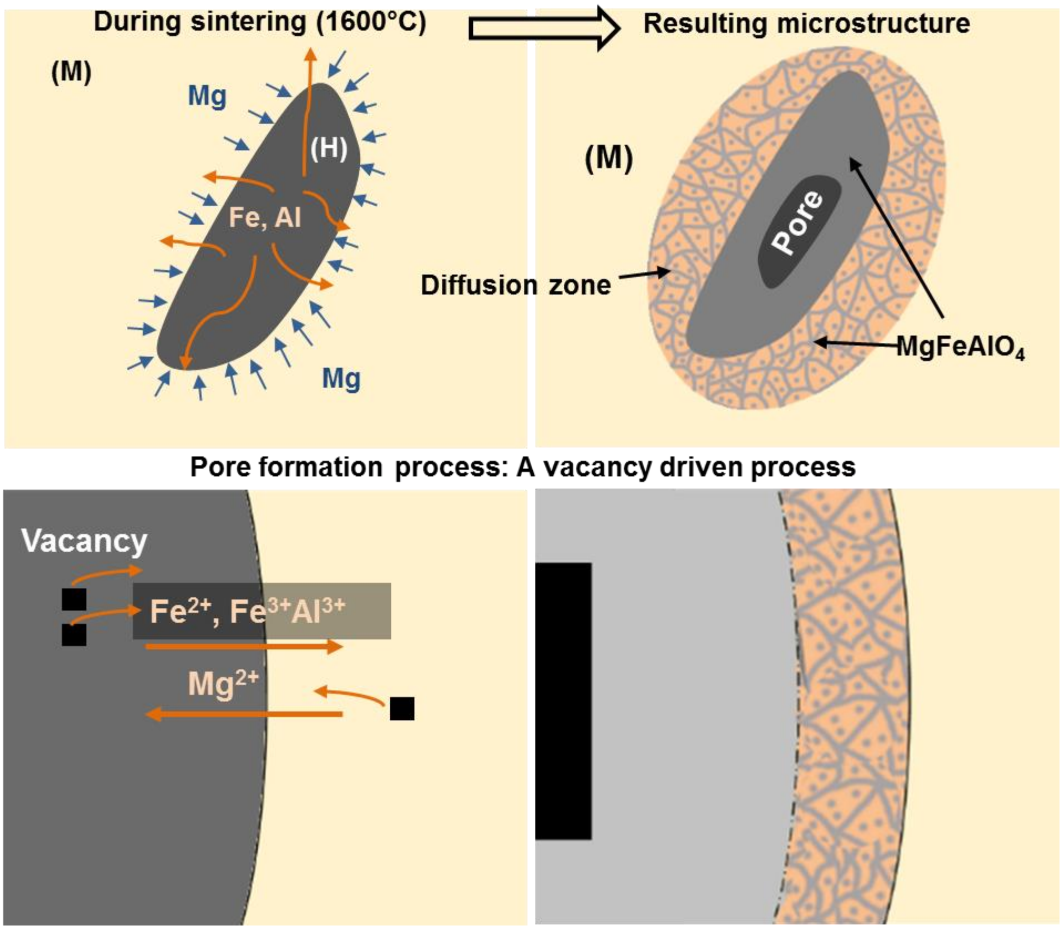

Figure IV-7: Schematic of diffusion mechanisms and pore formation effect in MH materials

In addition to this purely chemical aspect, some damage features and relatively fine microcracks mark the microstructure around this diffusion zone. Indeed, as highlighted in Figure IV-6, a micro-damage zone can be observed where many fine microcracks have propagated and numerous defects generated around the precipitates.

Indeed, microcracking patterns in these materials seem to be disturbed by the presence of precipitates in the diffusion zone, leading to some complex damage features. However, a clear pattern can be observed, especially in Figure IV-8, where microcrack networks have been formed through interconnection of cracks that propagated in a radial direction to the grains.

BY NC ND

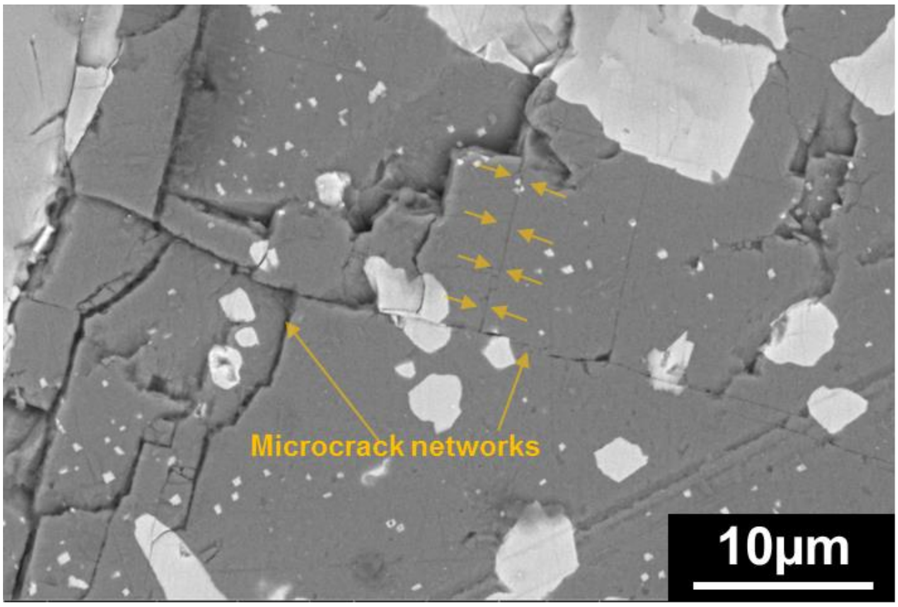

Figure IV-8: SEM micrograph of microcrack networks in an MH composite

These microcracking patterns imply possible interactions between stress fields coming from the large hercynite aggregate and the precipitates formed in the diffusion zone.

Finally, the presence of a diffusion zone in MH composites can be explained by the occurrence of vacancy driven interdiffusion mechanisms between magnesia and hercynite. These phenomena lead to the formation of precipitates whose chemical composition hints at the presence of a spinel solid solution. Moreover, the addition of hercynite aggregates in a magnesia matrix has multiple effects on the microstructure, important of which is microcrack occurrence, as a direct consequence of the CTE mismatch. Indeed, this mismatch seems to operate on two scales, the first one being at aggregate size while the second one is related to small spinel solid solution precipitates. Consequently, the interaction of thermally induced stresses between these two scales seems to induce a specific microcracking behaviour, marked by "large" microcracks and finer ones surrounded by micro-damage.

IV.2.2. Phase identification and quantification

In order to investigate further the microstructure of the composite model materials, XRD measurements and Rietveld quantifications were performed according to the protocol presented in II.3.1. Firstly, from Figure IV-9, the main phases were identified in each set of materials:

- MS materials contain only MgO and $MgAl_2O_4$ crystal phases

BY NC ND

- MH contains MgO, $FeAl_2O_4$ and $MgFeAlO_4$ (spinel solid solution) crystal phases.
- MSH contains MgO, $MgAl_2O^4$, $FeAl_2O_4$ and $MgFeAlO_4$ (spinel solid solution)

As expected from the chemical composition of these simplified model composites, a limited number of phases was identified especially for MS materials. These results confirm the presence of a spinel solid solution resulting from high temperature diffusion processes between the original hercynite spinel ($FeAl_2O_4$) and the magnesia present in the magnesia matrix.

BY NC ND

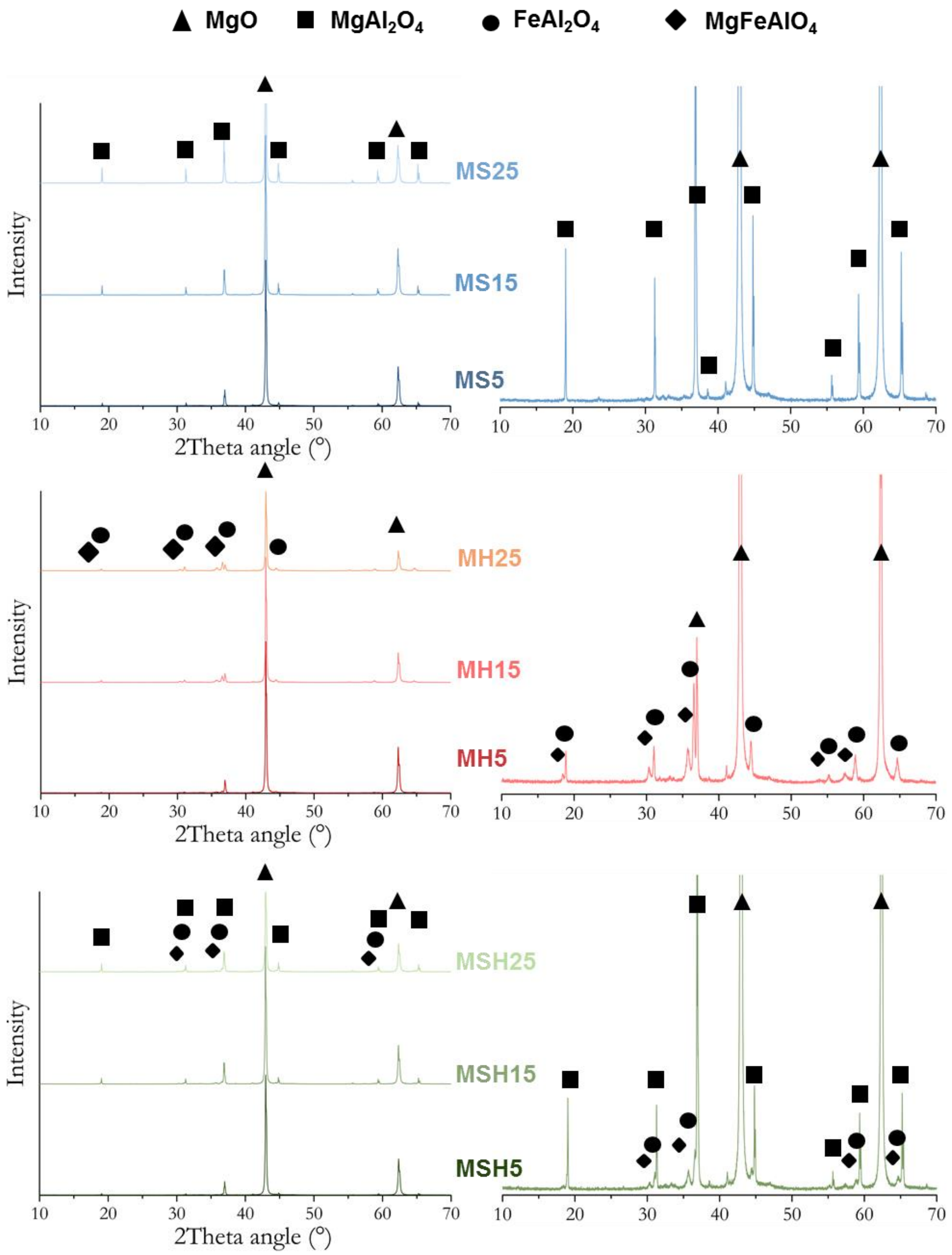

Figure IV-9: Diffractograms of MS, MH and MSH materials

Furthermore, these experimental diffractograms have been used in a Rietveld refinement analysis in order to quantify the amount of each phase in these composites. The results presented in Figure IV-10, show the weight composition of each phase in all of the materials.

BY NC ND

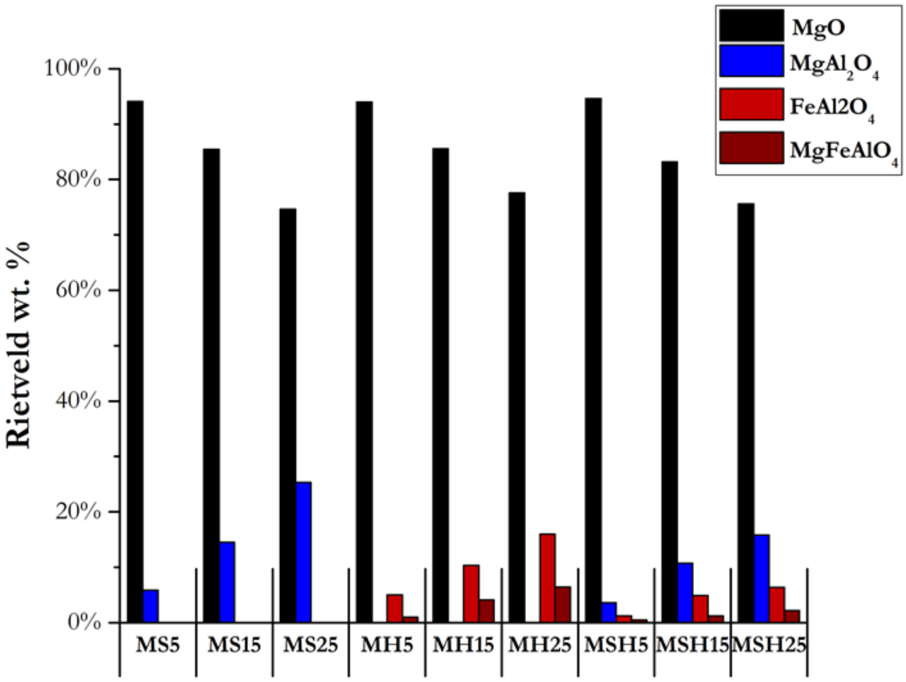

Figure IV-10: Composition of MS, MH and MSH materials in wt.% measured using Rietveld analysis

The measured weight compositions are quite in line with the compositions given by the material supplier, especially for MS composites. Given the high temperature interactions between hercynite and magnesia during sintering, a non-negligible amount of spinel solid solution is formed as the hercynite inclusion content is increased. Indeed, from Figure IV-11, a closer inspection of the various spinels' content suggests that 20% of the original hercynite (still according to manufacturing composition) transformed into spinel solid solution during sintering.

BY NC ND

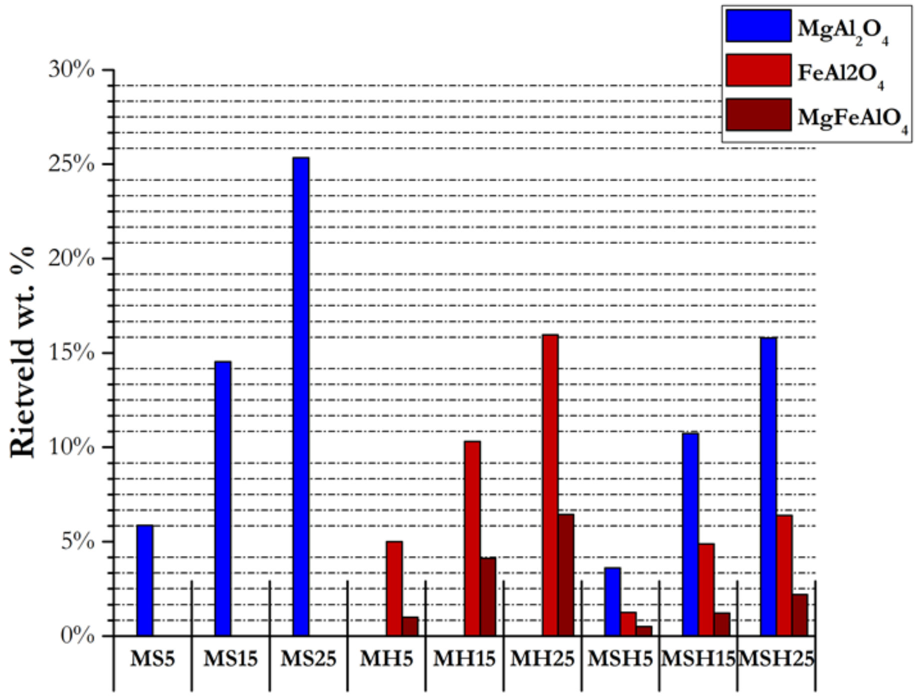

Figure IV-11: Spinel, hercynite and spinel solid solution content in wt.%

Thus, compared to spinel, hercynite is much more reactive at high temperatures in the presence of magnesia. Therefore, one might expect that, during usage in high temperature conditions, more hercynite would react with magnesia and further change the microstructure of the material. In this regard, the influence of hercynite on the microstructure is quite important whereby it is likely to lead to an evolutive microstructure at high temperatures.

IV.2.3. Influence of microcrack presence on density

As explained in Chapter I and Chapter II, the thermal expansion mismatch between magnesia and the various spinels present in the matrix leads to thermally induced stresses that induce microcracks. In an attempt to measure the proportion of microcracks present within the magnesia matrix of each composite, a comparison between an estimated composite density with the composite measured density is performed. The latter is simply measured for each material using Archimede’s principle for density measurements.

A composite density can be estimated by measuring the density of the matrix and the inclusions separately and then calculating the composite density from the known chemical composition. In this approach, an ideal microcrack-free composite is modelled conceptually by taking into account most microstructural features of actual composites such as granulometry, pores (both open and closed) and diffusion zone occurrence.

BY NC ND

In order to manage these measurements, raw aggregates of spinel were crushed to achieve the coarse granulometric distribution used in the actual composite, namely 1-3 mm in size. Then, their respective densities were measured using a pycnometer (Table IV-1). On the other hand, magnesia matrix density was simply measured with Archimede's principle using a pure magnesia material (Table IV-1).

Table IV-1: Measured and theoretical single constituent densities

	Measured density (g/cm^3)	Theoretical density (g/cm^3)
MgO (matrix)	2.98	3.58
$MgAl_2O_4$ (inclusion)	3.35	3.58
$FeAl_2O_4$ (inclusion)	4.21	4.28
$MgFeAlO_4$ (inclusion)	-	3.95

Theoretical inclusion densities and measured ones are not far off from each other, especially for hercynite, indicating that aggregates are quite dense, at least prior to sintering. The measured density of pure magnesia is naturally much lower than the theoretical one, since pores are taken into account in the measurement. The theoretical values are used for comparison purposes only, except for $MgFeAlO_4$ where it was used in composite density calculation since no measurement was possible.

By using single constituent measured densities to calculate a composite density, composites with non-spherical inclusions contained in a porous matrix with no thermally induced microcracks are considered. Indeed, this description naturally leaves out microcracks and is illustrated in Figure IV-12. The evolution of these densities as a function of each material can be observed on the graph below the schematic in Figure IV-12.

BY NC ND

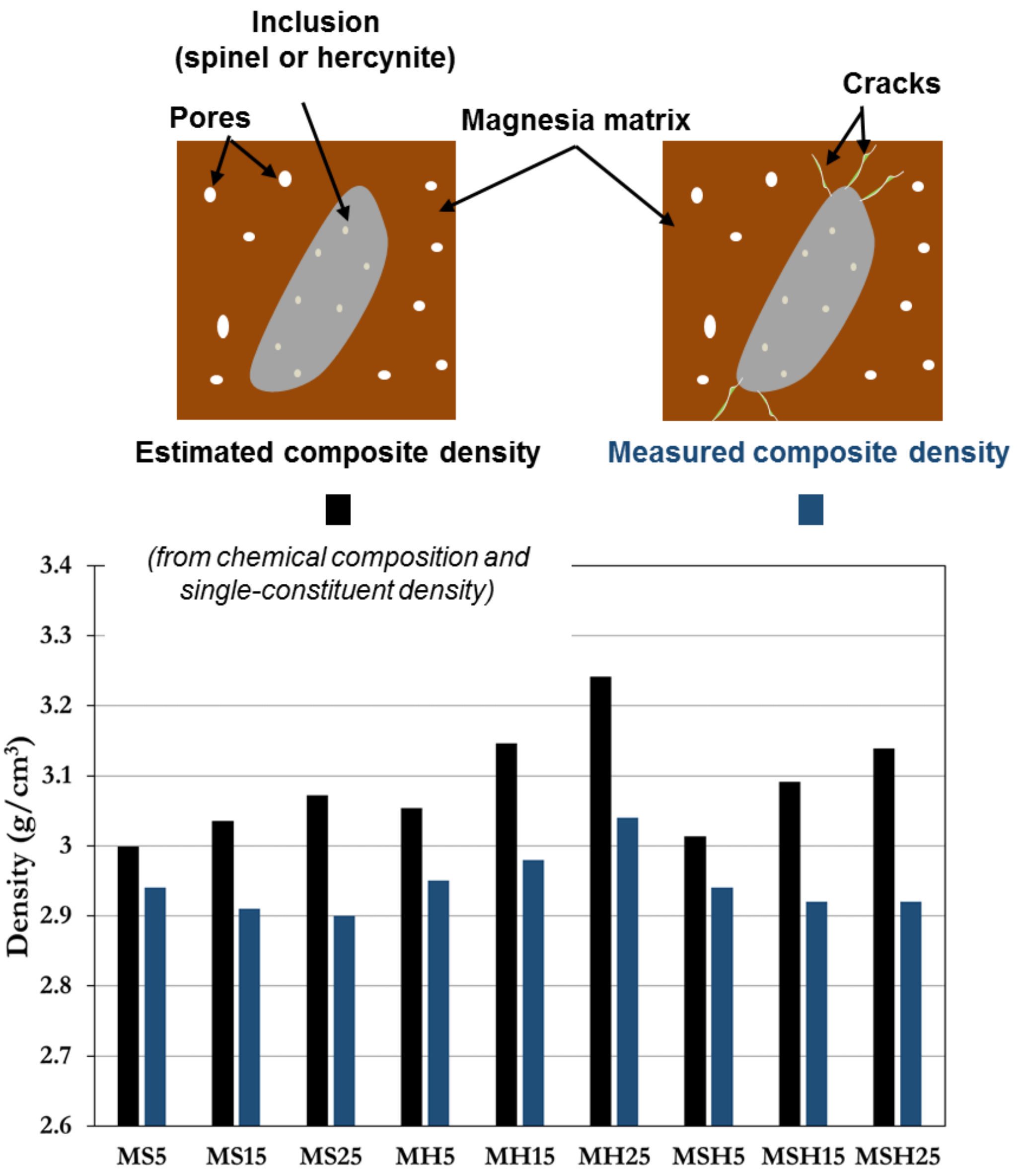

Figure IV-12: Schematic illustration of estimated composite density and measured composite density and corresponding density evolutions for each material

Given the presence of diffusion zones composed of a spinel solid solution in MH and MSH composite microstructures, the weight compositions obtained from Rietveld quantifications were used for composite density calculation.

The graph plotted in Figure IV-13 suggests that increasing inclusion fraction in the composites, for all spinel types combined, microcrack proportion increases.

BY NC ND

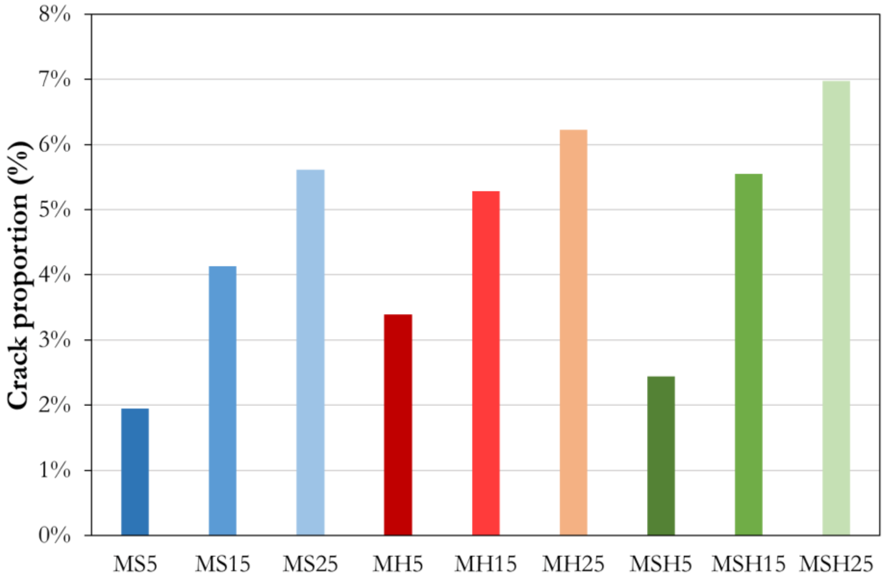

Figure IV-13: Evolution of calculated crack proportion in each material

Indeed, increasing inclusion fractions lead to more thermally induced damage, as confirmed for regular magnesia spinel materials in [Gras11]. Moreover, MSH composites tend to have the highest proportion of microcracks followed by MH and MS. Therefore, it is likely that the presence of a diffusion zone in hercynite containing materials leads to a higher occurrence of microcracks within the magnesia matrix, which in turn might have an impact on the thermomechanical behaviour of the composites.

In order to understand the impact of these thermally induced microcracks and to highlight the differences between the different sets of composites, the thermomechanical properties are presented in the next section, with an emphasis on the impact of damage occurrence.

IV.3. Microstructure related evolution of thermomechanical properties

The thermomechanical properties of magnesia-based composites depend mainly on single constituent properties and the resulting composite microstructure. As demonstrated in the previous sections of this chapter, microcrack occurrence is a key feature in the microstructure, where different microcracking patterns have been observed for spinel and hercynite containing materials.

Thus, given the importance of these features in enhancing material thermal shock resistance, their impact on Young’s modulus and thermal expansion evolution will be investigated at high temperature. The main objective of this approach is to provide valuable insight on material

BY NC ND

design parameters that can be tuned to enhance the thermomechanical properties of magnesia-based composites.

IV.3.1. Young's modulus evolution at high temperature for MS, MH and MSH materials

The evolution of Young's modulus as a function of temperature was measured for each material using ultrasonic long bar method presented in II.3.3. Experiments were performed up to 1400°C at a heating rate of 5°C/min for pure MgO and the three nuances of MS, MH and MSH materials. A comprehensive comparison between the different materials is performed to determine the impact of inclusion fraction and inclusion type on the thermomechanical behaviour.

The curve in Figure IV-14 shows the evolution of Young's modulus for a pure MgO material. The heating and cooling stages can be followed on the curve by using the red and blue arrows, respectively.

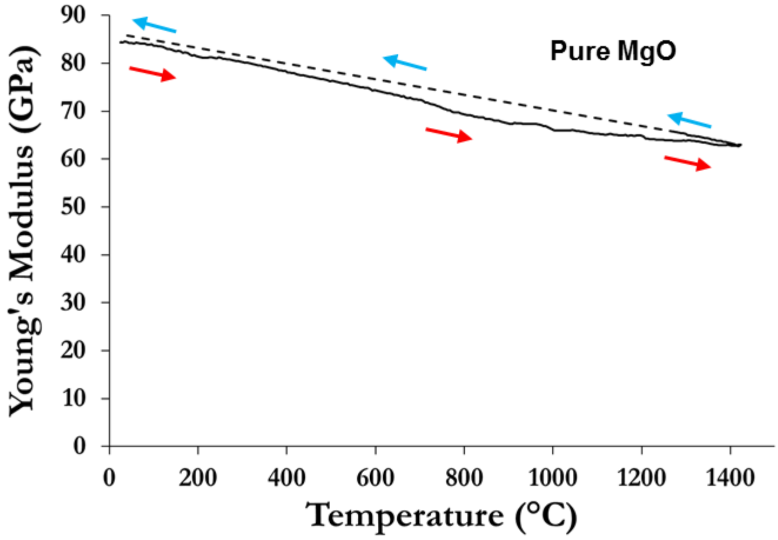

Figure IV-14: Evolution of Young's modulus of a pure MgO material

A quasi-linear decrease of Young's modulus can be observed during the heating stage of pure MgO. Then, during cooling, a progressive increase takes place where the material recovers its initial Young's modulus value at room temperature. Due to debonding of the sample with respect to the waveguide (coming from the CTE mismatch between magnesia and alumina rich cement), Young's modulus could not be followed throughout the cooling stage down from 1200°C. Nevertheless, a measurement was performed at room temperature after cooling to extrapolate data over the remaining cooling stage, assuming that no transformation takes

BY NC ND

place in the material at these temperatures. From the overall curve, the evolution of Young's modulus for this material is reversible, which is associated with most dense ceramics that do not exhibit damage within the microstructure.

The graphs in Figure IV-15, Figure IV-16 and Figure IV-17 show the evolution of Young's modulus for MS, MH and MSH materials respectively.

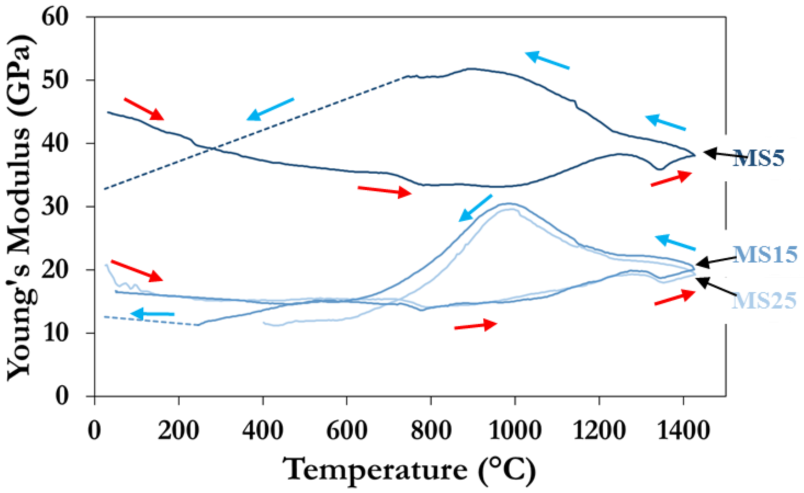

Figure IV-15: Evolution of Young's modulus as a function of temperature for MS materials

In contrast with pure MgO material, all materials within the MS, MH and MSH sets exhibit a hysteretic evolution of Young's modulus. This phenomenon presents itself in three stages:

- First stage: A general decrease of elastic properties during the beginning of heating. This stage is very similar to the behaviour of pure MgO. However, for MS materials, this decrease ends at 1000°C approx. while for MH and MSH it stops around 800¨C, except for MH25 and MSH25 since no decrease is observed during heating.
- Second stage: A progressive increase of Young's modulus takes place at the end of heating and accelerates at the beginning of cooling, leading to higher values of moduli compared to the initial ones. This increase is more pronounced for hercynite containing materials (MH followed by MSH) compared to MS ones. In particular, for MH15, and to a lesser extent MH25, the increase is considerable especially at the beginning of cooling.
- Third stage: Further cooling leads to a strong drop of Young's modulus, then a slow decrease continues until room temperature, leading to modulus values lower than the initial ones for materials containing 5% of inclusions (MS5, MH5 and MSH5).

BY NC ND

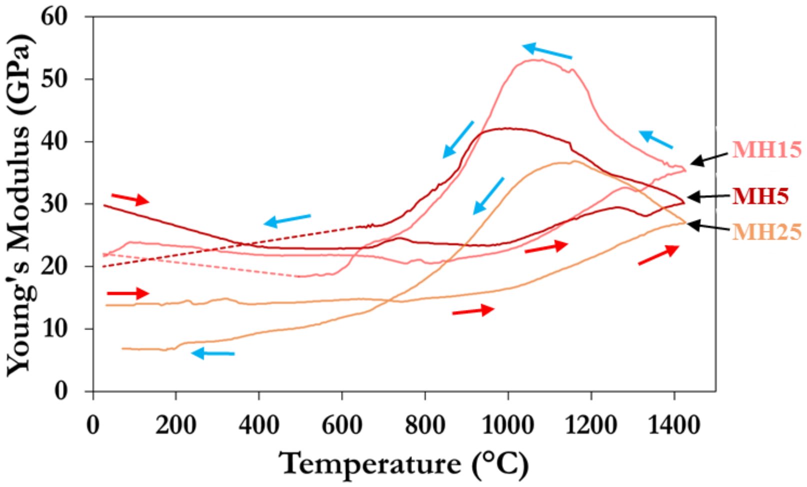

Figure IV-16: Evolution of Young's modulus as a function of temperature for MH materials

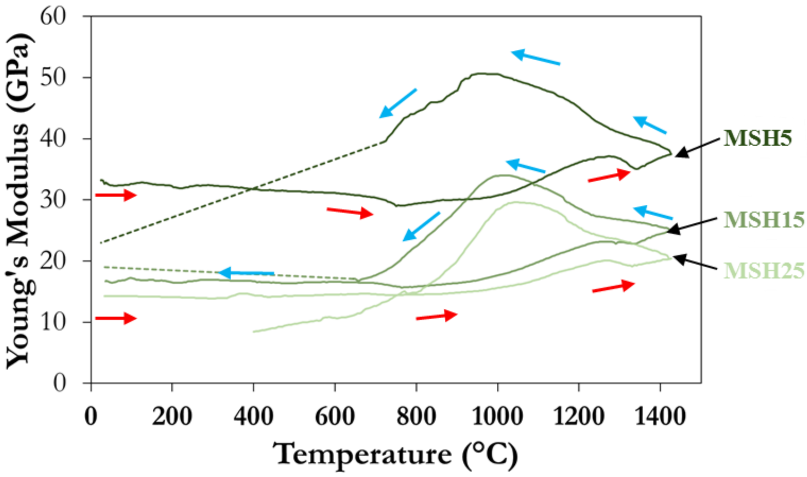

Figure IV-17: Evolution of Young's modulus as a function of temperature for MSH materials

Young's modulus increase at high temperature, during heating and the beginning of cooling, is typical of materials that exhibit pre-fabricated microcracks, which is the case for all of the studied materials. Indeed, such an increase is driven by various microcrack closure mechanisms, important of which are:

- Microcrack resorption thanks to a positive CTE mismatch ($\alpha_{MgO}>\alpha_{MgAl2O4}$, $\alpha_{FeAl2O4}$) in a stress-free configuration, since this phenomenon occurs at high temperatures.
- Microcrack healing due to viscous phase occurrence and flow through microcrack networks. This aspect is facilitated by low viscosity phases that are promoted by impurities and high temperature.

BY NC ND

These mechanisms can occur simultaneously at high temperatures, but their effectiveness in closing microcracks depends on intrinsic CTE of single constituents and the chemical composition of composites. In the case of hercynite containing materials, it can be expected that diffusion mechanisms participate actively in the closure of microcracks thanks to secondary spinel precipitation. This might explain, in part, the stronger Young's modulus recovery of MH and MSH materials.

After the strong increase, further cooling leads to a plateau-like evolution which leads thereafter to an abrupt drop in Young's modulus. This drop comes mainly from the thermal expansion mismatch between magnesia and the different spinel types. In fact, as discussed in I.1 and II.2.3, cooling leads to the development of thermally induced tensile stresses, orthoradial to the aggregates, that are ultimately released by formation of microcracks. In conjunction with the stronger Young's modulus increase of MH and MSH materials, the drop during cooling is just as important.

While all the materials share the three stages described above, some specific aspects of the curves, such as initial Young's modulus, maximum value at high temperature and finally, the temperature at which the drop occurs can be interesting indicators of a material's behaviour. Indeed, these parameters are different for each material and can serve as a basis for a more detailed comparison (Table IV-2).

Table IV-2: Summary of Young's modulus measurements at high temperature

Materials	E_{RT} (GPa) *Room temperature*	E_{MAX} (GPa) *During cooling*	E_{MAX}-E_{RT} (GPa)	Drop temperature (°C)
MS5	45	52	7	890
MS15	21	30	9	960
MS25	16	29	13	965
MH5	33	42	13	940
MH15	22	53	31	1035
MH25	14	37	23	1095
MSH5	33	50	17	935
MSH15	17	34	17	990
MSH25	14	29	15	1025

BY NC ND

From Table IV-2, a few trends can be extracted from these evolutions according to the correlation matrix in Figure IV-18 (Positive values up to "1" indicate a positive correlation between two parameters).

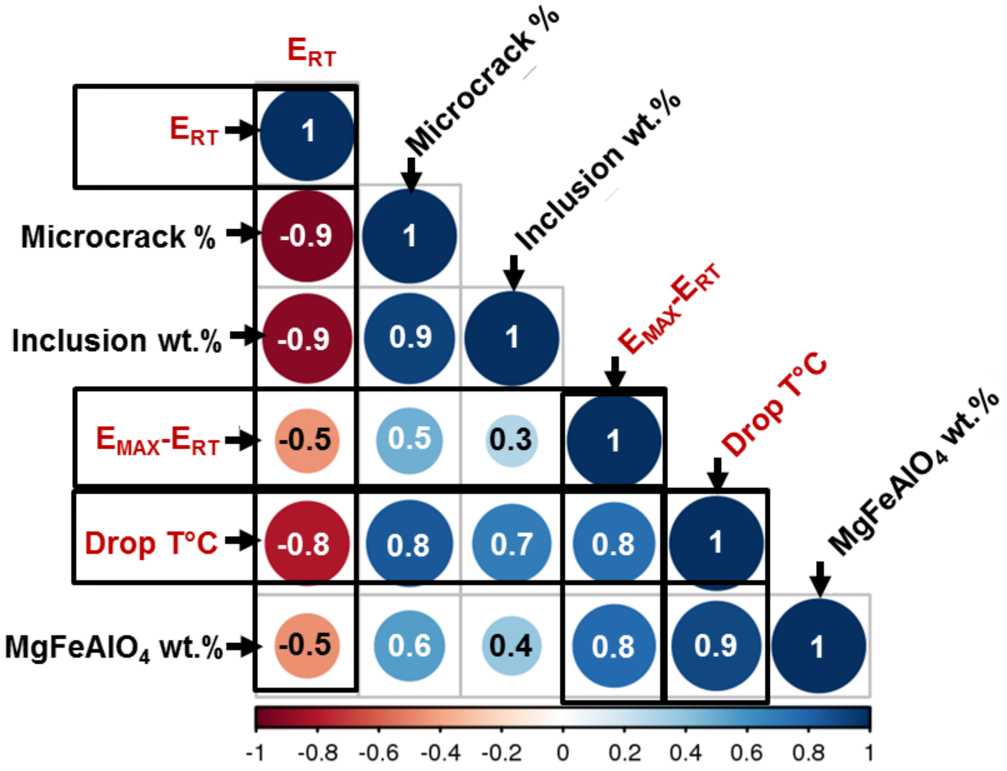

Figure IV-18: Correlation matrix of microstructure parameters and Young's modulus

Some strong correlations exist between Young's modulus, inclusion content and nature, which highlights some interesting differences between the different materials, namely:

- For each set of materials (MS, MH and MSH), increasing inclusion fractions always lead to lower Young's modulus values at room temperature. These lower Young's modulus values can be linked directly to the impact of microcrack networks (i.e microcrack %), which might present different characteristics with increasing inclusion fraction. In fact, microcracks could be more numerous and/or larger depending on the configuration and magnitude of stresses that are thermally induced in the magnesia matrix.
- Drop temperature increases with increasing inclusion fraction. In other words, microcracking starts earlier during cooling when inclusion content is increased. Indeed,

BY NC ND

increasing inclusion fractions leads to an increase of thermally induced stresses within the matrix [LiBr89], which might entail higher Young’s modulus drop as microcracks initiate earlier. This trend is especially observed for hercynite containing materials. Indeed, increasing $MgFeAlO_4$ content (precipitates formed from interdiffusion process) in the diffusion zone correlates more with drop temperature than the overall inclusion fraction.

- The amplitude of the difference between Young’s modulus at room temperature and at high temperature (E_{MAX}–E_{RT}) depends mainly on the ability of the material microstructure to resorb and heal microcracks at high temperatures. This parameter correlates best with $MgFeAlO_4$ content.

From the three points above, it can be concluded that inclusion fraction and type have an important impact on Young’s modulus through microcrack network resorption during heating and propagation during cooling. While the impact of inclusion fraction suggests increased damage coming from microcracks (i.e lowering Young’s modulus at room temperature), the characteristics of the generated microcrack networks are not explicit. However, comparing spinel nature (regular spinel or hercynite) impact on Young’s modulus evolution, in conjunction with microstructural investigations, some indications about microcracking patterns can be underlined.

Indeed, from the second point about drop temperature, it appears that inclusion distribution within the matrix might have a consequence on thermal stresses generated in the matrix, as schematised in Figure IV-19. Particularly so for hercynite containing composites, where interactions between thermal stresses coming from the large hercynite aggregate and the diffusion zone may take place, leading to an increase in micromechanical stresses locally within the matrix.

CC BY NC ND

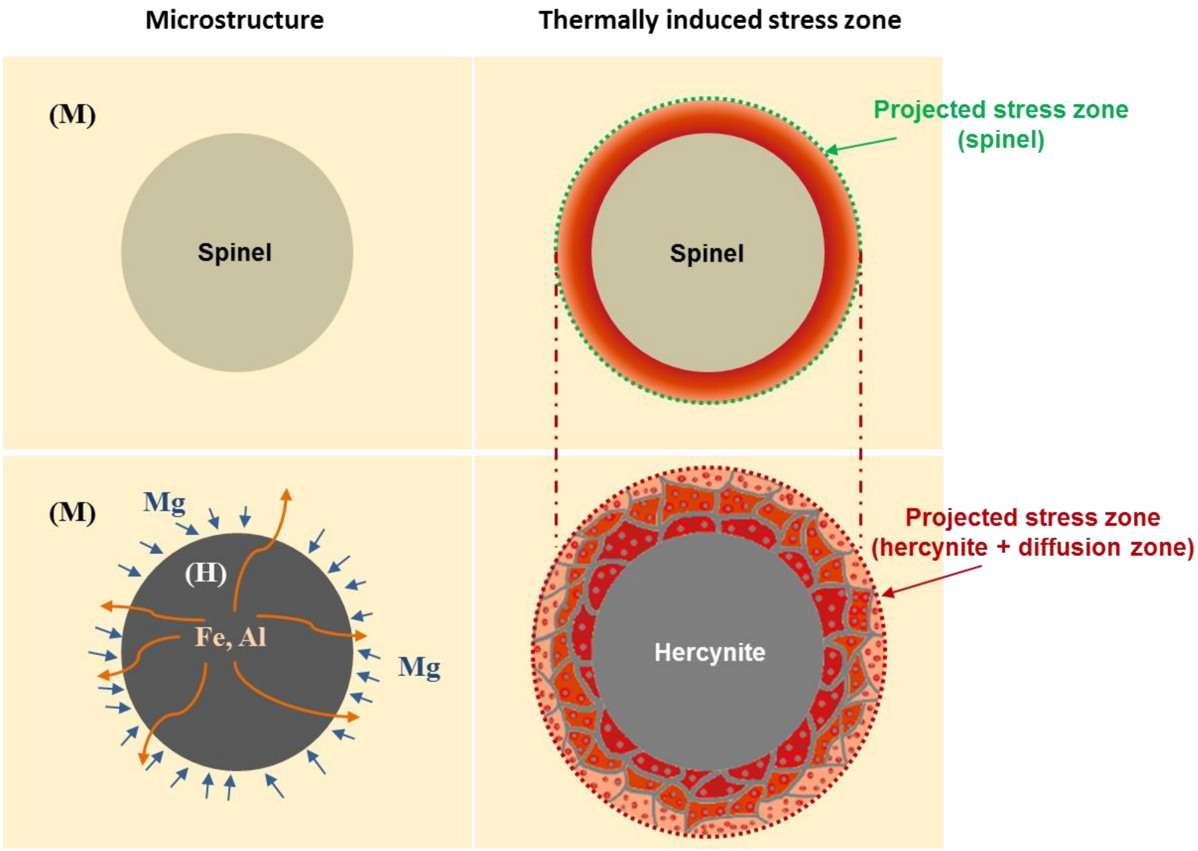

Figure IV-19: Schematic of the impact of CTE mismatch on thermal stress magnitude of spinel and hercynite containing composites

Such interactions might promote the formation of interconnected microcrack networks at the scale of the diffusion zone due to the high occurrence of $MgFeAlO_4$ precipitates around the hercynite aggregates.

Moreover, from microstructural observations in IV.2.1 and previous studies [Gras11], smaller inclusions are more prone to induce finer microcracks in relative terms. Therefore, it is very likely that MH, MSH materials, as opposed to MS, embed finer, and more numerous microcracks comparatively. As a result, these microcracks would be easier to resorb by the material matrix, especially if it is aided by extensive diffusion mechanisms, which is the case for hercynite-containing materials.

These subtle differences entail important implications on the thermomechanical behaviour as the microstructure plays a key role in temperature dependant evolutions. In the end, hercynite containing materials provide an interesting synergy between their complex microstructure and Young’s modulus evolution, which is likely to be beneficial.

BY NC ND

IV.3.2. Acoustic emission at high temperature

In order to complement Young's modulus evolution, acoustic emission experiments were performed using the same experimental conditions (up to 1400°C at a rate of 5°C/min). The main objective of this experiment was to detect damage occurrence as a result of CTE mismatch during cooling.

Figure IV-20 shows the evolution of cumulated acoustic emission hits as a function of temperature for MS, MH and MSH materials containing 5% and 15% of inclusions.

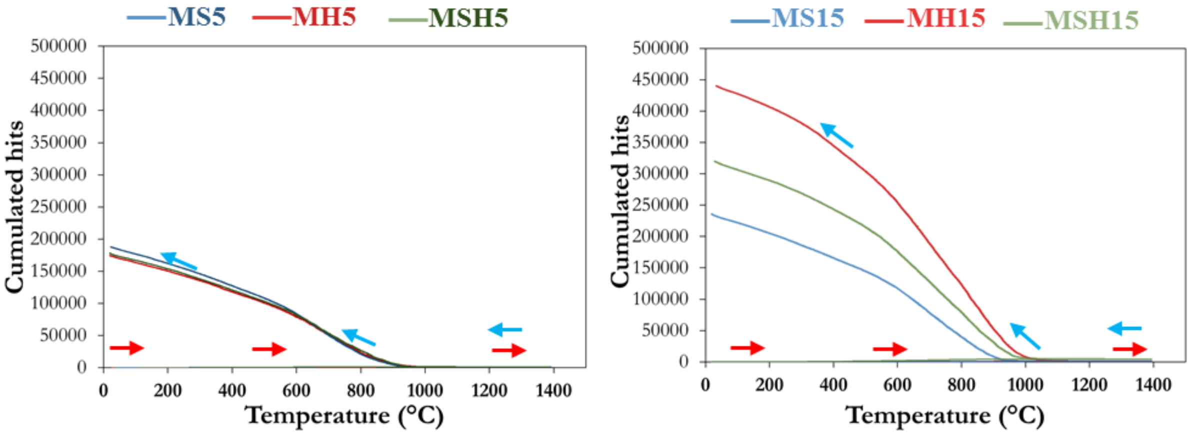

-a- -b-

Figure IV-20: Acoustic emission evolution as a function of temperature for MS, MH and MSH materials containing 5% and 15% of inclusions

As suggested by these curves, the number of hits during heating is negligible compared to the cooling phase. Indeed, starting at temperatures very close to those reported in Table IV-2 for Young's modulus drop, a strong increase of hits takes place, which can be associated with microcrack occurrence coming from CTE mismatch. The cumulated number of hits increases steeply for about 400°C after initiation, then this increase slows down until room temperature.

For composites containing 5% of inclusions, very similar values of cumulated hits are obtained regardless of the material. In comparison, composites containing 15% of inclusions exhibit a much higher number of cumulated hits, especially for hercynite containing materials. Indeed, within the 15% nuance of these composites, cumulated hits are highest for MH15, followed by MSH15 and then MS15. A higher number of cumulated hits often indicates a higher occurrence of defect related phenomena within the sample, which is confirmed by lower values of Young's modulus at room temperature after cooling (i.e $E_{MS5}<E_{MS15}$ from Table IV-2).

As suggested by Figure IV-21, AE hits correlate positively with all the parameters related to the impact of thermal damage such as E_{MAX}-E_{RT} or microcrack proportion.

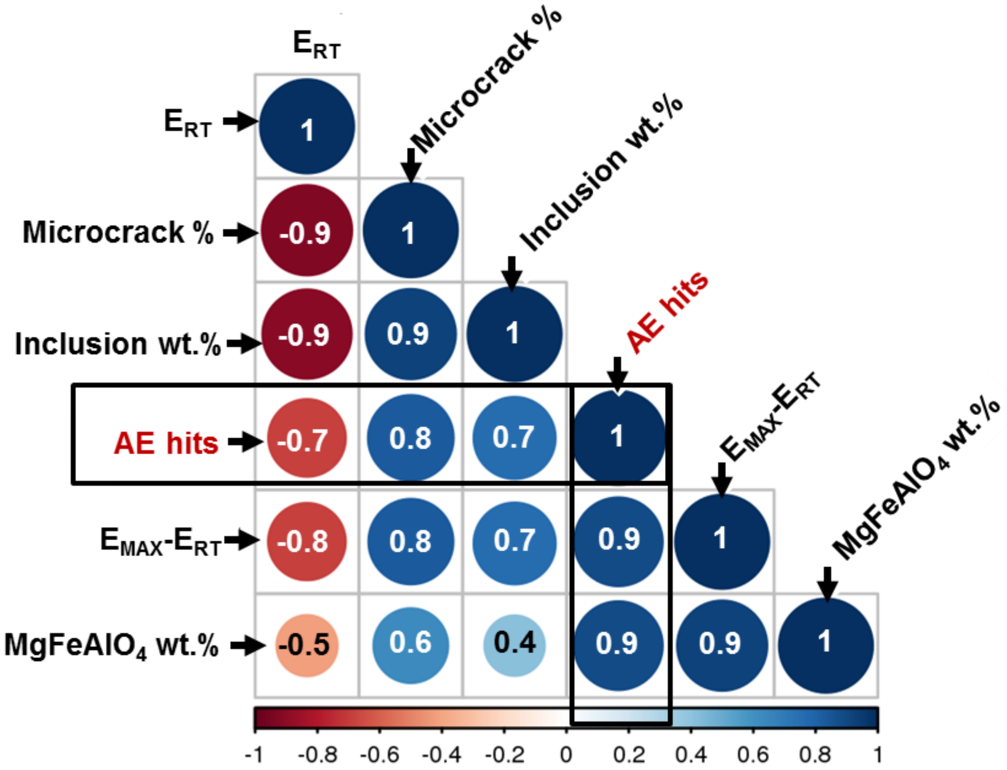

Figure IV-21: Correlation matrix on the impact of microstructure and thermomechanical parameters on AE hits

Moreover, $MgFeAlO_4$ content (present in MH and MSH composites) seems to have a stronger impact on AE hits than the overall inclusion content, once again demonstrating the peculiar behaviour induced by the so-called diffusion zone. Given the size of $MgFeAlO_4$ precipitates in the magnesia matrix, it is most likely that microcracks generated from these grains are equivalently fine in size and more numerous, thus leading to a high number of AE hits. Furthermore, the concentration of these precipitates around the so-called diffusion zone probably increases microcrack interconnections as a result of stress field interactions in the same zone.

These conclusions reaffirm some of the assumptions made in the previous section about thermal stress interactions and the resulting synergy between the microstructure and the thermomechanical behaviour.

BY NC ND

IV.3.3. Dilatometric behaviour

The dilatometric behaviour of all materials was investigated up to 1400°C and during cooling to room temperature with a heating rate of 5°C/min. The thermal expansion curves of MS and MH composites are reported in Figure IV-22, while average thermal expansion coefficients were calculated and plot in Figure IV-23 at different temperature ranges. In addition to this, the composite approach of Hashin and Shtrikman [HaSh62, HaSh63] has been used to model thermal expansion values for non-damaged materials. Indeed, this approach considers spherical inclusions embedded within a continuous matrix with perfect matrix/inclusion interfaces. Upper and lower bounds are defined for composite thermal expansion coefficients [RoHa70] depending on Young's modulus of single constituents (i.e the matrix or the inclusions).

The dilatometric curves exhibit a non-linear evolution during heating and cooling marked by some hysteresis. Moreover, these curves suggest that there is a clear impact of inclusion fraction on thermal expansion, especially during cooling where average CTE values were calculated.

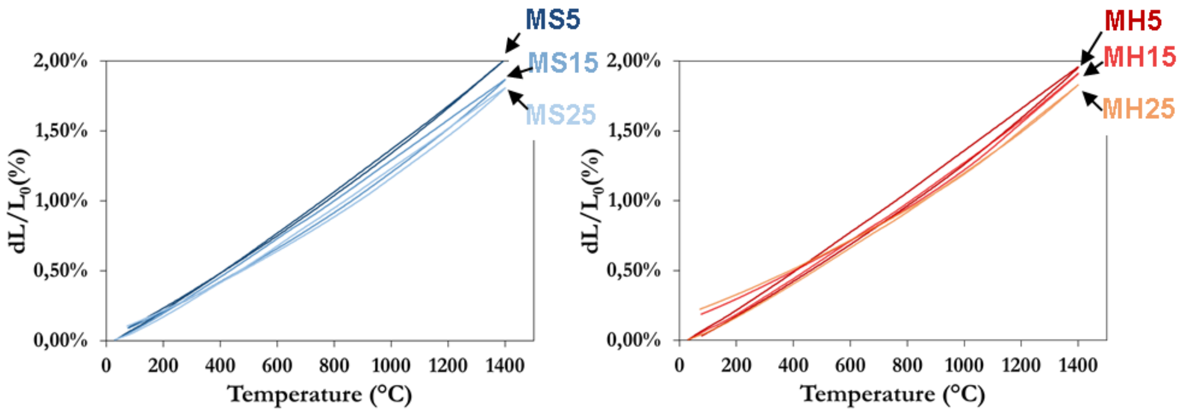

-a- -b-

Figure IV-22: Evolution of thermal expansion versus temperature for a) MS and b) MH materials

As observed from Young's modulus evolutions presented previously, the cooling stage is marked by the occurrence of microcracks. Microcrack initiation temperatures vary as a function of materials, but it can start from 1000°C for MH15 and MH25 to 900°C approximately for MS materials during cooling.

Therefore, it can be of interest to calculate the CTE just before microcrack initiation (1150°C to 1100°C) and at the end of the cooling stage (150-100°C). Moreover, as mentioned

BY NC ND

previously, experimental values have been compared to the HS model (Figure IV-23) in order to highlight the main differences and their possible origin.

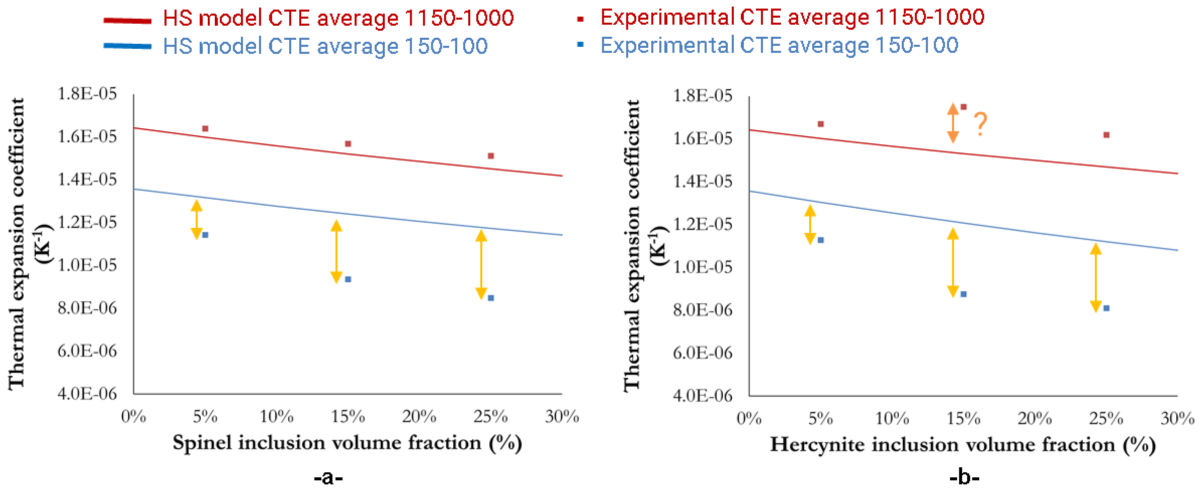

Figure IV-23: Comparison of calculated (using HS- model) and measured average CTE of a) MS and b) MH materials in the temperature ranges of 1150-1000°C and 150-100°C during cooling

Firstly, from Figure IV-23, the increase of spinel inclusion fraction leads to a decrease of the average CTE both prior and after microcrack initiation. The linear decrease of $CTE_{1150\text{-}1100°C}$ can be attributed mostly to the intrinsically lower thermal expansion of spinel and hercynite compared to magnesia.

At the beginning of cooling, there is a very good agreement between experimental $CTE_{1150\text{-}1100°C}$ and the HS model prior to microcrack initiation for MS materials. Indeed, at this stage the material is in a stress-free state and can be described accurately using the HS^- model. However, in the same temperature range for MH materials, the experimental CTE do not agree very well with the HS model.

This peculiar behaviour associated mostly with MH15 can also be linked to the strong increase of Young's modulus at the same temperature range. This phenomenon can be attributed to the influence extensive diffusion occurring in MH materials in general, which seem to be more effective for a hercynite content of 15%.

On the other hand, at the end of cooling, an increasing gap can be noticed between experimental and HS model CTE with increasing inclusion fraction for both MS and MH materials. This gap in CTE values comes as a result of microcrack occurrence starting from 1000°C, as demonstrated previously in IV.3.2. Indeed, given that HS approach models

BY NC ND

damage-free composites, the calculated CTE is higher than the measured one since microcrack occurrence leads to thermal stress relaxation and thus, lower experimental CTE.

By using the HS approach as a reference for a damage-free composite, the impact of microcrack occurrence on the CTE was appreciated for both MS and MH materials especially at the end of cooling.

Lastly, from Figure IV-24, MSH materials exhibit a behaviour relatively similar to that of MH materials where $\text{CTE}_{1150\text{-}1100°C}$ does not decrease significantly as expected from diffusion phenomena involving hercynite and magnesia. In addition to this, different intrinsic CTE of spinel and hercynite at this temperature range (Chapter II) might also lead to a peculiar evolution for the material.

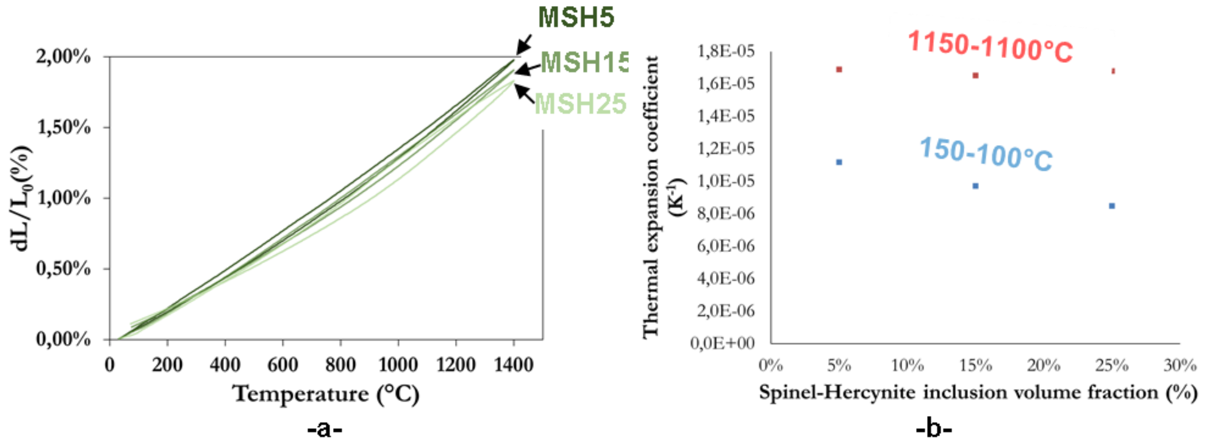

Figure IV-24: a) Thermal expansion of MSH materials as a function of temperature and b) average CTE for MSH materials.

For $\text{CTE}_{150\text{-}100°C}$ values, the decrease is very similar to that observed for MS and MH composites. As established through the Hashin and Shtrikman model comparison, these decreasing CTE values are mainly influenced by microcrack propagation during cooling.

In the end, the CTE values are strongly correlated with thermally induced microcracks, as confirmed by the correlation matrix in Figure IV-25. Thus, an inverse dependency can be observed whereby higher amounts of microcracks lead to lower $\text{CTE}_{150\text{-}100°C}$ values. In fact, a decreasing material CTE is beneficial for improving the thermal shock resistance of the composites.

BY NC ND

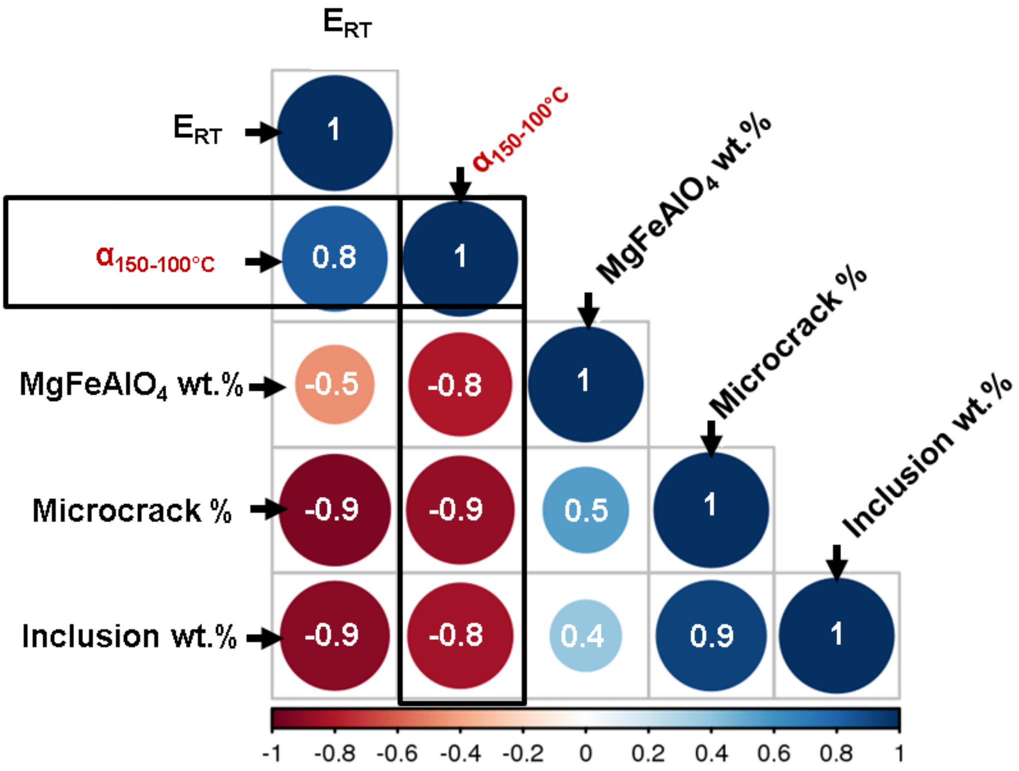

Figure IV-25: Correlation matrix showing the impact of thermally induced damage on CTE

IV.4. Conclusion

The combination of microstructural investigations and thermomechanical property characterisations allowed for a thorough study of magnesia-based composites. In particular, key microstructure-thermomechanical property relationships were established through correlation with some of the main material characteristics, namely inclusion fraction and nature (i.e regular spinel or hercynite).

In the one hand, microstructural investigations underlined some important differences between MS and hercynite containing composites (MH and MSH). Important of which is the occurrence of a diffusion zone in the latter, which is a consequence of extensive vacancy driven interdiffusion during sintering at high temperature. These mechanisms led to the formation of spinel solid solution precipitates in the magnesia matrix around hercynite aggregates.

BY NC ND

Moreover, due to the CTE mismatch between magnesia and all types of spinel included within the matrix, microcracks were formed. A higher proportion of microcracks was observed systematically for higher inclusion fraction volumes. By comparing the different composites, some characteristic microcracking patterns were revealed, especially regarding hercynite containing composites. In the case of MS composites, relatively large microcracks were observed radially from the regular spinel inclusions. In contrast, due to the presence of the so-called diffusion zone in MH composites, fine interconnected microcrack networks around hercynite aggregates were the dominant microcracking pattern. Naturally, MSH composites exhibited both microcracking behaviours.

On the other hand, the impact of these thermally induced microcracks on the thermomechanical behaviour was investigated through the evolution of Young’s modulus, acoustic emission and thermal expansion at high temperature. In essence, these results highlighted hysteretic and non-linear evolutions related to microcrack closure and opening mechanisms during a thermal cycle, which depend mainly on inclusion content and type.

Ultimately, these results provide insight on essential microstructure design parameters for improving the thermomechanical behaviour effectively. Based on the comparisons made in this study, it appears that hercynite containing composites offer a more interesting synergy between the microstructure and thermomechanical properties. In order to evaluate the extent of microstructure impact on the thermomechanical properties, the fracture behaviour will be investigated in the next chapter using the WST and optical methods (DIC and 2P-DIC).

BY NC ND

Chapter V

BY NC ND

Chapter V. Fracture behaviour analysis of magnesia-based model composites: From microcrack networks to FPZ development

V.1. Introduction

In order to provide a comprehensive investigation of magnesia-based materials' thermomechanical properties, it is necessary to consider the fracture behaviour of these composites. Indeed, as discussed in I.2, thermal shock resistance depends strongly on crack propagation resistance, which is improved through energy dissipating mechanisms in the Fracture Process Zone (FPZ).

Given the presence of microcrack networks in magnesia-based composites, a non-linear mechanical behaviour and a reduced brittleness are expected, where FPZ development contributes significantly to increase the fracture energy. Therefore, an energetic approach to fracture will be considered to describe the impact of FPZ mechanisms on the overall fracture behaviour.

Additionally, optical methods will be used to ensure that fracture energies are measured accurately, and that crack propagation is monitored during the WST. The latter point will be considered thoroughly to identify the main fracture mechanisms and quantify their impact on the fracture behaviour of the magnesia-based composites.

V.2. DIC coupled to the Wedge Splitting Test (WST) for fracture characterisation

V.2.1. Load-displacement curves characterised by the WST

The fracture behaviour of Pure MgO and magnesia-based composites has been investigated at room temperature by using DIC during the WST. Monotonic loading experiments have been performed on at least two samples of each material.

Horizontal Load-Displacement curves coming from these experiments have been reported in Figure V-1, Figure V-2 and Figure V-3. For an enhanced readability, the most representative experiments were presented.

In Figure V-1, a comparison between pure MgO and MS materials can be followed whereby the influence of spinel inclusion addition can be clearly identified. Three stages can be distinguished on the WST curves:

- Linear elastic stage: Corresponds to the linear elastic behaviour of materials at the beginning of loading.

cc BY NC ND

- Non-linear stage: Diffuse damage and microcrack coalescence before the maximum load is reached.
- Post-peak stage: Corresponds to the onset and propagation of a macro-crack.

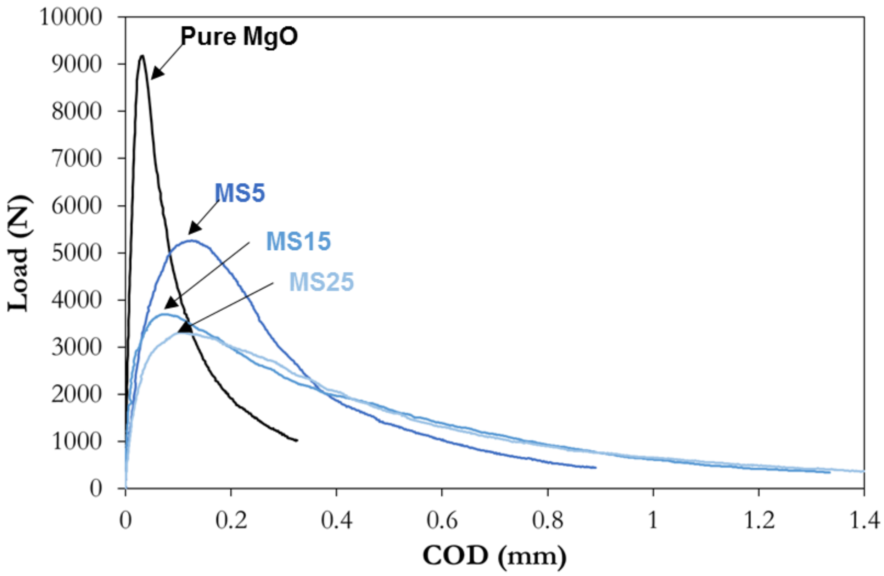

Figure V-1: Horizontal load-displacement curves of Pure MgO and MS materials

Essentially, pure MgO displays a rather linear elastic slope up to the maximum load with minimal post-peak behaviour, while MS composites exhibit non-linear curves as well as a rather large post-peak region. The non-linearity of the load-displacement curve is an important consequence of diffuse microcracking, where microcrack growth and coalescence lead to the onset of a macrocrack. As a consequence, the amount of diffuse damage and the resulting non-linearity have a direct influence on the extent of the post-peak region.

In this regard, increasing inclusion fraction decreases the maximum load and increases the overall material strain that leads to higher COD values for a given loading state. The latter results mainly in an extended post-peak region that is linked to crack propagation behaviour. Therefore, materials with an initial microcrack network such as MS, induce relatively large post-peak regions which usually translate into higher fracture energies. These materials are commonly referred to as quasi-brittle due to their ability to promote stable fracture, allowing them to effectively slow down crack propagation.

On the other hand, for MH composites in Figure V-2, a different evolution can clearly be observed when increasing hercynite content in the magnesia matrix.

BY NC ND

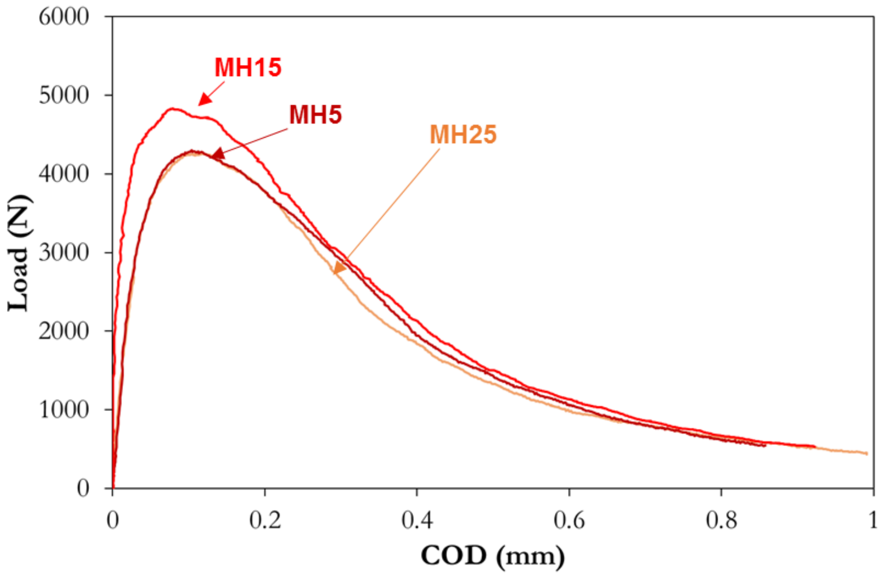

Figure V-2: Horizontal load-displacement curves of MH composites

While these materials exhibit a quasi-brittle behaviour with a non-linear evolution before the maximum load, increasing hercynite content does not lead to a systematic drop of the maximum load as noted for MS composites. In fact, a hercynite content of 15% increases the maximum load compared to MH5 and MH25. This peculiar fracture behaviour is yet another aspect of the distinctive thermomechanical behaviour of MH composites measured in the previous chapter.

As for MSH composites (in Figure V-3), the same trend as that of MS composites can be observed qualitatively. Increasing the combined regular and hercynite content decreases the maximum load systematically while enlarging the post-peak area.

BY NC ND

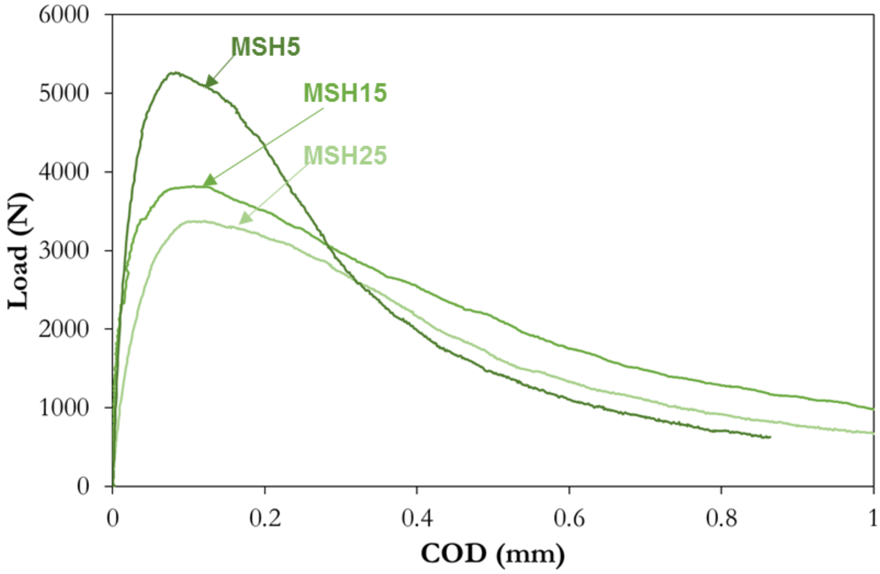

Figure V-3: Horizontal load-displacement curves of MSH composites

In order to analyse the fracture behaviour of these materials and provide a thorough analysis, some essential fracture parameters such as nominal tensile strength σ_{NT}, specific fracture energy G_f, and the brittleness number B' were measured from WST curves. This way, the impact of inclusion nature and fraction can be discussed with regard to previously established microstructural considerations.

V.2.2. Impact of inclusion nature and weight on WST fracture parameters

As explained in I.2.2.3, fracture energies were measured from the total area under the horizontal load-displacement curves up to 15% of the maximum load divided by the fracture area. Consequently, specific fracture energies were deduced from the total energy by subtracting the elastic energy contribution. Moreover, the nominal notch tensile strength, σ_{NT}, (Eq. III.2) and the brittleness number B' were calculated for each material.

The brittleness number, first introduced by [GoGS78] is an energetic concept that relates to the ratio of elastic energy stored in the material at crack initiation to the total fracture energy. Therefore, in order to improve crack propagation resistance and thus, thermal shock resistance, a reduced brittleness is sought. As suggested by [HaTs97], the brittleness number can be calculated as follows: $B' = \frac{\sigma_{NT}^2 . L}{G_f . E}$, where L is a WST specimen dimension.

As summarised in Table V-1, average fracture parameters have been calculated for each material. Pure MgO exhibits the lowest fracture energy and the highest nominal notch tensile

BY NC ND

strength whereas MSH composites have highest fracture energies and relatively low values of nominal tensile strength.

Table V-1: Average fracture parameter values obtained by WST on model materials

Materials	Nominal notch tensile strength σ_{NT} (MPa)	Specific fracture energy G_f (J.m^{-2})	Brittleness number B'
Pure MgO	9.2	130	0.77
MS5	5.1 ± 0.2	209 ± 33	0.27 ± 0.05
MS15	3.8 ± 0.2	250 ± 7	0.27 ± 0.03
MS25	3.24 ± 0.1	236 ± 22	0.28 ± 0.02
MH5	4.55 ± 0.3	213 ± 24	0.29 ± 0.07
MH15	5.06 ± 0.3	266 ± 9	0.44 ± 0.03
MH25	3.90 ± 0.2	281 ± 24	0.39 ± 0.06
MSH5	5.16 ± 0.3	283 ± 36	0.28 ± 0.07
MSH15	3.91 ± 0.2	341 ± 21	0.26 ± 0.06
MSH25	3.13	191.07	0.37

In order to propose a detailed comparison between the different materials, the impact of inclusion fraction and nature on fracture parameters have been plotted in Figure V-4Figure V-5Figure V-6. Measurement standard deviations (in Table V-1) were not included on the graphs for an enhanced readability.

Firstly, from Figure V-4 and as observed previously, increasing inclusion fraction leads to a systematic drop of the nominal notch tensile strength, especially when increasing from 0% (i.e pure MgO) to higher inclusion fractions. However, there is an exception when increasing hercynite content in MH composites from 5% to 15%.

BY NC ND

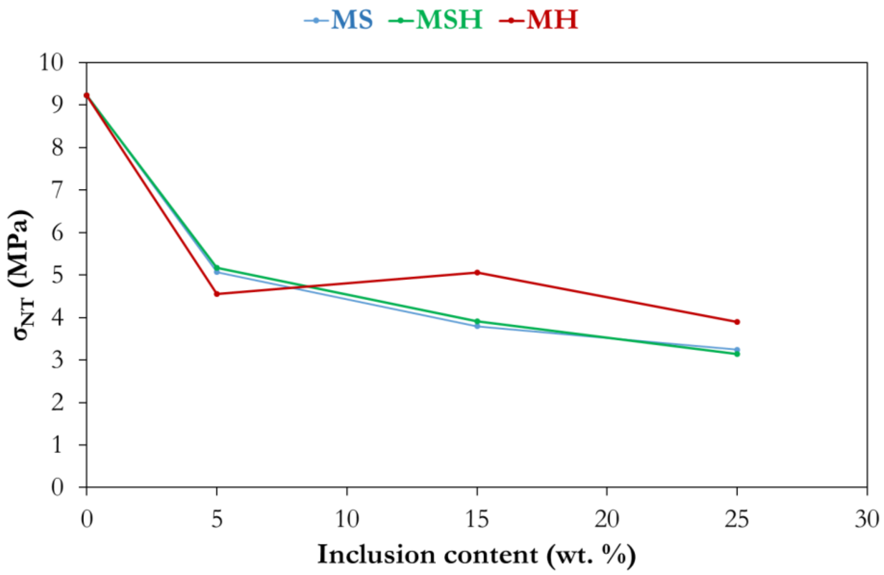

Figure V-4: Evolution of σ_{NT} as function of inclusion content in wt. %

In fact, MH composites exhibit slightly higher σ_{NT} values, compared to MS and MSH, starting from 15% inclusion content.

Figure V-5 shows the evolution of specific fracture energy for the different composites and inclusion contents. Given that fracture energy is measured from the area under the load-displacement curve, high values of energy often result from extended post-peak regions observed in most of the composites.

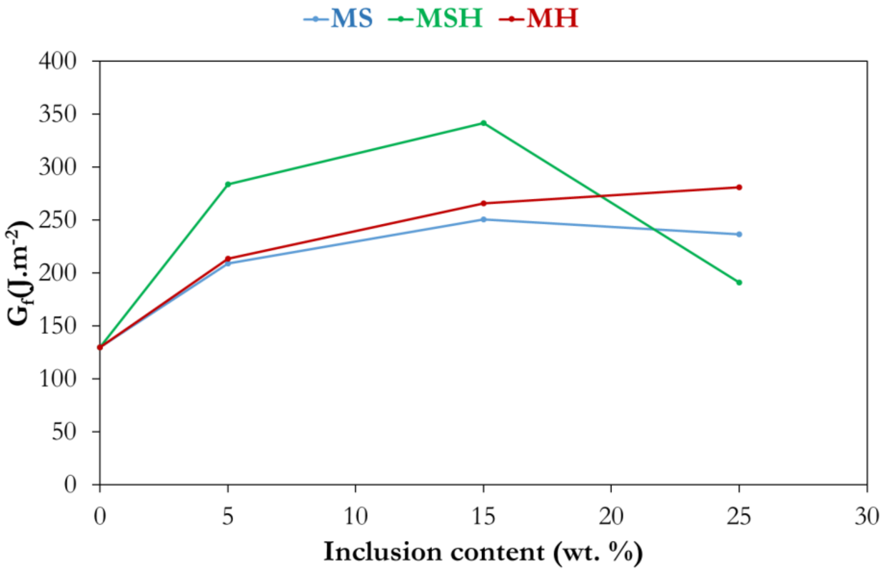

Figure V-5: Evolution of G_f as function of inclusion content in wt. %

BY NC ND

As such, increasing inclusion fraction increases the fracture energy systematically, except for MSH25 material where a drop is noticed going from 15% to 25% of inclusions.

In a similar way to the σ_{NT} parameter, the highest increase in fracture energy is observed going from 0% to higher inclusion fractions. Moreover, the highest energy values are exhibited by MSH composites, followed by MH and then MS.

Finally, by combining both parameters into B', the impact of inclusions on the brittleness of the composites is evaluated in Figure V-6.

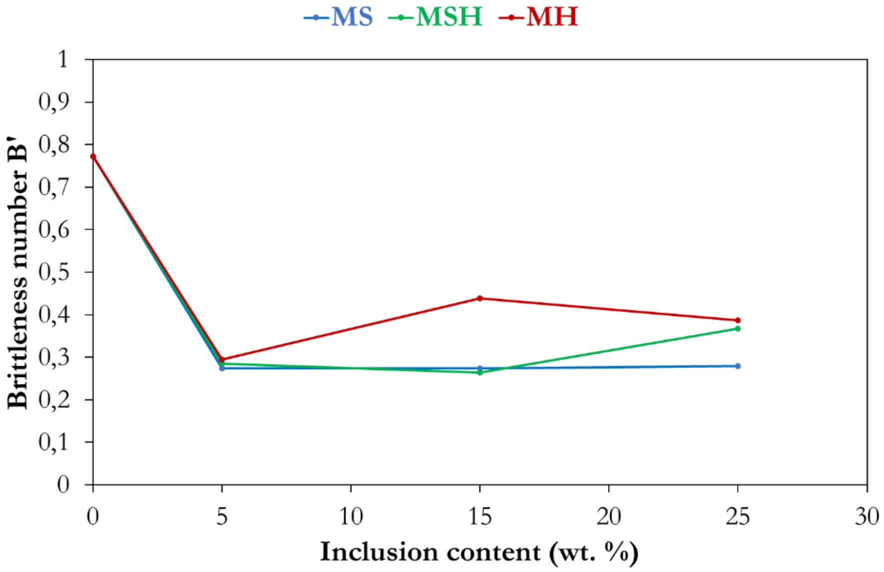

Figure V-6: Evolution of B' as a function of inclusion content in wt. %

The evolution of the B' number follows a decreasing trend with increasing inclusion fractions, with an exception for MH15 and MSH25, just as expected from the previous observation on fracture energy evolutions. The lowest values are observed for MS and MSH composites. Overall, these results confirm the reduced brittleness induced by microcracks. In contrast, the brittleness number increases for a hercynite content above 5% mainly due to higher strength values, but remains reasonably low.

In order to link these fracture parameters with previously established microstructural observations and measured properties, the correlation matrix in Figure V-7 summarises the main impact factors.

BY NC ND

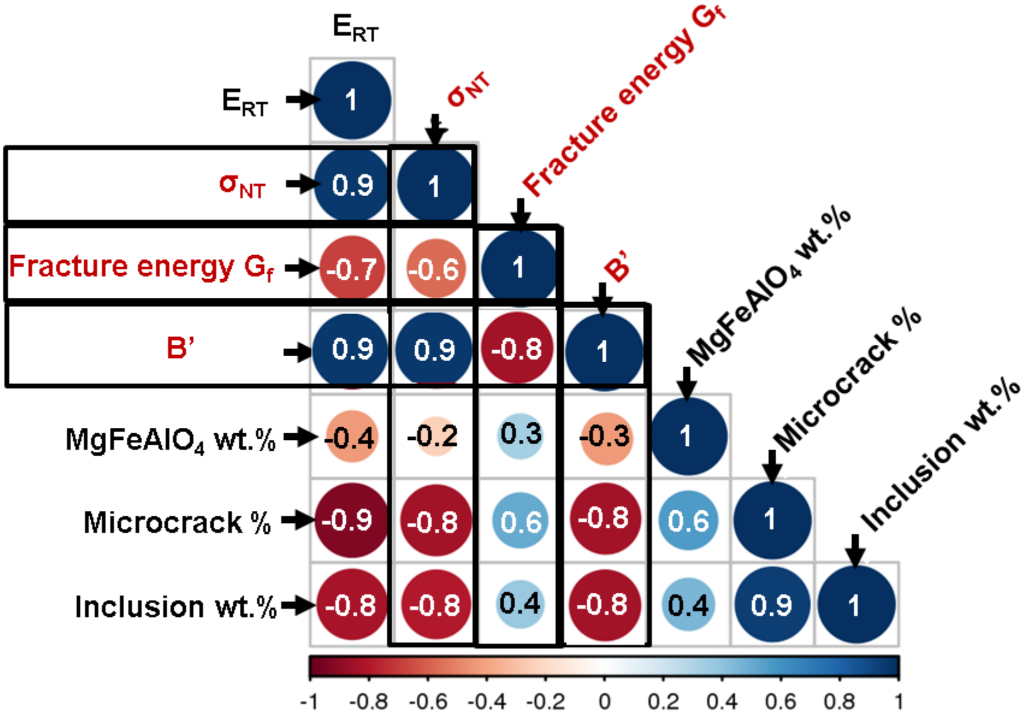

Figure V-7: Correlation matrix showing the impact of thermally induced damage on fracture parameters measured during the WST

A strong positive correlation exists between Young's modulus at room temperature and σ_{NT}. The latter correlates negatively with inclusion content and microcrack proportion, as expected. Conversely, the specific fracture energy correlates positively with inclusion content and microcrack volume while negatively with Young's modulus at room temperature. Moreover, the brittleness number B' correlates positively with Young's modulus and strength while a strong negative correlation is observed with the specific fracture energy and inclusion fraction. These conclusions support the fact that microcrack networks help considerably in reducing the brittleness of the materials by reducing the strength (σ_{NT}) and improving the crack propagation resistance (high values of G_f).

Comparing the impact of the two types of inclusions, namely regular spinel and hercynite, interesting conclusions can be drawn by combining microstructural considerations discussed in the previous chapter with WST results presented herein. Indeed, given the important impact of microcrack network occurrence on the fracture behaviour, relating these two aspects is primordial in understanding the main differences between MS, MH and MSH.

BY NC ND

In essence, MS composites were likely to exhibit large microcracks propagating radially from spinel aggregates, while MH composites had a predominantly more confined microcracking zone comprised within the so-called diffusion zone. Therefore, it is expected that MSH composites exhibit a combination of both microcracking patterns, leading to a much more complex interpretation of microstructure-fracture behaviour relationships. For this reason, the main focus will be on analysing the fracture behaviour of MS and MH composites.

In the one hand, the impact of inclusion nature on microcracking patterns leads to varying degrees of strength evolution with increasing inclusion fractions. Indeed, as demonstrated previously, increasing inclusion fractions in MS materials leads to a systematic drop of strength, also reported extensively in [ARRW02, GAHC13]. However, in the case of MH composites, increasing hercynite content from 5% to 15% leads to a higher strength followed by minimal strength reduction for 25% of hercynite compared to other materials. This observation comforts the idea that extensive diffusion, coming from high amounts of hercynite, participates strongly in creating fine microcracks confined around hercynite aggregates in diffusion zones. Therefore, the influence of hercynite content on the fracture behaviour is not trivial due to the occurrence of the so-called diffusion zone.

On the other hand, regardless of the material, the specific fracture energy increases systematically with increasing inclusion fractions. Therefore, this fracture parameter is mostly influenced by the amount of microcrack networks generated as a result of CTE mismatch, which effectively depends on inclusion content. In fact, as discussed in I.2.2, microcrack networks participate extensively in the development of so-called fracture process zone (FPZ), which consumes most of the energy involved during fracture. Given the predominant effect of microcracks and the presence of large aggregates in the studied materials, the fracture mechanisms described in Figure V-8 are expected to be the main energy dissipating phenomena.

BY NC ND

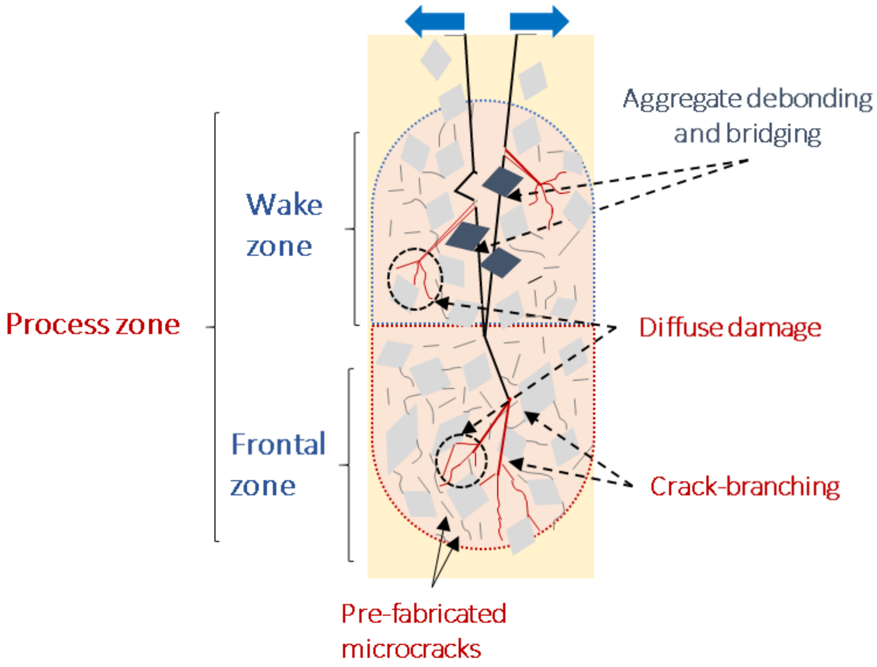

Figure V-8: Schematic description of the main fracture mechanisms in a Fracture Process Zone

In summary, microcracks in MS might have a more degrading effect on elastic properties and strength values than MH composites. At the same time, larger microcracks can be more beneficial for increasing the fracture energy and reducing the brittleness of the material. Overall, MSH composites are the most effective in increasing fracture energy and reducing brittleness.

Given the extensive measurements performed in the past for MS materials, leading to a deep understanding, the next part will focus on MH composites due to their relative complexity and peculiar fracture behaviour. In this sense, the refined 2P-DIC method will be applied to identify the underlying FPZ phenomena that lead to the quasi-brittle behaviour of MH composites.

V.3. FPZ monitoring using 2P-DIC and crack propagation resistance during the WST

V.3.1. FPZ monitoring of magnesia-hercynite materials using 2P-DIC

As demonstrated in the previous section, pure MgO exhibits a brittle fracture behaviour compared to MH composites based on the brittleness number analysis. The significant reduction of brittleness in MH composites results from a combination of diffuse damage and FPZ mechanisms that take place at the scale of the microstructure. The initial presence of

BY NC ND

microcrack networks in MH composites are key to enhancing the occurrence of energy dissipating mechanisms.

In order to identify the main fracture mechanisms and analyse the fracture behaviour, 2P-DIC calculations were performed to monitor crack propagation during the WST. Therefore, according to the 2P-DIC crack detection principle presented in III.4, an appropriate pseudo-strain threshold has been defined for each material in order to remove measurement noise. This way, damage length could be measured in the most accurate way using 2P-DIC.

Moreover, the evolution of damage is highlighted as the difference between the cumulated damage length and the equivalent crack length. This damage zone length represents the material's ability to develop fracture surfaces resulting from FPZ activation, mainly through its frontal zone. Combined with the visualisation of 2P-DIC fields, this quantification gives an insight on the predominant frontal process zone fracture mechanisms and, to a certain extent, their subsequent influence on the total fracture energy.

For each material, graphs describing the evolution of dissipated and elastic energies during loading and damage length are reported alongside 2P-DIC images. The latter relate to specific loading states marked in the load-displacement curves of each material. This representation facilitates correlations between fracture energy and damage zone length while observing the main fracture mechanisms on the actual 2P-DIC images.

As reported previously and according to Figure V-9, pure MgO exhibits a low fracture energy as well as limited average damage zone length, about 50 mm.

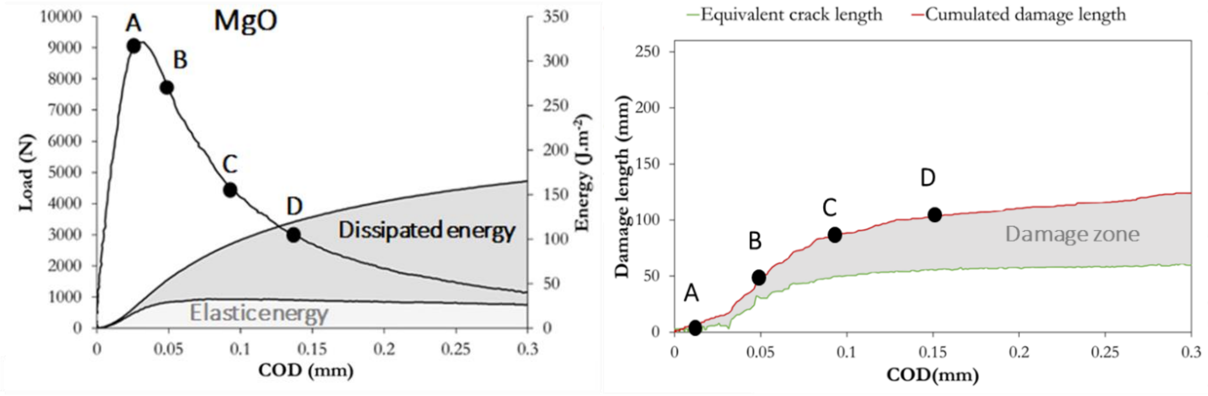

-a- -b-

Figure V-9: Fracture behaviour of Pure MgO a) Load-COD curve and evolution of energy, b) evolution of damage as a function of COD

BY NC ND

Moreover, using a threshold of 0.0015, fracture was followed from the initiation of the crack to its propagation through the WST sample (Figure V-10).

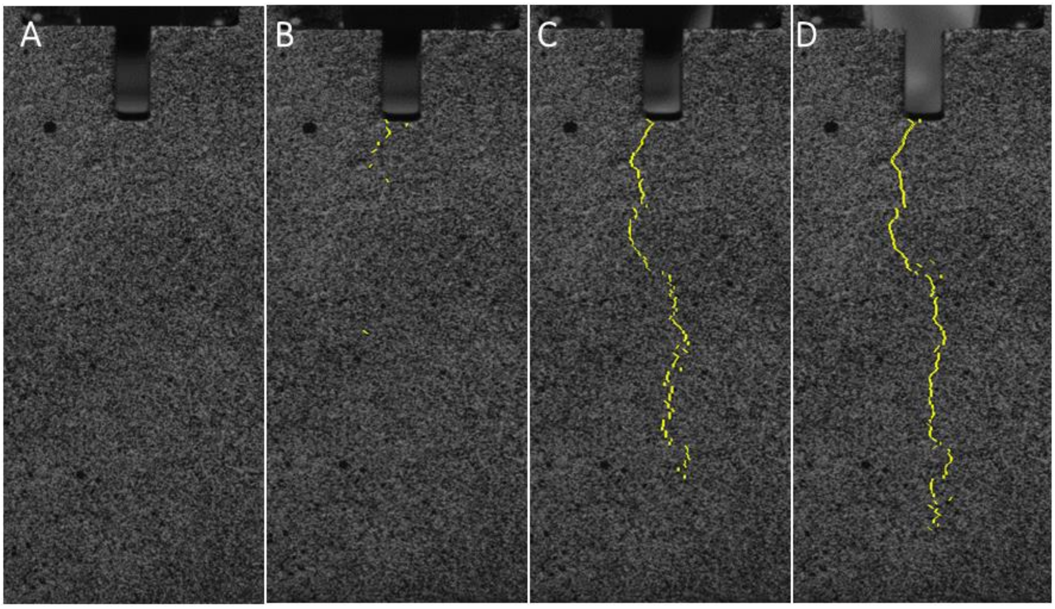

Figure V-10: 2P-DIC images of instantaneous crack propagation of Pure MgO during a WST

For Pure MgO, crack initiation occurs in state B just after the peak of the load-COD curve. It can clearly be seen from the images in the states going from B to D that the main fracture mechanism is related to deviations of the main crack path, which can be traced back to the presence of relatively large aggregates within the microstructure of the material. Therefore, the damage zone length that is deduced from Figure V-9.b, in this case 50 mm on average, is mainly a result of crack path tortuosity. These results clearly show the presence of a FPZ in pure MgO even though it is of limited size and therefore of limited impact on fracture energy.

In contrast, MH composites exhibit a much higher dissipated energy level (Figure V-11Figure V-13 and Figure V-15Figure V-14) and an extensive damage zone length. In these materials, crack initiation is detected slightly before the peak of the load-COD curve using similar thresholds of 0.003.

BY NC ND

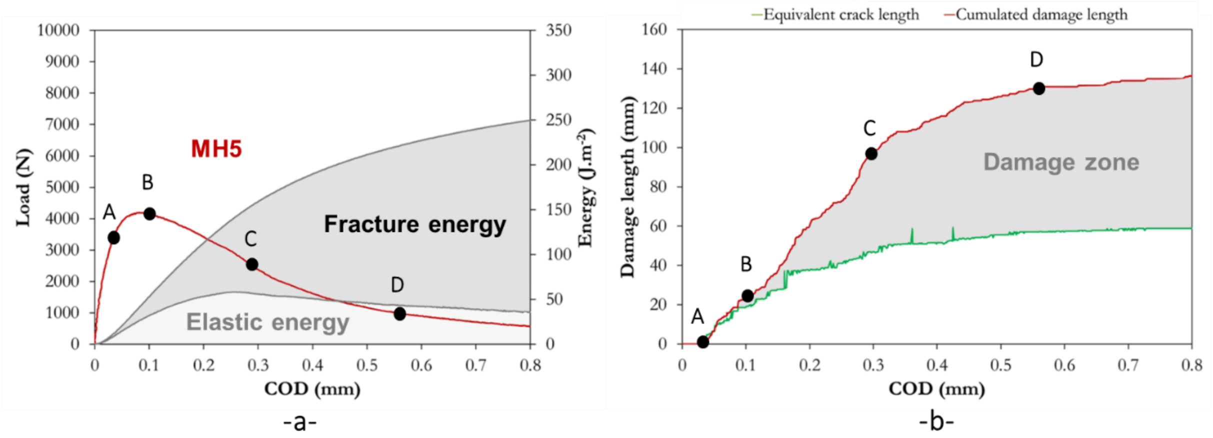

Figure V-11: Fracture behaviour of MH5 a) Load-COD curve and evolution of energy, b) evolution of damage as a function of COD

Indeed, for MH5, damage zone length is estimated to be 80 mm on average, which demonstrates the overall extension of the FPZ. Indeed, the cumulated damage length is quite high due the occurrence of multiple crack branches throughout the experiment. As shown in Figure V-12, the crack branching phenomenon leads to the propagation of three crack branches from the main crack tip at state C.

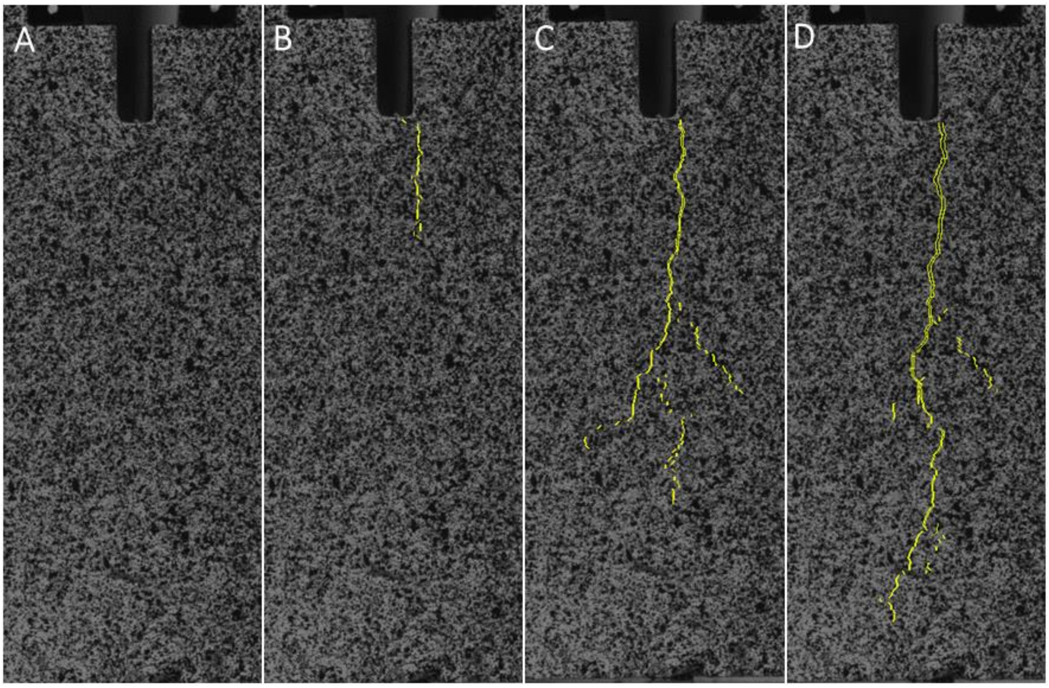

Figure V-12: 2P-DIC images of instantaneous crack propagation of MH5 during a WST

BY NC ND

In state D, crack branches can no longer be seen on the image due to local strain decrease away from the main crack tip. As explained in III.4.4, this is merely a visual artefact since the cumulated damage length takes into account all the cracks that have been observed during the experiment. Moreover, as noted in III.4.4.2, the high deviation angle of some cracks induces difficult detection by 2P-DIC, leading to a slight underestimation of crack length.

The MH15 material exhibits a slightly higher fracture energy and damage zone compared to MH5 according to Figure V-13. In fact, damage zone length for this material is about 110 mm on average.

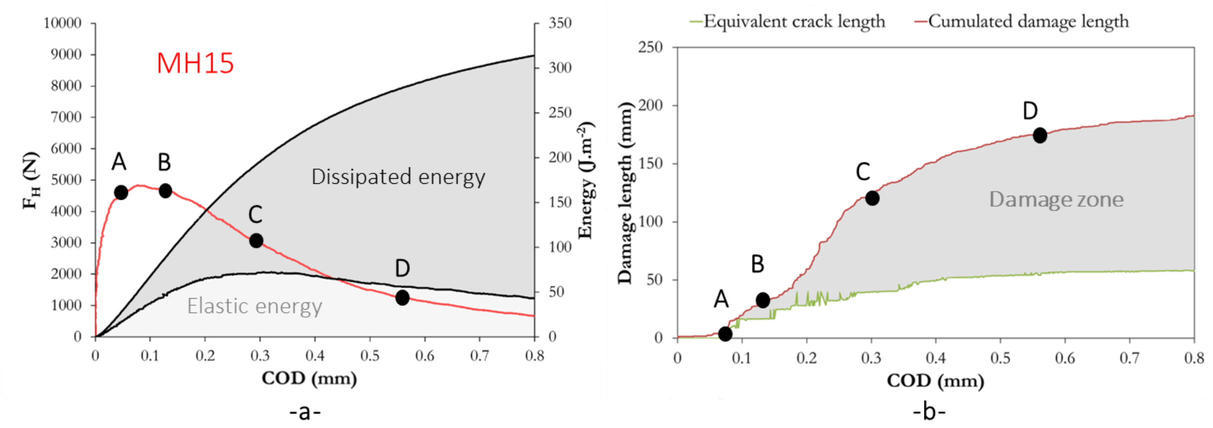

-a- -b-

Figure V-13: Fracture behaviour of MH15 a) Load-COD curve and evolution of energy versus horizontal displacement, b) evolution of damage as a function of COD

Similarly for MH15, crack propagation monitoring (Figure V-14) reveals the crack branching phenomenon along with crack deviations promoted by a higher number of aggregates. The cumulated length suggests that a higher occurrence of crack branching leads to more secondary cracks.

BY NC ND

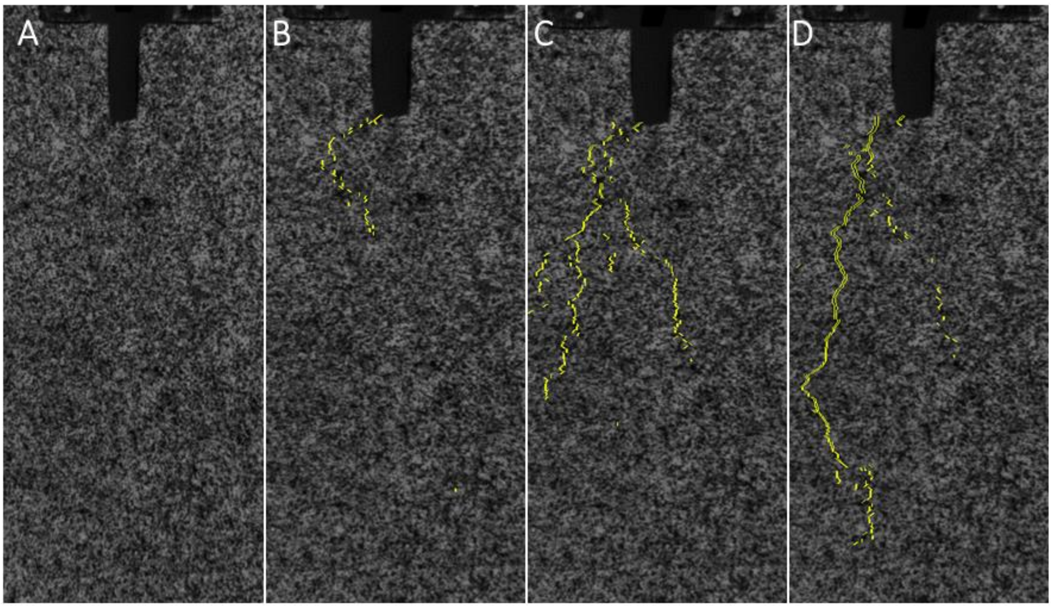

Figure V-14: 2P-DIC images of instantaneous crack propagation of MH15 during a WST

Finally, in accordance with the discussion in the previous section, MH25 exhibits a higher fracture energy along with a higher damage zone length (Figure V-15).

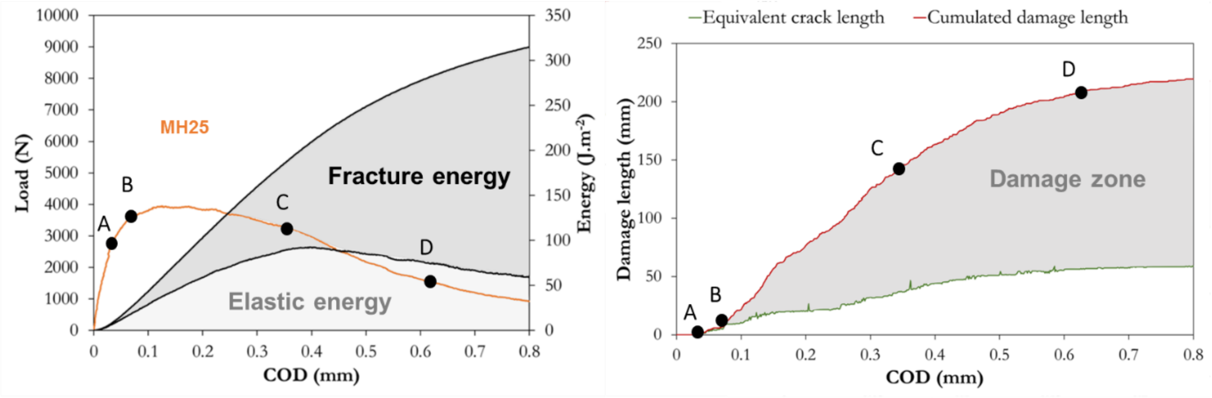

-a- -b-

Figure V-15: Fracture behaviour of MH25 a) Load-COD curve and evolution of energy, b) evolution of damage as a function of COD

From the images in Figure V-16, it is clear that MH25 exhibits extensive crack branching during the experiment. In the same way as for the rest of the materials, secondary cracks contribute strongly to increasing the damage zone length.

BY NC ND

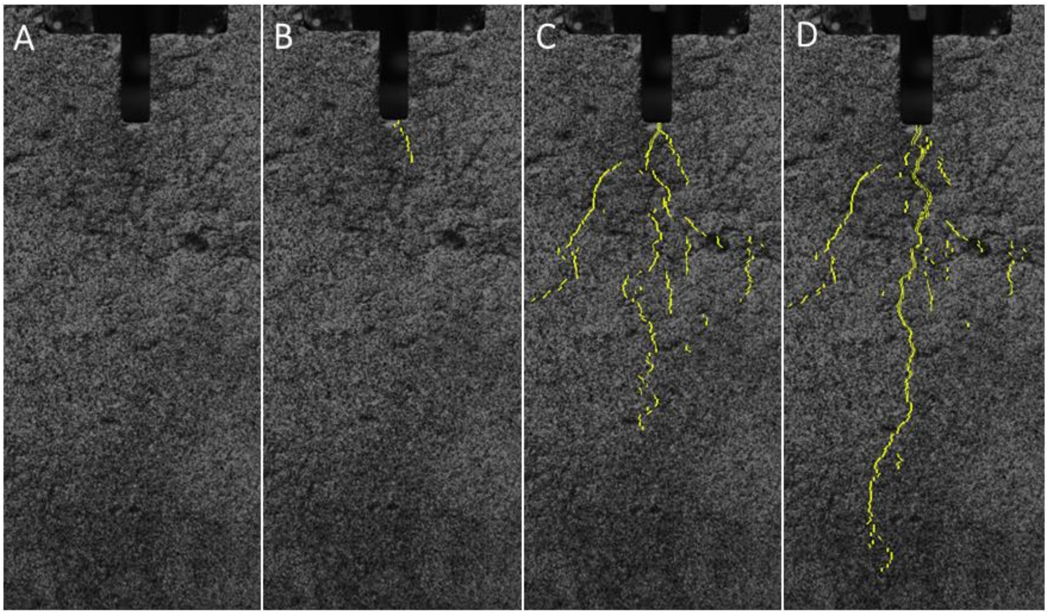

Figure V-16: 2P-DIC images of instantaneous crack propagation of MH25 during a WST

In the end, damage zone length relates to the extent of cracking induced by the frontal process zone throughout the experiment. These crack branches participate directly in the dissipation of elastic energy as they contribute to the tortuosity of the crack path. Additionally, this extensive damage zone length might thereafter increase the effectiveness of the FPZ in improving the crack propagation resistance.

Similar patterns have been observed for MS and MSH composites despite the important microstructural differences that exist between these materials. In fact, in order to observe differences in fracture mechanisms, which might exist given peculiar material microstructures, a finer measurement scale must be considered under an optical microscope or SEM. Such an approach is currently being carried out in the ATHOR European research project using the mini-WST developed by the University of Leoben.

The comparison between Pure MgO and MH materials clearly demonstrates the impact of microcracks initially engineered into the microstructure, whereby crack propagation progressively activates damage mechanisms at the crack tip and leads to further energy dissipation. In this regard, part of the energy is dissipated due to diffuse damage before localised damage takes place when a critical tensile stress is attained locally. Therefore, these results indicate the presence of a much larger process zone size with increasing inclusion fraction.

In the previous section, results demonstrated that MH composites retained strength despite adding more inclusions into the mix, which is presumably inconvenient for optimising the crack

BY NC ND

propagation resistance. Nevertheless, the microstructure of MH composites along with the existence of a network of microcracks are the leading factors in reducing the brittleness of the materials, thereby improving the crack propagation resistance.

From a fracture point of view, the crack propagation resistance of a material is considered to be the result of a good synergy between frontal process zone phenomena and process wake. The latter drives crack propagation resistance increase through crack bridging while the former contributes to the overall extension of FPZ size through diffuse microcracking and crack branching.

In the current approach, the specific fracture energies were calculated by dividing the total area under the load-COD curve by the ligament area. This approach led to some interesting comparisons between the materials while highlighting the impact of the FPZ.

In order to enrich FPZ understanding, a resistance curve (R-curve) analysis will be performed by combining fracture energies and crack lengths measured by 2P-DIC.

V.3.2. Crack propagation resistance of some magnesia-based composites

As discussed in the state of the art in I.2.2.3, R-curves can be used for the analysis of the FPZ. In the standard R-curve calculation approach, a numerical simulation is used to model the evolution of compliance versus an equivalent elastic crack length within the LEFM (Linear Elastic Fracture Mechanics) framework. The equivalent elastic crack, determined using the compliance method [TaPI85], corresponds to the crack length that induces a compliance increase that is similar to experimental observations. Such an approach has been extensively used for materials that exhibit an elastic behaviour with a confined FPZ [KnPa86, TAKK03]. However, limitations to this approach occur when deviations to linear elasticity are observed, which is the case for the materials studied herein. Indeed, as demonstrated in the previous section, the extent of FPZ size is increased by the occurrence of diffuse damage and crack branching phenomenon. Nevertheless, the compliance method has been applied on pure MgO, a material that is assumed to exhibit an elastic mechanical behaviour.

As shown in the example in Figure V-17, even a relatively brittle MgO material with limited non-linearity exhibits much more damage overall than what is obtained using the compliance method.

BY NC ND

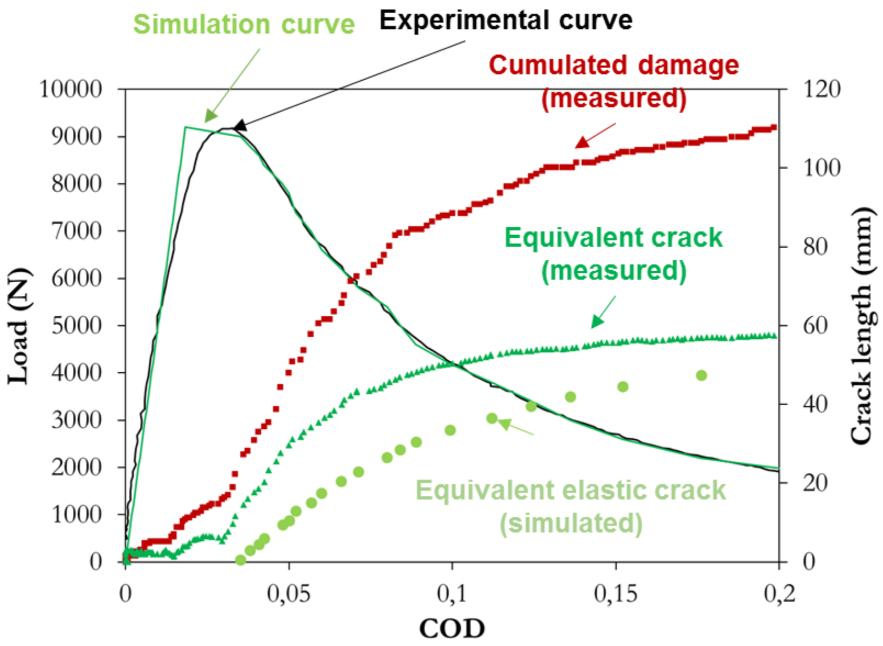

Figure V-17: Comparison of experimental and simulated load displacement curves and the resulting crack lengths for pure MgO

By using a linear elastic model, it is very difficult to achieve a satisfactory fitting between experimental and simulated CODs solely based on Young's modulus in the first part of the curve. This is mainly due to the visible non-linearity of MgO's load-COD curve, which can be associated with the plasticity of this material reported elsewhere in [AMTC18].

Nevertheless, once Young's modulus value is validated, crack length is used to fit experimental and simulated CODs. The resulting equivalent elastic crack length suggests a different evolution from the equivalent crack measured by 2P-DIC. In fact, while both crack lengths reach the same values at the end of the experiment, a clear underestimation of the crack length can be noticed for the simulated crack during FPZ development. Therefore, indirect crack length estimation methods, such as the compliance method, strongly underestimate the crack length of quasi-brittle materials during a WST for instance.

For the rest of the study, crack lengths related to the development of the FPZ will be measured by the 2P-DIC method and used to calculate fracture energies during the WST in a novel approach.

As presented previously in V.3.1, fracture energies were calculated at each loading state by dividing the area under the load-COD curve by the ligament area, which is a constant value calculated from the dimensions of the specimen.

BY NC ND

In the current analysis, the fracture energy will be calculated at each loading state of the WST using the corresponding crack length measured by 2P-DIC. In this sense, the equivalent crack length and cumulated damage length will be used for comparison. This analysis has been applied on model materials that contain 5% of inclusions. The objective of this approach is to evaluate the evolution of the crack propagation resistance of a material and, to a certain extent, the impact of FPZ on fracture energy.

In Figure V-18, the evolution of fracture energy as a function of equivalent crack length can be followed throughout the WST. In this case, the fracture energy is calculated by using the equivalent crack length measured by 2P-DIC as follows:

$$\mathbf{G_{eq,i}} = \frac{1}{\mathbf{L}_{eq,i}.\mathbf{B}}\left(\int_{0}^{\delta_{H,i}} \mathbf{F_H} \,.\, \mathbf{d\delta_H} - \frac{1}{2}.\,\mathbf{F_H\delta_H}\right) \qquad \text{Eq. V.1}$$

Where $L_{eq,i}$ is the equivalent crack length measured by 2P-DIC at a specific loading state i. As a reminder, this length corresponds to a straight crack going down from the bottom of the notch to the detected crack tip and B is the thickness of the WST sample. The grey area at the beginning of loading has been deliberately disregarded due to an unstable evolution of energy.

The overall curves of the materials exhibit the increasing trend that is associated with the rising R-curve effect reported in materials with toughening mechanisms.

BY NC ND

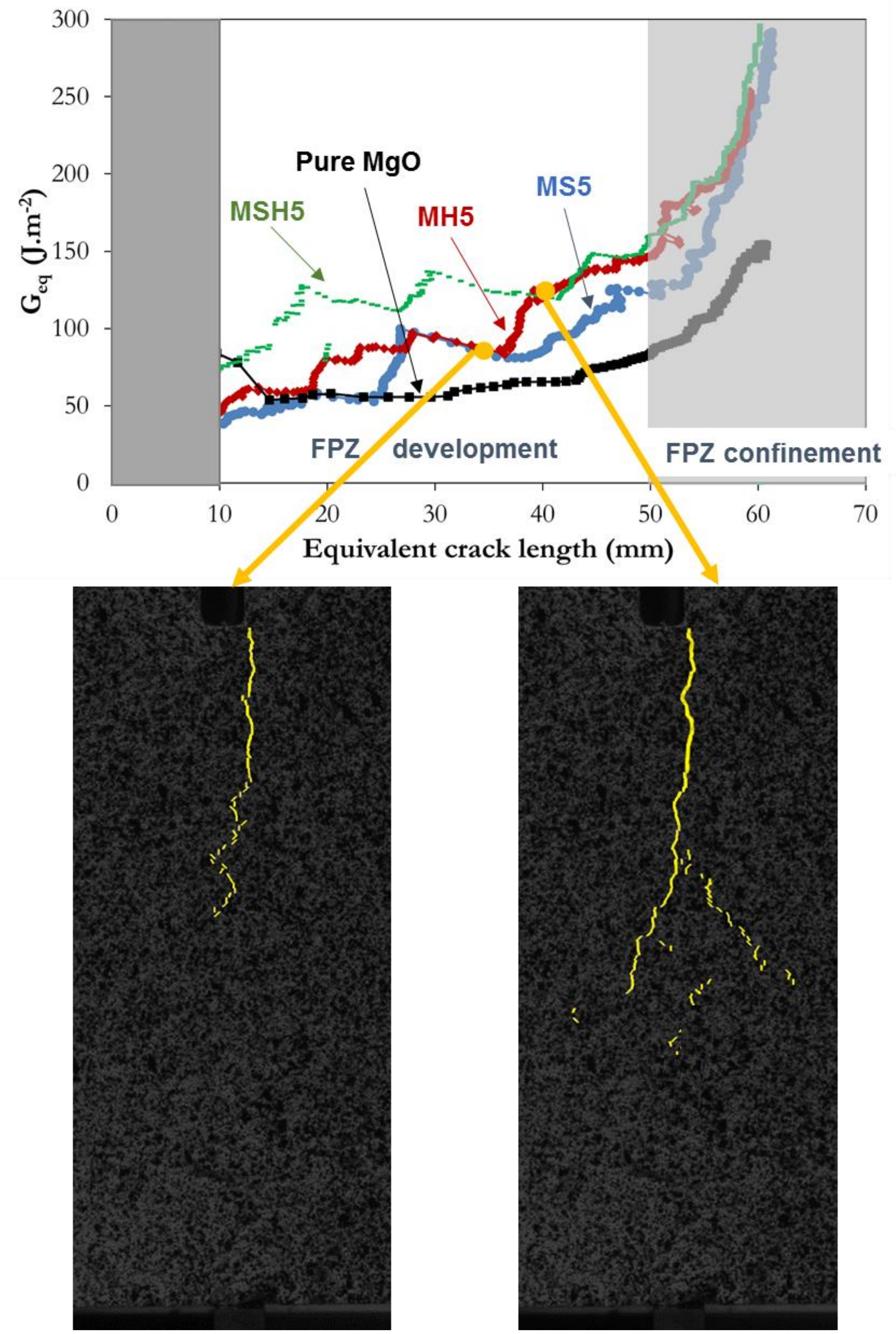

Figure V-18: Evolution of an equivalent fracture energy (G_{eq}) as a function of equivalent crack length for MgO, MS5, MH5 and MSH5 with 2P-DIC images illustrating crack branching in MH5

However, an unstable plateau evolution of fracture energy driven by a repeated increase in energy can be observed during most of the experiment for all materials except MgO. Such an instability has nothing to do with measurement noise but most likely relates to an unstable development of the FPZ. In fact, this increasing trend might be the result of successive FPZ developments as shown in Figure V-18 for MH5, where the crack branching phenomenon occurs. In fact, as noted on the images, no significant evolution of the equivalent crack length is recorded while equivalent fracture energy increases abruptly due to the occurrence of crack branching, which is not taken into account in the present measurement of crack length.

Moreover, when the bottom of the sample is reached at the end of the experiment, an exponential increase of fracture energy occurs. This effect is mostly related to the confinement of the FPZ by the compressive zone above the bottom WST linear support. In fact, the increase starts well before the end of the experiment around an equivalent crack length of 50 mm due to the large size of the compressive zone (Figure III-14). Therefore, geometric and experimental constraints lead to a difficult estimation of crack propagation resistance, especially when a large FPZ is developed.

Nevertheless, materials can be compared based on the fracture energy values prior to FPZ confinement (i.e before FPZ confinement). The highest energies are exhibited by MSH5, MH5, MS5 and then pure MgO respectively.

While the evolutions of fracture energy hint strongly at FPZ developments during the WST, the unstable character of the curves impedes the observation of the characteristic R-curve plateau after an initial increase of fracture energy. Therefore, the influence of FPZ development on fracture energy could hardly be evaluated by relying on the equivalent crack length. Nevertheless, while the latter does not account for damage coming from FPZ phenomena, fracture energy jumps provided essential information. In this sense, by taking into account damage coming from the FPZ using 2P-DIC, a stable plateau can be expected.

Therefore, the cumulated damage length can be used to calculate an effective fracture energy according to Eq.V.2.

$$\mathbf{G_{eff,i}} = \frac{\mathbf{1}}{\mathbf{L}_{\boldsymbol{eff,i}} . \mathbf{B}} \left(\int_{\mathbf{0}}^{\boldsymbol{\delta}_{\mathbf{H,i}}} \mathbf{F_H} \, . \, \mathbf{d}\boldsymbol{\delta}_{\mathbf{H}} - \frac{\mathbf{1}}{\mathbf{2}} . \mathbf{F_H} \boldsymbol{\delta}_{\mathbf{H}} \right) \qquad \text{Eq. V.2}$$

Indeed, by calculating the effective fracture energy, a much more stable plateau can be observed in Figure V-19 after an initial increase during crack propagation. Then, at the end of the experiment fracture energy increases due to FPZ confinement coming from the action of the compressive zone at the bottom of the sample.

BY NC ND

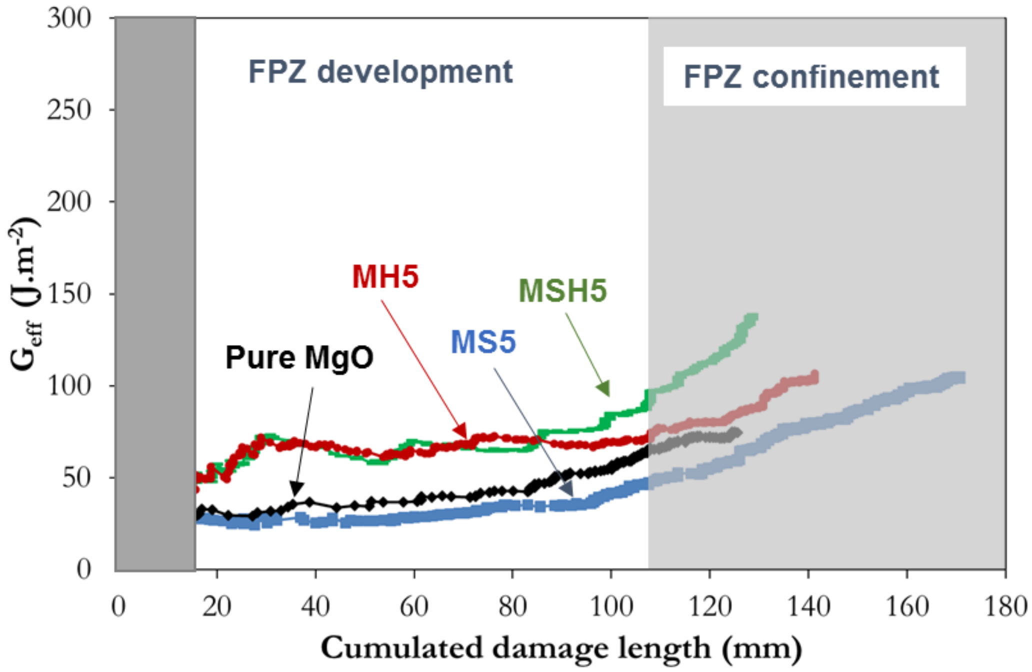

Figure V-19: Evolution of an effective fracture energy (G_{eff}) as a function of cumulated damage length for MgO, MS5, MH5 and MSH5

Using the cumulated damage length, plateau fracture energies are relatively low (around 70 J.m^{-2} for [MH, MSH] and 30 J.m^{-2} for [MgO, MS] given that most macro-cracks resulting from FPZ development are taken into account thanks to 2P-DIC.

Interestingly, effective fracture energy values during the plateau-evolution are quite similar for two groups of materials, namely [MH5; MSH5] and [Pure MgO; MS5]. The former group, which consists of hercynite containing materials, exhibits higher values than the latter. This observation might be a consequence of the microstructure of these materials.

Indeed, as noted previously in IV.2.1 and IV.3, hercynite based materials are likely to contain fine microcracks as opposed to regular spinel. As such, the impact of these fine microcracks might be invisible to the 2P-DIC method at this measurement scale given that some damage related mechanisms occur at a much lower scale. Thus, higher effective fracture energies were measured for MH5 and MSH5. Indeed, if all damage features could be measured, very similar effective fracture energies would be measured for the investigated materials. In essence, fracture energy values could be as low as a few J.m^{-2}, in accordance with the surface energies of the studied materials.

The present analysis underlined the characteristic rising R-curve behaviour that is associated with the full development of the FPZ and its wake. By using 2P-DIC to measure crack propagation features such as crack branching, effective fracture energies could be

BY NC ND

measured for the materials with great accuracy. Nevertheless, given the nature of the material microstructures, especially that of hercynite containing materials, it appears quite clearly that a single measurement at macro-scale is not sufficient to account for all cracking features that consume energy. Ultimately, the R-curve approach makes use of the full potential of 2P-DIC in measuring the evolution of crack propagation resistance, which is an essential material property.

V.4. Conclusion

The fracture behaviour of model materials has been evaluated accurately by coupling the WST with DIC. Strength and fracture energy values highlighted some clear differences between the materials and trends regarding the influence of inclusion nature and fraction. As such, increasing inclusion fraction leads to a decrease of strength while fracture energy increases. This impact has been attributed to the presence of an initial microcrack network in model materials containing inclusions, which leads to the development of a FPZ that consumes energy during crack propagation.

Indeed, the influence of the FPZ has been identified in magnesia-hercynite materials by using the 2P-DIC method, which revealed the presence of crack deviation and the crack branching phenomenon. These two mechanisms are responsible for a large part of the consumed energy during fracture as they lead to the creation of many crack surfaces.

In a more refined analysis, the R-curve approach has been used to provide additional insight on FPZ development in conjunction with the respective microstructures of magnesia-spinel and magnesia-hercynite materials. By following the evolution of an equivalent fracture energy and an effective one, defined using the different crack lengths measured by 2P-DIC, the impact of crack branching on the consumed energy was clearly shown. Moreover, given the presence of a diffusion zone in magnesia-hercynite materials leading to fine microcracks, higher fracture energies were observed for materials containing hercynite.

BY NC ND

General conclusion and perspectives

Thermal shock solicitations can lead to critical consequences for a refractory installation if material properties are not chosen accordingly. Moreover, this phenomenon is difficult to apprehend due to the complexity of thermal shock solicitations. In essence, severe and repeated thermal shocks can lead to brittle fracture, thus, materials with an improved crack propagation resistance are more likely to resist thermal shocks. In order to improve this property, an increased strain-to-rupture and a high level of fracture energy may be used as microstructure design criteria. Hence, materials with a non-linear mechanical behaviour, also known as "flexible" materials, can be considered. For instance, voluntarily introducing a network of microcracks in the initial material microstructure promotes energy dissipating mechanisms during loading, which increases the overall material strain while limiting crack extension.

As one of the key refractory properties, the characterisation of the thermomechanical behaviour and crack propagation resistance have been the main focus of the research work presented in this PhD thesis. In order to achieve this, Digital Image Correlation (DIC) methods have been applied extensively on model materials during fracture experiments.

Magnesia-spinel and magnesia-hercynite materials were specifically designed as model materials with a simplified composition in order to study the impact of inclusion nature (spinel or hercynite) and content (5, 15, 25 wt.%) in the magnesia matrix. In fact, these materials contain microcrack networks due to the thermal expansion mismatch between magnesia matrix and spinel/hercynite inclusions. The influence of this thermally induced damage on the thermomechanical properties of magnesia-spinel materials has been studied extensively in the past, as opposed to magnesia-hercynite. In fact, the latter exhibits enhanced thermal shock resistance according to industrial reports. Therefore, understanding the influence of hercynite on the thermomechanical properties and the fracture behaviour of magnesia-based materials might provide new insight on microstructure design. Especially since spinel and hercynite exhibit rather similar elastic and dilatometric properties.

The fracture behaviour of these model materials was investigated by applying Digital Image Correlation (DIC) methods during Wedge Splitting Tests (WST) in a novel approach. The main idea behind the coupling of sophisticated characterisation methods (DIC) and advanced fracture experiments (WST) was to provide an accurate set of information about model material fracture. Indeed, with a particular attention to experimental conditions, DIC was primarily used to measure crack-opening displacements (COD) during WST experiments, leading to an accurate determination of load-COD curves.

BY NC ND

For fracture monitoring, a refined DIC method, called 2P-DIC has proved to be more suitable than classic DIC for detecting and following crack propagation based on theoretical considerations. In conjunction with this, 2P-DIC proved its effectiveness in detecting cracks and quantifying their length with a very good accuracy during a WST experiment on a magnesia-based material. Indeed, this aspect has been validated by comparison with post-mortem SEM observations of the main crack of a WST sample.

After validating this key experimental step, a series of measurements were performed on model materials in order to understand microstructure-thermomechanical property relationships versus temperature before moving on to the fracture behaviour at room temperature. Mainly, microstructural observations revealed characteristic patterns of damage within model materials. In addition to microcrack networks, magnesia-hercynite materials contained extensive diffusion zones around hercynite aggregates, which included spinel solid-solutions and multiple fine microcracks. In essence, materials containing spinel had mostly large microcracks while magnesia-hercynite had both large microcracks and finer, more numerous, microcracks within diffusion zones.

The impact of thermal damage occurrence was highlighted through a hysteretic evolution of Young’s modulus versus temperature, a lower thermal expansion coefficients and a high level of acoustic emission hits during cooling. While increasing inclusion fractions led to lower Young’s modulus at room temperature, inclusion nature had a pronounced impact on its high temperature evolution. Indeed, the hysteretic evolution of Young’s modulus relied mainly on microcrack network characteristics and the ability of the microstructure to close them, at least partly, during heating. In this sense, it was difficult for materials containing only regular spinel inclusions to recover higher Young’s modulus values at high temperature, contrarily to hercynite containing materials. This difference was attributed mainly to the presence of the so-called diffusion zone in materials containing hercynite, leading to finer interconnected microcrack networks that are easier to heal at high temperature, especially as extensive diffusion occurs between magnesia grains and hercynite aggregates.

The implications of an initially engineered network of microcracks on the fracture behaviour were clearly observed during WST experiments at room temperature. In this sense, increasing inclusion fractions led to lower strength, higher fracture energies and thus, a reduced brittleness as expected. The application of 2P-DIC enabled the observation of characteristic energy consuming mechanisms, such as the crack branching phenomenon, during WST. It was shown that higher inclusion fractions led to a more significant development of the Fracture Process Zone (FPZ) through damage lengths measured by 2P-DIC.

BY NC ND

Moreover, the impact of diffuse damage and FPZ development resulting from an initial microcrack network was investigated in a refined Resistance-curve (R-curve) analysis. Effective fracture energy evolutions demonstrated a dual tendency, one for materials containing only spinel and one for those with hercynite inclusions. In light of this, it has been concluded that diffuse damage in materials containing hercynite had an important energetic contribution at micro-scale alongside FPZ phenomena acting on a macro-scale.

These tendencies were again confirmed, this time under thermal cycling using a novel thermal shock experiment. Essentially, materials containing hercynite had a superior resistance to crack propagation as the extension of the main crack was limited by diffuse damage and FPZ phenomena.

Thanks to the coupling of sophisticated characterisation methods (DIC) and advanced fracture experiments (WST), novel fracture analyses were developed and applied to understand the influence of microcrack networks on crack propagation resistance. From this approach, key microstructure design patterns were discussed based on the investigation of different model materials.

In association with the research work presented in this PhD, many perspectives can be foreseen and considered as a prospect. From a material science point of view, further investigating the impact of hercynite in magnesia materials could provide new microstructure design patterns for an enhanced crack propagation resistance. Indeed, given the significant influence of the diffusion zone on thermomechanical properties, this phenomenon still needs further investigation to build a better understanding of its impact, especially on the fracture behaviour.

In hindsight, DIC and 2P-DIC measurements provided essential information on crack propagation but much of the information relating to the extent of process zone influence is yet to be unveiled by experiments at one observation scale. One way could be to produce very fine speckle patterns in combination with a very high camera resolution to observe more details about fracture during a WST at macro-scale. Otherwise, the mini-WST fracture experiment developed by Montanuniversitat (Leoben, Austria), can be performed under an optical microscope or SEM in order to observe, at a very fine scale, the micro-damage processes that contribute to increasing fracture energy in a non-negligible way. These mechanisms can then be linked directly to the microstructure and provide very useful insight on material design for improving crack propagation resistance. In combination with this, the crack detection algorithm of 2P-DIC must be enhanced, especially when cracks deviate in an almost horizontal way.

BY NC ND

Furthermore, given that refractories are employed at high temperature, usually above 1000°C, it would be interesting to conduct fracture experiments in combination with DIC and 2-DIC at those temperatures. In this study, DIC and 2P-DIC have been applied mostly at room temperature due to the complexity of coupling high temperature experiments with optical methods. Indeed, the application of DIC and 2P-DIC at high temperature would require the development of a temperature resistant speckle pattern while ensuring stable experimental conditions, which is difficult to achieve. These experiments would enable the observation of the main fracture processes during crack propagation at high temperature. Nevertheless, as part of an ongoing European research program (ATHOR), brazillian tests have been successfully coupled with 2P-DIC at high temperature.

The advanced characterisation of the fracture behaviour of refractories would require the development of sophisticated measurement methods and experiments to enhance the understanding of refractory thermal shock resistance. In this perspective, some preliminary thermal cycling experiments have been performed during this PhD within the framework of the novel ATHORNA device (Advanced measurements for in-situ THermomechanical mORitoring of large samples uNder thermal gradient), as presented in Annex B : Application of 2P-DIC in a novel thermal shock test bed. Model materials investigated under the ATHORNA device were subjected to laser solicitations that induce thermal gradients within the sample, while optical cameras and an infrared camera were used to monitor damage occurrence and strains.

Preliminary experiments have shown promising results in the monitoring of cracks originating from thermal shocks in different model materials (pure MgO, MS5 and MH5). In the comparisons that were made, MS5 and MH5 in particular demonstrated a limited extension of the main crack as opposed to brittle pure MgO. In fact, these experiments confirmed the strong relationship between an initially microcracked microstructure and an improved fracture behaviour, leading to a higher resistance to thermal cycling. These first encouraging results may serve as a basis for future developments of the ATHORNA device, such as optimising the laser sequence for more robust experimental conditions and highly accurate comparisons between the investigated materials. Moreover, the implementation of acoustic emission sensors coupled with the existing 2P-DIC method can lead to a highly effective fracture characterisation. In the end, the ATHORNA device may be a very appropriate thermal shock test bed for the validation of refractory thermomechanical behaviour laws.

BY NC ND

Annex A : Marker tracking method

This non-contact optical method has been mainly used for local displacement and strain measurements [RTVD01, BrVD05]. It is particularly well adapted for the monitoring of the boundary conditions of mechanical tests [BGGD12]. One simply needs to draw as many marker points, on the sample or loading device, as necessary for the measurement. Thus, each marker point can be followed to obtain displacements. Moreover, a high contrast between the markers and the support on which they will be defined needs to be achieved in order to perform accurate measurements (i.e: White markers on black background and vice versa). The experimental setup for the application of the marker tracking method is shown in Figure A-1.

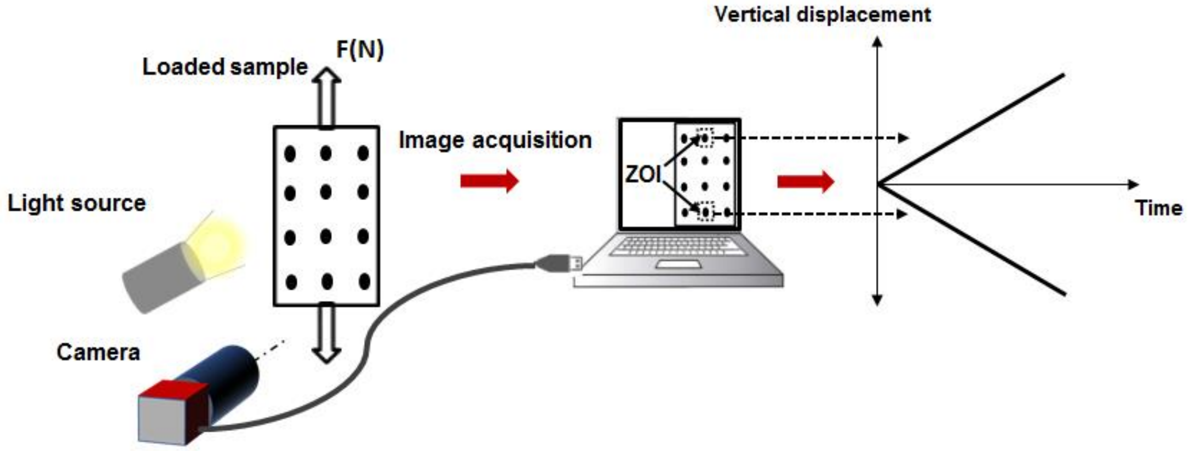

Figure A-1: Experimental setup for the application of the marker tracking method

Once the markers are defined physically on the support, a threshold needs to be applied on the images to enhance marker definition for optimal measurement accuracy. The displacements are calculated from the geometric centres of markers (x_g,y_g), which are pondered by grey levels. The coordinates of the geometric centres (x_g,y_g) can be calculated according to the following equations:

$$\begin{cases} x_g = \dfrac{\sum_i \sum_j x(i,j)(I(i,j) - I_S)}{\sum_i \sum_j (I(i,j) - I_S)} \\ \\ y_g = \dfrac{\sum_i \sum_j y(i,j)(I(i,j) - I_S)}{\sum_i \sum_j (I(i,j) - I_S)} \end{cases}$$

CC BY NC ND

Where x(i,j) and y(i,j) are pixel coordinates, I(I,j) the light intensity of the pixel and I_S the lower limit of the light intensity. The latter can be considered as a threshold that is used to distinguish the marker from the background throughout the measurement. This value is usually defined at the beginning of the analysis and is usually kept constant if no significant change of contrast occurs between the different images.

BY NC ND

Annex B : Application of 2P-DIC in a novel thermal shock test bed

As part of an ongoing experimental development around in-situ thermal shock characterisation of refractories, a novel thermal shock test bed involving photomechanical and acoustic emission measurement tools has been designed in a previous research program (SFERA-II). The current developments are now being carried out under ATHORNA, the new research project, which is the acronym of “Advanced measurements for in-situ THermomechanical mORitoring of large samples uNder thermal gradient”. The main objective of ATHORNA and in particular, the test bed, is to validate thermomechanical behaviour laws of refractory materials destined for thermal shock applications by subjecting samples to a thermal gradient while measuring, in-situ, the thermal and strain fields using infrared and optical cameras respectively.

Within the ATHORNA project, a special attention is given to ensure that optical measurements of strain fields and crack patterns are accurate and reliable in the current approach. Therefore, in order to validate this crucial aspect, measurements have been performed on model materials presented herein using appropriate experimental conditions, which will be presented in the following. Moreover, throughout the analysis, numerical simulations have been performed by Rafael Oliveira (PhD from the ATHOR project) to support experimental data.

B.1: Experimental setup

The experimental setup of the ATHORNA thermal shock test bed is described in Figure B-1. Acoustic emission sensors, optical cameras and an infrared camera are used to monitor damage occurrence and strains coming from laser solicitations applied from above a disk sample. The disk sample is positioned on three isostatic points, whereby the laser focuses the top face and the bottom of the sample faces the cameras.

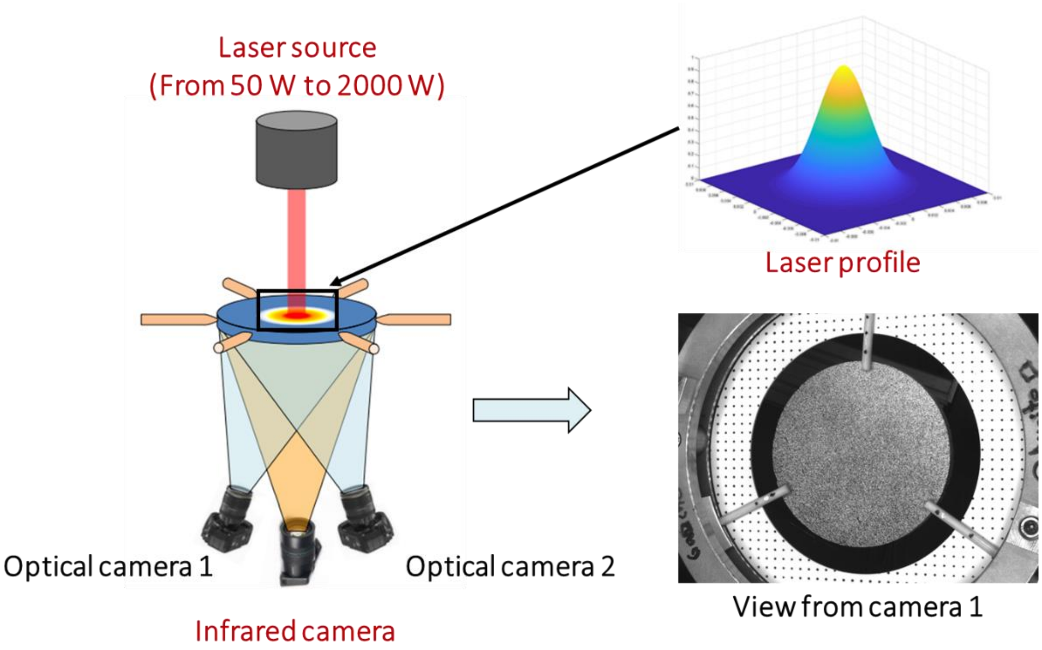

Figure B-1: Experimental setup of the ATHORNA thermal shock test bed

At this stage of development of the ATHORNA setup, only optical cameras and an infrared camera have been implemented along with a CO_2 laser source provided by ILP Laser. The laser serves as a heating source for a disk-shaped sample (Ø 100 mm and a thickness of 10 mm in this study).

A large laser profile has been privileged by removing focalisation lenses in the setup, leading to a laser diameter of 16 mm. This way, heating takes place over a larger zone in the middle of the sample to avoid overheating in the centre and brutal thermal gradients. The stereovision system consisting of two optical cameras can be used to provide out-of-plane displacements and 2D strain fields within the bottom surface.

In the current study, focus is on 2D measurements and especially crack monitoring by 2P-DIC. Therefore, images of the disk-shaped sample coming from one camera only will be analysed using DIC and 2P-DIC. The disk sample is subjected to a well-defined laser sequence that will be presented next.

B.2: Laser sequence and resulting thermal/mechanical fields of thermal shock experiments

The main purpose of the ATHORNA thermal shock experiment is to induce thermal gradients within the disk sample that lead to fracture in a progressive way. Therefore, starting from room temperature, a sufficiently low laser power (50 W) is applied initially and then incremented by 25 W at each cycle. Each cycle corresponds to a laser pulse that lasts 30 seconds in order to heat the sample, and then 60 seconds of off time are taken to observe a thermal gradient in the sample.

The laser sequence is presented in Figure B-2, with laser power starting at 50 W and going up to 400 W with an increment of 25 W at each cycle. This way, fracture could be monitored at each cycle throughout the laser sequence and comparisons can be made.

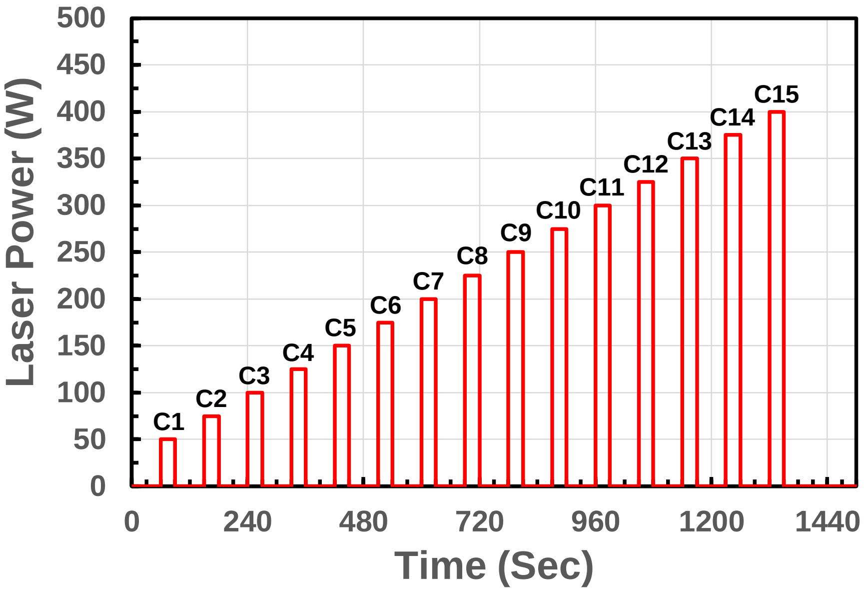

Figure B-2: Description of the laser sequence used for thermal shock experiments

As a result of laser application at the top surface of the sample, a thermal gradient is expected to take place within the thickness of the sample as well as between the middle and the periphery of the top face. In order to validate this and evaluate the temperature at the top face, numerical simulations have been performed on an industrial alumina-spinel material as part of preliminary studies. The numerical model was first validated by temperature measurements at the bottom face by the infrared camera as shown in Figure B-3.a.

BY NC ND

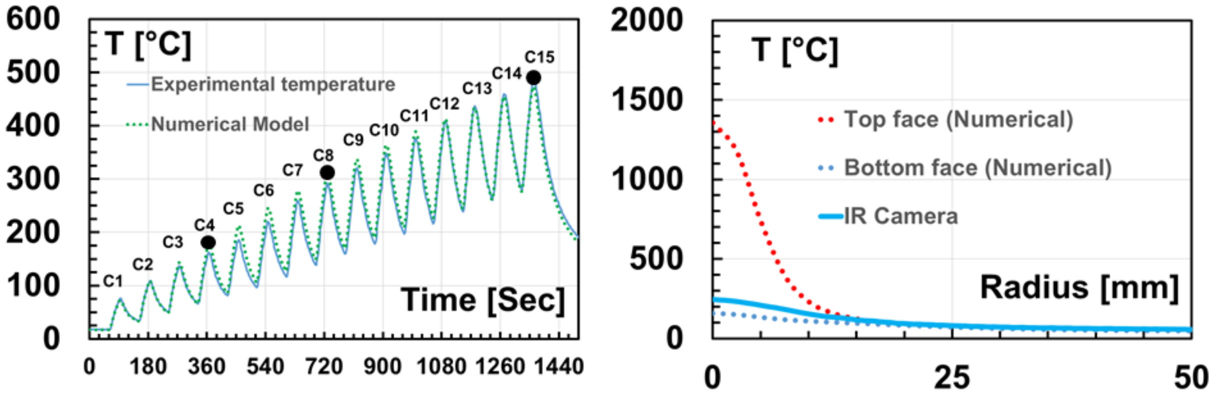

-a-

-b-

Figure B-3: Comparison of experimental and simulated temperatures for an alumina-spinel material: a) measured in a central zone for the whole experiment and b) measured profile along the radius of the sample

Indeed, a very good agreement is obtained between experimental and numerical temperature evaluations at the bottom face of the sample throughout the experiment. Moreover, from Figure B-3.b, the temperature profile along the radius of the sample has been reported using simulated and experimental data. It appears, as noted previously, that there is indeed a thermal gradient between the top face and bottom one, but also between the centre and the border.

In order to evaluate the impact of these thermal gradients for a given experiment, a preliminary analysis has been performed on an aluminium sample using marker tracking to measure thermomechanical strains. Firstly, principal strain fields (ε_{11} and ε_{22}) on the bottom face of the sample were calculated by diagonalization of (εxx, εyy, εxy) strains field measured by marker tracking. Then, the orientation of these first principal strains was compared to x and y axes using the angle α in Figure B-4.a.

BY NC ND

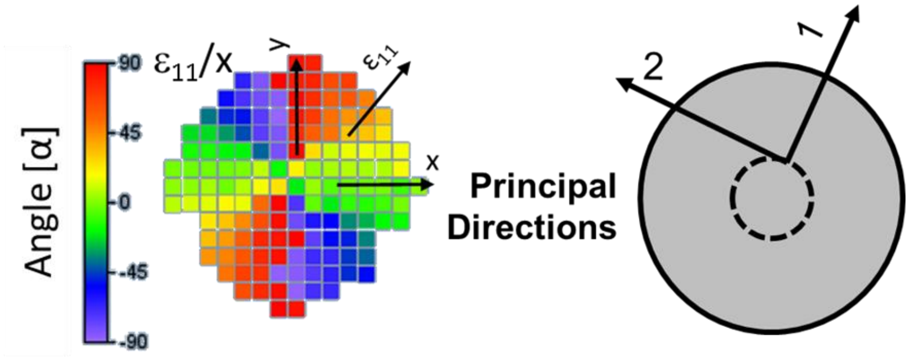

-a- -b-

Figure B-4: a) Diagram of the orientation of first principal stress compared to the x and y axes and b) Schematic of the two principal directions

From this analysis it can be concluded that the first principal stress has a radial direction while the second principal strain has an orthoradial direction (Figure B-4.b).

Moreover, as shown in Figure B-5, mechanical strain fields can be calculated by subtracting thermal strain associated with dilatation from the overall thermomechanical strain. The thermal strain was calculated using $\varepsilon_{th}=(\Delta T^{*}\alpha)$, where α is the thermal expansion.

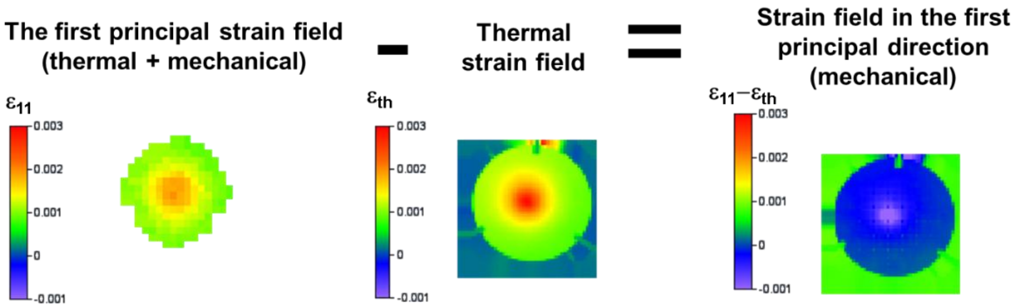

Figure B-5: Calculation of the mechanical strain field in the first principal direction by decoupling the total strain and thermal strain fields for an aluminium sample

This way, the nature of the first principal strain field has been evaluated over the bottom face of the sample. Thus, it can be observed that the centre of the sample is in compression while the stress in the periphery becomes close to zero. From these calculations, the second principal strain, which is orthoradial, is also expected to be in compression in the middle of the sample but in tension in the periphery. Taking this into account, crack initiation is very likely to occur starting from the periphery of the sample and moving towards the centre.

BY NC ND

Thanks to thermomechanical simulations performed by PhD candidate Rafael Oliveira from the ATHOR project, these experimental considerations have been validated using appropriate material properties and behaviour laws. From Figure B-6, the distribution of orthoradial secondary principal stresses can be visualised over a quarter of the sample for two cycles, namely C4 and C8 (as reported back in Figure B-3).

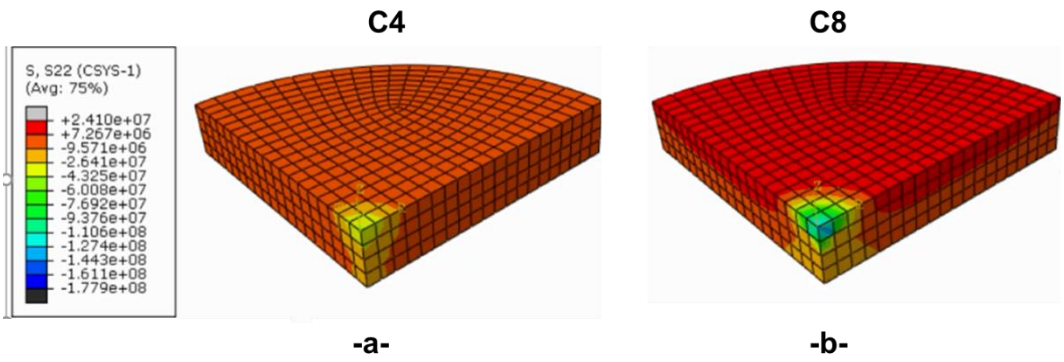

Figure B-6: Secondary principal stress obtained from numerical simulation in a) C4 and b) C8

Indeed, as suggested earlier, orthoradial compressive stresses at the centre and orthoradial tensile stresses in the periphery can be expected at the top of each thermal cycle, especially after C4 (where stress amplitude increases gradually with laser power i.e cycles).

B.3: Crack propagation monitoring of some magnesia-based composites during thermal shock experiments

After these preliminary validation steps, the ATHORNA experiments have been performed on model materials, namely pure MgO, MS5 and MH5. The main objective behind these experiments was to compare the fracture behaviour of these materials based on the laser sequence defined in Figure B-2. Therefore, 2P-DIC measurements have been performed to monitor crack propagation during specific laser cycles, namely C4, C8 and C15.

In Figure B-7, the evolution of temperature in a central zone at the bottom of the sample versus time can be followed along with laser power relating to the different laser cycles for all the three materials.

BY NC ND

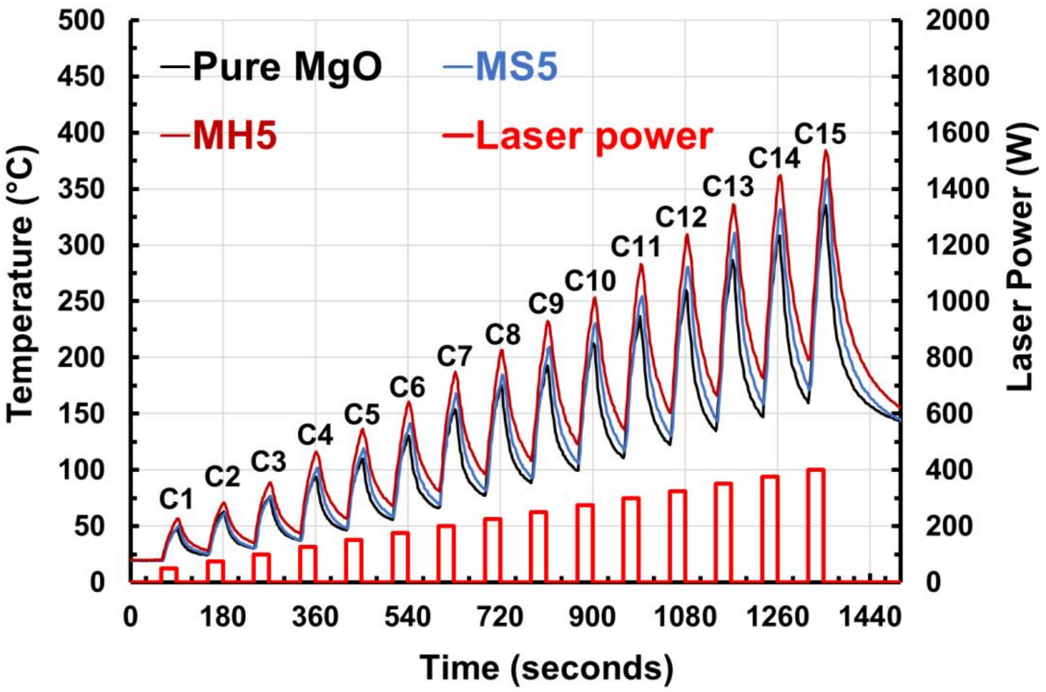

Figure B-7: Evolution of measured bottom temperature for Pure MgO, MS5 and MH5 during the experiment

The same evolution can be noticed for all materials with some slight differences in maximal temperatures at each cycle, especially for MH5 as it exhibits the highest values. These differences might be the result of different material thermal properties, and emissivity in particular. In this sense, darker materials such as MH5 tend to absorb more heat leading to higher temperatures recorded by the infrared camera, as observed in the graph from Figure B-7. Despite these slight differences, it can be considered that the materials have been submitted to similar experimental conditions, allowing for a proper comparison of their fracture behaviours.

As explained in the previous section, the thermal gradient responsible for critical tensile stresses results from the large temperature difference between the middle and the periphery on top of the disk sample where the laser is applied. Indeed, this is confirmed by the crack patterns observed in Figure B-8 for MgO, MS5 and MH5, where the crack initiates from the border of the disk-shaped sample.

BY NC ND

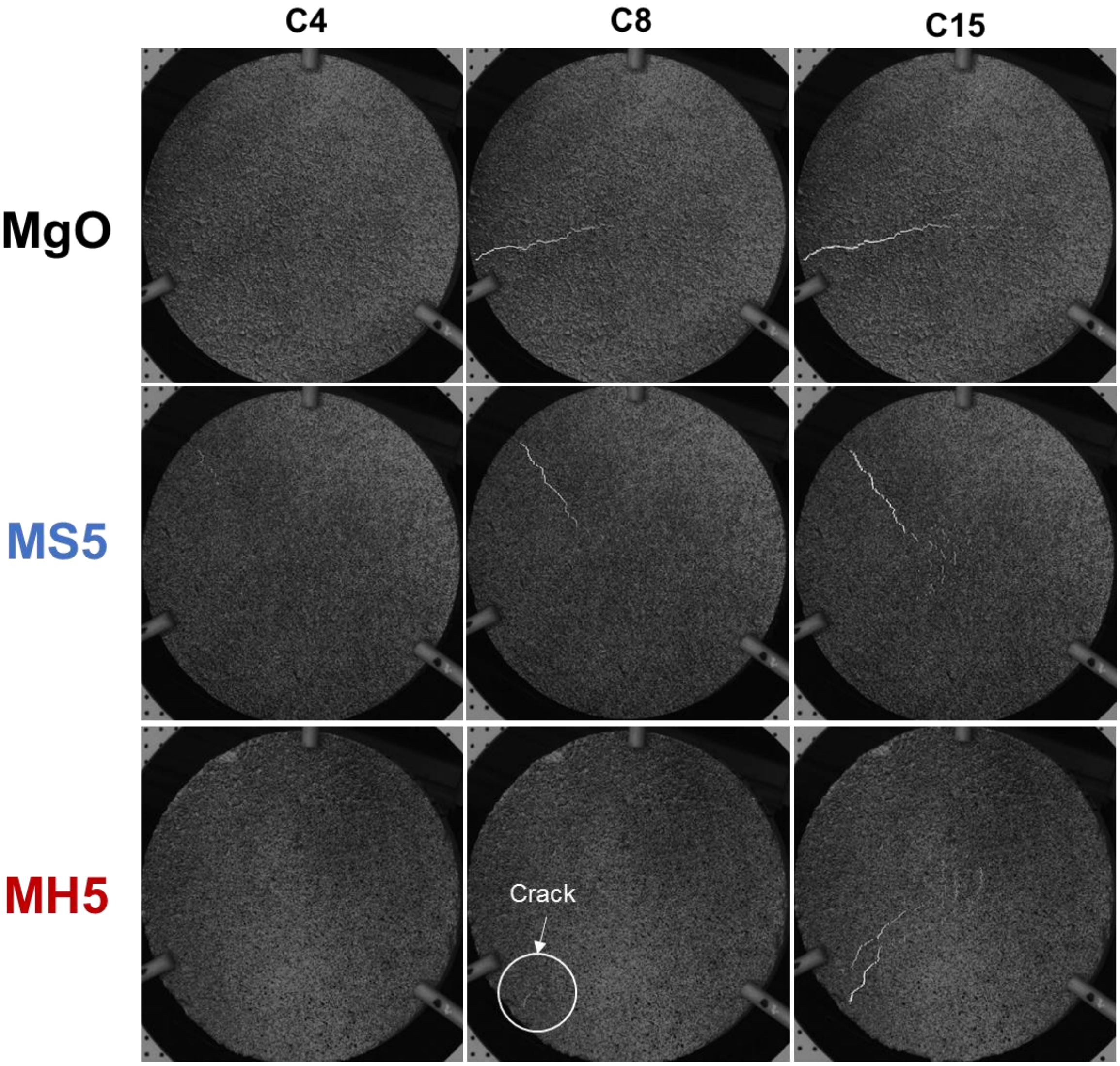

Figure B-8: 2P-DIC images of Pure MgO, MS5 and MH5 showing crack propagation at the top of C4, C8 and C15

As shown in the 2P-DIC images, no crack can be observed in C4 in any of the materials. It is only starting from C8 that cracks are revealed but with different propagation lengths. In fact, during C8, different observations can be made regarding the tortuosity of the crack and its relative position to the centre of the sample. For MgO and MS5 some crack tortuosity can be noticed as the crack has almost reached the centre of the sample at this stage. In contrast, the crack has barely propagated for MH5 at this loading stage.

At the end of the experiment, in C15, cracks have reached the central zone of all three materials where different patterns can be noted for each material. In fact, approximately from the position of the crack tip, the crack propagated farthest for MgO, followed by MS5 then MH5. For MgO the crack propagated in a relatively straight fashion towards the centre while MS5

BY NC ND

and MH5 in particular exhibit some secondary cracks that limit the extension of the main crack. Indeed, secondary cracks that occur in the middle of the sample are most likely induced by the thermal gradient between the top and the bottom of the sample, as discussed previously.

In association with the previous figure showing 2P-DIC images, the evolution of instantaneous crack lengths can be followed in Figure B-9. The crack lengths follow a cyclic evolution similar to the actual thermal cycling. Therefore, crack length increases at the top of the thermal cycle and then decreases at the bottom of the cycle. This artefact, discussed in detail previously in III.4.4, is mainly due to local strain decrease below the pseudo-strain threshold used in the 2P-DIC crack detection process. In this case, this feature results from thermal unloading that leads to a lower strain.

Moreover, the half-diameter of the sample has been reported on the graph (Figure B-9) using green dashed lines for an easier association with the 2P-DIC images shown previously.

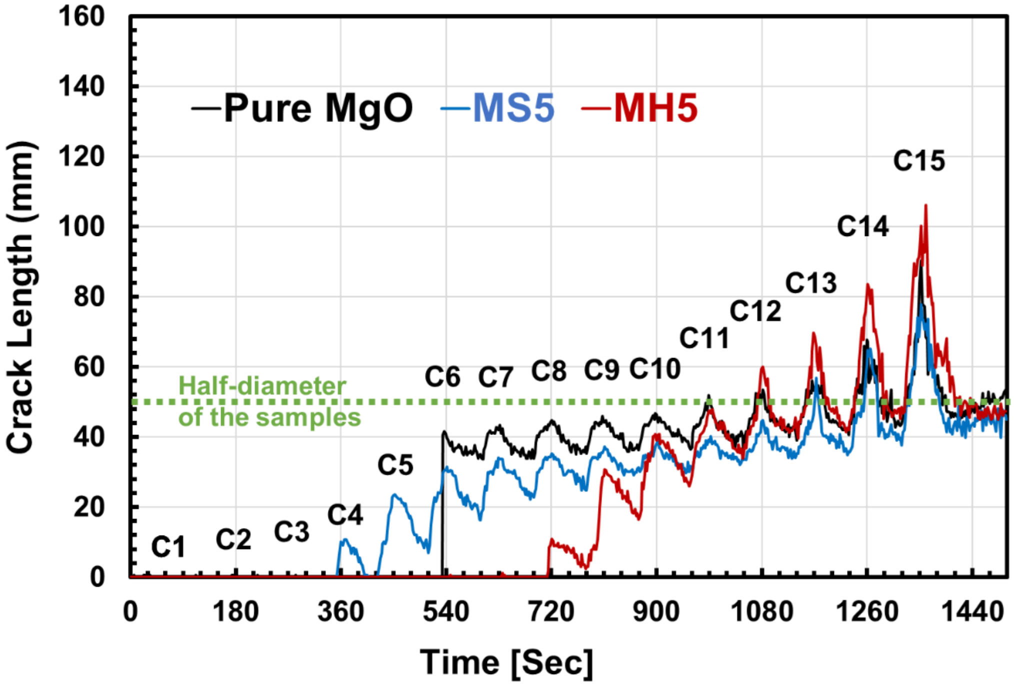

Figure B-9: Evolution of instantaneous crack length measured by 2P-DIC for Pure MgO, MS5 and MH5 during the different thermal cycles

Indeed, based on these two figures (Figure B-8 and B-9), clear differences can be noted between the fracture behaviour of the materials.

For pure MgO, crack occurs in a relatively brittle way starting from C6 and attains a length of over 45 mm up to C8, almost reaching the centre of the sample. After C8, crack propagation

BY NC ND

is rather slow until the end of the experiment, where crack length reaches 90 mm due to the occurrence of diffuse cracks in the middle.

In the case of MS5, as expected from the quasi-brittle behaviour of this material and the lower strength exhibited during WST, the crack occurs earlier starting from C4. Indeed, from WST results and Young's modulus of MS5, a lower fracture initiation resistance was expected. Moreover, from crack length evolution, crack propagation is much slower compared to pure MgO. From Figures B-8 and B-9, a lower overall crack extension is observed at C15 since the main crack stops before reaching the middle of the sample, with some secondary cracks forming around the centre of the sample as usual.

For MH5, the crack initiates later compared to MgO and MS5, at C8. In fact, as discussed previously in V.3.2 and given the presence of finer microcracks within the microstructure of this material (IV.2.1), it is strongly believed that diffuse damage, which is not perceived by 2P-DIC at this scale, plays a major role in delaying the occurrence of the main crack. After C8, the crack propagates in a stable way until the end of the experiment at C15. Moreover, a stronger increase of crack length can be noted from one cycle to the other compared to other materials. This leads to a relatively high crack length value at the end of the experiment. In fact, from Figure B-8, crack propagation at stages C8 and C15 can be compared. Only a small crack has propagated in C8 while in C15 numerous cracks can be observed with very limited main crack extension. In comparison to pure MgO and MS5, MH5 exhibits the highest crack propagation resistance under increasing thermal gradients.

In the end, the comparison of different materials highlights some interesting differences in terms of crack propagation, especially considering brittle pure MgO and quasi-brittle MS5 and MH5. These observations were quite in line with previous results and discussions regarding the thermomechanical and fracture behaviour of these model materials.

In future developments, further optimisation of experimental conditions may be considered to enhance the monitoring of fracture by 2P-DIC. Moreover, the implementation of acoustic emission sensors can provide quantitative information on the amount and the localisation of cracks during an experiment. Coupled with 2P-DIC, the instrumentation around ATHORNA device may provide a powerful validation experiment for the evaluation of thermal shock resistance of various refractory materials.

BY NC ND

References

[ARRW04] Aksel, C., Rand, B., Riley, F.L., Warren, P.D., 2004. Thermal shock behaviour of magnesia–spinel composites. J. Eur. Ceram. Soc. 24, 2839–2845.

[ARRW02] Aksel, C., Rand, B., Riley, F.L., Warren, P.D., 2002. Mechanical properties of magnesia-spinel composites. J. Eur. Ceram. Soc. 22, 745–754.

[AkWa03] Aksel, C., Warren, P.D., 2003. Work of fracture and fracture surface energy of magnesia-spinel composites. Compos. Sci. Technol. 63, 1433–1440.

[AkWR04] Aksel, C., Warren, P.D., Riley, F.L., 2004. Fracture behaviour of magnesia and magnesia–spinel composites before and after thermal shock. J. Eur. Ceram. Soc. 24, 2407–2416.

[AmBu88] Amazigo, J.C., Budiansky, B., 1988. Interaction of particulate and transformation toughening. J. Mech. Phys. Solids 36, 581–595.

[ABDD13] Amiot, F., Bornert, M., Doumalin, P., Dupré, J.-C., Fazzini, M., Orteu, J.-J., Poilâne, C., Robert, L., Rotinat, R., Toussaint, E., Wattrisse, B., Wienin, J.S., 2013. Assessment of Digital Image Correlation Measurement Accuracy in the Ultimate Error Regime: Main Results of a Collaborative Benchmark. Strain 49, 483–496.

[AMTC18] Amodeo, J., Merkel, S., Tromas, C., Carrez, P., Korte-Kerzel, S., Cordier, P., Chevalier, J., 2018. Dislocations and Plastic Deformation in MgO Crystals: A Review.

[AnIs95] Anderson, O.L., Isaak, D.G., 1995. Elastic constants of mantle minerals at high temperature. Miner. Phys. Crystallogr. Handb. Phys. Constants 2, 64–97.

[BMCH17] Barhli, S.M., Mostafavi, M., Cinar, A.F., Hollis, D., Marrow, T.J., 2017. J-Integral Calculation by Finite Element Processing of Measured Full-Field Surface Displacements. Exp. Mech. 57, 997–1009.

[BaSo01] Bartha, P., Sodje, J., 2001. Degradation of refractories in rotary cement kilns fired with waste fuels. CN Refract. 5, 62–71.

[BaKa91] Bažant, Z.P., Kazemi, M.T., 1991. Size dependence of concrete fracture energy determined by RILEM work-of-fracture method. Int. J. Fract. 51, 121–138.

[BaPl97] Bazant, Z.P., Planas, J., 1997. Fracture and Size Effect in Concrete and Other Quasibrittle Materials. CRC Press.

[BMTM12] Becker, T.H., Mostafavi, M., Tait, R.B., Marrow, T.J., 2012. An approach to calculate the J-integral by digital image correlation displacement field measurement. Fatigue Fract. Eng. Mater. Struct. 35, 971–984.

[Belr15] Belrhiti, Y., 2015. Etude de matériaux réfractaires à comportement mécanique non linéaire par mesure de champs de déformations (thesis). Limoges.

[BGGD12] Belrhiti, Y., Gallet-Doncieux, A., Germaneau, A., Doumalin, P., Dupre, J.C., Alzina, A., Michaud, P., Pop, I.O., Huger, M., Chotard, T., 2012. Application of optical methods to investigate the non-linear asymmetric behavior of ceramics exhibiting large strain to rupture by four-points bending test. J. Eur. Ceram. Soc. 32, 4073–4081.

[BHCP14] Belrhiti, Y., Huger, M., Chotard, T., Pop, O., Germaneau, A., Doumalin, P., Christophe Dupré, J., 2014. Characterization of the Mechanical Behavior of Magnesia Spinel Refractories Using Image Correlation. Int. J. Appl. Ceram. Technol. 11.

[BPGD15] Belrhiti, Y., Pop, O., Germaneau, A., Doumalin, P., Dupré, J.C., Harmuth, H., Huger, M., Chotard, T., 2015. Investigation of the impact of micro-cracks on fracture behavior of magnesia products using wedge splitting test and digital image correlation. J. Eur. Ceram. Soc. 35, 823–829.

[BeHR05] Bergonnier, S., Hild, F., Roux, S., 2005. Digital image correlation used for mechanical tests on crimped glass wool samples. J. Strain Anal. Eng. Des. 40, 185–197.

[BeHR06] Besnard, G., Hild, F., Roux, S., 2006. “Finite-Element” Displacement Fields Analysis from Digital Images: Application to Portevin–Le Châtelier Bands. Exp. Mech. 46, 789–803.

[BHRC17] Bomarito, G.F., Hochhalter, J.D., Ruggles, T.J., Cannon, A.H., 2017. Increasing accuracy and precision of digital image correlation through pattern optimization. Opt. Lasers Eng. 91, 73–85.

[BoKP85] Bornhauser, A., Kromp, K., Pabst, R.F., 1985. R-curve evaluation with ceramic materials at elevated temperatures by an energy approach using direct observation and compliance calculation of the crack length. J. Mater. Sci. 20, 2586–2596.

BY NC ND

[Boss13] Bossuyt, S., 2013. Optimized Patterns for Digital Image Correlation, in: Jin, H., Sciammarella, C., Furlong, C., Yoshida, S. (Eds.), Imaging Methods for Novel Materials and Challenging Applications, Volume 3, Conference Proceedings of the Society for Experimental Mechanics Series. Springer New York, pp. 239–248.

[BMMV14] Bouville, F., Maire, E., Meille, S., Van de Moortèle, B., Stevenson, A.J., Deville, S., 2014. Strong, tough and stiff bioinspired ceramics from brittle constituents. Nat. Mater. 13, 508–514.

[Brad04] Bradt, R.C., 2004. Fracture of Refractories, in: Refractories Handbook. CRC Press, pp. 11–38.

[Bray85] Bray, D.J., 1985. Toxicity of Chromium Compounds Formed in Refractories. Am. Ceram. Soc. Bull. 64, 1012–1016.

[BCDD11] Brémand, F., Cottron, M., Doumalin, P., Dupré, J.-C., Germaneau, A., Valle, V., 2011. Mesures en mécanique par méthodes optiques [WWW Document]. Ref TIP673WEB - Mes. Mécaniques Dimens.

[BrVD05] Bretagne, N., Valle, V., Dupré, J.C., 2005. Development of the marks tracking technique for strain field and volume variation measurements. NDT E Int. 38, 290–298.

[BTHC08] Briche, G., Tessier-Doyen, N., Huger, M., Chotard, T., 2008. Investigation of the damage behaviour of refractory model materials at high temperature by combined pulse echography and acoustic emission techniques. J. Eur. Ceram. Soc. 28, 2835–2843.

[BrSr66] Brown, W., Srawley, J., 1966. Plane Strain Crack Toughness Testing of High Strength Metallic Materials. Plane Strain Crack Toughness Test. High Strength Met. Mater.

[BMSP89] Bruck, H.A., McNeill, S.R., Sutton, M.A., Peters, W.H., 1989. Digital image correlation using Newton-Raphson method of partial differential correction. Exp. Mech. 29, 261–267.

[BrWi90a] Brühwiler, E., Wittmann, F.H., 1990. The wedge splitting test, a new method of performing stable fracture mechanics tests. Eng. Fract. Mech., Special Issue Fracture and Damage of Concrete and Rock 35, 117–125.

[BrWi90b] Brühwiler, E., Wittmann, F.H., 1990. The wedge splitting test, a new method of performing stable fracture mechanics tests. Eng. Fract. Mech., Special Issue Fracture and Damage of Concrete and Rock 35, 117–125.

[BKIP08] Bussiba, A., Kupiec, M., Ifergane, S., Piat, R., Böhlke, T., 2008. Damage evolution and fracture events sequence in various composites by acoustic emission technique. Compos. Sci. Technol. 68, 1144–1155.

[Ceau04] Ceausescu-Ersen, E.A., 2004. Application de la technique d'émission acoustique à la caractérisation de matériaux céramiques évolutifs (thesis). Limoges.

[CZZH10] Chen, J., Zhang, X., Zhan, N., Hu, X., 2010. Deformation measurement across crack using two-step extended digital image correlation method. Opt. Lasers Eng., Micro and Nano Metrology in Experimental Mechanics 48, 1126–1131.

[CSLH08] Chotard, T., Soro, J., Lemercier, H., Huger, M., Gault, C., 2008. High temperature characterisation of cordierite–mullite refractory by ultrasonic means. J. Eur. Ceram. Soc. 28, 2129–2135.

[ChRS85] Chu, T.C., Ranson, W.F., Sutton, M.A., 1985. Applications of digital-image-correlation techniques to experimental mechanics. Exp. Mech. 25, 232–244.

[CBHF17] Cinar, A.F., Barhli, S.M., Hollis, D., Flansbjer, M., Tomlinson, R.A., Marrow, T.J., Mostafavi, M., 2017. An autonomous surface discontinuity detection and quantification method by digital image correlation and phase congruency. Opt. Lasers Eng. 96, 94–106.

[CoHo82] Cooper, S.C., Hodson, P.T.A., 1982. Magnesia-magnesium aluminate spinel as a refractory. Trans J Br Ceram Soc 81, 12.

[CrBD13] Crammond, G., Boyd, S.W., Dulieu-Barton, J.M., 2013. Speckle pattern quality assessment for digital image correlation. Opt. Lasers Eng. 51, 1368–1378.

[DaGH17] Dai, Y., Gruber, D., Harmuth, H., 2017. Determination of the fracture behaviour of MgO-refractories using multi-cycle wedge splitting test and digital image correlation. J. Eur. Ceram. Soc. 37, 5035–5043.

[DaFF88] Dal Maschio, R., Fabbri, B., Fiori, C., 1988. Industrial applications of refractories containing magnesium aluminate spinel. Ind. Ceram. 8, 121–126.

[Davi79] Davidge, R.W., 1979. Mechanical Behaviour of Ceramics. CUP Archive.

[DZXZ16] Ding, X., Zhao, H., Xiang, Z., Zhang, H., He, Q., Li, J., 2016. Effect of hercynite content on the properties of magnesia-spinel composite refractories sintered in different atmospheres. Ceram. Int. 42, 19058–19062.

BY NC ND

[DDBK17] Dupré, J.-C., Doumalin, P., Belrhiti, Y., Khlifi, I., Pop, O., Huger, M., 2017. Detection of cracks in refractory materials by an enhanced digital image correlation technique. J. Mater. Sci. 53.

[DDHG15] Dupré, J.C., Doumalin, P., Husseini, H.A., Germaneau, A., Brémand, F., 2015. Displacement Discontinuity or Complex Shape of Sample: Assessment of Accuracy and Adaptation of Local DIC Approach. Strain 51, 391–404.

[DNRC13] Dusserre, G., Nazaret, F., Robert, L., Cutard, T., 2013. Applicability of image correlation techniques to characterise asymmetric refractory creep during bending tests. J. Eur. Ceram. Soc. 33, 221–231.

[EuHu60] Eusner, G.R., Hubble, D.H., 1960. Technology of Spinel-Bonded Periclase Brick. J. Am. Ceram. Soc. 43, 292–297.

[Evan90]Evans, A.G., 1990. Perspective on the Development of High-Toughness Ceramics. J. Am. Ceram. Soc. 73, 187–206.

[Evan76]Evans, A.G., 1976. On the formation of a crack tip microcrack zone. Scr. Metall. 10, 93–97.

[EvFa84] Evans, A.G., Faber, K.T., 1984. Crack-Growth Resistance of Microcracking Brittle Materials. J. Am. Ceram. Soc. 67, 255–260.

[EvHe80] Evans, A.G., Heuer, A.H., 1980. REVIEW—Transformation Toughening in Ceramics: Martensitic Transformations in Crack-Tip Stress Fields. J. Am. Ceram. Soc. 63, 241–248.

[FaBH13] Fagerholt, E., Børvik, T., Hopperstad, O.S., 2013. Measuring discontinuous displacement fields in cracked specimens using digital image correlation with mesh adaptation and crack-path optimization. Opt. Lasers Eng. 51, 299–310.

[FaGZ07] Fan, H.J., Gösele, U., Zacharias, M., 2007. Formation of nanotubes and hollow nanoparticles based on Kirkendall and diffusion processes: a review. Small Weinh. Bergstr. Ger. 3, 1660–1671.

[Fei95] Fei, Y., 1995. Thermal expansion. Miner. Phys. Crystallogr. Handb. Phys. Constants 2, 29–44.

[Gang16] Gangnant, A., 2016. Étude de la rupture quasi-fragile d’un béton à l’échelle mésoscopique : aspects expérimentaux et modélisation (thesis). Bordeaux.

[GaPL85] Gault, C., Platon, F., Le Bras, D., 1985. Ultrasonic measurements of Young’s modulus of Al2O3-based refractories at high temperatures. Mater. Sci. Eng. 74, 105–111.

[GoGS78] Gogotsi, G.A., Groushevsky, Ya.L., Strelov, K.K., 1978. The significance of non-elastic deformation in the fracture of heterogeneous ceramic materials. Ceramurg. Int. 4, 113–118.

[Gour16] Gouraud, F., 2016. Influence des transformations de phase de la zircone sur le comportement thermomécanique de réfractaires à très haute teneur en zircone (thesis). Limoges.

[Gras11] Grasset-Bourdel, R., 2011. Structure/property relations of magnesia-spinel refractories : experimental determination and simulation (thesis). Limoges.

[GAHC13] Grasset-Bourdel, R., Alzina, A., Huger, M., Chotard, T., Emler, R., Gruber, D., Harmuth, H., 2013. Tensile behaviour of magnesia-spinel refractories: Comparison of tensile and wedge splitting tests. J. Eur. Ceram. Soc. 33, 913–923.

[GAHG12] Grasset-Bourdel, R., Alzina, A., Huger, M., Gruber, D., Harmuth, H., Chotard, T., 2012. Influence of thermal damage occurrence at microstructural scale on the thermomechanical behaviour of magnesia–spinel refractories. J. Eur. Ceram. Soc. 32, 989–999.

[GrTa21] Griffith A.A., Taylor G.I., 1921. VI. The phenomena of rupture and flow in solids. Philos. Trans. R. Soc. Lond. Ser. Contain. Pap. Math. Phys. Character 221, 163–198.

[GLTC14] Guo, X., Liang, J., Tang, Z., Cao, B., Yu, M., 2014. High-temperature digital image correlation method for full-field deformation measurement captured with filters at 2600°C using spraying to form speckle patterns. Opt. Eng. 53, 063101.

[GuPR05] Guo, Z., Palco, S., Rigaud, M., 2005. Reaction Characteristics of Magnesia–Spinel Refractories with Cement Clinker. Int. J. Appl. Ceram. Technol. 2, 327–335.

[HRKT96] Harmuth, H., Rieder, K., Krobath, M., Tschegg, E., 1996. Investigation of the nonlinear fracture behaviour of ordinary ceramic refractory materials. Mater. Sci. Eng. A 214, 53–61.

[HaTs97] Harmuth, H., Tschegg, E.K., 1997. A Fracture Mechanics Approach for the Development of Refractory Materials with Reduced Brittleness. Fatigue Fract. Eng. Mater. Struct. 20, 1585–1603.

[HaSh63] Hashin, Z., Shtrikman, S., 1963. A variational approach to the theory of the elastic behaviour of multiphase materials. J. Mech. Phys. Solids 11, 127–140.

[HaSh62] Hashin, Z., Shtrikman, S., 1962. On some variational principles in anisotropic and nonhomogeneous elasticity. J. Mech. Phys. Solids 10, 335–342.

[Hass85]Hasselman, D.P.H., 1985. Thermal stress resistance of engineering ceramics. Mater. Sci. Eng., Proceedings of the International Symposium on Engineering Ceremics 71, 251–264.

[Hass69]Hasselman, D.P.H., 1969. Unified Theory of Thermal Shock Fracture Initiation and Crack Propagation in Brittle Ceramics. J. Am. Ceram. Soc. 52, 600–604.

[Hass63]Hasselman, D.P.H., 1963. Elastic Energy at Fracture and Surface Energy as Design Criteria for Thermal Shock. J. Am. Ceram. Soc. 46, 535–540.

[Helm08] Helm, J.D., 2008. Digital Image Correlation for Specimens with Multiple Growing Cracks. Exp. Mech. 48, 753–762.

[HiRo06]Hild, F., Roux, S., 2006. Digital Image Correlation: from Displacement Measurement to Identification of Elastic Properties – a Review. Strain 42, 69–80.

[HoEG75] Hoagland, R.G., Embury, J.D., Green, D.J., 1975. On the density of microcracks formed during the fracture of ceramics. Scr. Metall. 9, 907–909.

[HoBr85]Homeny, J., Bradt, R.C., 1985. Aggregate distribution effects on the mechanical properties and thermal shock behaviour of model monolithic refractory systems. Adv. Ceram. 13, 110.

[HuFG02] Huger, M., Fargeot, D., Gault, C., 2002. High-temperature measurement of ultrasonic wave velocity in refractory materials. High Temp. High Press. 34, 193–201.

[HTCG07] Huger, M., Tessier-Doyen, N., Chotard, T., Gault, C., 2007. Microstructural Effects Associated to CTE Mismatch for Enhancing the Thermal Shock Resistance of Refractories: Investigation by High Temperature Ultrasounds. Ceram Forum Int 84, 93–102.

[Huss14]Husseini, H.A., 2014. Adaptation de la méthode de corrélation d’images numériques pour la gestion des discontinuités du milieu et de la transformation (thesis). Poitiers.

[Irwi57] Irwin G. R., 1957. Analysis of Stresses and Strains near the End of a Crack Traversing a Plate. J. Appl. Mech. Vol. E24, 351–369.

[JSBS17] Jastrzębska, I., Szczerba, J., Błachowski, A., Stoch, P., 2017. Structure and microstructure evolution of hercynite spinel (Fe2+ Al2 O4) after annealing treatment. Eur. J. Mineral. 62–71.

[JCYL15] Jiang, P., Chen, J., Yan, M., Li, B., Su, J., Hou, X., 2015. Morphology characterization of periclase–hercynite refractories by reaction sintering. Int. J. Miner. Metall. Mater. 22, 1219–1224.

[JiBr05] Jin, H., Bruck, H.A., 2005. Pointwise Digital Image Correlation Using Genetic Algorithms. Exp. Tech. 29, 36–39.

[JiLK08] Jin, H., Lu, W.-Y., Korellis, J., 2008. Micro-scale deformation measurement using the digital image correlation technique and scanning electron microscope imaging. J. Strain Anal. Eng. Des. 43, 719–728.

[JCCS17] Justo, J., Castro, J., Cicero, S., Sánchez-Carro, M.A., Husillos, R., 2017. Notch effect on the fracture of several rocks: Application of the Theory of Critical Distances. Theor. Appl. Fract. Mech. 90, 251–258.

[Kane00] Kaneyasu, A., 2000. Trends of basic refractories raw materials-magnesia aggregates for chrome-free bricks. Taikabutsu Overseas 245–248.

[King55] Kingery, W.D., 1955. Factors Affecting Thermal Stress Resistance of Ceramic Materials. J. Am. Ceram. Soc. 38, 3–15.

[KnPa86] Knight, J.C., Page, T.F., 1986. Mechanical Properties of Highly Porous Ceramics. I. Modulus of Rupture and Fracture Toughness. Trans J Br Ceram Soc 85, 27–35.

[Lang79]Lange, F.F., 1979. Fracture Toughness of Si3N4 as a Function of the Initial α-Phase Content. J. Am. Ceram. Soc. 62, 428–430.

[LCHB74] Larson, D.R., Coppola, J.A., Hasselman, D.P.H., Bradt, R.C., 1974. Fracture Toughness and Spalling Behavior of High-Al2O3 Refractories. J. Am. Ceram. Soc. 57, 417–421.

[LPRH09] Leclerc, H., Périé, J.-N., Roux, S., Hild, F., 2009. Integrated Digital Image Correlation for the Identification of Mechanical Properties, in: Gagalowicz, A., Philips, W. (Eds.), Computer Vision/Computer Graphics CollaborationTechniques, Lecture Notes in Computer Science. Springer Berlin Heidelberg, pp. 161–171.

[LSBS06] Lecompte, D., Smits, A., Bossuyt, S., Sol, H., Vantomme, J., Van Hemelrijck, D., Habraken, A.M., 2006. Quality assessment of speckle patterns for digital image correlation. Opt. Lasers Eng. 44, 1132–1145.

BY NC ND

[LeLH15] Leplay, P., Lafforgue, O., Hild, F., 2015. Analysis of Asymmetrical Creep of a Ceramic at 1350°C by Digital Image Correlation. J. Am. Ceram. Soc. 98, 2240–2247.

[LRMB12] Leplay, P., Réthoré, J., Meille, S., Baietto, M.-C., 2012. Identification of asymmetric constitutive laws at high temperature based on Digital Image Correlation. J. Eur. Ceram. Soc., Fracture and Reliability of Ceramics and Hybrid Materials 32, 3949–3958.

[LRMB11] Leplay, P., Réthoré, J., Meille, S., Baietto, M.-C., 2011. Identification of damage and cracking behaviours based on energy dissipation mode analysis in a quasi-brittle material using digital image correlation. Int. J. Fract. 171, 35.

[LiBr89] Li, Z., Bradt, R.C., 1989. Micromechanical Stresses in SiC-Reinforced Al2O3 Composites. J. Am. Ceram. Soc. 72, 70–77.

[LWZX08] Liang, X., Wang, X., Zhuang, Y., Xu, B., Kuang, S., Li, Y., 2008. Formation of CeO2−ZrO2 Solid Solution Nanocages with Controllable Structures via Kirkendall Effect. J. Am. Chem. Soc. 130, 2736–2737.

[LLYT12] Liu, G., Li, N., Yan, W., Tao, G., Li, Y., 2012. Composition and structure of a composite spinel made from magnesia and hercynite. J. Ceram. Process. Res. 13, 480–485.

[LuCS94] Luo, P.-F., Chao, Y.J., Sutton, M.A., 1994. Application of stereo vision to three-dimensional deformation analyses in fracture experiments. Opt. Eng. 33, 981–991.

[LCSP93] Luo, P.F., Chao, Y.J., Sutton, M.A., Peters, W.H., 1993. Accurate measurement of three-dimensional deformations in deformable and rigid bodies using computer vision. Exp. Mech. 33, 123–132.

[MCSZ16] Mao, W.G., Chen, J., Si, M.S., Zhang, R.F., Ma, Q.S., Fang, D.N., Chen, X., 2016. High temperature digital image correlation evaluation of in-situ failure mechanism: An experimental framework with application to C/SiC composites. Mater. Sci. Eng. A 665, 26–34.

[MZMS15] Mazzoleni, P., Zappa, E., Matta, F., Sutton, M.A., 2015. Thermo-mechanical toner transfer for high-quality digital image correlation speckle patterns. Opt. Lasers Eng. 75, 72–80.

[MVCL99] McCusker, L.B., Von Dreele, R.B., Cox, D.E., Louër, D., Scardi, P., 1999. Rietveld refinement guidelines. J. Appl. Crystallogr. 32, 36–50.

[Mige11] Migeon, C., 2011. Émission acoustique et analyse vibratoire pour l’étude des défauts de roulements pour différents régimes moteurs 130.

[MoUl03] Mokrzycki, E., Uliasz-Bocheńczyk, A., 2003. Alternative fuels for the cement industry. Appl. Energy 74, 95–100.

[Naka65] Nakayama, J., 1965. Direct Measurement of Fracture Energies of Brittle Heterogeneous Materials. J. Am. Ceram. Soc. 48, 583–587.

[Naka64] Nakayama, J., 1964. A Bending Method for Direct Measurement of Fracture Energy of Brittle Material. Jpn. J. Appl. Phys. 3, 422.

[NaAB81] Nakayama, J., Abe, H., Bradt, R.C., 1981. Crack Stability in the Work-of-Fracture Test: Refractory Applications. J. Am. Ceram. Soc. 64, 671–675.

[NHVV11] Nguyen, T.L., Hall, S.A., Vacher, P., Viggiani, G., 2011. Fracture mechanisms in soft rock: Identification and quantification of evolving displacement discontinuities by extended digital image correlation. Tectonophysics, Thermo-Hydro-Chemo-Mechanical Couplings in Rock Physics and Rock Mechanics 503, 117–128.

[NiGS06] Nievoll, J., Guo, Z., Shi, S., 2006. Performance of magnesia hercynite bricks in large chinese cement rotary kilns, in: RHI Bulletin. Presented at the RHI Bulletin, pp. 15–17.

[Orte09] Orteu, J.-J., 2009. 3-D computer vision in experimental mechanics. Opt. Lasers Eng., Optical Measurements 47, 282–291.

[PaWL10] Pan, B., Wang, Z., Lu, Z., 2010. Genuine full-field deformation measurement of an object with complex shape using reliability-guided digital image correlation. Opt. Express 18, 1011–1023.

[PFLR74] Papadakis, E.P., Fowler, K.A., Lynnworth, L.C., Robertson, A., Zysk, E.D., 1974. Ultrasonic measurements of Young’s modulus and extensional wave attenuation in refractory metal wires at elevated temperatures with application to ultrasonic thermometry. J. Appl. Phys. 45, 2409–2420.

[PYKP17] Park, J., Yoon, S., Kwon, T.-H., Park, K., 2017. Assessment of speckle-pattern quality in digital image correlation based on gray intensity and speckle morphology. Opt. Lasers Eng. 91, 62–72.

BY NC ND

[PPMH10] Patapy, C., Proust, A., Marlot, D., Huger, M., Chotard, T., 2010. Characterization by acoustic emission pattern recognition of microstructure evolution in a fused-cast refractory during high temperature cycling. J. Eur. Ceram. Soc. 30, 3093–3101.

[PBPC18] Pelissari, P.I.B.G.B., Bouville, F., Pandolfelli, V.C., Carnelli, D., Giuliani, F., Luz, A.P., Saiz, E., Studart, A.R., 2018. Nacre-like ceramic refractories for high temperature applications. J. Eur. Ceram. Soc. 38, 2186–2193.

[Peru00] Peruzzi, S., 2000. Simulation numérique du comportement thérmomécanique de pièces réfractaires de coulée continue (thesis). Limoges.

[PeRa82] Peters, W.H., Ranson, W.F., 1982. Digital Imaging Techniques In Experimental Stress Analysis. Opt. Eng. 21, 213427.

[PRSC83] Peters, W.H., Ranson, W.F., Sutton, M.A., Chu, T.C., Anderson, J., 1983. Application Of Digital Correlation Methods To Rigid Body Mechanics. Opt. Eng. 22, 226738.

[Pine92] Pineau, A., 1992. Global and Local Approaches of Fracture — Transferability of Laboratory Test Results to Components, in: Argon, A.S. (Ed.), Topics in Fracture and Fatigue. Springer New York, New York, NY, pp. 197–234.

[PoBa10] Poissant, J., Barthelat, F., 2010. A Novel “Subset Splitting” Procedure for Digital Image Correlation on Discontinuous Displacement Fields. Exp. Mech. 50, 353–364.

[Popo99] Popov, E.P., 1999. Engineering Mechanics of Solids, 2nd Edition, 2nd Edition. ed. Prentice Hall.

[RéRH07] Réthoré, J., Roux, S., Hild, F., 2007. From pictures to extended finite elements: extended digital image correlation (X-DIC). Comptes Rendus Mécanique 335, 131–137.

[Rice68] Rice, J.R., 1968. A Path Independent Integral and the Approximate Analysis of Strain Concentration by Notches and Cracks. J. Appl. Mech. 35, 379–386.

[Rice81] Rice, R.W., 1981. Mechanisms of Toughening in Ceramic Matrix Composites, in: Proceedings of the 5th Annual Conference on Composites and Advanced Ceramic Materials: Ceramic Engineering and Science Proceedings. John Wiley & Sons, Ltd, pp. 661–701.

[Riet69] Rietveld, H., 1969. A profile refinement method for nuclear and magnetic structures. J. Appl. Crystallogr. 2, 65–71.

[RNCO07] Robert, L., Nazaret, F., Cutard, T., Orteu, J.-J., 2007. Use of 3-D Digital Image Correlation to Characterize the Mechanical Behavior of a Fiber Reinforced Refractory Castable. Exp. Mech. 47, 761–773.

[RLCR15] Rodríguez, E.A., Limones, A.K., Contreras, J.E., Ruiz-Valdés, J.J., Puente-Ornelas, R., Arato, A.M., Aguilar-Martínez, J.A., 2015. Effect of hercynite spinel content on the properties of magnesia–calcium zirconate dense refractory composite. J. Eur. Ceram. Soc. 35, 2631–2639.

[RoHa70] Rosen, B.W., Hashin, Z., 1970. Effective thermal expansion coefficients and specific heats of composite materials. Int. J. Eng. Sci. 8, 157–173.

[RTVD01] Rotinat, R., Tié, R. bi, Valle, V., Dupré, J.-C., 2001. Three Optical Procedures for Local Large-Strain Measurement. Strain 37, 89–98.

[RoHi06] Roux, S., Hild, F., 2006. Stress intensity factor measurements from digital image correlation: post-processing and integrated approaches. Int. J. Fract. 140, 141–157.

[RoHL12] Roux, S., Hild, F., Leclerc, H., 2012. Mechanical Assistance to DIC. Procedia IUTAM, IUTAM Symposium on Full-field Measurements and Identification in Solid Mechanics 4, 159–168.

[SaBr93] Sakai, M., Bradt, R.C., 1993. Fracture toughness testing of brittle materials. Int. Mater. Rev. 38, 53–78.

[SaBr86] Sakai, M., Bradt, R.C., 1986. Graphical Methods for Determining the Nonlinear Fracture Parameters of Silica and Graphite Refractory Composites, in: Bradt, R.C., Evans, A.G., Hasselman, D.P.H., Lange, F.F. (Eds.), Fracture Mechanics of Ceramics: Volume 7 Composites, Impact, Statistics, and High-Temperature Phenomena. Springer US, Boston, MA, pp. 127–142.

[SYGI88] Sakai, M., Yoshimura, J.-I., Goto, Y., Inagaki, M., 1988. R-Curve Behavior of a Polycrystalline Graphite: Microcracking and Grain Bridging in the Wake Region. J. Am. Ceram. Soc. 71, 609–616.

[ScBS00] Schreier, H.W., Braasch, J.R., Sutton, M.A., 2000. Systematic errors in digital image correlation caused by intensity interpolation. Opt. Eng. 39, 2915–2922.

[ScSu02] Schreier, H.W., Sutton, M.A., 2002. Systematic errors in digital image correlation due to undermatched subset shape functions. Exp. Mech. 42, 303–310.

BY NC ND

[Sels61] Selsing, J., 1961. Internal Stresses in Ceramics. J. Am. Ceram. Soc. 44, 419–419.

[ShSO95] Shah, S.P., Swartz, S.E., Ouyang, C., 1995. Fracture Mechanics of Concrete: Applications of Fracture Mechanics to Concrete, Rock and Other Quasi-Brittle Materials. John Wiley & Sons.

[Shub01] Shubin, V.I., 2001. Mechanical Effects on the Lining of Rotary Cement Kilns. Refract. Ind. Ceram. 42, 245–250.

[SXMF11] Sousa, A.M.R., Xavier, J., Morais, J.J.L., Filipe, V.M.J., Vaz, M., 2011. Processing discontinuous displacement fields by a spatio-temporal derivative technique. Opt. Lasers Eng. 49, 1402–1412.

[StRS90] Steinbrech, R.W., Reichl, A., Schaarwächter, W., 1990. R-Curve Behavior of Long Cracks in Alumina. J. Am. Ceram. Soc. 73, 2009–2015.

[SZXG16] Su, Y., Zhang, Q., Xu, X., Gao, Z., 2016. Quality assessment of speckle patterns for DIC by consideration of both systematic errors and random errors. Opt. Lasers Eng. 86, 132–142.

[SPWS05] Sun, Y., Pang, J.H.L., Wong, C.K., Su, F., 2005. Finite element formulation for a digital image correlation method. Appl. Opt. 44, 7357–7363.

[SuLM97] Sun, Z., Lyons, J.S., McNeill, S.R., 1997. Measuring Microscopic Deformations with Digital Image Correlation. Opt. Lasers Eng. 27, 409–428.

[SWPR83] Sutton, M., Wolters, W., Peters, W., Ranson, W., McNeill, S., 1983. Determination of displacements using an improved digital correlation method. Image Vis. Comput. 1, 133–139.

[SuHB01] Sutton, M.A., Helm, J.D., Boone, M.L., 2001. Experimental study of crack growth in thin sheet 2024-T3 aluminum under tension-torsion loading. Int. J. Fract. 109, 285–301.

[SJPB14] Szczerba, J., Jastrzębska, I., Pędzich, Z., Bucko, M., 2014. Corrosion of Basic Refractories in Contact with Cement Clinker and Kiln Hot Meal. J. Mater. Sci. Chem. Eng. 02, 16–25.

[TaPI85] Tada, H., Paris, P.C., Irwin, G.R., 1985. The Stress Analysis of Cracks Handbook, Third Edition. ASME, Three Park Avenue New York, NY 10016-5990.

[TAKK03] Tanaka, K., Akiniwa, Y., Kimachi, H., Kita, Y., 2003. R-curve behavior in fracture of notched porous ceramics. Eng. Fract. Mech. 70, 1101–1113.

[Tess03] Tessier-Doyen, N., 2003. Etude expérimentale et numérique du comportement thermomécanique de matériaux réfractaires modèles (thesis). Limoges.

[TeGH06] Tessier-Doyen, N., Glandus, J.C., Huger, M., 2006. Untypical Young's Modulus Evolution of Model Refractories at High Temperature. J. Eur. Ceram. Soc. 26, 289–295.

[TKHT91] Tokunaga, K., Kozuka, H., Honda, T., Tanemura, F., 1991. Further improvements in high temperature strength, coating adherence, and corrosion resistance of magnesia-spinel bricks for cement rotary kiln. Presented at the UNITECR 91, Aachen, Germany, pp. 431–435.

[Tsch91] Tschegg, E.K., 1991. New equipments for fracture tests on concrete. Materialpruefung 33, 338–342.

[Tsch86] Tschegg, E.K., 1986. Test method for the determination of fracture mechanics properties. Patent specification No. A-233/86 390 328.

[VHCF15] Valle, V., Hedan, S., Cosenza, P., Fauchille, A.L., Berdjane, M., 2015. Digital Image Correlation Development for the Study of Materials Including Multiple Crossing Cracks. Exp. Mech. 55, 379–391.

[VNCR16] Vargas, R., Neggers, J., Canto, R.B., Rodrigues, J.A., Hild, F., 2016. Analysis of wedge splitting test on refractory castable via integrated DIC. J. Eur. Ceram. Soc. 36, 4309–4317.

[WSBS09] Wang, Y.Q., Sutton, M.A., Bruck, H.A., Schreier, H.W., 2009. Quantitative Error Assessment in Pattern Matching: Effects of Intensity Pattern Noise, Interpolation, Strain and Image Contrast on Motion Measurements. Strain 45, 160–178.

[West39] Westergaard, H.M., 1939. Bearing pressures and cracks. J. Appl. Mech. 6, A49–A53.

[YOIN98] Yoshikawa, M., Ohtani, T., Ichikawa, K., Nakamura, R., Uchida, S., 1998. Evaluation of Layer Thickness to Reduce the Thermal Stress in Multilayer Submerged Entry Nozzles. Taikabutsu Overseas 18, 25–29.

[ZhZh13] Zhang, Q.B., Zhao, J., 2013. Determination of mechanical properties and full-field strain measurements of rock material under dynamic loads. Int. J. Rock Mech. Min. Sci. 60, 423–439.

BY NC ND

List of figures

BY NC ND

BY NC ND

BY NC ND

BY NC ND

CC BY NC ND

List of tables

BY NC ND

Abstract

Optimisation of optical methods for strain field measurements dedicated to the characterisation of the fracture behaviour of refractories: Application to magnesia-based materials.

Magnesia-spinel and magnesia-hercynite bricks destined for thermal shock applications in cement rotary kilns often show an enhanced crack propagation resistance due to an engineered microstructure design. In these materials, microcrack networks resulting from the thermal expansion mismatch between magnesia matrix and spinel/hercynite aggregates promote the activation of energy dissipating mechanisms within the so-called Fracture Process Zone (FPZ) during loading. In this research, the fracture behaviour of magnesia-based model materials was investigated by coupling a refined Digital Image Correlation method (2P-DIC) with the Wedge Splitting Test (WST). The coupling of these advanced characterisation methods has proven to be very effective in measuring important fracture parameters accurately and in highlighting characteristic fracture mechanisms, such as crack-branching. The investigation of microstructure-property relationships underlined the impact of thermally induced microcracks on the thermomechanical behaviour of magnesia-spinel and magnesia-hercynite materials. Despite the rather similar elastic and dilatometric properties of spinel and hercynite single constituents, peculiar microcracking patterns were observed, especially in magnesia-hercynite. In fact, extensive diffusion between magnesia and hercynite during sintering led to the formation of spinel solid solutions around hercynite aggregates. As a result of thermal expansion mismatch with magnesia, these solid solutions contributed to creating numerous fine microcracks confined within the diffusion zone. Initially present within the microstructure, microcrack networks promote an increase of the specific fracture energy during WST experiments. Moreover, the analysis of strain fields measured by 2P-DIC revealed extensive crack branching for magnesia-hercynite materials. In essence, 2P-DIC and WST measurements showed that microcrack networks promoted the development of the FPZ, which in turn induced higher fracture energies. In a refined R-curve approach, effective fracture energies were calculated using crack lengths measured by 2P-DIC, which helped establish strong links between FPZ development and an enhanced crack propagation resistance. The tendencies observed at room temperature during WST experiments were confirmed during thermal cycling experiments using a novel thermal shock device.

Keywords : Refractories, Magnesia-spinel, Hercynite, Thermal shock resistance, Fracture behaviour, Fracture process zone, Digital image correlation

Résumé

Optimisation des méthodes optiques de mesure de champs de déformation pour la caractérisation du comportement à rupture des réfractaires: Application aux matériaux à base de magnésie.

Les briques de magnésie-spinelle et magnésie-hercynite sont fréquemment utilisées dans les fours rotatifs de cimenterie pour leur tenue aux chocs thermiques venant d’une résistance accrue à la propagation de fissures conférée par leur microstructure. Les réseaux de microfissures résultant du différentiel de dilatation thermique entre la matrice magnésienne et les agrégats de spinelle/hercynite favorisent l'activation de mécanismes dissipatifs d’énergie au sein de la zone d’élaboration de la rupture (FPZ) lors d’un chargement mécanique. Dans cette étude, le comportement à la rupture de matériaux modèles à base de magnésie a été étudié en couplant une méthode de corrélation d'images numériques (2P-DIC) adaptée aux problématiques de fissuration avec l’essai de « Wedge Splitting » (WST). Le couplage judicieux de ces méthodes innovantes a fourni des mesures précises des propriétés de rupture et a mis en évidence des mécanismes de rupture caractéristiques, tels que la bifurcation de fissures. L’étude des relations propriété-microstructure a démontré l’impact des microfissures introduites volontairement au sein du matériau sur le comportement thermomécanique de la magnésie-spinelle et la magnésie-hercynite. Malgré des propriétés élastiques et dilatométriques assez similaires entre les inclusions de spinelle et d’hercynite, des mécanismes de microfissuration différents ont été observés, en particulier pour la magnésie-hercynite. En effet, la diffusion entre la magnésie et l’hercynite pendant le frittage a conduit à la formation de solutions solides de spinelles autour des agrégats d'hercynite. Ces solutions solides ont contribué à leur tour à la création de nombreuses microfissures fines par l’effet d’un différentiel de dilatation thermique avec la magnésie. Initialement présents dans la microstructure, les réseaux de microfissures favorisent l’augmentation de l'énergie de rupture des matériaux modèles pendant le WST. De plus, l’analyse des champs de déformation mesurée par 2P-DIC a révélé d’importantes bifurcation de la fissure principale pour les matériaux magnésie-hercynite. Le couplage de la 2P-DIC avec l’essai du WST a démontré que les réseaux de microfissures favorisaient le développement de la FPZ, qui induisait à son tour une augmentation notable de l’énergie de rupture. Dans une approche affinée des courbes-R, des énergies de rupture effectives ont été calculées à l'aide des longueurs de fissure mesurées par 2P-DIC. Cela a permis d'établir des liens étroits entre le développement de la FPZ et une résistance accrue à la propagation de la fissure. Les tendances observées à température ambiante lors des essais de WST ont été confirmées à l’aide d’essais de cyclage dans un nouveau banc de chocs thermiques.

Mots-clés : Réfractaires, Magnésie-spinelle, Hercynite, Résistance aux chocs thermiques, Comportement à rupture, Zone d’élaboration de la rupture, Corrélation d’images numériques